Multifrequency polarimetric microwave measurements of the Greenland ice sheet.

by Julie Anne-Marie Beale

A thesis submitted to the University of London
for the degree of Doctor of Philosophy.

September 1994

Mullard Space Science Laboratory
University College London
Holmbury St.Mary
Dorking
Surrey.
RH5 6NT

ProQuest Number: 10017787

ProQuest 10017787

Abstract.

The Greenland ice sheet is an important component of the global hydrological system and contributes to the global radiation budget. A knowledge of the extent and surface state of this ice sheet is therefore important in predicting and monitoring global climate change. This thesis shows how active and passive multifrequency polarimetric microwave remote sensing measurements may be used to provide such information.

The microwave response of the four different zones of the Greenland ice sheet is investigated. The four zones are the central dry zone, the percolation zone, the soaked zone and the ablation zone towards the edge of the ice sheet (Benson, 1962). High resolution active data from the NASA/JPL AIRSAR airborne synthetic aperture radar, and lower resolution, more extensive, passive data from the Defense Meteorological Satellite Program Special Sensor Microwave Imager (DMSP SSM/I) are used.

A multifrequency polarimetric matrix based computer model is developed to determine the theoretical 3D polarimetric response of simulated geophysical surfaces. This model is based on conservation of energy and predicts the polarimetric content of the reflected signal (amplitude and phase components) and the emitted energy. A method is developed to determine the dielectric constant (and hence moisture content) of imaged areas using the remotely sensed polarimetric signals. This allows classification of the different zones of the ice sheet, so providing a useful tool for mapping the extent of the different ice sheet zones. The annual variation of the polarimetric signals is investigated to determine the seasonal change of the surface state of each zone.

The polarimetric data suggest that subsurface layers or other discontinuities (for example, subsurface ice layers or depth hoar) play a major role in the microwave response of the Greenland ice sheet. This should be considered in future climatological and topographical studies of ice sheets.

Acknowledgements.

To S

Contents   page   number:

List of figures -   page number:

3 Development of new matrix model -

4 Measurements, campaigns and data analysis -

5 Results -

6 Discussion and Conclusions -

Appendix 1 Theory -

6 Discussion and Conclusions -

Appendix 1 Theory -

1 Introduction -

1.1 The Earth's climatic system and global change.

The Earth's climatic system may be symbolized by the diagram given below (figure 1.1). The five major components of the system are the atmosphere, ocean, biosphere (i.e. vegetation), geosphere (i.e. land) and **cryosphere** (i.e. snow and ice).
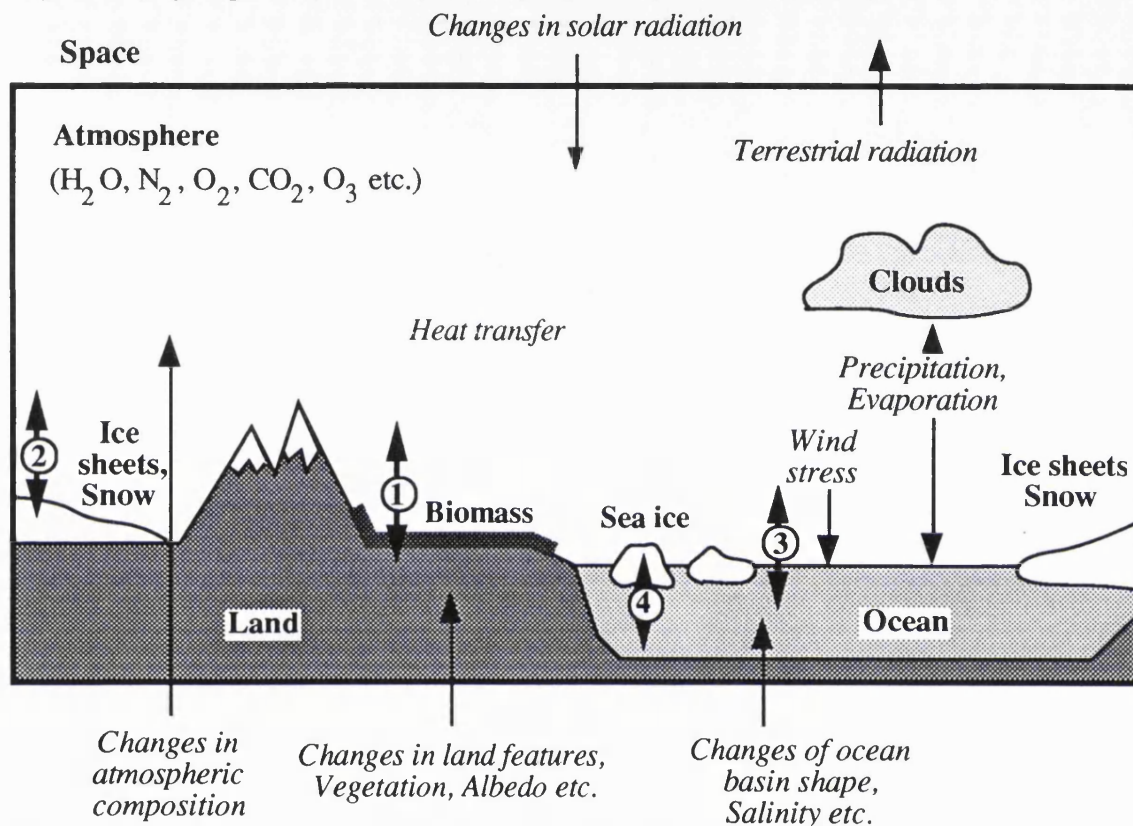
coupled atmosphere - land - ocean - ice system, where the heat transfer between the components are summarized as:

1) atmosphere - land

2) atmosphere - ice

3) atmosphere - ocean

4) ice - ocean

where the biosphere and cryosphere are included within both the land and ocean.

Figure 1.1: Schematic diagram of the Earth's climatic system (after Houghton, 1984, presented in Houghton *et al.*, 1990).

The main energy budget is determined by the incoming short wave solar radiation and the outgoing long wave terrestrial radiation, due to the reflection, absorption and transmission of the atmosphere as shown in figure 1.2.

Sun some solar radiation
is reflected by the earth
and the atmosphere

short wave
(high frequency)
solar radiation

long wave (infrared)
terrestrial radiation

some infrared radiation is absorbed
and re-emitted by the greenhouse gases:
this warms the earth's surface and
the lower atmosphere

Atmosphere

Earth's surface

absorption of solar radiation
warming earth's surface

infrared radiation
emitted from the earth's surface

Earth

Figure 1.2: Effect of the atmosphere, illustrating the energy budget (from Houghton *et al.*, 1990).

The incoming short wave radiation (0.2 - 3µm) is mainly absorbed by the Earth's surface (soil, vegetation, ocean, ice) after passing through the Earth's **atmosphere**.
The incoming solar energy is partly reflected at the underlying land surface. The ratio of the amount of solar radiation reflected from the surface to the total amount incident on it is defined as the albedo of the surface.

The absorbed energy is then re-emitted from the Earth's surface as infrared radiation (3-100µm). The wavelength of the emitted radiation is longer than that of the incident solar radiation as the Earth is cooler than the sun. Some of this emitted radiation is then absorbed and re-emitted by the greenhouse gases within the atmosphere (main natural greenhouse gases are H_2O, CO_2, CH_4, N_2O; and O_3 in the troposphere (lowest 10-15km of the atmosphere) and stratosphere). The presence of these atmospheric gases determines the radiative cooling and heating of the atmosphere.

The evaporation of moisture and the direct heating of the Earth's surface is determined by the interaction of the atmosphere and the underlying land. This provides the heat transfer mechanism by which the energy is transported. The atmospheric processes respond to changes in climate with a timescale of the order of hours or days.

The ocean absorbs approximately half of the solar radiation that reaches the Earth's surface, stores this energy, then redistributes it due to the various currents before releasing it back into the atmosphere, largely by evaporation. The timescale of the response of the ocean to changes in climate depends on the depth, and is of the order of days for the surface, and thousands of years for the depths of the ocean.

The **biosphere** controls the magnitude of the flux of some of the greenhouse gases (including CH_4 and CO_2) between the atmosphere and the underlying land surface. The biosphere processes react on the timescale order of hours (plankton growth) to centuries (tree growth).

The effect of the **geosphere** on climate is mainly concerned with the hydrological cycle. The amount of water stored as soil moisture influences the biosphere; water run off influences the ocean circulation and the interaction of soil with the atmosphere influences the flux of greenhouse gases. These land processes react on the timescale order of days to months.

The **cryosphere**, classified as seasonal snow on land, sea ice, permafrost, river and lake ice, mountain glaciers and ice sheets, ice shelves and icebergs; plays an important part in the climatic system. The extent of seasonal snow cover, and ice formation and melt, causes large changes in albedo which affect the global radiation budget. Changes occur on a timescale of days for snow cover and of seasons for the ice.

The ice sheets contain ~80% of the Earth's fresh water supply and therefore act as an important global hydrological reservoir. Any changes in their size will affect the global sea level. Complete melting of the Earth's ice could cause a 72m rise in mean sea level (Oerlemans and van der Veen, 1984). The response time for the ice sheets ranges from decades to millennia (Houghton *et al.,* 1990).

1.1.1 The ice sheets and global change.

Ice sheets are nearly continuous masses of glacier ice, formed by the accumulation of snow and ice. The contents of the ice sheets are continually changing due to the accumulation from snow fall and the ablation processes; including evaporation, surface melting, draining by subsurface ice streams and the calving of icebergs.

The ice sheets are an important part of the terrestrial cryosphere as snow, ice and glacial extent are key parameters in the climatic system due to their effect on the atmospheric heat

transfer and the global radiation budget.

The ice and snow albedo feedback mechanism is positive, which therefore acts to accelerate climatic change. For an increase in temperature, the snow and ice cover decreases, thus decreasing the albedo and increasing the absorption, therefore resulting in further temperature increase. This relationship is discussed further in section 1.1.2.2 with specific reference to the Greenland ice sheet.

Details of the snow moisture content and the extent of the snow cover are necessary for hydrological calculations. The water balance, ocean salinity and sea level are affected by the ice sheets, which must therefore be considered in determining the global hydrological cycle.

The ice sheets act as an important store of fresh water. If they should melt it would have a great effect on the global sea level with important economic and social consequences. The amount of fresh water stored in glaciers varies due to changes in climate. Studies of ice sheets are therefore made to provide both climatological and important economic information.

1.1.2 The Greenland ice sheet and global change.

The Greenland ice sheet is a remnant of the last ice age and remains because its height is sufficient to keep the temperature low enough to maintain it. If it were to melt it would not reform in today's climate.

If the Greenland ice sheet were to completely melt the effect would be to increase the mean sea level by approximately 6m. This is calculated from the ice volume expressed as an equivalent sea level rise, with other factors remaining constant (Oerlemans and van der Veen, 1984).

Recent models of the behaviour of the ice sheets in a doubled CO_2 climate indicate that surface warming would occur sooner over Greenland than over the larger Antarctic ice sheet indicating that it may be particularly important to study Greenland for the detection of climate change (Houghton *et al.*, 1990).

1.1.2.1 The position and structure of the Greenland ice sheet.

Greenland is an island situated in the Northern hemisphere, between ~60° and ~83° N, and ~20° to ~66° W in the Arctic Ocean. The exposed rock areas at the coastal edges of Greenland are permanently ice free, but the central area is covered with ice. The bedrock of Greenland is dipped, with mountainous edges and the interior bedrock is close to sea level. The maximum surface elevation of the ice sheet is ~3300m and the profile of the ice sheet may be assumed to be approximately parabolic in shape, with the highest part in the dry central region and the lowest at the edges near the coast.

The total area of the Greenland ice sheet is ~$1.7*10^6$ km^2 and the mean ice thickness is 1530m, with the total ice volume ~$2.6*10^6$ km^3. About 20 large glaciers at the edge of the ice sheet form the outlet of the ice sheet into the sea, where large icebergs are formed. Loss of ice by the calving of icebergs and the other ablation processes (evaporation, melting and draining) are almost equally responsible for the loss from the ice sheet. The annual accumulation due to snowfall is ~34cm of ice depth per year. These dimensions are all taken from Oerlemans and van der Veen (1984). In today's climate it is presently assumed that the mass balance of the Greenland ice sheet is zero and that Greenland is in dynamic equilibrium (Oerlemans and van der Veen, 1984).

The Greenland ice sheet may be considered to consist of four different zones: (1) dry zone, (2) percolation zone, (3) soaked and (4) ablation zones. These zones are defined by Benson (1962). The dry snow area is mainly unaffected by melting and exists in the Northern interior or highest elevations of the Greenland ice sheet. The percolation zone exists where localized melting in summer causes the water to percolate through the surface layers of snow before refreezing, forming ice lenses and layers beneath the surface. The wet snow area is that where all the snow deposited over winter becomes saturated during the melt season. The ablation zone is the area nearest the end of the glacier where the production of melt water is the main ablation process. This ablation zone extends from the firn line (the highest elevation to which the snow line recedes in summer) to the end of the glacier (Hall and Martinec, 1985). The original definition of the zones as given by Benson (1962) is still widely used. More details of the different snow facies may be found in Paterson (1981).

A schematic diagram showing the different zones of the ice sheet is given in figure 1.3 and the location of these zones over the Greenland ice sheet is given in figure 1.4.
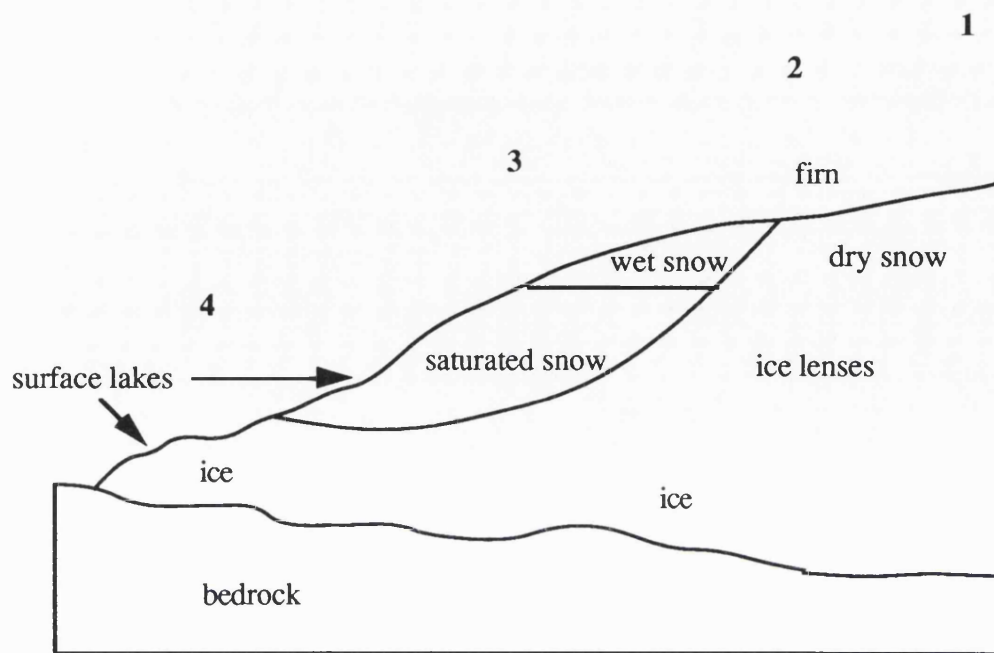
Figure 1.3: Different zones of glacial ice sheets in order of glacier descent:
1) dry snow
2) percolation zone
3) wet snow
4) ablation zone.
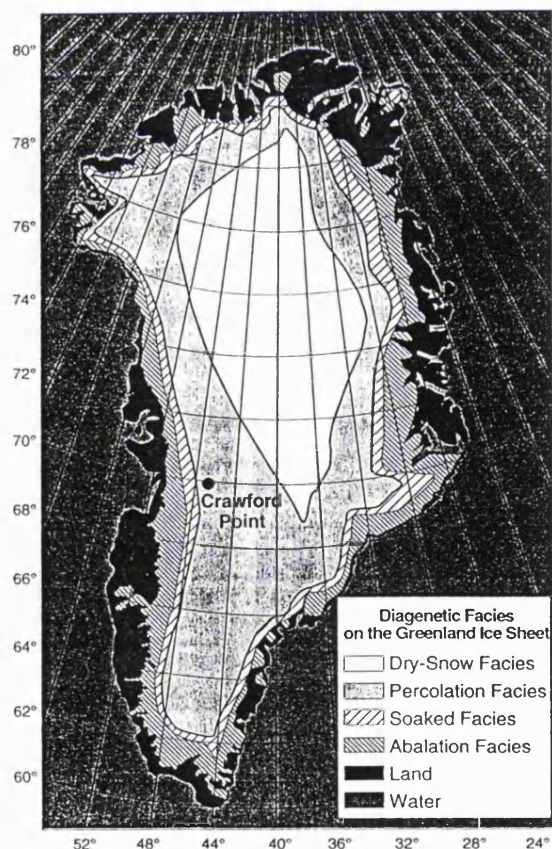
Figure 1.4: Location of zones of the Greenland ice sheet (Benson, 1962)
(from Jezek, 1994, showing Crawford Point test-site in the percolation zone).

1.1.2.2 Mass balance of the Greenland ice sheet.

Kuhn (1989) gives the following equation to describe the factors affecting the mass balance (B) of the ice sheets:

Mass Balance = Accumulation - |Ablation|

where Accumulation = Precipitation (P) + Redistribution by snow drift (D) + Deposition or erosion of snow by avalanches (A)   (usually positive terms)

and Ablation = Evaporation (E) + Melting (M) + Calving (C)   (negative terms)

or B = P + D + A + E + M + C

Equation 1.1: Kuhn's equation of mass balance.

These different processes must all be considered to determine the net effect on the ice sheets.

Exactly how the Greenland ice sheet would respond to changes in temperature is uncertain. It is thought that the precipitation rate would increase at this latitude in a warmer climate, producing more snowfall on the ice sheet. This therefore causes the accumulation rate to increase and the overall mass balance of the ice sheet would also then increase. On a short timescale it is thought that the mass balance would increase, but any rises in the surface temperature would increase the surface melting and lead to the retreat of the ice sheet and decrease its size.

Key parameters to be measured include the extent, surface state, and surface velocity of the ice sheet as these all affect the net balance of the ice sheets.

The extent of the ice sheet is important for the overall mass balance, and any changes observed in the size may indicate climate change. Mapping the extent of the different zones of the ice sheet and monitoring any differences in the zones over a period of time gives information on the variation within the ice sheet which may occur due to climatic changes.

The extent of melt is a particularly important parameter to be measured for predictions of the ablation rate of the ice sheet. Knowledge of the surface state over a period of time gives valuable input for climate modelling.

In addition, the surface velocity of the ice sheet may be measured by temporal studies of high resolution imagery of the surface. The repeat measurements may show the movement of discontinuities within the ice sheet and the surface flow may be calculated. This information is useful for modelling the dynamics of the ice sheet.

There is presently considerable uncertainty as to the current state of the Greenland ice sheet, mainly due to the lack of available data. Estimates of the total mass budget of the Greenland ice sheet made over the last 30 years are summarized in table 1.1 below (mass budget given in 10^{12} kg yr $^{-1}$).

The error in these estimates is thought to be in the region of 30% (Houghton *et al.*, 1990) and more measurements are therefore needed to improve these estimates. The difference in these estimated figures are large, and the zeros in the balance column do not indicate stability but rather, dynamic equilibrium. The equilibrium is then assumed, where: Balance = Accumulation - |(Ablation + Calving)|.

Mass budget of the Greenland ice sheet (in 10^{12} kg yr^{-1})

Source	Accumulation	Ablation	Calving	Balance
Bader(1961)	+630	-120 to -270	-240	+270 to +120
Benson(1962)	+500	-272	-215	+13
Bauer(1968)	+500	-330	-280	-110
Weidick(1984)	+500	-295	-205	0
Reeh(1985)	+487	-169	-318	0
Ohmura and Reeh(1990)	+535	/	/	/

Table 1.1: Estimates of the mass budget of the Greenland ice sheet in 10^{12} kg yr $^{-1}$ (Houghton *et al.*, 1990).

The variation in the estimates of the mass budget of the Greenland ice sheet made over the last 30 years are large and uncertain. The sensitivity of the ice sheet to global change is also unknown. It is thought that the precipitation rate may increase over Greenland in a warmer climate, therefore increasing the snow accumulation rate and increasing the mass balance. However, the ice sheet would retreat in a warmer climate due to the ablation processes of surface melt, calving of icebergs and increased basal water flow (run off).

Changes in the precipitation rate and cloud cover as well as temperature changes will affect the overall state of the ice sheet. An increase in the global mean annual air temperature of $1^\circ C$ would cause an increase in the annual precipitation by about 5%, which counteracts the overall effect on the mass balance of the ice sheet by about 30% (Houghton *et al.*, 1990).

Recent estimates of the sensitivity of the Greenland mass balance to climate change are given in table 1.2 below, in rate of change of global mean sea level (mm yr^{-1}).

Source	T(+1°C)	P(+5%)	C(+5%)	Comments
Ambach and Kuhn(1989)	+0.31	-0.13		Analysis of EGIG data
Bindschadler (1985)	+0.45			EGIG data/ retreating margin
Braithwaite and Olesen(1990)	+0.36 to +0.48			Energy balance calculation
Oerlemans (1990)	+0.37	-0.11	-0.06	Energy balance model

Table 1.2: Estimates of the sensitivity of the Greenland mass balance to climate change in rate of change of global mean sea level (mm yr^{-1}) (Houghton *et al.*, 1990) where T = temperature, P = precipitation, C = cloudiness.

The error in predicting the sensitivity of the Greenland ice sheet to changes in climate is large (0.3 ± 0.2mm yr^{-1} per degree warming) mainly due to the unknown change in the precipitation patterns over Greenland in a warmer climate.

The effect of iceberg calving is also uncertain as it is not known whether the calving will increase with increasing basal flow. Also, the ice near the edge of the ice sheet is almost afloat and therefore the contribution to sea level change would be negligible. The thinning of the ice sheet further inland is unlikely to affect the sea level in the next 100 years (Houghton *et al.*, 1990).

The global sea level has been rising ($\sim$1-2mm yr^{-1}) over the last 100 years, apparently due largely to the thermal expansion of the oceans and also from the increased melting of

glaciers and the margins of the Greenland ice sheet (Houghton *et al.*, 1990). The possible contribution of this past sea level rise from the decadal changes in summer temperature over Greenland is calculated to be ~ 0.23mm yr^{-1} ($\pm$0.16mm yr^{-1}) and therefore the contribution from Greenland is seen to be rather less than that from glaciers and thermal expansion of the oceans (Houghton *et al.*, 1990).

The overall effect of the Greenland ice sheet in a warmer climate is still uncertain though, as the increased snowfall may offset the increased melting and runoff (Houghton *et al.*, 1990).

1.2 Remote sensing.

Remote sensing instruments such as imaging radar are an increasingly important method of data collection especially over inaccessible and inhospitable areas such as the polar ice sheets.

The advantages of Earth observation by remote sensing techniques include the ability to collect vast amounts of data quickly and accurately, and the uniform method of data collection by satellite instruments enables the measurements to be correlated as they are continued over a period of time. These repeat measurements are useful for monitoring and investigating changes.

The key parameters of the extent and the surface state of ice sheets may be measured by microwave remote sensing instruments such as active Synthetic Aperture Radar (SAR) systems (Curlander and McDonough, 1991), and passive microwave radiometry systems (Massom, 1991).

1.2.1 Polarimetric microwave remote sensing.

The particular advantage of microwave instruments (compared with visible and infra-red methods) is that they offer all weather and day/night viewing thereby continuing to provide data regardless of weather or daylight conditions.

The additional advantage of polarimetric systems is that the response for the imaged surface for incident waves of different polarization states may be determined. This polarimetric data can give extra information of the imaged area. For example, the difference between the linear polarization states (HH and VV) of return power may be

used to calculate the mean dielectric constant of the surface. This information may then be used to determine actual geophysical properties of the imaged surface, for example the water content of snow.

1.3 Basics of polarimetric remote sensing: Polarimetry.

The state of polarization of an electromagnetic wave is determined by the path of the tip of the electric field vector, perpendicular to the direction of propagation of the wave. A diagram showing a linear vertically polarized electro-magnetic plane wave is given below (figure 1.5). As the wave travels along the y direction, the E vector oscillates in the vertical (z) direction and hence this type of wave is of linear vertical polarization. Conversely, if the E vector were to oscillate in the x direction only, the wave would be a linear horizontally polarized wave.

Any wave may be represented by its vertical and horizontal components, whether it is of simple linear, circular or any general elliptical polarization. The amplitude and phase of the two mutually perpendicular components and their behaviour with time is sufficient to describe the complete nature of the wave.

The co-ordinate system adopted to describe these components is important. For the work in this thesis a right-hand system is adopted and the definition of parallel and perpendicular polarization used is given in Appendix A1.1.

(Further details of the polarization state of an electromagnetic wave, the ellipticity and orientation, Poincaré sphere representation with co, cross and conjugate points, and the 3D polarimetric response plots are given in chapter 2 of this thesis. Useful references are: Born and Wolf (1980); Mott (1986); Stutzman (1993); Kong (1990); Feynmann (1963)).

E field
(vertically polarized wave)
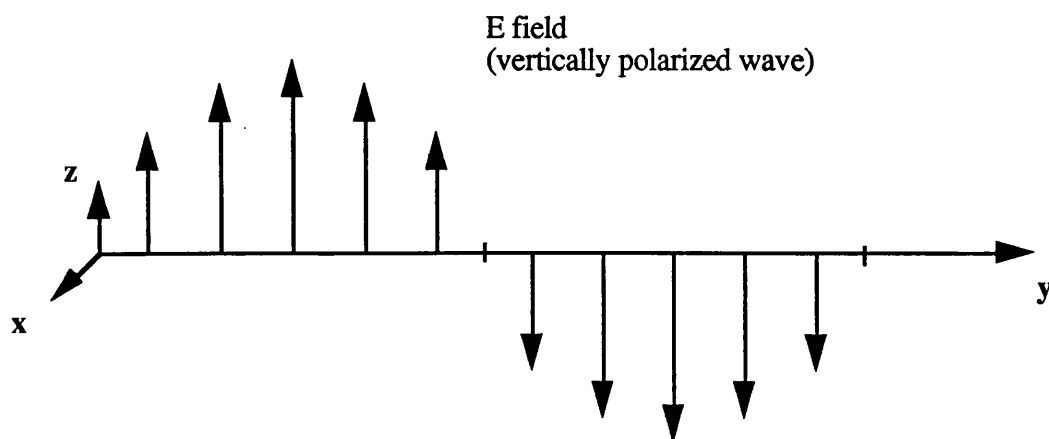
Figure 1.5: Electromagnetic plane wave (vertical polarization).

The interaction of active radar with an imaged target depends on the polarization state of the incident signal. Recording the complex return signal (amplitude and phase components) for two mutually perpendicular incident polarization states enables the total polarimetric radar response of the imaged surface to be determined. This technique, known as radar polarimetry, gives greater information about the parameters describing the surface than for the more conventional single fixed polarization radar.

The use of polarization diversity in radars is reviewed by Guili (1986).

The transmit polarization diversity of the NASA/JPL AIRSAR imaging polarimetry system is achieved by alternately transmitting horizontal and vertical polarization signals. The receive polarization diversity is attained by measuring the complex components (amplitude and phase information) of the return signal at both horizontal and vertical polarization (van Zyl *et al.*, 1992).

This active imaging radar polarimeter measures the amplitude and phase components of the returned signal which allows the determination of the scattering matrix for a small element of the imaged surface. The complex scattering coefficients for all transmit and receive polarizations are determined by polarimetric antenna synthesis techniques (Zebker *et al.*, 1987; van Zyl *et al.*, 1987). The theory relevant to the work in this thesis is detailed in chapter 2.

The return power as measured by the polarimeter is displayed as a 3D plot showing the polarimetric response of the surface. These 3D polarimetric response plots show the variation of the co and cross polar power of the reflected signal from the surface as a function of the orientation and ellipticity of the incidence wave. The co polar and cross polar return power is plotted on 3D grids as shown below in figure 1.6. The normalized output power is given on the z axis, for all possible input polarization states of ellipticity (-45 to +45 degrees, on y axis) and orientation (0 to 180 degrees, on x axis) of the incident wave.
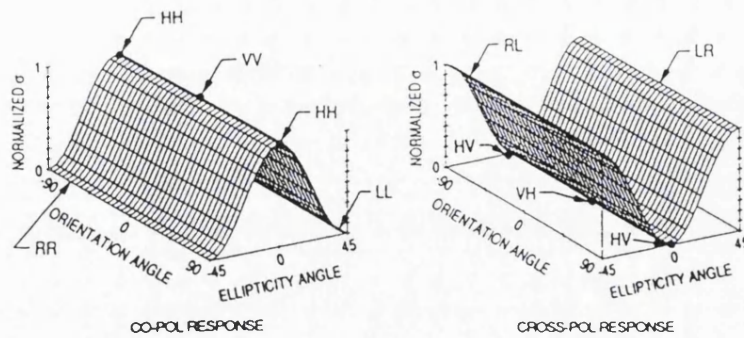
Figure 1.6: 3D polarimetric co and cross polar output power response plots.

The use of radar polarimetry for geoscience applications is discussed by Ulaby and Elachi (1990). The range of applications include glaciology, hydrology, oceanography, ecology and vegetation science, geology, land use and terrain classification.

1.3.1 Active systems.

Active microwave radars measure the imaged area to high resolution, independent of the weather or daylight conditions.

The multifrequency fully polarimetric data sets from active multifrequency fully polarimetric radar systems such as the NASA/JPL AIRSAR, offer additional information as the different frequency radar will penetrate certain surfaces (e.g. snow and ice) to different depths, giving information about the dielectric constant of the surface and subsurface material and the internal discontinuities. The penetration depth is dependent on the wavelength (and therefore the frequency) of the operating radar. Use of a variety of different frequencies provides a range of penetration depths into the snowpack of low dielectric constant. High frequency radar is used for imaging the surface whereas lower frequency radar may be used to penetrate the snowpack and give details of the dielectric constant of the subsurface material.

The radar is sensitive to features comparable to the size of the operating wavelength and is affected by the orientation of discontinuities. Multifrequency, fully polarimetric radar with a range of operating wavelengths and full polarization capability may provide additional information about the size, nature and orientation of discontinuities. This is particularly important for studies of subsurface features; for example ice lenses and layers within the ice sheets.

1.3.1.1 NASA/JPL DC8 AIRSAR system.

The AIRSAR multifrequency fully polarimetric images analysed in this thesis are measured using the NASA/JPL DC8 AIRSAR system. The AIRSAR instrument operates at three frequencies; P, L and C band (0.4, 1.2, 5.3 GHz) with full polarization capability. Both the amplitude and phase information of the received signal is retained for both the horizontal and vertical (H and V) polarization transmit/receive antennas, enabling the production of full multipolarization imagery (Zebker *et al.*, 1987; van Zyl *et al.*, 1987).

This active airborne polarimetric radar system consists of a Synthetic Aperture Radar viewing to the left-hand-side of the McDonald Douglas DC8 aeroplane. Typical values of the range of incidence angles are ~20 degrees for the near edge of the image and ~60 degrees for the far edge. A typical image size is ~12*8 km^2 (azimuth*slant range), with pixel size ~ 12*7m^2 (van Zyl *et al.*, 1992).

The geometry of this airborne imaging system is given in figure 1.7 below.
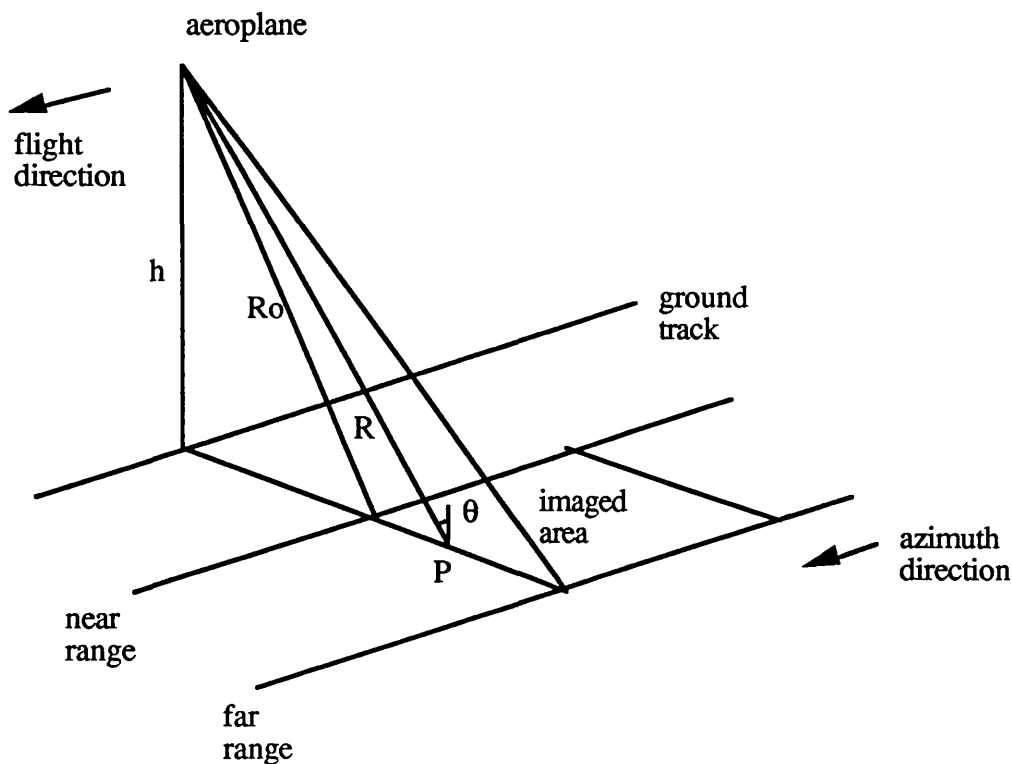
Figure 1.7: Geometry of the NASA/JPL DC8 AIRSAR system, where
Ro = slant range to near edge of image, R = slant range to imaged point P
θ = incidence angle at point P, h = altitude.

The AIRSAR system is successfully used to collect data for a wide range of different investigations. Many papers detailing the progress in using AIRSAR for the applications of terrain classification, geology, ecology and vegetation science, hydrology, oceanography and glaciology are given in the AIRSAR workshop summaries (van Zyl, 1992).

The NASA/JPL DC8 AIRSAR system may also be used in interferometric mode. The along-track and across-track interferometers (ATI, XTI) are described by van Zyl et al. (1992). The across-track interferometer measures surface heights and the along-track interferometer measures surface velocities.

The TOPSAR system (across-track interferometer) uses the two C band antennas (vertical polarization) mounted vertically above each other to measure topography. The TOPSAR system and across track interferometric results are detailed by Zebker and Goldstein (1986) and Zebker et al. (1992).

The along-track interferometer (C, L bands) is used to measure surface velocities of, for example, ocean surface currents, as described by Goldstein and Zebker (1987).

1.3.1.2 Use of multifrequency multipolarization SAR for polar climate studies:

i) Snow moisture content.

The moisture content of snow may be measured and monitored using SAR as the radar is sensitive to the electrical properties of the imaged area. The dielectric constant of snow is dependent on the water content, so the moisture content may be determined from the radar return. The radar parameters of frequency, incidence angle and polarization, and the physical parameters of the snow including density, liquid water content, particle size and shape, ice content, and roughness parameters all affect the radar backscatter.

Recent work by Shi and Dozier (1992a,b) evaluates the radar response to snow wetness. An algorithm for determining the moisture content of snow using C band polarimetric measurements is developed.

Shi and Dozier (1992a) note that the current understanding of the radar response of snow is limited due to few ground and airborne measurements, covering only a small range of

the possible snow conditions, and the lack of understanding of the importance of determining the correct scattering mechanism. Most importantly, the need for a complete polarimetric model to describe the backscattering at different polarization and incidence angles in terms of the snow physical parameters is stated.

ii) Snow extent and seasonal snow cover.

Snow extent may be mapped using SAR. A method of mapping snow and glacier covered areas is described by Shi, Dozier and Rott (1992) using polarimetric SAR data. The polarimetric response from NASA/JPL AIRSAR is analysed for three different data sets; of wet snow, glacier ice and a rock and moraine region. Using C band AIRSAR data it is found that this classification method accurately determines the snow and glacier regions but has less success in discriminating between the glacier and moraine regions, independent of the surface roughness. The ability to map snow covered regions without any topographic information is found to be effective.

The seasonal snow cover may be determined from multitemporal SAR imagery. The multifrequency radar system allows information about the surface and subsurface material to be obtained. The depth of penetration of the radar signal depends on the wavelength (or operating frequency) of the SAR, so multifrequency SAR imagery gives additional information. The surface characteristics are more easily discernible using high frequencies, and lower frequencies may be used to give information about subsurface effects.

iii) Ice sheet surface state.

Seasonal melt areas of ice sheets may be determined and monitored using SAR from the change in the return power noted for the melt areas. Areas covered by the melt pools on the ice sheet appear dark on a SAR image due to the low return power from the open water. This is due to the smooth surface of the open water acting as a specular reflector, directing the energy away from the receive direction. The surrounding snow appears as the brighter areas on the SAR image. This is illustrated by an image measured by the AIRSAR instrument over the ablation zone in SouthWestern Greenland, Aug.1989 (Jezek et al. 1993). See chapter 5 for a copy of this image (Total power 233-1 image).

Information on the extent of the melt pools in the ablation zone is important in determining the temporal changes over the ice sheets. The extent of the melt pools and the duration of the melt season is determined and monitored as any changes noted from temporal studies

may indicate climate change. This is especially important for the Greenland ice sheet as it is thought to be extremely sensitive to climate changes (Houghton *et al.*, 1990).

Jezek *et al.*(1993) also note that the multi-frequency AIRSAR data show that the subsurface crevasses appear to be more noticeable at P band than at C band due to the greater penetration depth of the lower frequency radar. Some modelling work is undertaken with results that compare well for the C band data.

The AIRSAR (1989) data is compared with SEASAT SAR (1978) data (L band, single polarization HH) over the same area. These two sets of data show that the location of the surface lakes remained unchanged over the ten year time interval of the two data takes. The position of the surface lakes is therefore thought to be related to basal topography as the ice flow of the glacier is continuous, but the overall shape appears to remain constant.

Previous work using single polarization SAR imagery to study the Greenland ice sheet includes work by Vornberger and Bindschadler (1992), Bindschadler *et al.* (1987). Vornberger and Bindschadler (1992) use Landsat (passive, visible and infrared) and airborne SAR (active, X band, HH polarization) data over Greenland to produce co-registered scenes. Two study areas were used: a moraine area and a lakes area in Southern Greenland. The penetration of the SAR data through winter snowpack is noted, and the effect of liquid water is discussed.

Bindschadler *et al.* (1987) discuss the glaciological features that may be studied using satellite and airborne SAR. Scenes from SEASAT SAR (L band, single polarization HH) and X band HH airborne SAR over Greenland are discussed and compared. Surface lakes and stream systems are identified and the mottling of the surface on the image is thought to be related to topography, possibly due to the wind crust.

iv) **Mass balance of ice sheets.**

Polarimetric SAR information may be used in conjunction with interferometric SAR for topographic studies and velocity measurements of the ice sheets. These high resolution data sets from active SAR are important in calculating the mass balance of the ice sheets and for determining any changes that may be occurring.

The polarimetric data are used to determine the dielectric properties of the imaged area. This knowledge of the mean dielectric constant of the imaged area enables the penetration depth of the incident signal to be determined.

The across-track interferometric data may used to calculate the topography of the imaged area if the penetration of the radar signal into the ice sheet is also considered using information of the dielectric constant from the coincident polarimetric data. The C band interferometric radar (TOPSAR system) will penetrate different surfaces to different depths, depending on the complex dielectric constant of the material. The real and imaginary parts of the complex dielectric constant of dry snow are lower than that for ice or water and so the radar signal will penetrate surface firn to a greater depth than if the surface were, for example, ice or water where there is very little penetration. This penetration factor must be taken into account for topographic studies. As an example; the major source of the return radar signal measured at a test-site in the percolation zone of the Greenland ice sheet is found to be from a subsurface ice layer (Jezek and Gogineni, 1992).

The information of the dielectric constant from polarimetric data may therefore be used to determine the penetration depth of the radar signal and hence give the topography of the ice sheet using the across-track interferometric SAR data. This information of the topography may then be used to study changes of the profile of the ice sheet, then used for calculations of the mass balance of the ice sheet. Typical values of the surface velocity of the Greenland ice sheet are ~5m/a in the central region and ~100m/a towards the edge of the ice sheet (Oerlemans and van der Veen, 1984).

Along-track interferometric data may be used to measure the velocity of the ice sheet. This knowledge of the ice velocities over the ice sheet is useful for studies of the ablation rate of the ice sheet. The ice moves slowly in the central part of the ice sheet and more quickly at the edges due to conservation of mass (Oerlemans and van der Veen, 1984). Any temporal changes in the measured velocities at any position over the ice sheet may indicate a change in the ablation rate and hence the overall mass balance of the ice sheet.

The velocity profile at any position of the ice sheet also changes with the vertical depth as shown in figure 1.8 below (from Oerlemans and van der Veen, 1984). It is therefore necessary to know the penetration depth of the incident radar signal in order to determine the origin of the return radar signal, and hence the position at which the velocity is measured within the snowpack. This may be determined using coincident polarimetric data.

This information of the dielectric constant of the imaged position enables any changes noticed in the repeat measurements of the velocities at any one position to be identified as either being due to actual differences in the measured velocity of the ice sheet at the

measured point, or simply due to a change in the vertical structure of the ice sheet at that particular point. If the dielectric constant of the ice sheet at the particular imaged position has changed then the penetration depth will also have changed. The return signal may then originate from a different position within the snowpack and hence record a different ice velocity. The noted change in the measured velocity then indicates this change in vertical structure of the ice sheet at that position and may not necessary be directly indicative of a change in the overall ice velocity and ablation rate.
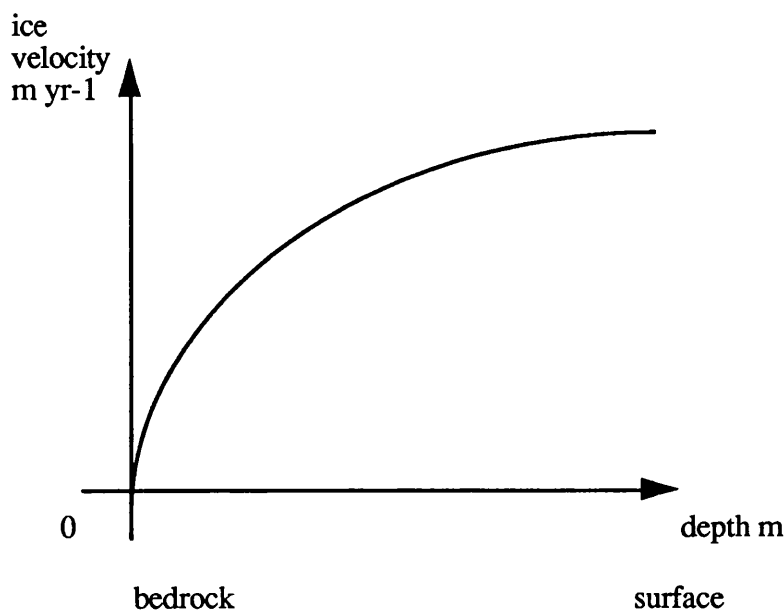
Figure 1.8: Typical velocity profile of the ice sheet with depth (from Oerlemans and van der Veen, 1984).

1.3.2 Passive systems.

Passive microwave systems measure the emitted radiation from the imaged area. Passive microwave radiometry is used to measure the extent, surface state and temperature, and the snow water equivalent of snow covered surfaces. Knowledge of these parameters is important for climate studies as the presence of even a thin layer of snow cover changes the albedo of the surface from ~0.2 (land) to ~0.8 (snow) which affects the local radiation balance by reducing the heat exchange between the atmosphere and the ground (Oerlemans and van der Veen, 1984). Information on the extent and coverage, and the melting of the snow cover is also important for hydrological studies.

The main limitation of the passive microwave systems (such as the SSM/I) compared with

the active microwave radar systems (for example, the SAR systems, section 1.3.1) is the large footprint size of the passive antenna, leading to low resolution of images (pixel size $25*25$ km^2 for SSM/I).

1.3.2.1 Passive microwave (SSM/I).

Passive microwave data as measured by the DMSP SSM/I instrument (Defense Meteorological Satellite Program Special Sensor Microwave Imager) for the various zones over the Greenland ice sheet are analysed in this thesis. A diagram of the conically scanning instrument is given in figure 1.9 below. The SSM/I has a sun-synchronous, near-polar orbit, at altitude 883km, with a swath width of 1400km. The data as supplied by The National Snow and Ice Data Center (NSIDC) are binned into a $25*25$km^2 polar grid. The resolution (pixel size) of the data is therefore $\sim25*25$km^2, with incidence angle ~53.1 degrees on a horizontal surface depending on the frequency used, as shown in figure 1.9 below. For the 19.2 GHz microwave channel the incidence angle is ~53.2 degrees.

The SSM/I instrument measures the passive emitted radiation at 19.2 GHz (V and H polarizations), 22 GHz (V polarization only), 37 GHz (V and H polarizations) and 85 GHz (V and H polarizations). The 19.2 and 37 GHz values are analysed in this thesis as the difference for the two polarizations at frequencies closest to that of the AIRSAR instrument is of the main interest. These frequencies are still much higher than that of the AIRSAR instrument (which operates at C, L and P band; 5.3, 1.2, 0.4 GHz) so direct comparisons of the passive (SSM/I) and active (AIRSAR) data cannot be made.

The SSM/I instrument measures the brightness temperature T_B for parallel (H) and perpendicular (V) polarizations, given by T_{Bh} and T_{Bv} ; where $T_B = E\,T_s$ and E is Emissivity, and T_s is the surface temperature, where the effects of atmospheric attenuation are removed in the calibration of the data. The emissivity of the surface is polarization dependent for the oblique incidence operation of this system, represented by E_H for horizontal polarization and E_V for vertical polarization.

The mean daily average values of the brightness temperatures are used in the analysis as this removes the need to include the diurnal temperature effect since the day/night temperature difference is averaged out.

Further details on the operation of the instrument and information on the data produced are given by Massom (1991) and the SSM/I user's guide (1992).
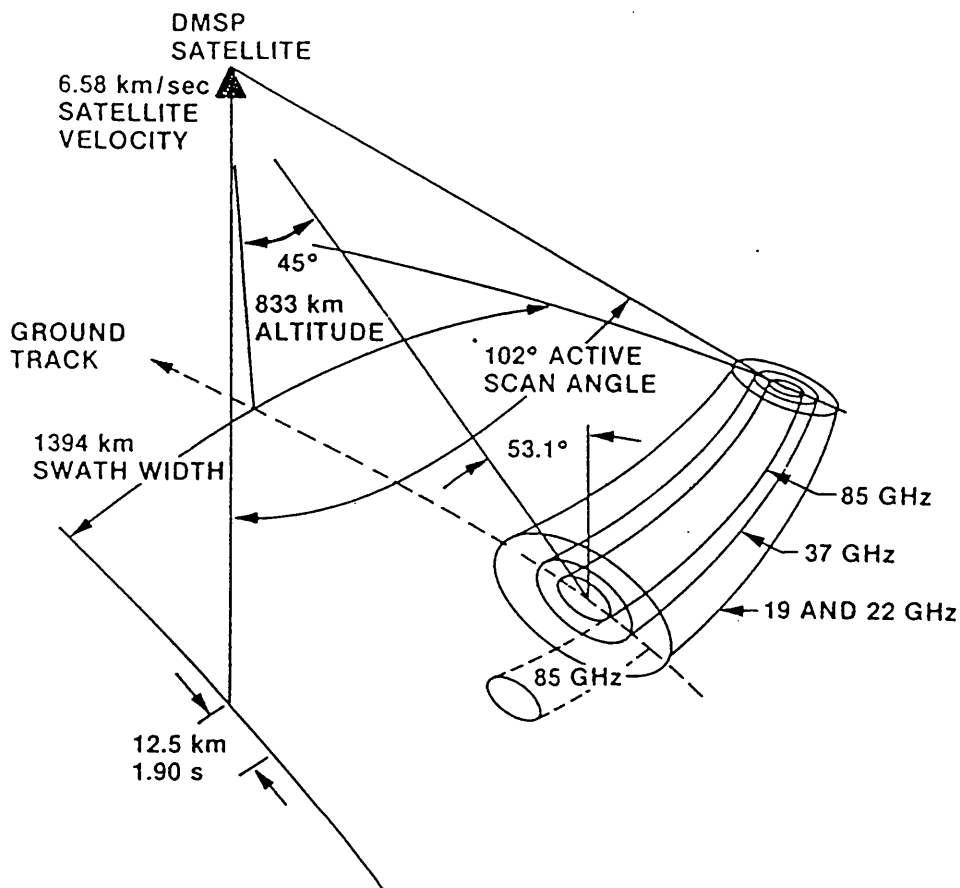
Figure 1.9: Geometry of DMSP SSM/I instrument (Massom, 1991).

1.3.2.2 Use of passive microwave radiometry for polar climate studies:

i) Seasonal snow cover.

Passive microwave radiometry is used to measure the extent and the snowline of seasonal snow, the surface state (wet or dry snow) and the water equivalent or depth of this snow cover.

The snow boundaries may be measured by noting the sharp drop in the measured brightness temperatures on passing over land to snow surfaces, simply from the surface temperature difference of land and snow covered surfaces. The surface temperature of

snow covered surfaces is lower than that for land. In order to distinguish between melting snow and snow free surfaces, knowledge of the snow extent from visible imagery is required as the measured temperature for these two surfaces may appear similar (Foster, 1984).

Snow water equivalent/snow depth may be estimated as the microwave attenuation increases with snow water content/ depth. The brightness temperature decreases as snow depth increases (from measured data with snow layer increasing up to 1m depth) as the measured temperature is increasingly from the colder snow rather than from the underlying ground. The empirical relationships between snow cover depth/ water equivalent and measured brightness temperature are valid for specific test-sites and it is not easy to extrapolate the relationship between measured brightness temperature and snow depth/snow water equivalent for other areas (Foster in Ulaby et al., 1986, Chapter 19, p.1627).

Radiometry at 50° incidence angle is found to give lower brightness temperatures and the best correlation between the measured brightness temperatures and snow depth as the oblique incidence angle increases the penetration of the signal. The extent and water equivalent/depth of dry snow may be determined using radiometry at 37GHz (Ulaby et al. 1986).

The onset of snow melt may be measured as the emissivity of snow initially increases with the production of liquid water in the snowpack. For increasing water content (by volume) from 0 (dry snow) to 4%, the water coats the snow grains and increases the internal absorption. This decreases the volume scattering and increases the emissivity, thus causing the brightness temperature to increase. Therefore, for increasing water content by volume (W) from 0 to 4%, the emissivity and brightness temperature increase. The polarization difference is found to decrease on the initial production of liquid water in the snowpack. For a further increase in water content (W > 5%) the emissivity decreases as the dielectric constant of the snowpack increases with increasing liquid water content (Foster, 1984). The polarization difference then increases.

The onset of snow melt may alternatively be noted by multitemporal observations of the same test-site. Prior to melting, the surface undergoes many thawing and freezing stages with a corresponding variation in the measured brightness temperatures. Areas that show a rapid change in the measured temperature for consecutive passes are designated melt areas (Ulaby et al., 1986).

ii) Ice sheet surface state.

Passive microwave radiometry may also be used to measure the surface temperature and surface state of the ice sheets.

Swift *et al.* (1985) detail results from active and passive airborne measurements over the Southern Greenland ice sheet. The passive microwave C band radiometric data show a decrease in the measured brightness temperature on descent of the ice sheet, from the dry zone over the percolation zone to the soaked/ablation zone, where the brightness temperature is found to increase. This radiometer operates at nadir, with circular polarization. The decrease of the passive emitted radiation in the percolation zone is thought to be caused by the presence of subsurface ice lenses and ice layers increasing the volume scattering, and hence decreasing the emissivity and the measured temperature in this zone.

The active data from the X band scatterometer, 0 to 60^0 incidence angle, HH, VV and VH polarization for the flight line are also given. The active backscattered radiation is found to be greatest when the passive emitted radiation is at the minimum values (over the percolation zone), and least when the passive emission is greatest. These results indicate that the ice lenses form a strong source of backscattered radiation. There is little difference measured between the HH and VV signals for the active scatterometer data across the ice sheet.

The emission behaviour of firn is described by Rott (1989) using SMMR data over Antarctica. SMMR (Scanning Multichannel Microwave Radiometer, Nimbus-7 described by Ulaby *et al.*, 1986) is a five frequency (6.6, 10.7, 21, 18, 37GHz), dual polarized (HH, VV), passive microwave remote sensing system. The data for 18 and 37GHz show that the emissivity for vertical polarization decreases with increasing frequency, but the data for horizontal polarization are similar for both frequencies. The polarization difference for the passive signals (Ev - Eh) decreases with increasing frequency. This is due to the vertically polarized emission being strongly affected by the subsurface interfaces at higher frequencies, whereas the horizontal emission is less affected by subsurface features. The incidence angle is ~50^0 for the SMMR, leading to a reflectivity for perpendicular (VV) polarization of ~ 0.00006 for snow of dielectric constant Er ~1.2, and a reflectivity for HH polarization of ~0.009 (using the value of the effective dielectric constant for this polarization at this incidence angle and Fresnel reflectivity at the surface,

see chapter 3 this thesis). The emissivity of VV polarization is therefore greater than that for HH polarization, and the vertically polarized passive radiation may therefore originate from greater depths within the snowpack. HH polarization emitted radiation is concerned with the surface (lower emissivity, so less penetration) and is therefore less affected by changing the operating frequency.

Rott (1989) states that the complex patterns of the microwave emissivities of Antarctica with changes of polarization and frequency cannot be fully understood by presently available emission models. More detailed measurements of the snow properties and emission measurements at test-sites are needed to develop models to explain the emission behaviour of snow.

1.4 The data sets used in this thesis.

In this thesis the radar response from the different areas of the Greenland ice sheet is investigated using data from both active and passive microwave remote sensing instruments.

Active airborne microwave radar data as measured by the NASA/JPL AIRSAR instrument for the different zones of the Greenland ice sheet are analysed. In addition to the change in the radar response for the different areas, the use of different polarizations and frequencies to extract additional information about the surface and subsurface dielectric content of the ice sheet is investigated.

The seasonal effects of the response from the different areas of the ice sheet are noted using data from the passive microwave DMSP SSM/I instrument with particular reference to the change in the measured signal during the spring/summer (melt) season.

1.4.1 NASA/JPL DC8 AIRSAR active airborne data.

The polarimetric radar images measured by the NASA/JPL AIRSAR instrument of four different areas of the Greenland ice sheet are analysed, corresponding to the dry zone, percolation zone, soaked and ablation zones as characterized by Benson (1962). Details of the location and identification of these Greenland AIRSAR images are summarized in table 1.3 below. Figure 1.10 shows the approximate location and heading of these images on the Greenland ice sheet.
10th June 1991 is the date of the AIRSAR flight.

Identification of AIRSAR images:

zone number and type:

1	2	3	4
dry	**percolation**	**soaked/ ablation**	**ablation**
GISP2	Crawford Point		Swiss Camp
test-site	corner reflector scene		

image numbers (P, L, C band):

i7, i8, i9	i10, i11, i12	i1, i2, i3	i13, i14, i15

tape and flight numbers:

CM3189	CM3206	CM3137	CM3247
019-2	026-5	068-1	158-1

co-ordinates, lat., long., (degrees):

+73 20.0	+69 52.1	+69 40.9	+69 34.4
-037 28.5	-047 06.7	-048 31.1	-049 17.7

near range incidence angle (degrees):

29.5	18.0	34.8	21.9

Table 1.3: Details of Greenland AIRSAR images, measured 10 June 1991.

2
percolation zone
heading 24.4°

3
soaked/ ablation zone
heading 68.1°

4
ablation zone
heading 159.1°

1
dry zone
heading 23.6°
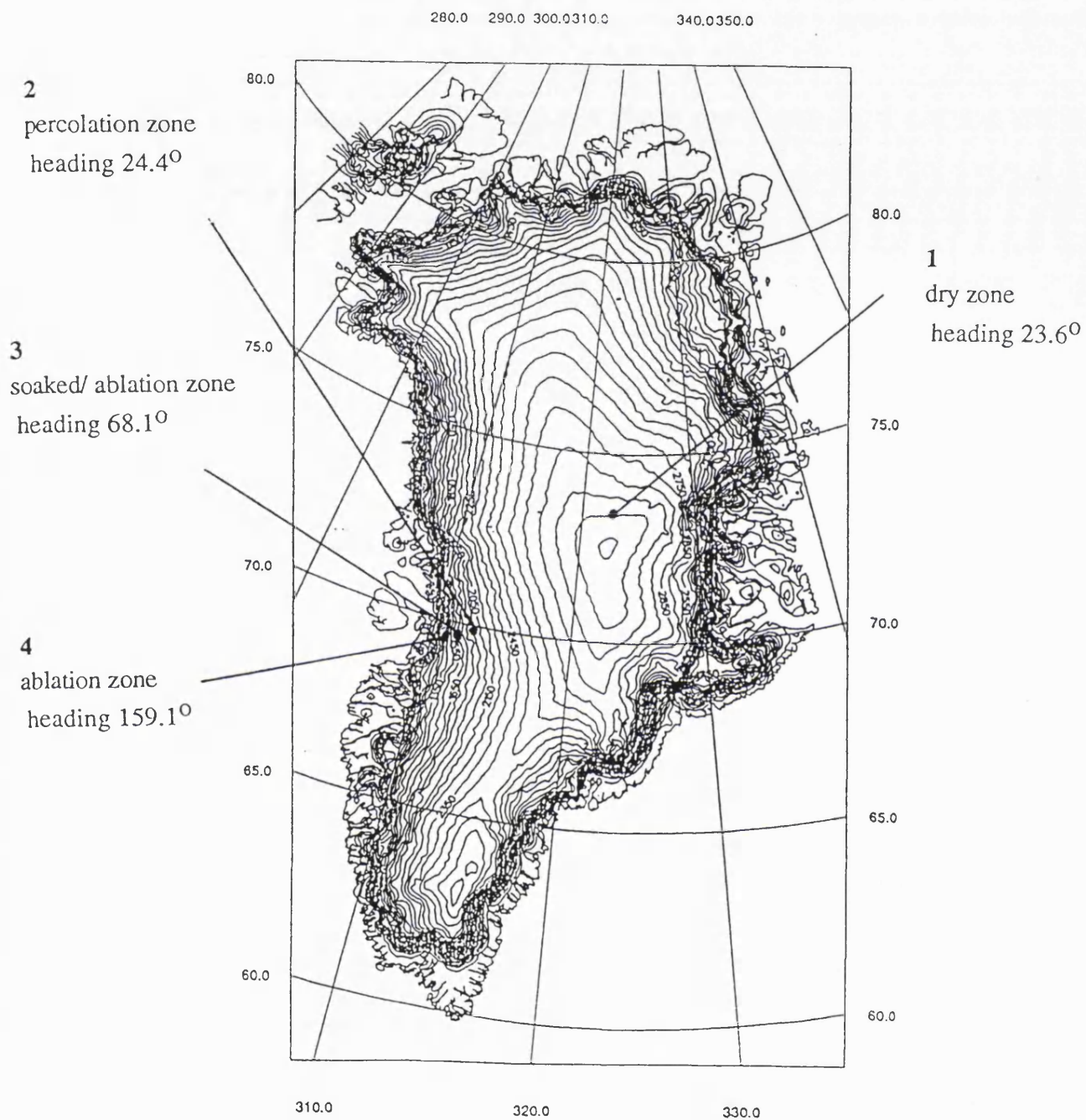
Figure 1.10: Approximate location of the AIRSAR images on the Greenland ice sheet and flight line direction *(topographic map courtesy J. Morley MSSL, UCL 1993)*.

1.4.2 SSM/I passive satellite data.

Data from four areas corresponding to those covered by the AIRSAR imagery are selected. Point 1 corresponds to the dry zone, point 2 to the percolation zone, point 3 to the soaked/ablation zone and point 4 to the ablation zone. The coordinates of the areas measured are given in table 1.4 below, and the approximate location shown above, in figure 1.10.

Coordinates of Greenland ice sheet, passive microwave data points:

point number and zone type	latitude (+) (degrees and minutes)	longitude (-) (degrees and minutes)
1 dry	73 20.0	037 28.5
2 percolation	69 52.1	047 06.7
3 soaked/ablation	69 40.9	048 31.1
4 ablation	69 34.4	049 17.7

Table 1.4: Coordinates of points measured in the different zones of the Greenland ice sheet, corresponding to the location of the Greenland AIRSAR images measured 10 June 1991.

A complete year's worth of data of the mean daily brightness temperature for the four areas over the Greenland ice sheet are analysed to determine the change in emitted passive microwave radiation over the year; considering the effect of the different seasons and the different zones of the ice sheet. The complete year of data covers the period from the beginning of April 1990 until the end of March 1991. The data from April 1991 until the end of June 1991 are also compared with that for the previous year; April to June 1990.

The mean daily brightness temperatures as measured by the SSM/I instrument for the particular day of the AIRSAR overflight (10th June 1991) are used for the comparison work with the active AIRSAR data. The pixel size for the SSM/I data is ~25*25km^2 and the AIRSAR images each cover a region of ~12*8km^2, pixel size ~12*7m^2, so there is a vast difference in the areas measured by, and the resolution of, the passive SSM/I instrument and the active AIRSAR system.

The AIRSAR images are each positioned in a different zone descending the ice sheet and the passive SSM/I data from these points are assumed to be typical of the response from the four different zones of the ice sheet. Details of the snowpack measured during

concurrent field campaigns by teams at three of the four test-sites (GISP2 at point 1 in the dry zone, K.Jezek's team at Crawford Point in the percolation zone, and the ETH field party at the test-site in the ablation zone) confirm that the snow characteristics at the test-sites are typical of the different zones (Jezek, personal communication). Refer to chapter 4 for details of the field campaigns.

1.5 Aims of the thesis.

The aim of this thesis is to investigate the active and passive polarimetric microwave response of the four different zones of the Greenland ice sheet. The relationship between scattering and emission from snowpack is analysed by the synergistic use of the active and passive sensors. The interaction mechanism of microwaves with the layered complex dielectric media of snowpack is studied and a greater understanding of the measured response from each zone of the ice sheet is gained by considering the physical characteristics of the various snow conditions at each of the imaged areas.

The work undertaken in this thesis includes the full analysis of the multi-frequency, fully polarimetric active AIRSAR images over the four different zones of the Greenland ice sheet. The scattering mechanism is determined from the measured polarimetric response for each zone, and the variation of this scattering mechanism with the incidence angle and operating frequency of the radar is determined.

The use of different polarizations and combinations of different frequencies to show different features in each image is investigated. The location and orientation of these features of the ice sheet observed by the airborne SAR system are discussed with reference to details of the surface slope and direction of the ice sheet as determined using ERS-1 radar altimeter data.

The backscattered power of the airborne (AIRSAR) data is correlated with data from the ERS-1 SAR (satellite system) showing the change in the measured return power for the different zones of the ice sheet. This variation in backscattered power for each of the different zones of the ice sheet is discussed.

The data for the percolation zone are analysed in detail. The variation in the measured backscattered power for the percolation zone with change in the incidence angle and frequency and polarization state of the incident radar is determined. The effect of the position and orientation of subsurface ice layers within the snowpack of the percolation zone on the measured polarimetric response is discussed.

Passive microwave (SSM/I) data at positions corresponding to that of the above AIRSAR images, over the four different zones of the Greenland ice sheet are also analysed. A temporal study of the measured brightness temperatures for a complete year of data at the four positions is undertaken to show the annual change in the measured passive response for each of the four zones of the ice sheet. The variation in the measured brightness temperature due to the location is studied and the change in the measured brightness temperature for each position due to the seasonal variation is noted.

The effect of the polarization of the measured passive signals is determined. The difference in the emitted signal for horizontal and vertical polarization is investigated for each of the four zones of the ice sheet. This passive polarimetric data is used to determine the polarization ratio of the measured signals and the mean dielectric constant of the imaged area is then calculated. This calculated value of the dielectric constant of the imaged area is then used to infer the wetness content of the snow. The annual variation in moisture content of the snow at each of the four zones of the ice sheet is determined.

The passive microwave data from the SSM/I for the day of the AIRSAR overflight is correlated with the active data from the AIRSAR instrument. The mean dielectric constant of the imaged area is determined using the passive data and the moisture content of the snow of the imaged area is determined. The approximate area of the test area in the ablation zone covered by surface water in the form of melt pools is calculated using the polarimetric signals of the remotely sensed data.

The measured passive signals from the four different zones of the ice sheet are investigated in detail for the spring-summer season, and the apparent change of the measured radiometric signals during melt is discussed.

The difference in the passive data measured at the different frequencies of the SSM/I system is investigated. The data measured by the SSM/I at 19GHz and 37GHz are analysed in detail for each of the four zones of the ice sheet. The frequency difference data for a full year, and for the spring-summer season in particular are investigated for all four zones.

The effect of the presence of ice layers on the measured passive response is also discussed.

A fully-polarimetric, multi-frequency matrix based computer model to determine the theoretical 3D polarimetric response of any simulated geophysical surface is developed. Snowpack, for example, is simulated by a system of layers of complex dielectric material of different depths. This computer model is based on conservation of energy and determines both the polarimetric content of the reflected signal (amplitude and phase components) for active systems and that of the emitted (= absorbed) energy for passive systems for a full range of incidence angles (0 - 90 degrees).

Validation work is undertaken, correlating the computed response with published values. The model is used for theoretical analysis work which investigates the effect of the incidence angle of the radar, and the physical parameters of the imaged material (for example the dielectric content and depth of subsurface layers) on the polarimetric response.

A theoretical classification method is developed using the polarimetric signals to determine the dielectric content of the imaged areas. The calculated dielectric content is then used to indicate the type of the imaged area. This classification method may be used to identify the melt areas of the ice sheet as illustrated using the measured polarimetric data of the AIRSAR image of the ablation zone.

The theoretical active and passive signals are correlated and the relationship between the active and passive response from the simulated snowpack is determined. The polarimetric information of the emitted signal (using measured passive data) is used to give the dielectric constant and moisture content of the snow.

Polarimetric theory and existing models are reviewed in chapter 2. The new matrix model is developed in chapter 3. Information on the measurements, campaigns and data analysis is given in chapter 4. The results from the measured data are given in chapter 5 and discussed further in chapter 6, together with suggestions for future work and the conclusions.

2 Polarimetric theory and models -

This chapter gives an introduction to polarimetric theory and reviews existing radiation interaction models, with specific reference to the polarimetric signals. The justification for developing a new model is given, with the assumptions and deficiencies (and suggestions for rectification) of this new model. The basis of the new model is outlined in this chapter and developed further in chapter 3.

2.1 Theory of polarimetry.

The use of polarimetry is to obtain more complete information of the scattering characteristics of the imaged terrain. This is achieved by synthesizing the different polarization states of the incident electromagnetic field. The imaging radar polarimeter measures the amplitude and phase components of the return signal and uses antenna synthesis techniques to determine the response from the imaged terrain at all possible incident polarization states (van Zyl, 1987). For the polarimetry work in this thesis the definition of parallel and perpendicular polarization is as given in Appendix A1.1.

2.1.1 Polarization state and Poincaré sphere.

The polarization state of the incident wave may be described by the amplitude and relative phase of the components of the electromagnetic field parallel and perpendicular to the surface (a1, a2, δ). Linear, circular or any general elliptically polarized wave may be described in this way. The full range of polarization states may be illustrated by positions on the Poincaré sphere as shown in figure 2.1.

rhc at "N pole"

δ = -90

δ = -ve

P co polar

linear polarization states
around "equator"

0

P'
cross polar

P*
conjugate

δ = +ve

lhc at "S pole"

δ = +90
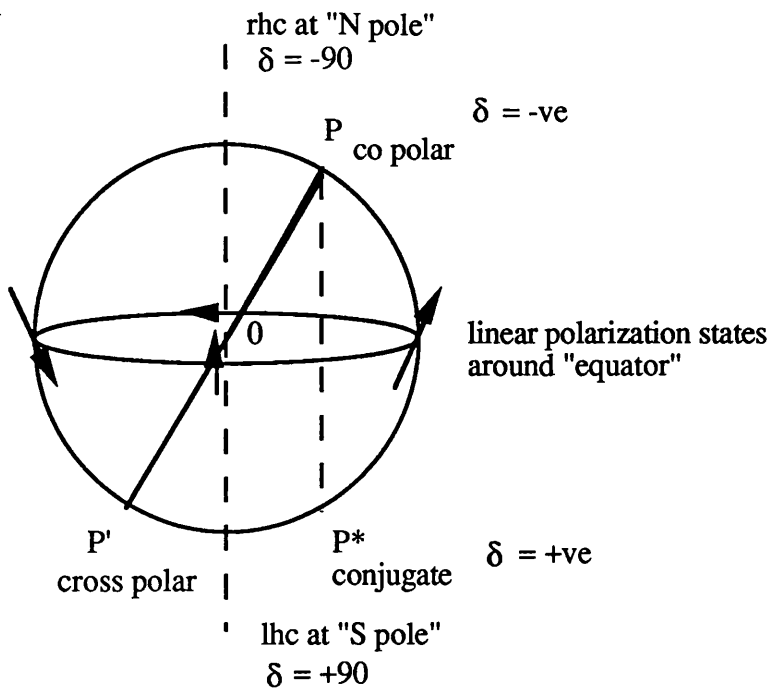
Figure 2.1: Poincaré sphere representation of polarimetric states, showing co, cross and conjugate points (P, P', P*).

Where:

rhc = right hand circular polarization, at "north pole" of sphere;

lhc = left hand circular polarization, at "south pole";

linear polarization states around equator of sphere.

The value of longitude gives the orientation and the value of latitude gives the ellipticity.

Any point on the Poincaré sphere may be represented by considering the amplitude and relative phase of the parallel and perpendicular components of the wave.

The general point P on the surface of the sphere is given by:

$$P = j \left| \frac{a1}{a2} \right| e^{j\delta}$$

Equation 2.1: General point P on Poincaré sphere.

The cross polar and conjugate points P' and P* are discussed in section 2.1.1.2 below.

2.1.1.1 Polarization ellipse.
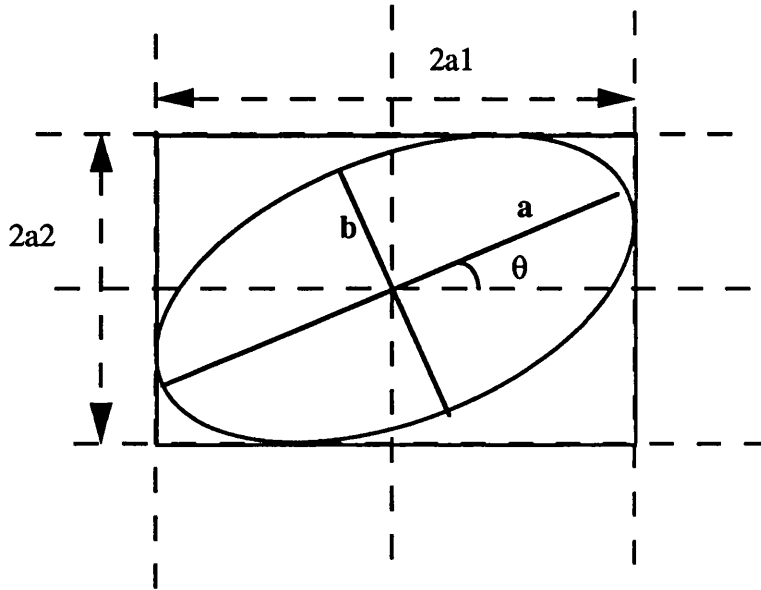
Figure 2.2: Polarization ellipse.

The polarization ellipse of an electromagnetic wave gives details of the parallel and perpendicular components of the wave, as well as the orientation, θ (tilt), and ellipticity, ε (handedness) of the wave.

The following equations relate the parallel and perpendicular amplitude components (a1, a2) and phase difference δ, to the ellipticity ε, and orientation θ of the input signal (equations 2.2). The principal semi-axes a, b of the ellipse, and the angle θ that the major axis makes with the horizontal are also given:

$$a^2 + b^2 = a1^2 + a2^2$$

$$\tan \alpha = a2/a1$$

where α is an intermediate angle, giving expressions for orientation and ellipticity as follows:

$$\tan 2\theta = (\tan 2\alpha) \cos \delta$$

$$\sin 2\varepsilon = (\sin 2\alpha) \sin \delta$$

$$\tan \varepsilon = \pm \, b/a$$

Equations 2.2: Ellipticity and orientation of polarimetric signal.

The state of polarization of any general electromagnetic wave may be represented by a unique point on the Poincaré sphere (figure 2.1), which gives information about the handedness of the ellipse (handedness or ellipticity = latitude of the point on the sphere) and the amplitude ratio of the parallel and perpendicular components (tilt or orientation = longitude of the point on the sphere).

The value of δ, the phase difference (degrees) between the parallel and perpendicular components determines the handedness of the ellipse. If δ is negative then the ellipse is said to be right-handed (in that the E vector appears to rotate in a clockwise direction as the wave progresses away from the observer) and if δ is positive then the wave is left-handed, or proceeds in an anti-clockwise direction. The limits of δ are +90 (left hand circular, represented by South pole of sphere) and -90 (right hand circular polarization represented by North pole of sphere). If δ is zero then the polarization is linear represented by points on the equator of the sphere. The latitude of the point on the sphere represents the ellipticity of the wave.

The amplitude ratio of the parallel and perpendicular components of the wave give the orientation of the E vector. If the components parallel and perpendicular are equal, and 90 degrees out of phase then circular polarization is attained, given by the poles of the sphere. If these two equal components have an intermediate value of phase difference then an elliptical wave is produced, of orientation 45 degrees. If the phase difference is zero then 45 degree slant linear polarization is achieved, given by the points on the equator as shown. The longitude of the point on the sphere gives the orientation of the E vector (rotates from vertical polarization, to 45 degree slant linear, to horizontal polarization, and to the opposite 45 degree slant linear on travelling round the equator of the sphere). Any intermediate value of amplitude ratio and phase difference is indicated by a point in the upper (righthanded) and lower (lefthanded) hemispheres.

2.1.1.2 Co and cross polar, and conjugate points.

Co polar and cross polar points on the Poincaré sphere are seen to be at positions given by inverting the amplitude ratio and of negative phase difference.

If P is the co polar point, where:

$$P = j \left| \frac{a_1}{a_2} \right| e^{j\delta}$$

(Equation 2.1)

then the corresponding cross polar point is given by P', where:

$$P' = -\frac{1}{P}$$

$$P' = j \left| \frac{a_2}{a_1} \right| e^{-j\delta}$$

Equation 2.3: Cross polar point P'.

The cross polar point P' has opposite handedness, and opposite tilt, and may be found at the opposite end of the diameter from P through the centre of the sphere.

The conjugate point P* has the same amplitude ratio but negative phase difference, and is found by dropping a vertical line from the co polar point P to the position where it intersects the sphere again. If P is the co polar point, where:

$$P = j \left| \frac{a_1}{a_2} \right| e^{j\delta}$$

then the corresponding conjugate point is given by P*, where:

$$P* = -j \left| \frac{a_1}{a_2} \right| e^{-j\delta}$$

Equation 2.4: Conjugate point P*.

This conjugate point is at the same longitude but opposite latitude to the co polar point (same orientation, opposite ellipticity).

Figure 2.1 shows the relative locations of the co, cross and conjugate polarization points: P, P' and P* respectively, on the Poincaré sphere.

2.1.2 3D polarimetric response plots.

The 3D polarimetric response plots show the variation of the co and cross polar power of the reflected signal from the surface as a function of the orientation and ellipticity of the incidence wave (Zebker *et al.*, 1987; van Zyl *et al.*, 1987). This method of illustrating the response on the 3D axes shows the normalized return power for all the possible incident polarization states as given by the Poincaré sphere representation. The base grid of the 3D plots gives the equivalent positions as an unwrapped Poincaré sphere as shown in figure 2.3 below.

The 3D representation of the output co and cross polar power is produced by considering the amount of power reflected co and cross polar to the incident wave for all possible states of this incident wave. The normalized output power is plotted on the z axis, the ellipticity ε (-45 to +45 degrees) of the input wave along the y axis, and the orientation of the input wave θ (0 to 180 degrees) along the x axis.

All possible input wave states are represented by the 3D plot. It may be considered as an unwrapped Poincaré sphere, where the centre line (ellipticity = 0, δ = 0, for all orientations) denotes the linear polarizations (= equator of Poincaré sphere).
The position given by θ = 0, ε = 0 corresponds to HH polarization (parallel polarization), and the position θ = 90, ε = 0 corresponds to VV polarization (perpendicular polarization). The position θ = 180, ε = 0 is also HH, with 180° phase inversion.
Circular polarizations are given by the edges (ellipticity = $\pm$ 45 for all orientations), right-hand circular being the LH edge δ = - 90, and left-hand circular being the RH edge δ = + 90. The elliptical polarization states are denoted by positions within the four quadrants of the plot, corresponding to the hemispherical sectors of the Poincaré sphere.

The 3D polarimetric plots of the normalized return power for the co and cross polar response of scattering from dielectric material at 0° incidence are given in figure 2.4. The terms co and cross polar power are defined in section 2.1.1.2 above and specific matrix calculations for the model are given in chapter 3 (section 3.1.6).
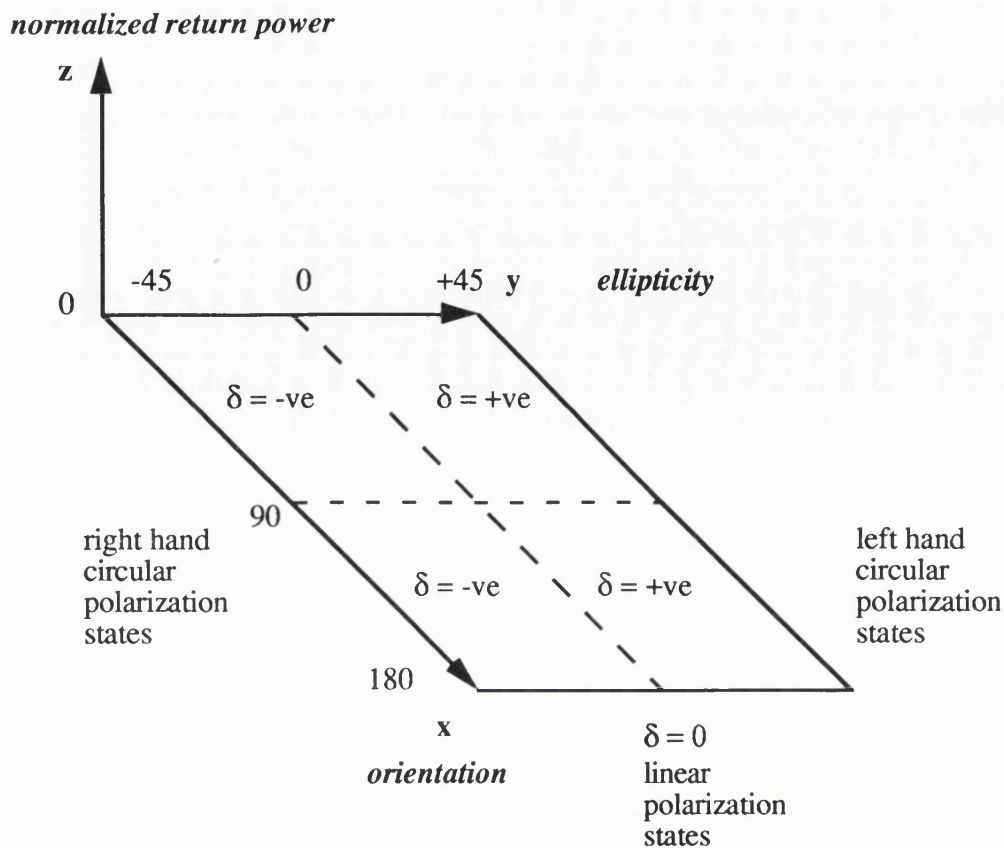
Figure 2.3: Grid of 3D polarimetric response plot.
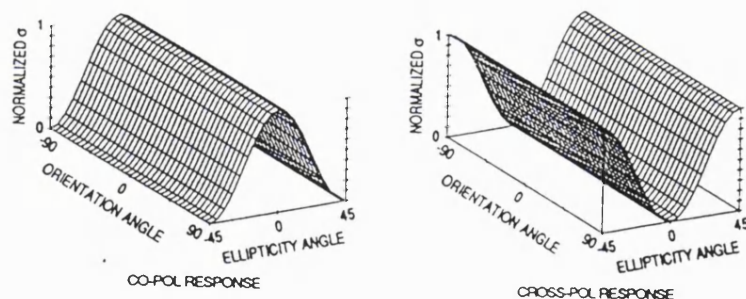
Figure 2.4: 3D polarimetric plot showing co and cross polar response of scattering from dielectric material, 0° incidence.

For the above plots of single surface scattering for normal incidence, the co polar power is zero for circular polarizations (along the left and right hand edges of the 3D plots, where ellipticity $= \pm 45$) and the cross polar power is of unity value as the sense of the circular polarization signals is reversed on reflection. At normal incidence there is no difference between all the linear polarization states which is indicated by the centre linear section of the plots (where ellipticity $= 0$). The response for the intermediate elliptical polarization states is given by the corresponding values on the 3D co and cross polar plots.

2.1.3 Scattering mechanisms.

The dominant scattering mechanism may be determined from the 3D polarimetric response plots as described by Freeman and Durden (1992). The above example (figure 2.4) shows single surface scattering from a dielectric material.

The interaction of radar with the Earth's surface occurs via three main types of scattering mechanism; namely direct scattering, double bounce and diffuse/volume scattering. These types of scattering are shown diagrammatically in figure 2.5(i). Typical polarimetric response plots (co and cross polar power) for direct scattering, double bounce and diffuse/ volume scattering are given in figure 2.5(ii).

The first plot shows the polarimetric response for direct scattering. The shape of this plot is similar to that given above (figure 2.4) for single reflection from dielectric material. At oblique incidence angles the co polar response may show a single dip. This shape forms as the co polar return power for vertical polarization is less than that for horizontal polarization.

The plot for double bounce scattering shows a distinct shape with minima (for the co polar response) and maxima (for the cross polar response) for 45 degree slant linear polarization states. This is due to the extra 180 degree phase difference which occurs for the additional reflection.

The shape of the plot for diffuse/volume scattering shows a definite pedestal. This is formed by the diffuse nature of the return signal which originates from multiple scattering within the volume of the material with a resulting loss of coherency. This part of the return signal remains at a constant level and is independent of the polarization state of the incident signal and cannot therefore be removed by altering the incident polarization state. The height of the pedestal can be used to indicate the amount of diffuse scattering that occurs.

The three main types of scattering mechanism discussed above may occur over the ice sheet. Direct scattering is likely to occur for the smooth surfaces of the ice sheet. The double bounce effect may occur if there is either a sudden change in topography, for example, at the vertical ice wall at the edge of the ice sheet, or if there are sudden changes in the dielectric material, by, for example, a subsurface horizontal ice layer and vertical ice pipes within the snowpack. The distance between the two points of contact in the double

bounce mechanism should be greater than the wavelength of the incident radar signal for a coherent return signal. The third type of scattering, diffuse scattering, occurs when the radar signal penetrates the snow pack. This is common for low dielectric materials such as dry snow.

The shape of the polarization response is not unique as similar forms of response may occur for different objects or for various combinations of scattering mechanisms. Great care must therefore be taken when interpreting measured data to determine the correct scattering mechanism. The polarimetric responses are plotted on a normalised scale and so the measured value of the total return power may assist in distinguishing between similar responses for different areas of an image.
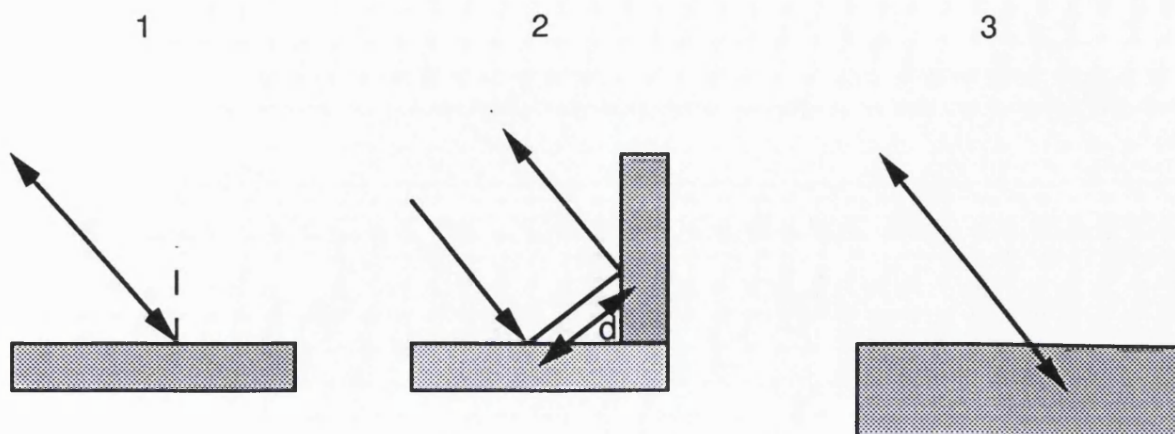
Figure 2.5: i) Physical mechanisms for 1) direct scattering (scale d>λ for a coherent return), 2) double bounce and 3) diffuse/ volume scattering over ice sheets.

1)
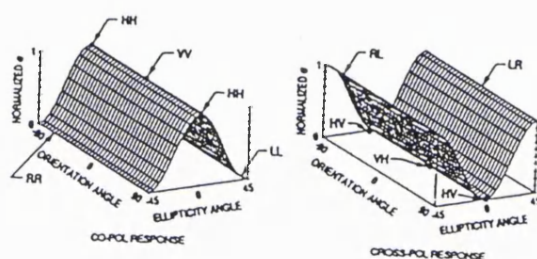
2)
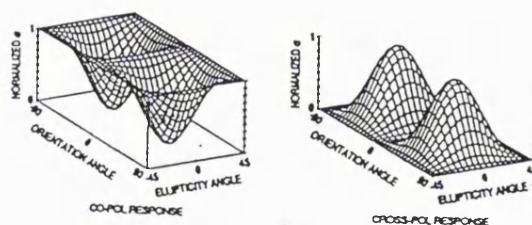
3)
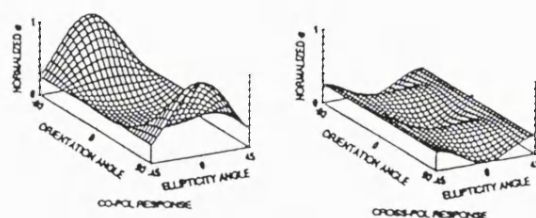
Figure 2.5: ii) 3D polarization plots (co and cross polar) for 1) direct scattering, 2) double bounce and 3) diffuse/ volume scattering.

The typical scattering mechanisms for glaciated regions are discussed by Curlander and McDonough (1991). Surface scattering (single bounce) occurs from the ice surface and volume scattering (diffuse scattering) may occur within the glacier ice. A double bounce reflection may occur, for example, from a surface layer of ice over water in a glacial lake if there are discontinuities within the surface material to produce the return signal. Open water would give a specular reflection of the signal away from the SAR, showing low return power. The presence of subsurface ice lenses would give a strong directly reflected signal (Jezek *et al.*, 1993). Complex multiple scatter between several discontinuities within the snowpack, however, can result in loss of coherence and give a diffuse return signal. The physical size, spacing and orientation of the discontinuities should be considered with reference to the operating frequency and direction of the imaging radar. This is discussed further in section 2.2.

A diagram showing the main scattering sources for the ablation and wet snow region of the glacier (corresponding to the area covered by the AIRSAR image 233-1) is given in figure 2.6 below.
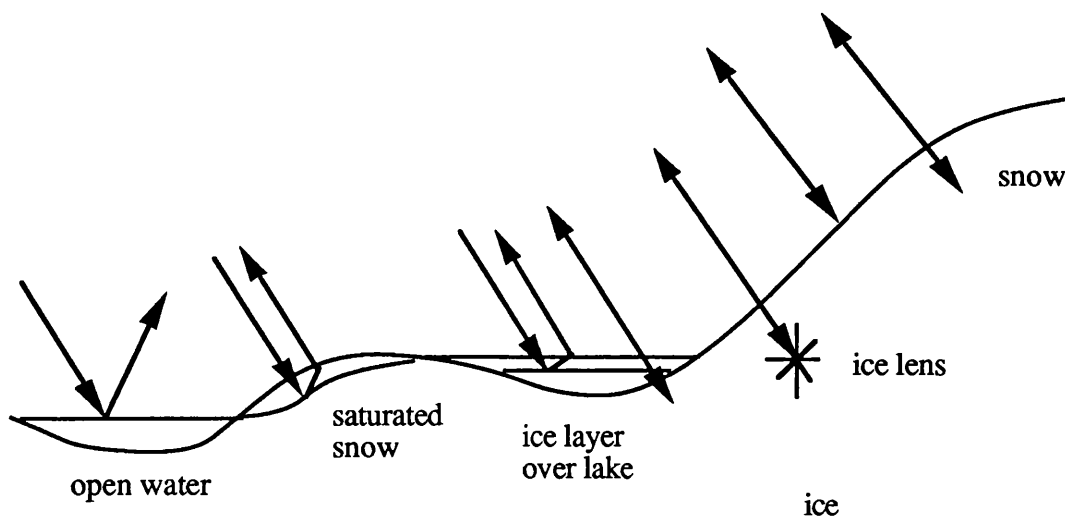
Figure 2.6: Scattering mechanisms over glaciated surfaces.

2.1.4 Interaction of electromagnetic waves with dielectric material.

2.1.4.1 Theoretical forward scattering from smooth dielectric material.

The incident radar wave is reflected at any discontinuity. A change in the dielectric constant of the media which the wave traverses will cause a sudden change in the impedance for the electromagnetic wave and result in a reflection at the boundary between the two media.

The reflected power R_0 may be calculated using the Fresnel relationship for smooth dielectric surfaces given below in equation 2.5, where R_0, the Fresnel fractional reflected power, is calculated for normal incidence on a smooth surface of relative complex dielectric constant (modulus Er).

$$R_0 = \left[\frac{\left(\sqrt{Er} - 1\right)}{\left(\sqrt{Er} + 1\right)} \right]^2$$

Equation 2.5: Fresnel fractional reflected power, R_0.

The reflected signal is dependent on the incidence angle and polarization of the incident wave, and the complex dielectric constant of the material. The definition of parallel and perpendicular polarization as used for this work is given in Appendix A1.1. Details of matrix calculations of reflection and transmission at dielectric interfaces for the model are given in chapter 3.

For a smooth surface the reflected signal for parallel and perpendicular polarization incident waves for the range of incidence angles 0 to 90 degrees (value of incidence angle measured from normal) is given in figure 2.7.

The Brewster effect is noted for perpendicular polarization at the angle θ_B given by equation 2.6 below. At this angle the reflected signal from the surface of dielectric constant Er is of zero power for perpendicular polarization.

$$\theta_B = \tan^{-1}\left(\sqrt{Er}\right)$$

Equation 2.6: Brewster angle θ_B.

For dry snow (0% wetness content by volume) the dielectric constant at P band is 1.66, giving the Brewster angle $\theta_B = 52.18$ degrees. For free water the dielectric constant is

larger (Er = 78.694), causing a higher discontinuity (higher reflected power) and the Brewster angle is greater (θ_B = 83.568 degrees). These values of dielectric constant for dry snow and free water are typical values taken from Jezek *et al*. (1993) and Ulaby *et al*. (1986).

The difference between the parallel and perpendicular polarization (HH and VV) components of the reflected wave is dependent on the dielectric constant of the material and the incidence angle.

Fresnel reflectivity of free water and dry snow surfaces
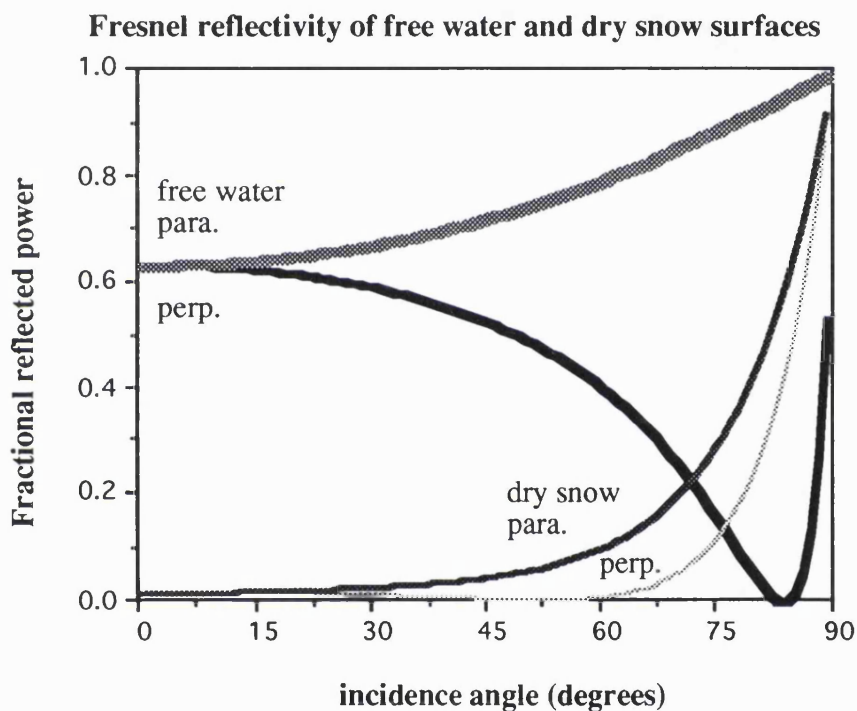
Figure 2.7: P band parallel and perpendicular components of reflected signal due to oblique incidence on smooth dielectric material (dry snow Er = 1.66; free water Er = 78.694).

The amount of energy reflected is dependent on the dielectric constant of the surface material. A high dielectric material will cause a high discontinuity and so the reflected signal, for normal incidence, is larger. Typical values of the dielectric constant for water, pure ice and dry snow at P band are given in the table below (table 2.1) with the corresponding values of Fresnel reflectivity at normal incidence.

Dielectric constant and Fresnel reflectivity for polar materials:

	free water	pure ice	(0%) dry snow
relative dielectric constant (Er)	78.694	2.9	1.66
Fresnel reflectivity (0 deg.) (fractional reflected power)	0.636	0.068	0.016

Table 2.1: Dielectric constant of free water, pure ice and dry snow (at P band) and values of Fresnel reflectivity for normal incidence.

2.1.4.1.1 Refraction at dielectric interface.

The transmitted signal is refracted at the boundary of materials of different dielectric constant according to Snell's Law (equation 2.7), which gives the relationship between the refractive index n, the angle of incidence i, and the angle of refraction r.

$$n = \frac{\sin(i)}{\sin(r)}$$

where $n = \sqrt{Er}$

Equation 2.7: Snell's Law.

On passing from air into a more dense material (of relative dielectric constant Er) the signal is refracted towards the normal as shown in figure 2.8 below.
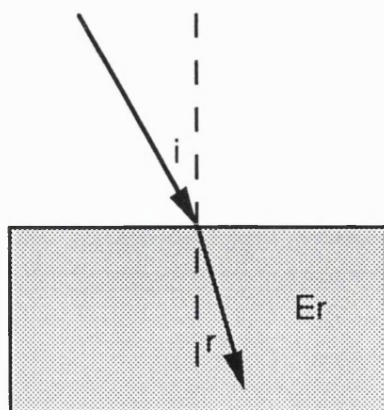
Figure 2.8: Refraction at dielectric interface.

2.1.4.1.2 Penetration and absorption.

On travelling through dielectric material the incident signal will be attenuated due to the lossy nature of the material.

The rate of attenuation and the phase change of the electromagnetic wave is given by, F_b, which describes the amplitude ratio and phase change of a wave, free-space wavelength λ, travelling a distance x through the dielectric material of relative complex dielectric constant E^*, where $E^* = Er(1 - jtan\delta)$.

$$F_b = e^{-j\frac{2\pi x}{\lambda}\sqrt{E^*}}$$

Equation 2.8: Amplitude ratio F_b.

The skin depth, δ_s, describes the distance at which the incident wave becomes 1/e of its original value. This is used to compare penetration depths of incident waves of different frequencies in different media.

The equation giving skin depth (mm) in terms of the complex dielectric constant (Er, tanδ) is given by equation 2.9 below, where F (GHz) is the frequency of the incident wave (Born and Wolf, 1980).

$$\delta_s = \frac{300}{\pi\, F\sqrt{Er}\, tan\delta}$$

Equation 2.9: Skin depth δ_s.

For P, L, C band (0.4, 1.2, 5.3GHz) correlating to JPL AIRSAR frequencies the skin depths for various materials (of different dielectric constant) are given in table 2.2 below. The values of the skin depths for each of the polar materials are seen to decrease with increasing frequency. When operating over polar regions the multifrequency radar signals will therefore penetrate the imaged snowpack to increasing depths on decreasing the operating frequency of the incident signal.

Complex dielectric constant and skin depth for polar materials:

P band

material	Er	tanδ	skin depth (m)
0% snow	1.66	0.00003	6176.41
6% snow	2.38	0.013	11.9036
15% snow	4.23	0.026	4.46445
pure ice	2.9	0.00038	368.917
free water	78.694	0.0201	1.33889

L band

material	Er	tanδ	skin depth (m)
0% snow	1.66	0.00003	2058.803
6% snow	2.37	0.04	1.292
15% snow	4.19	0.08	0.48595
pure ice	2.95	0.00034	136.27
free water	78.674	0.0604	0.1485

C band

material	Er	tanδ	skin depth (m)
0% snow	1.66	0.00006	233.072
6% snow	2.2	0.136	0.0893
15% snow	3.6	0.297	0.032
pure ice	3.15	0.0032	3.172
free water	73.457	0.2654	0.0079

Table 2.2: Table of values of complex dielectric constant of different materials for P, L, C band with values of skin depths. Dielectric values taken from Jezek *et al.* (1993) and Ulaby *et al.* (1986).

2.1.4.2 Scattering from polar terrain.

The incidence angle at the near edge of AIRSAR images is approximately 20 degrees. At this value of incidence the reflectivity of dry snow is ~0.013 and ~0.019, for parallel (HH) and perpendicular (VV) polarization respectively, so much of the incident energy (~98%) is transmitted into the snowpack. The radar wave is then further reflected by subsurface discontinuities, such as the boundaries between the different layers of snow and ice, and also by subsurface ice particles and ice lenses. The nature of the layered structure of snowpack is described by Benson (1971) and, more recently, by Colbeck (1991). Multiple reflections and absorption within the different layers of the ice sheet cause the polarization differences and attenuation of the signal. The following diagram shows the interaction of the incident radar wave on polar surfaces and the physical mechanisms of the surface and volume scattering which may occur (figure 2.9).

1) For a smooth surface of high dielectric material (for example; smooth ice or free water):
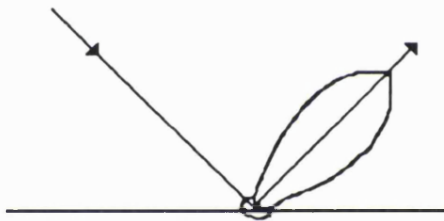
2) For a smooth surface of low dielectric material (for example; dry snow or firn), there is much penetration of the incident signal into the snowpack and multiple reflections occur within the subsurface layers of the snowpack. A high return signal may originate from a subsurface layer of high dielectric (for example, a subsurface ice layer within the snowpack):
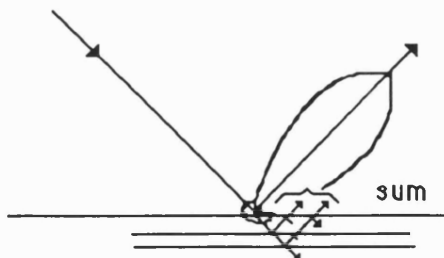
Figure 2.9: Interaction of the incident radar wave on polar terrain.

2.1.4.3 Variation of backscattered total power with incidence angle.

The variation of the backscattered power with change in the incidence angle is given by the general characteristics plotted below in figure 2.10 (Ulaby and Dobson, 1989). This empirical curve is plotted from published measured data.
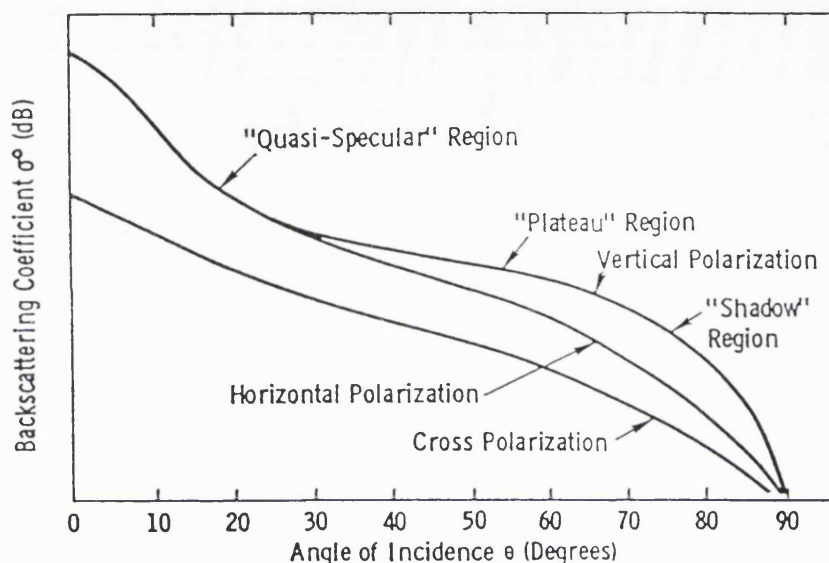
Figure 2.10: Backscattered power variation with angle of incidence (Ulaby and Dobson, 1989).

The backscattering coefficient for the co polar signal may be considered in three regions:
1) quasi-specular region (near normal incidence, from 0 to ~30 degrees)
2) plateau region (~30 to ~60 degrees incidence)
3) shadow region (~60 to 90 degrees incidence)

The backscattered signal is found to decrease in intensity as the value of the incidence angle is increased from normal. For the quasi-specular region (up to ~30 degrees from normal incidence) there is little difference in the backscattered signal for the different polarization states. For both the plateau and shadow regions the backscattered power for vertical polarization is greater than that for horizontal polarization. The cross polar signal is notably less than the co polar signal for the complete range of incidence angles.

Measured backscatter curves for dry and wet snow at L and C band are also given (Ulaby and Dobson, 1989). Wet snow is classified here as snow of greater than 1% moisture

content by volume. The mean value of backscattering coefficient for C band tends to be higher than that for L band, both for dry and wet snow, for the range of incidence angles 20 to 60 degrees, corresponding to AIRSAR values. The cross polar backscattering coefficient is much less than that for the co polar signal. There is little difference in the backscattering coefficient for the different polarizations HH and VV of the co polar signal.

Table 2.3 below shows the mean measured values of backscattering coefficient for dry and wet snow at L and C band for the range of incidence angles 20 to 60 degrees as covered by the AIRSAR images.

Backscattering coefficient (dB) for dry and wet snow at L and C band, for incidence angle range 20 - 60 degrees.

Angle (degrees)	20	40	60
Dry snow			
L band			
HH	-17	-22.5	-27
HV	-30	-34	-35
VV	-15	-22.5	-25
C band			
HH	-12.5	-15	-20
HV	-22.5	-25	-27.5
VV	-12.5	-17	-20
Wet snow			
L band			
HH	-15	-22.5	-24
HV	-27	-30	-32
VV	-15	-21	-24
C band			
HH	-12.5	-17	-20
HV	-22.5	-25	-27
VV	-12.5	-17	-20

Table 2.3: Backscatter coefficient (dB) for dry and wet snow at L and C band, for incidence angle range 20 - 60 degrees (approximate values from Ulaby and Dobson, 1989).

2.2 Review of existing polarimetric models.

Present models do not adequately represent the radar response of snow surfaces.
Shi and Dozier (1992a) note that the current understanding of the radar response of snow is limited due to few ground and airborne measurements. These cover only a small range of the possible snow conditions, so there is a requirement for more field measurements to assist the understanding of the radar response from snow surfaces. In addition, there is a general lack of understanding of the importance of determining the correct scattering mechanism from the snow surfaces.

Most importantly, there is a need for a complete polarimetric model to describe the backscattering at different polarization and incidence angles in terms of the physical parameters of snow.

Present polarimetric models of wet snow covered terrain are based on radiative transfer theory. The geometry of the problem is simplified to a half space of inhomogeneous dielectric (snow volume) and a rough air:snow interface. The radiative transfer theory used simply involves adding the scattered power from the two sources.

Shi and Dozier (1992a) study the relationship between the scattering mechanism and incidence angle in order to retrieve information of snow wetness from SAR measurements. For low wetness snow, surface scattering dominates at low incidence angles and volume scattering dominates for high incidence angles. Both terms need to be included in backscatter calculations for the complete range of incidence angles. For high wetness snow only the surface scattering term is of importance due to the high dielectric discontinuity at the air:snow interface. There is little penetration and therefore little contribution from volume scattering due to the high water content.

The inversion model of Shi and Dozier (1992a) uses the two components, surface scattered power and volume scattered power, for both polarizations, from the first-order radiative transfer scattering model. The power ratios for HH and VV polarizations are a function only of incidence angle and permittivity of snow. This model is found to work well for determining the snow wetness content from C band polarimetric SAR data and is used to map snow covered regions using co-registered DEM (Digital Elevation Model) data.

At microwave frequencies the radar signal penetrates the snow cover which gives details

of the content of the snowpack. The snowpack has a layered structure due to different snow densities which causes an impedance change for the radar at each layer interface. Studies of the stratigraphy of snow layers at test-sites in Antarctica and Greenland are detailed by Benson (1971). Colbeck (1991) discusses the physical properties and characteristics of layered snow covers. The electromagnetic response of snow at microwave frequencies depends on the value of the complex dielectric constant used to represent each snow layer. The real part increases with the liquid and ice content; the imaginary part is even more sensitive to water content. The grain size of particles also affects the scattering processes. The complication of multiple scattering within the layers adds to the problem of determining the radar backscatter. Modelling work by Tsang and Kong (1980) begins to approach these problems by simulating a three-layer random medium and calculating the thermal emission.

Recent work by Wen *et al.*(1990) uses dense medium radiative transfer theory for modelling the radar backscatter of snow. The results from the model are compared with active radar measurements of remote sensing of snow. It is shown that one effect of multiple scattering is to raise the pedestal height of the co-polar response.

An investigation of the emission and backscattering properties of snow is described by Sturm and Rott (1992). Ground measurements of snow at test-sites in the Alps and Antarctica are made using a radiometer-scatterometer system, at C and X band.
The penetration of the radar into the surface material is found to affect the backscatter as reflections from subsurface interfaces affect the return signal. The frozen ground beneath the dry snow layer is found to dominate the scattered signal for the Alpine test results. The layered structure of the Antarctic snow due to density changes of the snow pack also affects the measurements made at the test-site there. The active and passive radar signatures may be explained by specular and diffuse reflections at the interfaces between layers with different densities.

The polarimetric response of snow regions is described by Rott *et al.*(1992) using measurements from NASA/JPL AIRSAR over an Alpine test-site. The height of the pedestal of the polarization response for the co-polar plots increases with decreasing frequency. This indicates that the diffuse scattering component increases with the increase in penetration depth corresponding to the decrease in frequency from C, L to P band data. The effect of surface roughness is also studied. The artificial surface roughness of the test-site was set up by making a series of ski tracks in the snow, parallel to the flight line. This undulating surface was found to produce a greater change in the polarization response for C band than for L and P band results. The polarimetric response for the

undisturbed and artificially rough surfaces at C, L and P band, ~45° incidence are compared. This work is discussed further in Appendix A1.2.

Passive signals from SMMR over Antarctica are discussed by Van der Veen and Jezek (1993). The seasonal difference in the measured brightness temperature is investigated and the radiative transfer equation (as developed by Zwally, described by Ulaby *et al.*, 1986) is modified and used to calculate the seasonal variation in brightness temperature as shown in figure 2.11. The radiative transfer equation is multiplied by the factor $(1 - R_p)$ to account for the reflection of the upwelling radiation at the surface. This factor is polarization dependent, and the reflected power for vertical polarization is near zero. As a first approximation, the authors state that the brightness temperature for horizontal polarization is expected to be related to the vertical brightness temperature by the relationship:

$$T_{Bh} = (1 - R_p) \, T_{Bv}$$

Equation 2.10: Relationship between horizontal and vertical polarization brightness temperatures (Van der Veen and Jezek, 1993).

However, this model does not fit the measured data. The authors conclude that the horizontal brightness temperature is not linked to the vertical brightness temperature by this simple constant power reflection coefficient. A large value of reflection coefficient (R_p ~0.176, 0.193 @ 19GHz, SSM/I data) is needed to fit the model to the maximum and minimum values of the measured data and the model cannot explain the seasonal variation in the measured brightness temperatures for horizontal polarization.

The power reflection coefficient may be seasonally dependent, although the authors consider this to be unlikely (van der Veen and Jezek, 1993). The scattering and absorption coefficients for vertical and horizontal polarization may also be different. Jezek (personal communication) notes that much more work is needed to interpret the information contained within the polarimetric signals from the ice sheets.
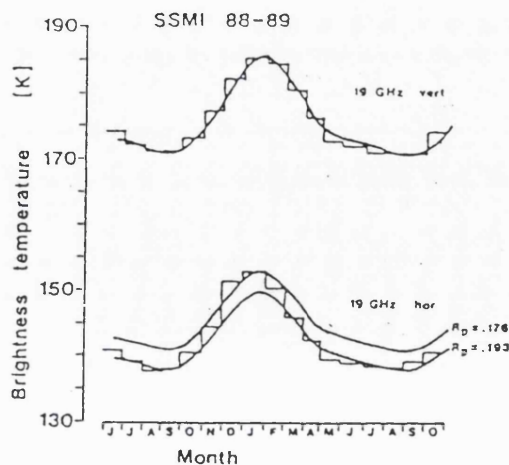
Figure 2.11: Calculated (heavy curves) and measured (stepped curves) brightness temperature for Vostok, East Antarctica, June '88 to October '89 from the 19GHz SSM/I vertical (upper panel) and horizontal (lower panel) channels. The horizontal brightness temperature is calculated from the vertical one using equation 2.10 (above) using a constant power reflection coefficient (= 0.176, 0.193) by van der Veen and Jezek (1993).

Additional work following the work of van der Veen and Jezek (1993) and using the same data set is continued here, with suggestions for a refinement of this model.

The large values of the reflection coefficient (= 0.176, 0.193) as calculated by van der Veen and Jezek (1993) would correspond to a mean value of dielectric constant of ~5.98 and ~6.59 using Fresnel reflectivity at a smooth surface (see section 2.1.4 of this thesis for calculations of Fresnel reflectivity). However, measured values of the dielectric constant of snow covered surfaces range up to 3.15, the dielectric constant of pure ice (Ulaby *et al.*, 1986).

If, however, the polarization of the signal and the incidence angle are taken into account, as described in section 3.1 of this thesis, the calculated values of effective dielectric constant are ~2.79 and 3.01 (for the max. and min. measured brightness temperatures respectively), which are far more typical of snow covered surfaces. The corresponding reflection coefficients for vertical polarization are then ~ 0.00426 and 0.00620 for the max. and min. values of measured brightness temperature.

A refinement of the model of van der Veen and Jezek (1993) would include the following factors:

1) The effective dielectric constant and the change in the reflectivity for the two polarizations at the oblique incidence angle (= 53.2° for SSM/I, 50° for SMMR) should be taken into account when considering the measured brightness temperatures from these instruments.

2) The radiative transfer model should be adapted to account for the effective dielectric constant and the resulting reflections at interfaces.

3) The reflected power for perpendicular polarization, whilst small, is not zero, and setting Rv = 0 is invalid.

4) The effect of multiple reflections within the layered snowpack should be taken into account (the radiative transfer model does not include this effect as the emitted power from each layer is simply added).

5) The phase of the reflected signals should also be considered (as the signals may constructively or destructively interfere) and the effect of the complex signals (amplitude and phase information) should be calculated.

All these conditions are achieved using the matrix method described in section 2.3 and developed further in chapter 3 of this thesis.

The calculations using this matrix method show that a small change in the dielectric constant of the snow (due to a slight increase in wetness content for example, or ice formation) may cause a large apparent change in the reflectivity as calculated, explaining the resulting change in the brightness temperature values.

The seasonal change in the dielectric content of the snowpack should therefore be taken into account. The emitted radiation for vertical polarization originates from greater depths within the snowpack than for horizontal polarization and may therefore be affected by subsurface changes in dielectric, caused, for example, by the formation of depth hoar (Seligman, 1980). Depth hoar is formed due to the changing thermal gradient which exists in the layered snowpack. The upward movement of warm air trapped within the subsurface snow causes large ice crystals to form at a depth within the snowpack. The formation of this depth hoar then causes a change in the density and hence the dielectric constant of the subsurface snowpack.

The effect of changes in the physical material, depths and structure of the subsurface layers causes the dielectric content of the subsurface material to change. This affects the

complex sum of the microwave signals from the snowpack, resulting in an overall change in the reflected (and emitted) polarimetric signals for each operating frequency for active (and passive) systems.

In summary; small changes in the dielectric constant of the imaged terrain during the year may cause the observed seasonal differences in the measured brightness temperatures for the two polarizations. The reflected power for horizontal polarization (parallel) is greater and will change more rapidly than that for vertical (perpendicular) polarization during the year due to this change in dielectric constant of the imaged terrain. The shape of the brightness temperatures curve for horizontal polarization is not related to that of the vertical polarization by the simple reflection coefficient as used by van der Veen and Jezek (1993) but the effective dielectric constant at the oblique incidence angle for each polarization should be considered and the change in emissivity (= 1 - reflected power) should be used to calculate the difference in the signals from the two polarizations. This may be achieved using the complex matrix model of layered media as described in section 2.3 and chapter 3 of this thesis.

2.2.1 Effect of roughness on the polarimetric response.

The effect of roughness on the scattered energy depends on the frequency and incidence angle of the incident signal and is considered to be independent of the polarization as a first assumption (Shi *et al.*, 1991).

For high dielectric material with rough moving surfaces the mean expected value of the polarization ratio for the backscattered signal is given by the relationship described by Barrick *et al.* (1968) as described in section 2.2.1.1 below.

2.2.1.1 Roughness criteria.

The roughness for a particular surface is dependent on the frequency of the incident wave and is defined by the Rayleigh or Fraunhofer criteria given by equation 2.12 below, where h is the mean surface height variation, λ the wavelength of the incident wave and θ_0 the angle of incidence.

i) **Rayleigh:**   ii) **Fraunhofer:**

$$h > \frac{\lambda}{8 \cos \theta_o} \qquad\qquad h > \frac{\lambda}{32 \cos \theta_o}$$

Equation 2.12: i) Rayleigh and ii) Fraunhofer criteria of roughness.

Table 2.4 below gives the mean height variation of surfaces to be considered as rough for the two criteria, for P, L, C band radar, at 20 and 60 degrees incidence angle (the range measured by the AIRSAR instrument):

mean **height variation** for rough surface (mm), **h >** :

band	Rayleigh 20	60	Fraunhofer 20	60 degree incidence angle
P (0.4GHz)	99.77	187.50	24.94	46.88
L (1.2GHz)	33.26	62.50	8.31	15.63
C (5.3GHz)	7.53	14.15	1.88	3.54

Table 2.4: Height variation (mm) for rough surface for P, L, C band radar, for 20 and 60 degrees incidence angle.

For P band radar at the near edge of the AIRSAR image the Rayleigh criterion requires a mean height variation of less than ~10cm for the surface to be considered smooth.

For the AIRSAR images the pixel size is ~12*7 m^2 so over this sample area the snow surface of the ice sheet must have a mean height variation of less than 10cm for the surface to be considered smooth. This is thought to be a reasonable assumption for the Greenland test-sites.

2.2.1.2 Rough surface models.

Models for scattering from rough surfaces have been developed. Scattering from a rough surface may be considered as scattering from a series of small facets (Beckmann and Spizzichino, 1963). The actual surface is modelled as a series of small facets where each facet is tangential to the actual surface. The length of each facet is greater than the incident wavelength and the deviation of the facets from the real surface is much smaller than the wavelength. The facets then behave as individual specular reflectors.

The geometry of the rough surface may alternatively be considered as a superposition of the Fourier components which mathematically describe its shape. The combined effect of the components may be described by the sum of the Bragg scattered waves from the surface. Bragg models to describe the scattering behaviour of rough surfaces, and from tilted surfaces are developed by Valenzuela et al. (in Ulaby and Elachi, 1990). Work on

describing the scattering from ocean-like surfaces is undertaken by Durden (1986).

Models to describe the nature of surface scattering include Kirchoff methods, Physical optics (PO) and Geometric optics (GO), and Small perturbation methods (SPM), which are defined by Ulaby and Elachi (1990); Chen and Fung (1988). A selection of these theoretical models and the region of validity for rough surfaces is discussed by Noll and Borgeaud (1992).

2.2.1.3 Polarimetric signals for rough surfaces.

For rough surfaces the linear HH and VV backscattered signal may be determined using the equations of Barrick et al.(1968) as used also in the Small Perturbation Model. The VV/HH power ratio is given by equation 2.13 where θ = incidence angle, and s = sin θ and c = cos θ respectively.

$$\frac{VV}{HH} = \frac{\left\{ \frac{(Er - 1)[(Er - 1)s^2 + Er]}{\left[Er\,c + \sqrt{(Er - s^2)} \right]^2} \right\}^2}{\left\{ \frac{(Er - 1)}{\left[c + \sqrt{(Er - s^2)} \right]^2} \right\}^2}$$

Equation 2.13: Polarization ratio for backscatter from rough surfaces (Barrick, 1968).

For all values of incidence angle this power ratio is greater than 1 (VV/HH >1). This equation may be applied to areas of a measured AIRSAR image where the return signal is caused by scattering from a rough surface. The measured 3D polarimetric response would then show greater co polar return power for vertical polarization than for horizontal polarization i.e. VV>HH. The shape of the 3D co polar response plot would be of a single "hump" where this occurs, as the values of VV and HH power are given at (ϵ,θ) positions (0,90) for VV, and (0,0) for HH respectively.

The above relationship for VV/HH power for rough surfaces is the mean expected value for an area, assumed to consist of n independent samples, where the accuracy depends on the value of n used. This relationship cannot be applied to individual pixels, unless the number of times the particular sample is measured is significantly large (the number of looks per sample for AIRSAR data is 4). Taking line averages for a uniform area of an image (assuming the terrain is the same across the image) gives a large enough sample (1023 pixels) to help avoid this problem.

This relationship for the linear polarization return signals is used in the Small Perturbation Model. The value of the vertically polarized signal is often found to be surprisingly high when compared with measured results (Durden, 1986). This relationship is used to give a mean value of the expected response from very rough, moving high dielectric surfaces such as scattering from ocean-like surfaces.

2.2.2 Effect of inhomogenieties on the polarimetric response.

The effect of inhomogenieties within the material would be to cause further scattering and attenuation of the microwave radar signal. The physical size of the discontinuities is an important factor to be considered for the multifrequency radar data set. The effect of the orientation and shape of the discontinuities may cause a change in the relative level of the polarimetric reflected signal.

Anisotropic firn and the presence of ice lenses may affect the return polarimetric signal from polar terrain. For the range of frequencies of the AIRSAR instrument (0.4 - 5.3GHz) the effect of anisotropic firn on the normalized polarimetric return signal is probably minimal (the size of the ice particles within the firn fabric is small compared with the radar wavelength) as discussed in this thesis in section 2.2.2.2. The effect of subsurface ice lenses would, however, change the return polarimetric signal, particularly for P band radar due to the increased penetration of the radar into the snowpack at this frequency. The theoretical polarimetric response for dielectric cylinders, such as these subsurface ice lenses, is given by Ulaby and Elachi (1990) as discussed in this thesis in section 2.2.2.3. Measured data from the percolation zone of the Greenland ice sheet are discussed in chapter 5 (section 5.1.7).

2.2.2.1 Volume scattering.

Volume scattering occurs in natural materials such as vegetation and dry snow. The incident wave penetrates the medium and is scattered due to inhomogenieties within the material. The dielectric discontinuities within the volume cause this scattering. Parameters which affect the volume scattering are the density, shape and size of these scatterers and their position within the medium. The dielectric constant of the body of the material and the incidence angle and frequency of the incident wave determine the depth of penetration. A review of volume scatter theories for modelling applications is detailed by Fung (1982), including radiative transfer and iterative matrix doubling methods.

2.2.2.2 Mie scattering.

The effect of small finite discontinuities caused by the presence of impurities within the medium is to produce additional scattering. The polar scattering response of spherical particles is described by the Mie effect. The intensity of the scattered energy varies with angle (Born and Wolf, 1980). This effect is important for inhomogeneous materials (for example, ice particles within snow layers may cause this effect).

For spherical particles there is no difference in the scattered signal for parallel and perpendicular polarized signals. The effect of Mie scattering is not included in the theoretical matrix model described below in section 2.3 (developed fully in chapter 3) as the linear polarimetric results for VV and HH are used for the following classification work, and the effect of Mie scattering from spherical particles has no discernible difference for these two polarization states.

The presence of elliptical particles in snow firn would tend to cause a difference in the return polarimetric signals for higher frequency work as the physical size of the particles become more apparent at smaller operating wavelengths. It is thought that the elliptical grains in the snow fabric may be orientated vertically, especially those in depth hoar. Depth hoar forms within the snow layers from the redistribution of mass under certain conditions, usually in autumn. This is due to the temperature gradient and the upwards vapour movement (K. Jezek, J. Bolzan, personal communication). The nature and structure of depth hoar is described by Seligman (1980).

The effect of different polarizations on various shapes of particles could be studied to determine if the effect of the scattering results in any polarization difference in the reflected signal. This is of particular interest for use with higher frequency systems where the particle size becomes comparable to the operating wavelength. The physical shape and structure of the individual grains of the snowpack is not thought to cause any difference in the polarimetric signal at the AIRSAR frequencies, but the overall effect may simply be represented by a change in the dielectric constant used to represent each layer within the snowpack. The polarimetric response of subsurface ice pipes and ice lenses (of similar size to AIRSAR wavelengths) is discussed in the following section (2.2.2.3).

2.2.2.3 Subsurface cylindrical ice lenses.

The 3D polarimetric response may be used to detect unusual shaped objects, for example, the presence of cylindrical ice lenses within the percolation region of the ice sheet. The theoretical polarimetric radar response of cylindrical objects is given in figure 2.12 below (from Ulaby and Elachi, 1990). This figure shows the form of the 3D polarimetric response for cylindrical objects, and that the response changes with the relative orientation of the cylindrical object to the E vector of the radar.

Measured data from the percolation zone image (i10) are discussed in chapter 5 (section
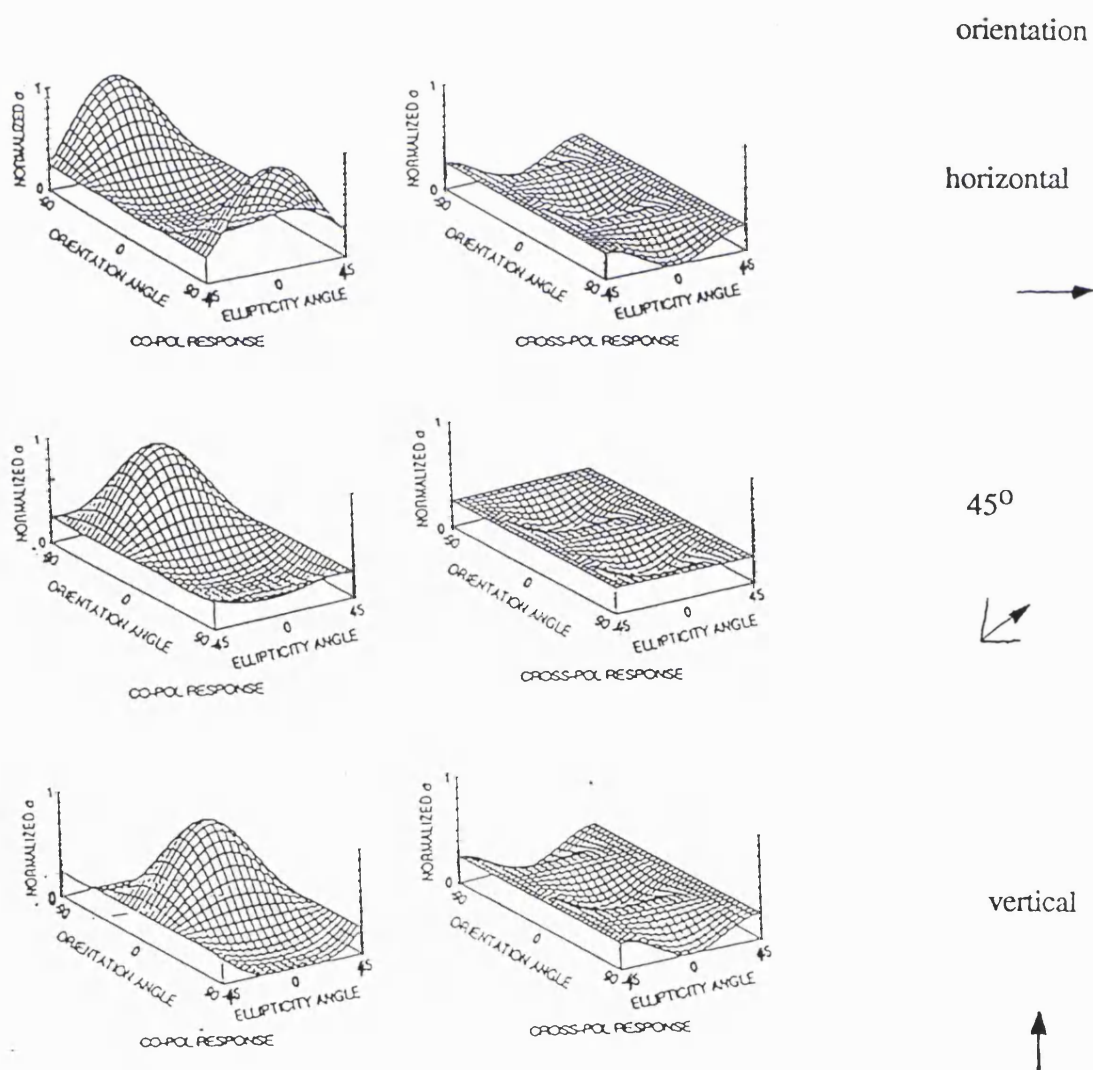
Figure 2.12: Theoretical 3D polarimetric response for cylindrical objects (from Ulaby and Elachi, 1990).

2.3 Justification and basis of new model.

The understanding of the information contained within the active (and passive) polarimetric radar signals from polar surfaces is an extremely complex problem. Shi *et al.* (1992a) state the urgent requirement for a polarimetric model to assist with the analysis and understanding of the scattering from polar surfaces.

Deficiencies of existing models as discussed above (section 2.2) show that the interaction of electromagnetic waves at oblique incidence on dielectric material may be explained by the inclusion of effective dielectrics. The polarization state of the incident, reflected and transmitted signals should be considered and the phase of these signals should also be preserved to account for the effect of multiple reflections within layered medium (such as snowpack). The complex dielectric constant of the geophysical material should also be considered and the depths of the surface and subsurface layers should be included in the analysis.

The polarization ratio calculated by existing rough surface models - for example, the Small Perturbation Model, using the relationship as derived by Barrick and Peake (1968) - has been found to be too high for rough surfaces (Durden, 1986). This relationship does not account for the low polarization ratio of the measured AIRSAR data over snow surfaces. These snow surfaces appear smooth for P band AIRSAR, so quasi-specular scattering may be assumed.

All these factors are included in the new model.

2.3.1 Basis of new model.

A theoretical polarimetric model based on conservation of energy is developed to assist with the understanding of polarimetric radar signals. The reflected, transmitted and absorbed energies are calculated by considering the interaction of the radar with the imaged terrain. This is simulated by considering the interaction of the incident electromagnetic radar wave with the complex dielectric of natural materials (which is dependent largely on the water content). The amplitude and phase components of the electromagnetic wave are considered so phase coherency is maintained. This is achieved using complex matrix analysis.

The new model includes the use of effective dielectrics to explain the interaction of polarimetric electromagnetic waves at oblique incidence.

2.3.1.1 Active signal.

The forward reflected polarimetric signal may be calculated for any incident polarization state, for any input frequency and for the full range of incidence angles for any system of layers of different complex dielectric material and depths. This calculated theoretical polarimetric signal is plotted on a normalized 3D plot (normalized output power versus change in ellipticity from -45 to +45 degrees, and orientation 0 to 180 degrees corresponding to the format of the measured AIRSAR data).

2.3.1.2 Passive signal.

The absorbed component may be equated to the passive emitted energy for the system of simulated layers as the ability to emit is directly proportional to the absorbivity of the material. The VV and HH absorbed components are therefore directly related to the vertical and horizontal polarization brightness temperatures T_{Bv} and T_{Bh} as measured by passive microwave radar systems (section 3.4.1).

2.3.1.3 Matrix analysis.

This theoretical complex matrix based program determines the polarimetric reflected signal from a system of n layers of complex dielectric material of independent depths. The passive emitted signal is also calculated by consideration of the absorbed energy.

A plane wave model is adopted to trace the path of the incident radar wave through the system of layers at any incident angle and for any operating frequency. The Fresnel reflection at dielectric interfaces is considered and the absorption within the layers of material is calculated due to the attenuation of the radar signal in the lossy dielectric. The complex dielectric content of the material is considered so information of both the amplitude and phase of the wave is retained.

A full range of polarimetric incident waves is modelled (the ellipticity and orientation of the input wave vary from -45 to 45 degrees and 0 to 180 degrees corresponding to the base grid positions on the 3D polarimetric plots as given by the AIRSAR data) and the output wave is calculated. This is resolved into the co and cross polar components and the theoretical results are plotted in the 3D format corresponding to the measured AIRSAR data. The calculations using complex matrix analysis are detailed in chapter 3.

2.3.2 Assumptions and deficiencies of new model.

A plane wave model is adopted to trace the path of the incident radar wave. Actual systems may produce edge effects due to the physical size of the beam. This may be removed using calibration data for specific systems and details of the individual antenna characteristics.

Quasi-specular scattering is assumed, so the model is only valid for near normal incidence for the active response. Measured data of the backscatter of snow over the full range of incidence angles away from nadir are given in figure 2.10 (Ulaby and Dobson, 1989). To extend the model further (for greater incidence angles for the active response) the new model should be combined with a model of the backscatter of snow, possibly by adapting the Small Perturbation Model and including the empirical results (section 2.1.4.3).

The model is valid for a complete range of incidence angles for passive systems for smooth surfaces only. The effect of rough surfaces may possibly be included by combining the quasi-specular response (as calculated using the new model) with the response for rough surfaces using an existing rough surface model (for example, the Small Perturbation Model).

The effect of rough surfaces is not included for the work in this thesis as the snow surface appears smooth for P band AIRSAR (section 2.2.1).

The effect of scattering from inhomogenieties may also be included in the model (section 2.2.2). At present the model assumes homogeneous layers of dielectric material. The effect of a gradual change in dielectric constant within a layer may be simulated by introducing a series of matrices to describe the response. The effect of scattering from small particles within a layer may be considered using Mie scattering (Born and Wolf, 1980).

At AIRSAR frequencies the snowpack appears homogeneous and the individual grain size of the snow particles is much smaller than the operating wavelength so Mie scattering is not included for the work in this thesis (section 2.2.2.2).

In addition, the polarization ratio gives indiscernible difference for Mie scattering from spherical particles. As the polarization ratio of the linear polarization states are used in the analysis of the polarimetric data this is assumed to be unaffected by Mie scattering from individual particles (section 2.2.2.2).

The polarization response from larger cylindrical ice lenses is investigated in this thesis using existing models of the scattering characteristics of cylindrical objects (Ulaby and Elachi, 1990). This information may be added to the model. The shape of the 3D polarimetric response depends on the orientation of the cylinders - it is similar to the response for direct scattering for horizontal cylinders, whereas the vertical cylinders give an unsymmetrical polarization response plot (section 2.2.2.3).

3 Development of new matrix model -

The new matrix model is developed in detail in this chapter. The new model is based on a
series of complex matrices which mathematically describe the interaction of the
electromagnetic waves with layered geophysical material, such as snowpack. The
complex vector representation of the electromagnetic wave and the complex matrix
simulation of the reflection, transmission and absorption properties of the layered
complex dielectric material are analysed.

The detailed theory and programming methods are given in the first section, followed by
theoretical validation and correlation work. The model is then used to develop a
classification method for active polarimetric data, as measured by polarimetric systems
such as the AIRSAR instrument.

An inversion method of obtaining the dielectric constant of imaged areas and the moisture
content of snow is developed using the theoretical computed polarization ratio and
measured polarimetric data.

3.1 Detailed theory and programming methods.

This section discusses the theory used in the computer model to determine the scattering
properties of the surfaces considered. The complex reflected and transmitted signals (both
amplitude and phase information) and energy absorbed for any state of incident wave
(frequency, polarization, angle of incidence) is calculated by considering the path of this
incident wave as it impinges on the ground surface. A fraction of this incident wave is
immediately reflected (the Fresnel value) and the remainder is transmitted at the surface
interface to the subsurface layers. This part of the incident wave then undergoes further,
multiple reflections and is partly absorbed due to the layered structure of the subsurface
dielectric material, and produces additional reflections, in time, from the ground surface.
The overall sum of the multiple reflections occurring in the system of layers is determined
to give the steady state solution of the reflected signal from the ground surface. The nature
of the dielectric material is described by considering the complex dielectric constant (Er,
tanδ) of the various layers of different thicknesses at each particular depth, at the surface
or a subsurface layer at depth.
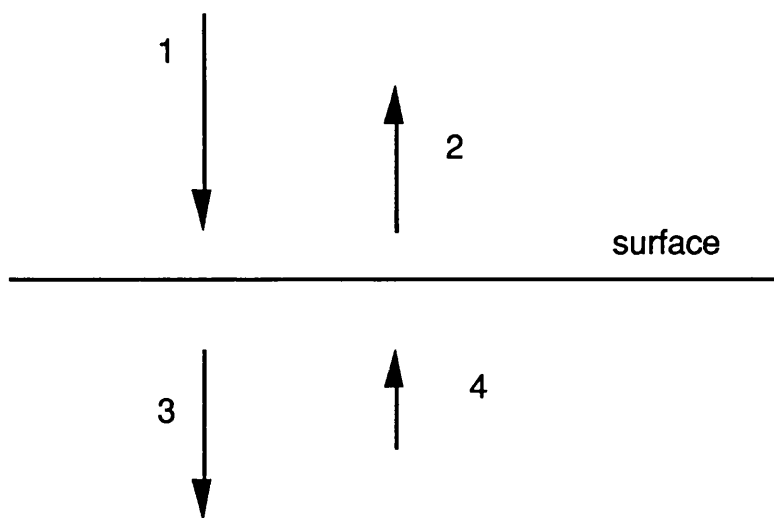
Figure 3.1: Representation of electromagnetic waves in the vicinity of the ground surface.

The fields in the region of the discontinuity include:

1) incident wave (unity value power)

2) reflected wave

3) transmitted wave

4) reflected wave originating from any other further discontinuities, from subsurface layers.

The definition of polarization used in the following analysis is given in Appendix A1.1, with diagrams to show the sign conventions adopted, and the difference between perpendicular and parallel polarization (with respect to the surface considered).

3.1.1 Polarization State.

The complex reflected and transmitted signals, and absorbed power are calculated by considering the polarization state (power, phase, direction) of the incident wave. For the programming work, the incident wave is considered as a complex vector in two mutually perpendicular directions (chosen, for simplicity, to be perpendicular and parallel to the material surface), where the real and imaginary parts of these vectors give both the amplitude and phase information of the incident signal.

The input polarization is given by the normalized amplitudes (a1, a2) and relative phase (δ) of the parallel and perpendicular E vectors, for unity power input. The values of these input parameters corresponding to each x,y position of the 3D plot are given in figure 3.2 i, ii and iii):

i)   ii)   iii)

Figure 3.2: Input polarization states

i) a1 = parallel polarization amplitude (z axis, plot range 0 to 1)

ii) a2 = perpendicular polarization amplitude (z axis, plot range 0 to 1)

iii) δ = phase difference between parallel and perpendicular components of input wave (z axis, plot range -90 to +90 degrees).

The combinations of a1, a2 and δ for each x,y point given above (figure 3.2) give the polarization state of the input signal of unity power. The program calculates the relative output power for all possible input polarization states.

The co and cross polar power is calculated and plotted on the z axis for each x, y position, corresponding to the input polarization state, to give the 3D polarization response of any simulated geophysical surface.

The complex incident wave is of unity power and all the following calculations of reflected and transmitted waves and absorbed energy are given as fractional powers, thus related to the input power value.

3.1.2 Reflection and transmission at dielectric interfaces.

The reflection and transmission of the incidence wave at any boundary between two different dielectric materials is determined by considering the reflectivity and transmissivity of the interface. The amount of power immediately reflected is dependent on the size of the initial mismatch at the surface discontinuity, given by the Fresnel Reflectivity.

The Fresnel Reflectivity gives the initial power reflected at the boundary of two different media. The discontinuity causes an impedance change for the electromagnetic wave. The reflected power R(0) is proportional to the magnitude of the discontinuity.

$$R(0) = \left[\frac{\sqrt{Er} - 1}{\sqrt{Er} + 1} \right]^2$$

The corresponding transmitted power T(0), is 1-R(0);

$$T(0) = 1 - \left[\frac{\sqrt{Er} - 1}{\sqrt{Er} + 1} \right]^2$$

from conservation of energy, as no absorption is considered to take place at the discontinuity (by equating the fields on either side of the boundary at the instant of incidence, time t = 0).

Equation 3.1: Fresnel reflectivity and transmissivity.

The reflection and transmission of the incidence wave at any boundary between two different dielectric materials is determined by considering the reflection and transmission coefficients of the interface.

When the input wave is incident on a planar boundary between two different media part of the wave is reflected and part is transmitted by the discontinuity.

The fields in the region of the discontinuity include:
1) incident wave (unity value power)
2) reflected wave
3) transmitted wave
4) reflected wave originating from any other discontinuities to the right of this boundary (subsurface layers).
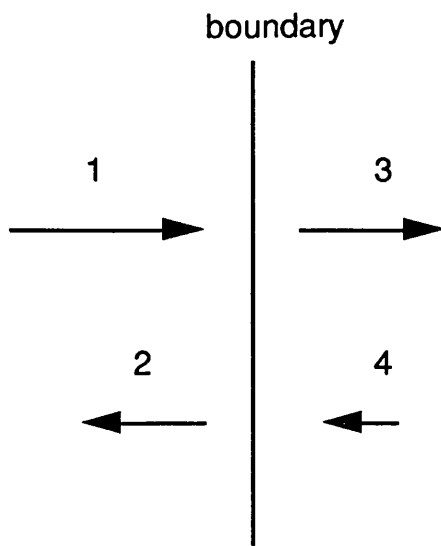
Figure 3.3: Electromagnetic fields at a boundary between two different media.

The interface may be expanded to show the separate reflection and transmission properties for parallel (y) and perpendicular (x) polarization.
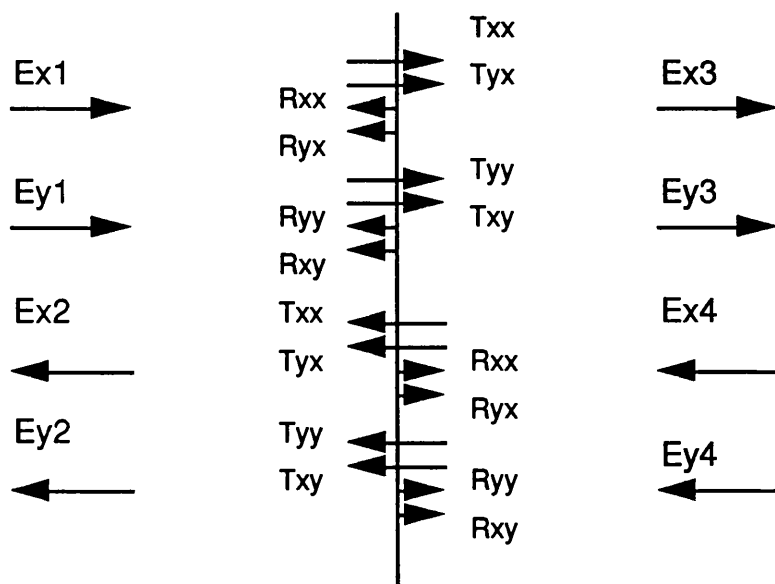
Figure 3.4: Reflection and transmission of incident wave at a boundary.

The reflection and transmission coefficients (R,T) with subscripts (i,ii) denote:

i) polarization of output wave, due to

ii) polarization of input wave at surface.

The reflected and transmitted fields may be written in terms of the individual components:

$$E_{x2} = R_{xx}E_{x1} + R_{xy}E_{y1} + T_{xx}E_{x4} + T_{xy}E_{y4}$$
$$E_{y2} = R_{yx}E_{x1} + R_{yy}E_{y1} + T_{yx}E_{x4} + T_{yy}E_{y4}$$
$$E_{x3} = T_{xx}E_{x1} + T_{xy}E_{y1} + R_{xx}E_{x4} + R_{xy}E_{y4}$$
$$E_{y3} = T_{yx}E_{x1} + T_{yy}E_{y1} + R_{yx}E_{x4} + R_{yy}E_{y4}$$

Equation 3.2: Reflected (E_{x2}, E_{y2}) and transmitted (E_{x3}, E_{y3}) fields.

3.1.3 Representation of dielectric material.

The complex dielectric constant used to represent the effect of the dielectric material is symbolized by the complex value E* or by the real values Er and tanδ where:
$$E^{*} = Er(1 - j\tan\delta)$$

The value of $\sqrt{E^{*}}$ is often needed as it occurs frequently in the equations for reflection and transmission in dielectrics.

Writing $\sqrt{E^{*}}$ as real(g) and imaginary(h) components, where g, h are real, gives:

$$\sqrt{E^{*}} = \sqrt{\left[Er(1 - j\tan\delta)\right]}$$
$$= g - ih$$
$$g \cong \sqrt{Er} \text{ and } h \cong \frac{\sqrt{Er}\tan\delta}{2}$$
using the Binomial expansion.

Equation 3.3: Complex dielectric constant E*.

3.1.3.1 Adaptation of effective complex dielectric constant for oblique incidence.

The values of Er and tanδ for the complex dielectric material are dependent on the angle of incidence and the polarization of the incident wave.

The effective complex dielectric constant Er$_{effective}$ and tan$\delta_{effective}$ for perpendicular(1) and parallel(2) polarization at angle of incidence θ are calculated from the value of Er and tanδ at normal incidence using the following equations:

1) Perpendicular polarization:

$$Er_{effective \perp} = \frac{Er^2}{\left(1 + \frac{(Er-1)}{\cos^2\theta}\right)}$$

$$tan\delta_{effective \perp} = \frac{\left(Er - 2\sin^2\theta\right)\tan\delta}{Er - \sin^2\theta}$$

2) Parallel polarization:

$$Er_{effective \parallel} = 1 + \frac{(Er-1)}{\cos^2\theta}$$

$$tan\delta_{effective \parallel} = \frac{Er\tan\delta}{Er - \sin^2\theta}$$

using equations given by Cady *et al.*, 1948, p.352.

Equation 3.4: Effective complex dielectric for parallel and perpendicular polarization at oblique incidence.

3.1.3.2 Reflection coefficient r_{ab}.

The reflection coefficient r_{ab} for a wave incident on complex dielectric material (Er, tanδ) from air (Er = 1, tanδ = 0) is given by:

$$r_{ab} = \left[\frac{\sqrt{E^*} - 1}{\sqrt{E^*} + 1} \right]$$

$$= \frac{\sqrt{Er}\sqrt{(1 - j\tan\delta)} - 1}{\sqrt{Er}\sqrt{(1 - j\tan\delta)} + 1}$$

or:

$$= \frac{g - 1 - ih}{g + 1 - ih}$$

this gives:

$$r_{ab} = \sqrt{\left(\frac{(g-1)^2 + h^2}{(g+1)^2 + h^2} \right)} e^{j\phi}$$

where:

$$\phi = \tan^{-1}\left(\frac{-h}{g-1} \right) - \tan^{-1}\left(\frac{-h}{g+1} \right)$$

$$= x - y$$

where:

$$\tan(x - y) = \frac{\tan x - \tan y}{1 + \tan x \tan y}$$

$$= \frac{\left(\frac{-h}{g-1} \right) - \left(\frac{-h}{g+1} \right)}{1 + \left(\frac{-h}{g-1} \right)\left(\frac{-h}{g+1} \right)}$$

$$= \left(\frac{-h(g+1) + h(g-1)}{(g-1)(g+1) + h^2} \right)$$

$$= \frac{-2h}{\left(g^2 - 1 + h^2 \right)}$$

Ignoring terms in tan$^2\delta$ and above:

$$\phi = \tan^{-1}\left(\frac{-\sqrt{Er}\tan\delta}{(Er - 1)} \right)$$

The reflection coefficient r_{ab} may therefore be written:

$$r_{ab} = \frac{\left(\sqrt{Er} - 1\right)}{\left(\sqrt{Er} + 1\right)} e^{-j\tan^{-1}\left(\frac{\sqrt{Er}\tan\delta}{Er-1}\right)}$$

or:

$$r_{ab} = M1\,e^{-jM2}$$

where amplitude, $M1 = \dfrac{\left(\sqrt{Er} - 1\right)}{\left(\sqrt{Er} + 1\right)}$

and phase, $M2 = \tan^{-1}\left(\dfrac{\sqrt{Er}\tan\delta}{Er-1}\right)$

where the values of Er and $\tan\delta$ are those of the effective dielectric constant for (1) perpendicular and (2) parallel polarizations for oblique incidence as required.

Equation 3.5: Reflection coefficient r_{ab}.

3.1.4 Layered medium.

If the surface and subsurface materials form a stratified medium further multiple reflections occur at the many different boundaries below the surface. The initial transmitted wave through the ground surface as calculated above undergoes many further reflections and transmissions at the boundaries between the surface and subsurface layers, resulting in additional reflections, in time, from the ground surface. On passing through each layer of dielectric material the incident wave is attenuated and the overall loss may be determined. The stratified medium is represented by distinct layers of different complex dielectric material of finite thickness and the overall sum of the multiple reflections occurring in this system of layers is determined to give the steady state solution (both amplitude and phase information) of the reflected signal from the ground surface.

The behaviour of the incident wave as it passes through the layered complex dielectric material is determined by considering the theory of multiple reflections within the layered system and by determining the amplitude ratio (loss) of the incident wave travelling through each of the individual layers.

3.1.4.1 Theory of multiple reflections.

The theory of multiple reflections is used to calculate the multiple reflected signal from the layers.
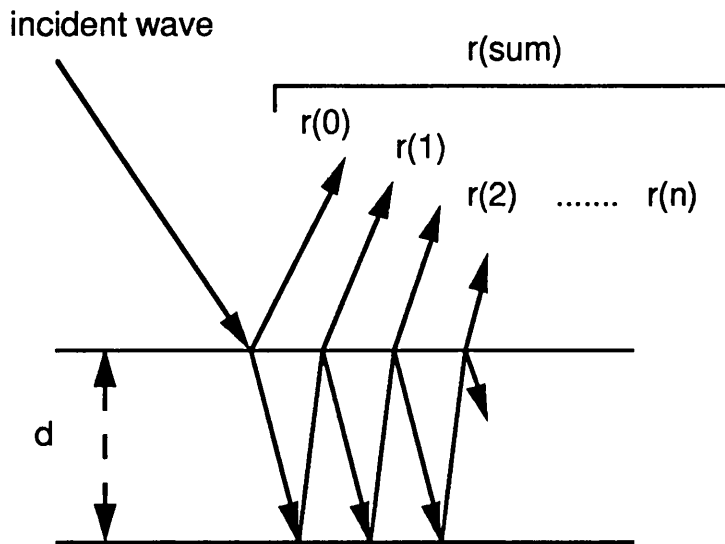
Figure 3.5: Multiple reflections within a layer of dielectric material.

Consider the path of a wave incident on a layer of dielectric material. As it travels from left to right from region a, through region b to region c it crosses two boundaries a:b, b:c. At the boundaries the wave is partially reflected and partially transmitted. The total reflected wave is therefore a sum of the component reflections $r_0, r_1, r_2, r_3.....r_n$ due to multiple reflections occurring within the central region.

Let the incident wave be of unity value.

Let r_{ab}, t_{ab} be the reflection and transmission amplitude components for region a to b, where:

$r_{ab} = -r_{ba}$

$t_{ab} = t_{ba}$

and $t_{ab} = 1 + r_{ab}$

Let F_b represent the amplitude ratio (z = d:z = 0) of the wave travelling in region b (from region a towards region c).

The component reflections r_0, r_1, r_2, r_3....r_n may be written as a multiplication of the relevant reflection, transmission and amplitude coefficients (with similar sections grouped) as follows:

$r_0 = r_{ab}$

$r_1 = t_{ab} F_b\, r_{bc} F_b\, t_{ba}$

$r_2 = t_{ab} F_b\, r_{bc} F_b\, r_{ba} F_b\, r_{bc} F_b\, t_{ba}$

$r_3 = t_{ab} F_b\, r_{bc} F_b\, r_{ba} F_b\, r_{bc} F_b\, r_{ba} F_b\, r_{bc} F_b\, t_{ba}$

etc.

therefore:

$r_{ac} = r_{ab} + t_{ab}\, t_{ba}\, F_b{}^2\, r_{bc} \left(1 + F_b{}^2\, r_{ba}\, r_{bc} + (F_b{}^2\, r_{ba}\, r_{bc})^2 + ...\right)$

$$= r_{ab} + t_{ab} t_{ba} F_b{}^2 r_{bc} \left(\frac{1}{1 - F_b{}^2 r_{ba} r_{bc}} \right)$$

= sum of reflected components

Similarly, the sum of the transmitted components may be found:

$t_1 = t_{ab} F_b\, t_{bc}$

$t_2 = t_{ab} F_b\, r_{bc} F_b\, r_{ba} F_b\, t_{ba}$

etc.

therefore:

$t_{ac} = t_{ab} F_b\, t_{bc} \left(1 + (F_b{}^2\, r_{bc}\, r_{ba}) + ...\right)$

$$= \left(\frac{t_{ab} F_b t_{bc}}{1 - F_b{}^2 r_{bc} r_{ba}} \right)$$

= sum of transmitted components

From the above, the sum of the reflected components is given by r_{ac} , where:

$$r_{ac} = r_{ab} + \left(\frac{t_{ab} t_{ba} F_b{}^2 r_{bc}}{1 - F_b{}^2 r_{ba} r_{bc}} \right)$$

substituting for r_{ba}, t_{ab}, t_{ba}:

$$r_{ac} = \frac{r_{ab}\left(1 + F_b^2 r_{bc} r_{ab}\right) + \left(1 + r_{ab}\right)\left(1 - r_{ab}\right)F_b^2 r_{bc}}{1 + F_b^2 r_{bc} r_{ab}}$$

$$R = \frac{r_{ab} + F_b^2 r_{bc}}{1 + F_b^2 r_{bc} r_{ab}}$$

= sum of reflected components

Also, the sum of transmitted components is given by t_{ac}, where:

$$t_{ac} = \left(\frac{t_{ab} F_b t_{bc}}{1 - F_b^2 r_{bc} r_{ba}}\right)$$

$$T = \frac{F_b\left(1 + r_{ab}\right)\left(1 + r_{bc}\right)}{1 + F_b^2 r_{bc} r_{ab}}$$

= sum of transmitted components

If the interface is symmetrical (material 1 the same as material 3) then:

$r_{ac} = r_{ca}$

and therefore the amplitude sum of reflected components R may be written as follows:

$$R = \frac{r_{ab}\left(1 - F_b^2\right)}{1 - r_{ab}^2 F_b^2}$$

as $r_{ab} = -r_{bc}$

Also:

$t_{ac} = t_{ca}$

and therefore the amplitude sum of transmitted components T may be written as follows:

$$T = \frac{F_b\left(1 + r_{ab}\right)\left(1 - r_{ab}\right)}{1 - r_{ab}^2 F_b^2}$$

$$= \frac{F_b\left(1 - r_{ab}^2\right)}{1 - r_{ab}^2 F_b^2}$$

This may be summarized by the following diagram (figure 3.6):
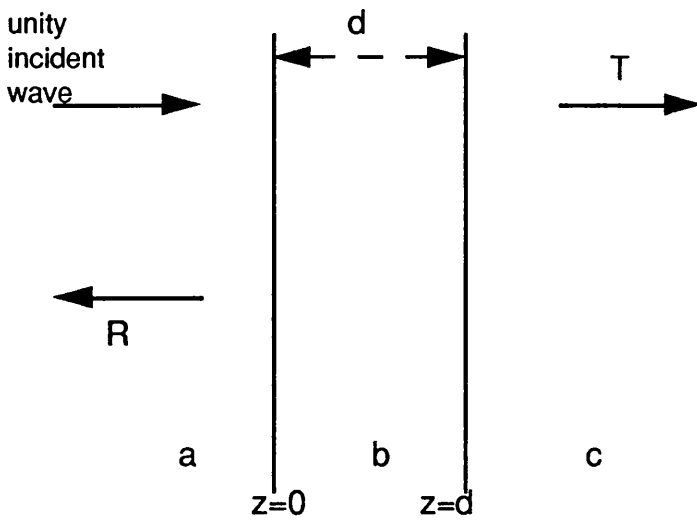
Figure 3.6: Multiple reflections within a layer.

Where the sum of the reflected components is given by:

$$r_{ac} = r_{ab} + \frac{t_{ab}t_{ba}F_b{}^2r_{bc}}{\left(1 - F_b{}^2r_{ba}r_{bc}\right)}$$

and the sum of the transmitted components is given by:

$$t_{ac} = \frac{t_{ab}F_bt_{bc}}{\left(1 - F_b{}^2r_{ba}r_{bc}\right)}$$

The steady state solution for the reflected signal, R, from this layer is given by:

$$R = \frac{r_{ab}\left(1 - F_b{}^2\right)}{1 - r_{ab}{}^2F_b{}^2}$$

and the steady state transmitted signal, T, is:

$$T = \frac{F_b\left(1 - r_{ab}{}^2\right)}{1 - r_{ab}{}^2F_b{}^2}$$

Equation 3.6: Steady state reflected (R) and transmitted (T) signals for multiple reflections within a layer.

3.1.4.2 Amplitude ratio of incident wave travelling through layer.

The amplitude ratio of the incident wave travelling through the layer of thickness d (for a single pass only) is determined by considering the amplitude at x = 0, compared with that at x = d. The wave is attenuated by the factor $e^{-j\frac{2\pi x\sqrt{E^*}}{\lambda}}$ on travelling through the dielectric medium. This factor may be represented by F_b, for the dielectric layer of thickness d, where:

$$F_b = e^{-j\frac{2\pi d\sqrt{E^*}}{\lambda}}$$

and $E^* = Er(1 - j\tan\delta)$

Writing $\sqrt{E^*}$ as g - ih where g, h are real and then substituting for these values of g, h in the original expression for F_b gives:

$$F_b = e^{-\frac{2\pi d\, i(g-ih)}{\lambda}}$$

$$= e^{-\frac{2\pi d\, h}{\lambda}} e^{-\frac{2\pi d\, ig}{\lambda}}$$

$$= e^{-\frac{2\pi d\sqrt{Er}\tan\delta}{2\lambda}} e^{-\frac{2\pi d\, i\sqrt{Er}}{\lambda}}$$

$$= Ae^{-j\phi}$$

where $A = e^{-\frac{\pi d\sqrt{Er}\tan\delta}{\lambda}}$

and $\phi = \dfrac{2\pi d\sqrt{Er}}{\lambda}$

For oblique incidence the amplitude ratio changes (F_{bia}) due to the incidence angle (θ):

$F_{bia} = A_{ia}\, e^{-j\phi_{ia}}$ is the amplitude ratio for oblique incidence,

where $A_{ia} = e^{-\frac{2\pi d\, Er\tan\delta}{2\lambda\sqrt{(Er-\sin^2\theta)}}}$

and $\phi_{ia} = \dfrac{2\pi d\sqrt{(Er - \sin^2\theta)}}{\lambda}$

Equation 3.7: Amplitude ratio F_b for normal incidence and F_{bia} for oblique incidence.

The values Er, tanδ as given here in the equations for F_{bia} are the original values to describe the layer, and do not change with polarization or incidence angle.

3.1.5 Matrix method.

This section describes the specific complex matrix method used for the computer model. The dielectric layers are mathematically represented by scattering matrices. These represent the effect of the layers on the radar signal which is determined using the theory of reflection and transmission at the interfaces, and the theory of multiple reflections within the layers.

The reflection, transmission and absorption properties of the dielectric material depend on the complex relative dielectric constant for the material, the frequency, polarization state (orientation, ellipticity) and angle of incidence of the incidence wave, and the depth of the layers. The effect of each layer also depends on the properties of the other layers so cascaded matrices are used to calculate the combined effect.

3.1.5.1 Matrix representation.

The multiple layers of dielectric material are represented by a series of matrices. Each matrix relates the fields on one side of the layer to the fields on the other side of the layer. The complex cascaded transmission matrix for each layer therefore represents the total effect of that individual dielectric layer. Multiplication of the matrices for each layer in turn gives the overall reflection and transmission properties of the series of layers.

The reflected and transmitted fields may be written in terms of the individual components (from equation 3.2):

$$E_{x2} = R_{xx}E_{x1} + R_{xy}E_{y1} + T_{xx}E_{x4} + T_{xy}E_{y4}$$
$$E_{y2} = R_{yx}E_{x1} + R_{yy}E_{y1} + T_{yx}E_{x4} + T_{yy}E_{y4}$$
$$E_{x3} = T_{xx}E_{x1} + T_{xy}E_{y1} + R_{xx}E_{x4} + R_{xy}E_{y4}$$
$$E_{y3} = T_{yx}E_{x1} + T_{yy}E_{y1} + R_{yx}E_{x4} + R_{yy}E_{y4}$$

Which may be written in matrix form:

$$
\begin{bmatrix} E_{x2} \\ E_{y2} \\ E_{x3} \\ E_{y3} \end{bmatrix} =
\begin{bmatrix} R_{xx} & R_{xy} & T_{xx} & T_{xy} \\ R_{yx} & R_{yy} & T_{yx} & T_{yy} \\ T_{xx} & T_{xy} & R_{xx} & R_{xy} \\ T_{yx} & T_{yy} & R_{yx} & R_{yy} \end{bmatrix}
\begin{bmatrix} E_{x1} \\ E_{y1} \\ E_{x4} \\ E_{y4} \end{bmatrix}
$$

where x,y denote perpendicular and parallel polarization respectively (in fields 1, 2, 3, and 4), and the reflection and transmission coefficients of perpendicular(x) and parallel(y) polarization components are denoted by R and T, giving the general form of the transmission matrix [TM] :

$$[TM] = \begin{bmatrix} R_{xx} & R_{xy} & T_{xx} & T_{xy} \\ R_{yx} & R_{yy} & T_{yx} & T_{yy} \\ T_{xx} & T_{xy} & R_{xx} & R_{xy} \\ T_{yx} & T_{yy} & R_{yx} & R_{yy} \end{bmatrix}$$

where subscripts x and y denote perpendicular and parallel polarization respectively.

For the dielectric material, $R_{xy} = R_{yx} = T_{xy} = T_{yx} = 0$ so the transmission matrix reduces to:

$$[TM] = \begin{bmatrix} R_{xx} & 0 & T_{xx} & 0 \\ 0 & R_{yy} & 0 & T_{yy} \\ T_{xx} & 0 & R_{xx} & 0 \\ 0 & T_{yy} & 0 & R_{yy} \end{bmatrix}$$

Replacing subscripts xx, yy with 1, 2 (perp., para. polarization):

$$[TM] = \begin{bmatrix} R_1 & 0 & T_1 & 0 \\ 0 & R_2 & 0 & T_2 \\ T_1 & 0 & R_1 & 0 \\ 0 & T_2 & 0 & R_2 \end{bmatrix}$$

where:

$$\begin{bmatrix} E_{x2} \\ E_{y2} \\ E_{x3} \\ E_{y3} \end{bmatrix} = [TM] \begin{bmatrix} E_{x1} \\ E_{y1} \\ E_{x4} \\ E_{y4} \end{bmatrix}$$

Rearranging to give the fields on one side of the boundary in terms of the fields on the other:

[fields on RHS] = [C] [fields on LHS]

$$\begin{bmatrix} E_{x3} \\ E_{y3} \\ E_{x4} \\ E_{y4} \end{bmatrix} = [C] \begin{bmatrix} E_{x1} \\ E_{y1} \\ E_{x2} \\ E_{y2} \end{bmatrix}$$

where [C] is the complex cascaded transmission matrix.

Solution for complex cascaded transmission matrix:

$$E_{x2} = R_1 E_{x1} + T_1 E_{x4}$$
$$E_{y2} = R_2 E_{y1} + T_2 E_{y4}$$
$$E_{x3} = T_1 E_{x1} + R_1 E_{x4}$$
$$E_{y3} = T_2 E_{y1} + R_2 E_{y4}$$

therefore:

$$E_{x3} = T_1 E_{x1} + \frac{R_1}{T_1}\left(E_{x2} - R_1 E_{x1}\right)$$

$$= \left(T_1 - \frac{R_1^2}{T_1}\right)E_{x1} + \frac{R_1}{T_1}E_{x2}$$

$$E_{y3} = T_2 E_{y1} + \frac{R_2}{T_2}\left(E_{y2} - R_2 E_{y1}\right)$$

$$= \left(T_2 - \frac{R_2^2}{T_2}\right)E_{y1} + \frac{R_2}{T_2}E_{y2}$$

$$E_{x4} = \frac{1}{R_1}\left(E_{x3} - T_1 E_{x1}\right)$$

$$= \frac{-T_1}{R_1}E_{x1} + \frac{1}{R_1}\left\{\left(T_1 - \frac{R_1^2}{T_1}\right)E_{x1} + \frac{R_1}{T_1}E_{x2}\right\}$$

$$= \frac{-R_1}{T_1}E_{x1} + \frac{1}{T_1}E_{x2}$$

$$E_{y4} = \frac{1}{R_2}\left(E_{y3} - T_2 E_{y1}\right)$$

$$= \frac{-T_2}{R_2}E_{y1} + \frac{1}{R_2}\left\{\left(T_2 - \frac{R_2{}^2}{T_2}\right)E_{y1} + \frac{R_2}{T_2}E_{y2}\right\}$$

$$= \frac{-R_2}{T_2}E_{y1} + \frac{1}{T_2}E_{y2}$$

In matrix form:

$$
\begin{bmatrix} E_{x3} \\ E_{y3} \\ E_{x4} \\ E_{y4} \end{bmatrix} =
\begin{bmatrix}
T_1 - \dfrac{R_1{}^2}{T_1} & 0 & \dfrac{R_1}{T_1} & 0 \\
0 & T_2 - \dfrac{R_2{}^2}{T_2} & 0 & \dfrac{R_2}{T_2} \\
\dfrac{-R_1}{T_1} & 0 & \dfrac{1}{T_1} & 0 \\
0 & \dfrac{-R_2}{T_2} & 0 & \dfrac{1}{T_2}
\end{bmatrix}
\begin{bmatrix} E_{x1} \\ E_{y1} \\ E_{x2} \\ E_{y2} \end{bmatrix}
$$

$$= [C]\begin{bmatrix} E_{x1} \\ E_{y1} \\ E_{x2} \\ E_{y2} \end{bmatrix}$$

where [C] is the complex cascaded transmission matrix.

3.1.5.1.1 Total complex cascaded matrix.

The total complex cascaded matrix [C] describing the effect of all the dielectric layers is calculated by multiplication of the individual matrices for each layer in turn.

$$[C] = \sum_{i=0}^{n}[C]_i [C]_{i-1}$$

where $[C]_0 = I$ (identity matrix)

The complex cascaded transmission matrices for each of the dielectric layers are multiplied together in turn. The method of matrix multiplication involves considering the effects of the different layers in reverse order to that in which the incident wave passes through.

3.1.5.1.2 Reflected and transmitted fields.

Once the total cascaded transmission matrix [C] is known (effect of all the layers of dielectric material) the reflected and transmitted fields for particular incident fields may be calculated:

$$
\begin{bmatrix} E_{x3} \\ E_{y3} \\ E_{x4} \\ E_{y4} \end{bmatrix} = [C] \begin{bmatrix} E_{x1} \\ E_{y1} \\ E_{x2} \\ E_{y2} \end{bmatrix}
$$

1) incident field
2) reflected field
3) transmitted field
4) reflected field from further discontinuities

The input signal (1) may be described by E_{x1} and E_{y1}, the complex incident wave vectors (components of perpendicular and parallel polarization, amplitude and phase information: a1, a2, δ as given in 3.1.1).

The reflected field (4) may be assumed to be zero for the overall system (for free space operation, neglecting passive microwave effects from deeper layers). The reflected field(2) and transmitted field(3) may therefore be found in terms of the incident field(1).

Writing $E_{x1} = X$, and $E_{y1} = Y$, where X and Y are complex vectors, and setting E_{x4} and E_{y4} to zero, gives:

$$
\begin{bmatrix} E_{x3} \\ E_{y3} \\ 0 \\ 0 \end{bmatrix} = [C] \begin{bmatrix} X \\ Y \\ E_{x2} \\ E_{y2} \end{bmatrix}
$$

The reflected field(2) and transmitted field(3) components may therefore be found in terms of the incident field components X, Y.

The above matrix may be solved for E_{x2} and E_{y2}, the reflected components:

3) $0 = XC_{31} + YC_{32} + E_{x2}C_{33} + E_{y2}C_{34}$

4) $0 = XC_{41} + YC_{42} + E_{x2}C_{43} + E_{y2}C_{44}$

3)*C_{43} - 4)*C_{33} gives:

$$0 = XC_{31}C_{43} + YC_{32}C_{43} + E_{y2}C_{34}C_{43}$$
$$- (XC_{41}C_{33} + YC_{42}C_{33} + E_{y2}C_{44}C_{33})$$

$$E_{y2} = \frac{X(C_{31}C_{43} - C_{41}C_{33}) + Y(C_{32}C_{43} - C_{42}C_{33})}{C_{44}C_{33} - C_{34}C_{43}}$$

where E_{y2} is the parallel component of the reflected wave.

Similarly:

3)*C_{44} - 4)*C_{34} gives:

$$E_{x2} = \frac{X(C_{31}C_{44} - C_{41}C_{34}) + Y(C_{32}C_{44} - C_{42}C_{34})}{C_{43}C_{34} - C_{33}C_{44}}$$

where E_{x2} is the perpendicular component of the reflected wave.

The transmitted components E_{x3}, E_{y3} may then be found:

$$E_{x3} = C_{11}X + C_{12}Y + C_{13}E_{x2} + C_{14}E_{y2}$$

where E_{x3} is the perpendicular component of the transmitted wave.

$$E_{y3} = C_{21}X + C_{22}Y + C_{23}E_{x2} + C_{24}E_{y2}$$

where E_{y3} is the parallel component of the transmitted wave.

3.1.5.1.3 Total reflected and transmitted power, and energy absorbed.

The total reflected power is given by:

$$\text{reflectvoltsq} = ((E_{x2})^2 + (E_{y2})^2)$$

The total transmitted power is given by:

$$\text{transvoltsq} = ((E_{x3})^2 + (E_{y3})^2)$$

The absorbed energy is 1 - (reflectvoltsq + transvoltsq)

Equation 3.8: Reflected and transmitted power and absorbed energy.

3.1.6 Calculation of co and cross polar power.

The co and cross polar output power for all possible input polarization states is calculated to produce the 3D polarization response plots. The input polarization states are given in section 3.1.1.

The co and cross polar power is determined by analyzing the content of the output signal. For maximum power transfer the receiver is set to be the complex conjugate of the transmitted signal. The co polar power (coposq) may therefore be found by multiplying the received signal by the complex conjugate of the incident transmitted signal. The cross polar power (crposq) is then given by the remainder when the co polar power is subtracted from the total reflected power (reflectvoltsq).

If the incident wave is given by a1, a2 $e^{+j\delta}$ (representing the perpendicular and parallel components of incident signal), the necessary receiver to calculate the co polar power is given by a1, a2 $e^{-j\delta}$ i.e. same orientation but opposite hand (ellipticity).
The output vector must therefore be multiplied by the conjugate of the input signal to get the co polar power.

if the complex input vector (real, imag.) is given by:
ypolarc = (a1, 0),
xpolarc = (a2.cos(δ), a2.sin(δ)) for the two polarizations

receiver (rx) complex vector is given by:

rxy = ypolarc,

rxx = (a2.cos(δ), -a2.sin(δ))

if the output reflected components are r1c, r2c

then the two components of the co polar power co1 and co2 are:

co1 = r1c * rxy,

co2 = r2c * rxx

taking the absolute value of these complex field vectors, and squaring to get the power gives:

co1po = (abs(co1))^2 ,

co2po = (abs(co2))^2

and adding these two components gives the total co polar power output (coposq):

coposq = co1po + co2po

The cross polar power output (crposq) is given by:

crposq = reflectvoltsq - coposq

Equation 3.9: Co polar and cross polar power.

3.2 Theoretical validation and correlation work.

Confidence in the computer model is gained by correlating the computed values of output power and phase with theoretical design curves, published theoretical values, and published measured results over geophysical surfaces. The reflected signal from various terrestrial surfaces is computed and the theoretical results are compared with published values.

Validation and correlation work using this theoretical program is given in Appendix A1.2.

As an example, the theoretical emissivity of a layer of sea ice over sea water is computed. The plot giving the variation of the theoretical calculated emissivity of the ice layer with changing depth is given in figure 3.7. This correlates well with the plot given by Ulaby *et al.* (1986). These data are related to the brightness temperatures which would be measured by a passive microwave remote sensing system (sections 2.3.1.2, 3.4.1).

i)

Change in emissivity of sea ice layer of increasing depth.

ii)

Frequency = 1 GHz
Nadir Angle = 0°
$\varepsilon_{si} = 3.2 - j\,0.2$
$T_s = -5°C$
Water Salinity = 36 ‰.
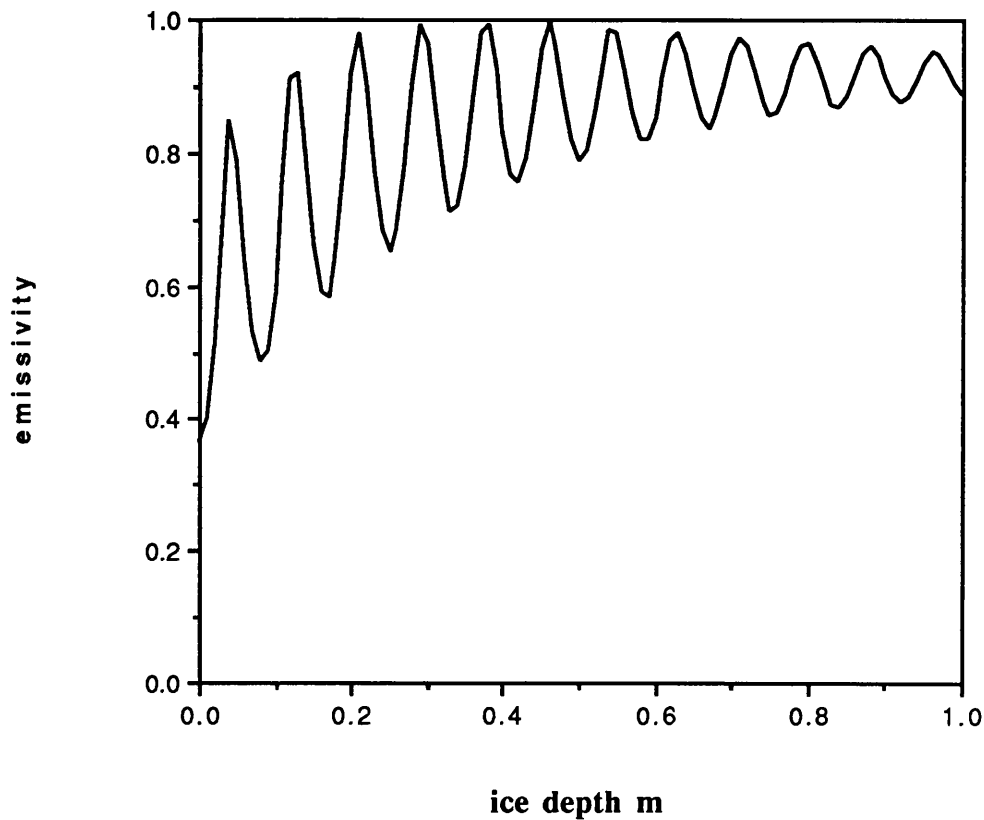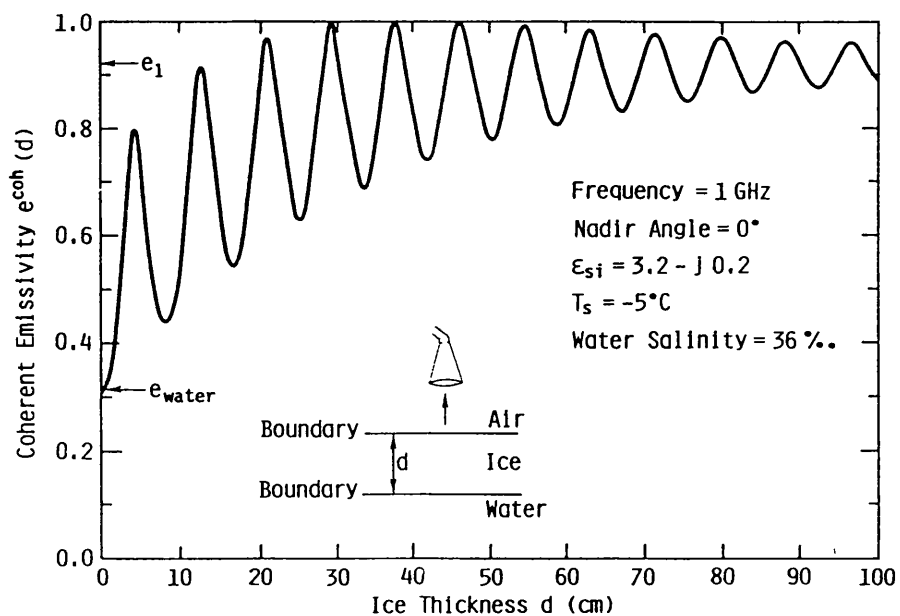
Figure 3.7: Crosscheck of model:- i) Theoretical computed emissivity of sea ice layer of depth 0-1m over sea water, ii) published data from Ulaby *et al.* (1986), chapter 18, p.1483.

Theoretical investigations using the model are detailed in Appendix A1.3. These investigations assist with the theoretical development and validation of the computer model.

The importance of including the effect of multiple reflections in surface and subsurface layers is analysed, showing that the initial Fresnel reflection from the surface and the transient signals may be vastly different to the steady state value of the multiple reflected signal. An example is given in which the contribution of multiple reflections occurring in a layer results in the received power being increased by three times the Fresnel value.

3.3 Classification methods using active polarimetric data.

3.3.1 Total power values.

Different areas of the images may be classified into the terrain type by considering the return power of the radar signal. This method of classification of images into terrain type is useful, for example, in determining the area of the ice sheet in the ablation zone which is covered by surface water (melt pools) or by snow. This ablation area may be monitored over the melt season to give information on the extent of surface melting of the ice sheet. This is important for mass balance work over the Greenland ice sheet for studies of climate change. Previous work on the C band AIRSAR 233-1 image in SouthWestern Greenland (measured Aug.1989, located at 64 30.7 N, 48 48.7 W, further down the ice sheet in the ablation zone) clearly shows the melt pools as dark areas and the snow covered areas as lighter areas (Jezek *et al.*, 1993). The melt pools show up as dark areas (low backscatter) due to the water surface acting as a specular reflector, scattering the incident radar signal forwards, away from the direction of the receive antenna. The snow covered areas appear lighter (brighter) due to higher backscatter (discussed in this thesis in section 1.3.1.2 and shown in figure 5.11 Total power image of 233-1 AIRSAR scene).

3.3.2 Linear polarization signals.

Further analysis of the measured return polarimetric radar signal may be used to infer more detailed information of the complex dielectric constant (and hence the material) of the imaged area.

The power ratio versus phase difference method using the relative power and phase information from two linear co polarized signals (VV/HH power and VV-HH phase) may in future be able to be used to classify the imaged area into more specific areas. The polarimetric content of the reflected signal is used to calculate the power ratio of the perpendicular and parallel polarized signals (VV/HH power), and the phase difference between them (VV-HH phase). If this co polar power ratio is plotted against the co polar phase difference the theoretical values for different surfaces are seen to occupy different areas on the plot. The comparison of these points for different surfaces at the same incidence angle, and operating frequency, can potentially provide a method of classification of the imaged terrain.

Figure 3.8 shows the theoretical power ratio versus phase difference between

polarizations plots for typical polar surfaces (dry snow, pure ice and free water, for depth change to 3*skin depth) for C band at 20° incidence angle. A uniform homogeneous layer of the material is simulated, of depth increasing to ~3* skin depth. The complex dielectric constant (Er, tanδ) to represent the materials and the skin depth at C band (5.3GHz) are: (73.457, 0.2654) and 7.92mm for free water, (3.15, 0.0032) and 3.172m for pure ice and (1.66, 0.00006) and 233m for dry snow. These values are taken from table 2.2. The depth change intervals for figure 3.8 are 0.5 to 20mm, 0.5mm increment for free water; 0.25 to 10m, increment 0.25m for pure ice; and for dry snow: 25 to 700m, increment 25m.

The data points for the different materials occupy different, distinct regions on the plot. The data points for free water occupy the highest area on the plot, with those for pure ice in the central region, and those for dry snow in the lowest region of the plot. The response for each of the polar materials shows that free water has the highest power ratio, then pure ice, then dry snow has the lowest values. The response for each of the layers of changing depth spiral in towards the Fresnel value (for very deep layers) as the multiple reflections occurring within the layers change the reflected signal as the depth changes.

The position of each data point on power ratio vs phase difference plots depends on the value of the complex dielectric constant of the material, the depth of the layer, the incidence angle and the operating frequency. The effect of these variables on the polarimetric signal is investigated in detail in Appendix A1.4.
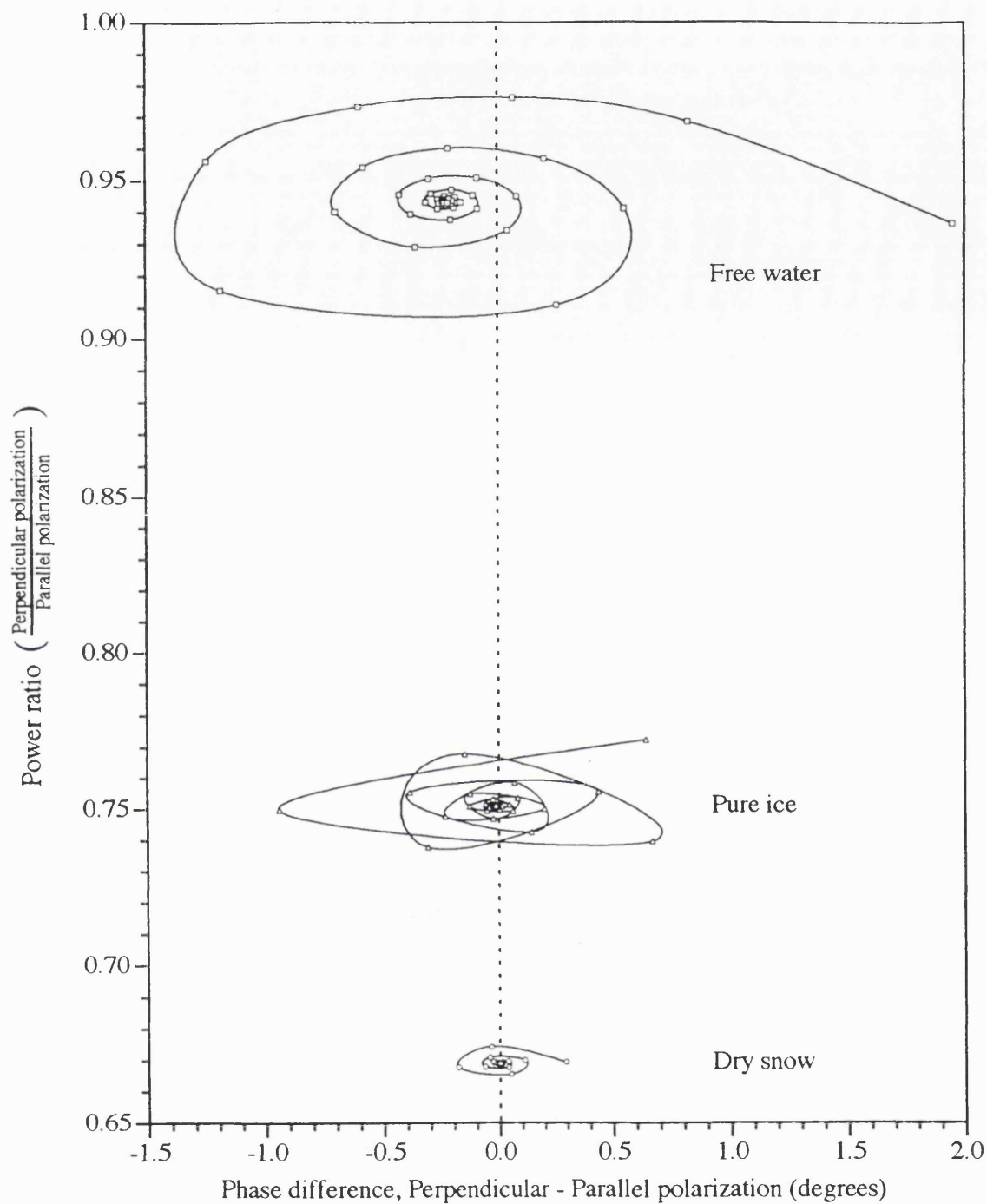
Figure 3.8: Power ratio vs. phase difference plot of theoretical values for C band polar surfaces; free water, pure ice and dry snow (of depths 0 to 3*skin depth) at 20° incidence angle.

This classification method of determining the dielectric constant of the surface and (possibly) the subsurface material using the complex components (amplitude and phase information) of the polarimetric active radar data is valid for the forward reflected signal, and should ideally be used for a bistatic system. In such a system the receive and transmit antennas are separate and symmetrically positioned about the imaged point. The receive antenna measures the active forward scattered signal from the imaged point. In a monostatic system a single antenna is used to both receive and transmit. In such a system the backscattered signal is measured by the receive antenna. In the AIRSAR system the active polarimetric antennas are used to measure the polarimetric content of the backscattered signal from the imaged surface.

Using the program, the theoretical value of the power ratio of the two linear polarization signals (VV/HH power) and the phase difference of these two signals (VV-HH phase) may be calculated for any incidence angle, from any system of dielectric materials of various complex dielectric constant and depths, for any frequency. These theoretical values for forward scatter are compared with the measured values of VV and HH power and phase at a particular incidence angle to determine the dielectric constant of the imaged area. For the analysis work in this thesis the coherent part of the backscattered signal received by the AIRSAR instrument is considered, and data from the near region of the image is used (@ ~20 degrees incidence) to try to maximize the relationship between the measured and the calculated signal. The measured data from the C band 233-1 AIRSAR image of the ablation zone are analysed in chapter 5.

3.3.3 Variation of dielectric constant of snow with frequency and water content.

The dielectric constant of snow depends largely on the water content, the frequency of the incident radiation, and the physical properties of the snow, including the density, grain size, impurities, temperature etc. (Glen and Paren, 1975; Paren and Glen, 1978).
The greater the water content the higher the dielectric constant of the snow. Table 3.1 shows the variation of dielectric constant of snow due to the change in water content (measured as % volume), and also the variation with frequency (values from Jezek *et al.*, 1993). The greater the frequency (for AIRSAR values, from P, L to C band) the lower the real part of the dielectric constant, but the greater the loss tangent (imaginary part of the dielectric constant). This is shown in table 3.1 below (repeated from table 2.2 earlier):

i) **Er:**

% wetness	P band	L band	C band
0	1.66	1.66	1.66
6	2.38	2.37	2.2
15	4.23	4.19	3.6

ii) **tanδ:**

% wetness	P band	L band	C band
0	0.00003	0.00003	0.00006
6	0.013	0.040	0.136
15	0.026	0.080	0.297

Table 3.1 i) and ii): Variation of dielectric constant of snow with change in water content (measured as % volume), and frequency; i) real part Er, ii) imaginary part tanδ (from Jezek *et al.*, 1993).

The water content by volume (% wetness of the snow) may be inferred using the power ratio vs phase difference method of analyzing the measured data, as the dielectric constant of snow is strongly dependent on its water content. Multifrequency data sets give additional results for the same area which help to determine the % wetness of the snow. These results may be correlated to give a more accurate value of the predicted dielectric constant of the surface (and hence the water content of the snow) as the dielectric constant of water is frequency dependent (Debye equation).

$$E_{fw} = E' - jE''$$

where:

$$E' = E_\infty + \frac{\left(E_s - E_\infty\right)}{\left(1 + \omega^2\tau^2\right)}$$

and:

$$E'' = \frac{\omega\tau\left(E_s - E_\infty\right)}{\left(1 - \omega^2\tau^2\right)}$$

where E_s and E_∞ are the static and high frequency permittivities

and τ the dipole relaxation time.

This simplifies to:

$$E_{fw} = 4.9 + \frac{74.1}{\left(1 + j\dfrac{f}{f_o}\right)}$$

where $f_o = 18.64\,GHz$, relaxation frequency of water molecules,

and f is the operating frequency of the radar.

Equation 3.10: Debye equation for the dielectric constant of water.

The Mätzler mixing formula may be used to determine the dielectric constant of snow of different water content (Mätzler, 1987). This formula gives the dielectric constant of the wet snow as a function of the wetness content and the dielectric constant of dry snow.

$$Er_{wet\,snow} = Er_{dry\,snow} + \frac{23W}{\left(1 - i\dfrac{f}{f_o}\right)}$$

where W is the wetness content by volume,

and f_o, the relaxation frequency of wet snow,

is taken to be 10 GHz.

Equation 3.11: Mätzler mixing formula for the dielectric constant of wet snow (1987).

3.3.4 Theoretical dependence of polarimetric response on radar and surface parameters.

The shape of the polarimetric response depends on the dominant type of scattering mechanism as discussed in section 2.1.3 (figure 2.5). The theoretical response for direct scattering depends on the incidence angle of the radar on the surface, the operating frequency of the radar, the dielectric constant of the surface (and subsurface layers) and the depth of the surface (and subsurface) layers.

Previous theoretical modelling work using field data from the Simpson Desert shows that the return signal is mainly dependent on the complex dielectric constant of the surface material and the depth of this surface layer, but a subsurface layer of relatively high dielectric constant will dominate the response; all other layers also affect the response but to a lesser extent.

The structure of the subsurface material of polar regions also consists of horizontal layers of different dielectric constants and different depths representing the variation of the different snowfall events. For example, a subsurface ice layer may be found where the melt water has percolated through the snowpack and refrozen at depth. The formation of depth hoar also produces a distinct layer within the snowpack, causing a dielectric discontinuity. The variation of the snowpack material with depth should therefore be considered in the interpretation of the radar response of the area.

Ground radar measurements (at C and Ku band) made by Jezek *et al.* during a field campaign (Summer 1992) on the Greenland ice sheet show that the return signal from subsurface ice layers dominate the measured radar signal at the test site in the percolation zone (Jezek and Gogineni, 1992; Jezek *et al.* 1994).

3.3.4.1 Theoretical variation of polarimetric response due to change in incidence angle.

The change in the shape of the polarimetric response (for direct scattering) due to the change in incidence angle of the radar is investigated. The theoretical response is computed for dry snow (0% snow, percentage water content, by volume) for P band radar, for forward scatter at 20, 40 and 60 degree incidence angles. These values of incidence angles are chosen to correspond with the range measured by the NASA/JPL AIRSAR. The theoretical plots and the measured data at these incidence angles from the

AIRSAR images are given together in chapter 5 (figure 5.10).

The shape of the co polar power plots show an increase in the central dip as the incidence angle increases. This is due to the ratio of the co polar return power for the two linear polarizations (VV/HH) decreasing as the incidence angle increases, computed using the Fresnel reflectivity of the surface.

The theoretical values are calculated for a uniform deep homogeneous layer of dry snow. Changes in the dielectric constant of the imaged material or the presence of any subsurface discontinuities would change the polarimetric response. This is investigated in the following sections which consider the effect of the dielectric of the surface and also the effect of a subsurface ice layer and the depth of the surface firn layer (sections 3.3.4.2, 3.3.4.3).

3.3.4.2 Theoretical variation of polarimetric response due to change in dielectric constant.

The change in the shape of the forward scattered polarimetric response due to the different dielectric constant of natural terrain, for example, dry snow, pure ice and water for polar surfaces, is shown in figure 3.9 below. The relative dielectric constant of these materials is the lowest for dry snow, higher for pure ice and the largest for free water (refer to table 2.2).

The theoretical polarization response for P band radar at 20 degree incidence on dry snow (0% moisture content by volume), pure ice and free water surfaces show that the lower the dielectric contrast at the air:surface interface, the lower the "dip" in the co polar 3D response plot. The relative difference in return power for the two linear polarizations (HH and VV) causing this dip is greater for a low dielectric constant than for a high value. The relative difference in the HH and VV polarization return signals for the low dielectric snow surface is therefore greater than that for the higher dielectric pure ice surface. Free water is of the highest dielectric constant and so the response shows the least relative difference in the HH and VV polarization return signals for this incidence angle. These differences in the values of the linear polarimetric return signal (HH and VV) are related to the Fresnel reflectivity of the surface material.
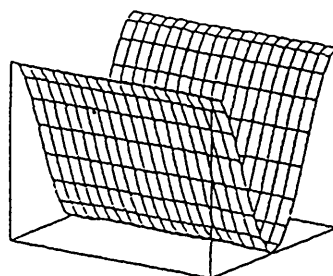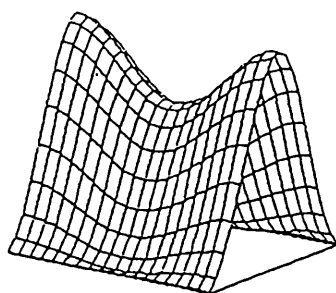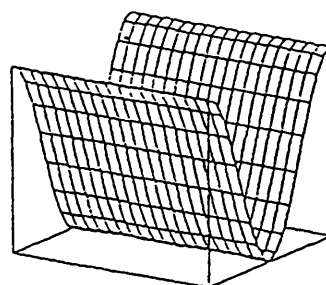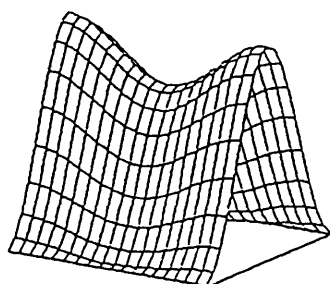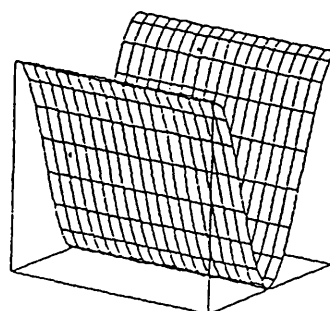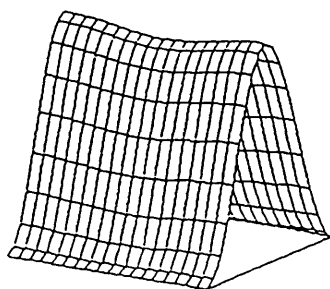
pure ice

free water

Figure 3.9: Theoretical 3D polarimetric response for different dielectrics (0% snow, pure ice, free water) for P band radar at 20 degree incidence (forward scatter).

3.3.4.3 Theoretical variation of polarimetric response due to change in position of subsurface layer.

The position of an ice layer beneath a surface layer of firn is found to affect the polarization response. The theoretical forward scatter P band 3D polarization response at 20 degree incidence, for the snow and ice layers is analysed. The depth of the surface firn layer above the ice layer is varied from 20 to 300mm and the resulting change in the theoretical response is noted. The HH and VV polarization signals are analysed and the VV/HH power ratio vs. VV-HH phase difference plot (figure 3.10) shows that the depth of firn above the ice layer determines the position of the polarimetric return signal on this plot. The results from the theoretical analysis indicate that the position of an ice layer within snowpack may be inferred from measured polarimetric signals, and the accumulation rate of firn may be monitored using polarimetric data from remote sensing systems.

On increasing the depth of firn (d) further , the power ratio: phase difference plot is of the form of close overlapping spirals. This plot is given in chapter 5 (figure 5.11 i and ii), together with the measured data from the AIRSAR image over the percolation zone. The computed data spirals for every ~300mm depth of firn which corresponds to the depth equal to the half the wavelength of the operating frequency. In dielectric material the effective wavelength is reduced as given in equation 3.11 below.

$$\lambda_{effective} = \frac{\lambda}{\sqrt{Er}}$$

Equation 3.11: Effective wavelength ($\lambda_{effective}$).

At P band, the wavelength λ is given by:

$$\lambda = \frac{300}{0.4} = 750mm$$

In the firn (dielectric $Er \cong 1.66$) the effective wavelength is reduced

$$\lambda_{effective} = \frac{\lambda}{\sqrt{Er}} = 582mm$$

so $\frac{\lambda_{effective}}{2} = 291mm$

The total power return will also change as d increases, so the value of the depth of firn may be identified from the polarimetric data and the total power information.
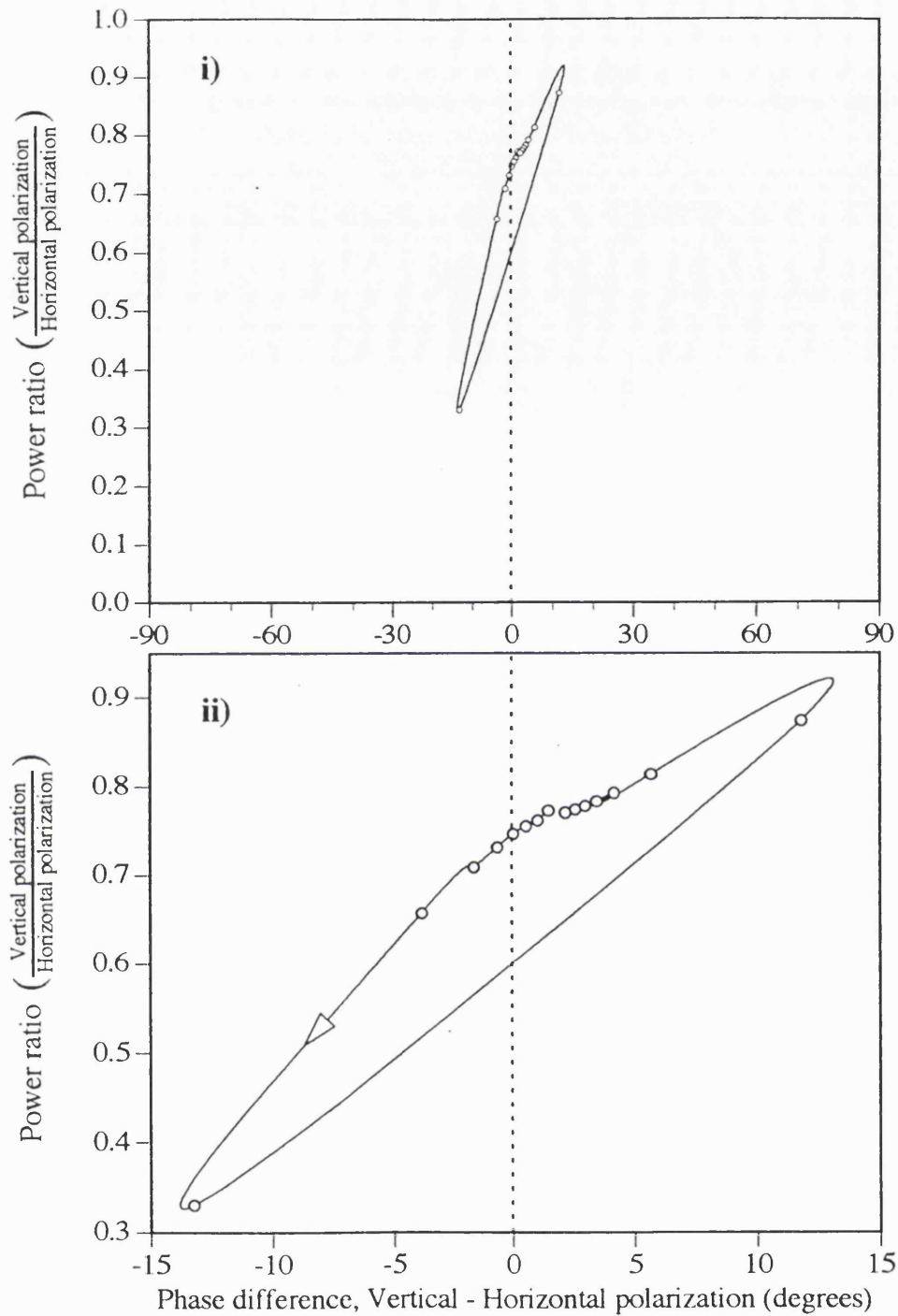
Figure 3.10 i) and, expanded scale ii): Theoretical power ratio versus phase difference plot for VV and HH polarization (P band, 20 degree incidence angle, forward scatter) for change in position of ice layer (depth of firn) from 20 to 300mm depth (20mm steps).

The results from the theoretical polarimetric computer model suggest that the position of an ice layer beneath a layer of surface snow, for example, in the percolation region of the ice sheet, may be determined by polarimetric analysis of the measured return radar signal. The theoretical polarimetric signal is found to be dependent on the depth of the layer of snow above the ice layer. The results from the computer model indicate that the depth of the firn and the accumulation rate may be measured and monitored over each season by analyzing measured polarimetric SAR data. The typical accumulation of snow is of the order of 1m per year for this area of the Greenland ice sheet and this depth is comparable to the wavelength of P band radar. Measurements of the accumulation rate are important for mass balance studies of the ice sheet (Kuhn, 1989) as discussed previously in section 1.1.2.2.

3.4 Inversion of passive polarimetric data to give values of dielectric constant of imaged area and moisture content of snow.

3.4.1 Brightness temperatures (passive data).

The brightness temperature T_B as measured by the SSM/I instrument is given by $T_B = E$ T_S, where for a smooth surface, E, the emissivity, is proportional to (1 - R), where R is the Fresnel reflectivity, and T_S is the physical temperature of the surface.
i.e.
$$T_B = E T_s$$
and
$$E \propto (1 - R)$$
Equation 3.13: Brightness temperature T_B.

The reflectivity (R) of a smooth surface is a function of the polarization of the incidence wave, the angle of incidence (θ), and the complex dielectric constant (Er) of the surface. The reflectivity (R) at 53.2 degrees incidence (correlating to the incidence angle of the SSM/I instrument) is calculated for different dielectrics for perpendicular (v) and parallel (h) polarization respectively (where $R_h > R_v$ for smooth surfaces).
The value of the effective dielectric constant ($Er_{effective}$) for the surface for incidence angle (θ) and polarization (v or h) is used for the calculation, where:

$$R(\text{polarization}, \theta, \text{dielectric}) = \left| \frac{\left(\sqrt{Er_{effective}} - 1 \right)}{\left(\sqrt{Er_{effective}} + 1 \right)} \right|^2$$

Equation 3.14: Fresnel fractional reflected power for oblique incidence.

The reflectivity increases with increasing Er, the value of the dielectric constant describing the electrical properties of the imaged area. The emissivity therefore decreases with increasing Er.

The effective values of the dielectric constant ($Er_{effective}$) are calculated using the equations of Cady *et al.* (1948) as given in section 3.1.3.1.

The emissivity for parallel polarization (E_h) is smaller than that for perpendicular polarization (E_v) for smooth surfaces giving $E_h < E_v$, and hence the measured brightness temperatures for the two polarizations are of the form $T_{Bh} < T_{Bv}$.

The ratio of the brightness temperatures for the two polarizations, T_{Bh} / T_{Bv}, may be written as a function of the dielectric constant of the imaged material as follows:

$$T_{Bh} = E_h \, T_s$$

$$T_{Bv} = E_v \, T_s$$

so

$$\frac{T_{Bh}}{T_{Bv}} = \frac{E_h}{E_v}$$

or

$$\frac{T_{Bh}}{T_{Bv}} = \frac{(1 - R_h)}{(1 - R_v)}$$

where

$$R_{h,v} = f\left(Er_{effective}\right)$$

Equation 3.15: Polarization ratio of brightness temperatures.

The difference in the brightness temperature values for the two polarizations may then be inverted to give the mean value of the dielectric constant Er. The computed polarization ratio T_{Bh} / T_{Bv} for a range of dielectrics at 53.2 degrees incidence angle (corresponding to SSM/I) is given in figure 3.11 below.

i)

Polarization ratio (@53.2deg.) for a range of dielectrics Er (1 - 3)

Dielectric constant Er
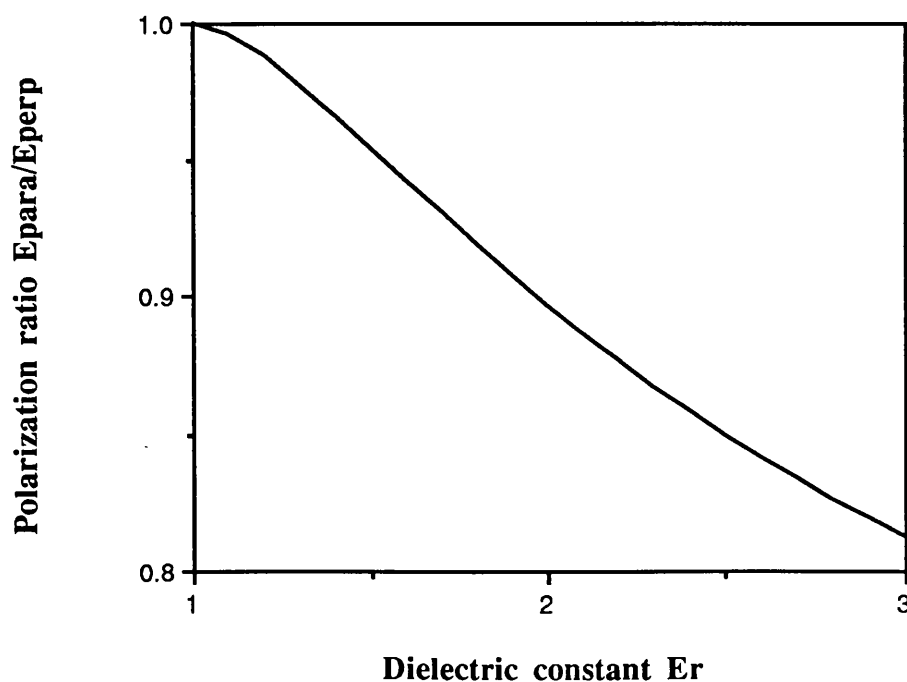
ii)

Polarization ratio (@53.2deg.) for a range of dielectrics Er (2 - 80)
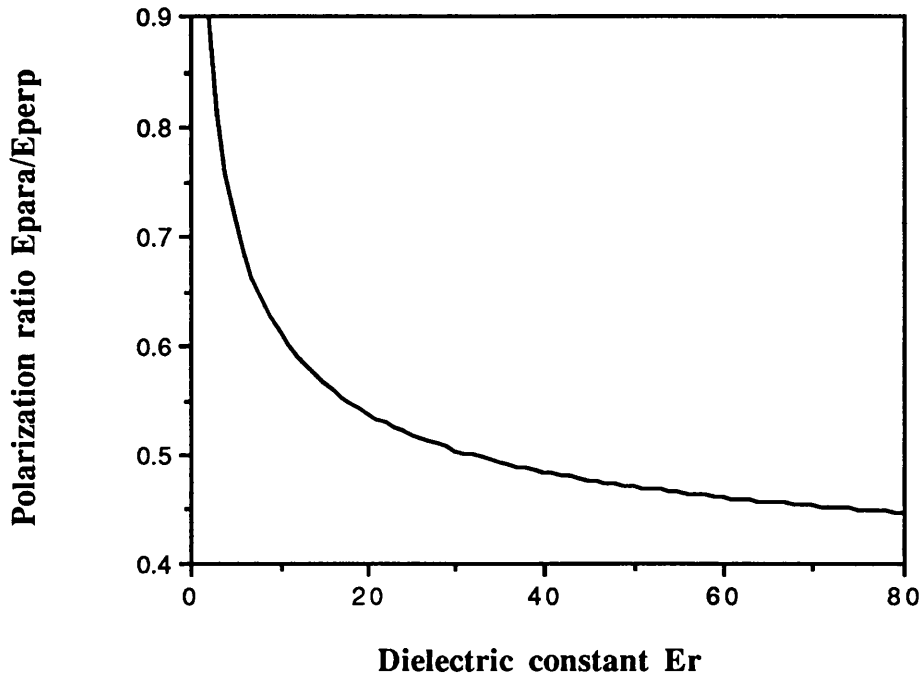
Figure 3.11: Theoretical polarization ratio T_{Bh} / T_{Bv} @53.2 degrees (corresponding to incidence angle of SSM/I instrument) for range of dielectrics i) 1 - 3, ii) 2 - 80.

3.4.2 Polarization ratios (passive data).

The ratio of the brightness temperatures for the two polarizations is investigated using both the standard polarization ratio and the simple polarization ratio (x) given by equation 3.16 below.

$$ i) \frac{(T_{Bv} - T_{Bh})}{(T_{Bv} + T_{Bh})} \qquad ii) \frac{T_{Bh}}{T_{Bv}} $$

Equation 3.16: i) Standard, and ii) Simple polarization ratios.

The standard polarization ratio is equivalent to (1-x)/(1+x) where x is the ratio of the brightness temperatures for the two polarizations. This value x is the most important factor to consider when considering the difference between the two polarizations as it is a direct measure of the relative difference between the emitted radiation for the two linear polarization states. Taking the ratio of the brightness temperatures for the two polarizations is useful as it removes the need to know the surface temperature, T_s.

The standard polarization ratio is the normalized form, and has bounds ± 1. Emission from smooth surfaces gives a positive value of standard polarization ratio, whereas that from a rough or highly vegetated surface gives a negative value.

The simple polarization ratio x will always be positive and of a value < 1 for smooth surfaces and >1 for rough or vegetated areas.

The polarization ratio x of the measured emitted radiation may be inverted to predict the dielectric constant of the imaged material using the theoretical values of the emitted radiation for the two polarization states. The theoretical values are computed using the Fresnel reflection formula for smooth dielectric surfaces and are plotted in figure 3.11 above.

3.4.3 Inversion of passive data to give dielectric constant and % wetness of snow.

The predicted value of the dielectric constant (Er) from the measured passive data may be used to indicate the % wetness by volume (W) of the snow from the snow mixing formula of Mätzler (1987);

$$Er_{wet\,snow} = Er_{dry\,snow} + \frac{23W}{\left(1 - i\frac{f}{f_o}\right)}$$

where $Er_{dry\,snow}$ at 19 GHz is taken to be ~1.2,

and f_o, the relaxation frequency of wet snow,

is taken to be 10 GHz,

so % wetness (W) of the snow is given by:

$$W = \frac{\left[1 + \left(\frac{f}{f_o}\right)^2\right]\left[Er_{mixture} - Er_{dry\,snow}\right]}{23}$$

or

$$W = 0.2038\left[Er_{predicted\,value} - 1.2\right]$$

Equation 3.17: % wetness (W) of snow inferred from Mätzler mixing formula (1987).

The predicted value of the dielectric constant at other frequencies may also be estimated once the % wetness (W) of the snow is determined.

3.4.4 Frequency difference (19-37)T$_B$ (passive data).

The difference in the brightness temperatures for same polarization for the two frequencies 19 and 37GHz are plotted as (19-37)T$_{Bv}$ and (19-37)T$_{Bh}$.

The difference in the value of the measured brightness temperature at the two frequencies is due to the different depths of penetration at the two frequencies, and to the frequency dependence of the emission of the snowpack due to the change in dielectric constant with frequency.

The 19GHz data will include emission from subsurface layers whereas the 37GHz data is from the near surface material. The typical penetration depth of 19GHz and 37GHz radar into snowpack is given by Ulaby et al. (1986), and is of the approximate order of metres (m) for 19GHz and centimetres (cm) for 37GHz; with the actual values depending on various factors including the wetness of the snow and ice particle size, together with the layering details of the snowpack, the presence of inhomogenieties and impurities, and the temperature etc.

The emissivity of the snowpack layers is also frequency dependent as the dielectric constant of snow is largely dependent on the water content, and the dielectric constant of water is frequency dependent. The values of the dielectric constant of water may be calculated from the Debye equation (Equation 3.10) as follows:

dielectric of water at 19.2 Ghz and 37 Ghz from Debye equation:

$$E_{fw} = 4.9 + \frac{74.1}{\left(1 + j\dfrac{f}{f_o}\right)}$$

where $f_o = 18.64\,GHz$, relaxation frequency of water molecules,
and f is the operating frequency of the radar, giving:

$Er_{fw(19.2)} \cong 20$, $\tan\delta_{fw(19.2)} \cong 1.5$ for 19.2 GHz, and

$Er_{fw(37)} \cong 8$, $\tan\delta_{fw(37)} \cong 2.5$ for 37 GHz.

3.5 Error analysis.

The passive microwave brightness temperature data as measured by the SSM/I are accurate to within 1K (CIRES, 1992) from measurement (averaging) errors and instrument noise etc.

The measurements from the AIRSAR system are accurate to ~1dB for total power values from the JPL internal calibration for each campaign. The polarization stability is better than this (A. Freeman, personal communication). Using the power ratio classification method, taking the ratio for the return power of the two linear co polar signals (VV/HH power) and the relative phase difference for these two polarization states (VV-HH phase) therefore gives a greater accuracy.

The effect of the variation in the value of the local incidence angle due to the change of slope of the ice sheet should be taken into account. Details of the local surface slope of the ice sheet (mean slope, and estimated direction of the slope) may be gained using the slopes database derived from ERS-1 radar altimeter data for areas ~25*25km^2 (J. Morley, personal communication). For the dry zone of the ice sheet the mean slope is negligible (~0°) but for the ablation zone at the edge of the ice sheet the surface slope may be as much as 8°. The particular geometry for the system and the imaged area should be considered. The local incidence angle may be calculated from the values of the flight direction of the imaging system and the viewing angle, together with the relative direction and value of the surface slope.
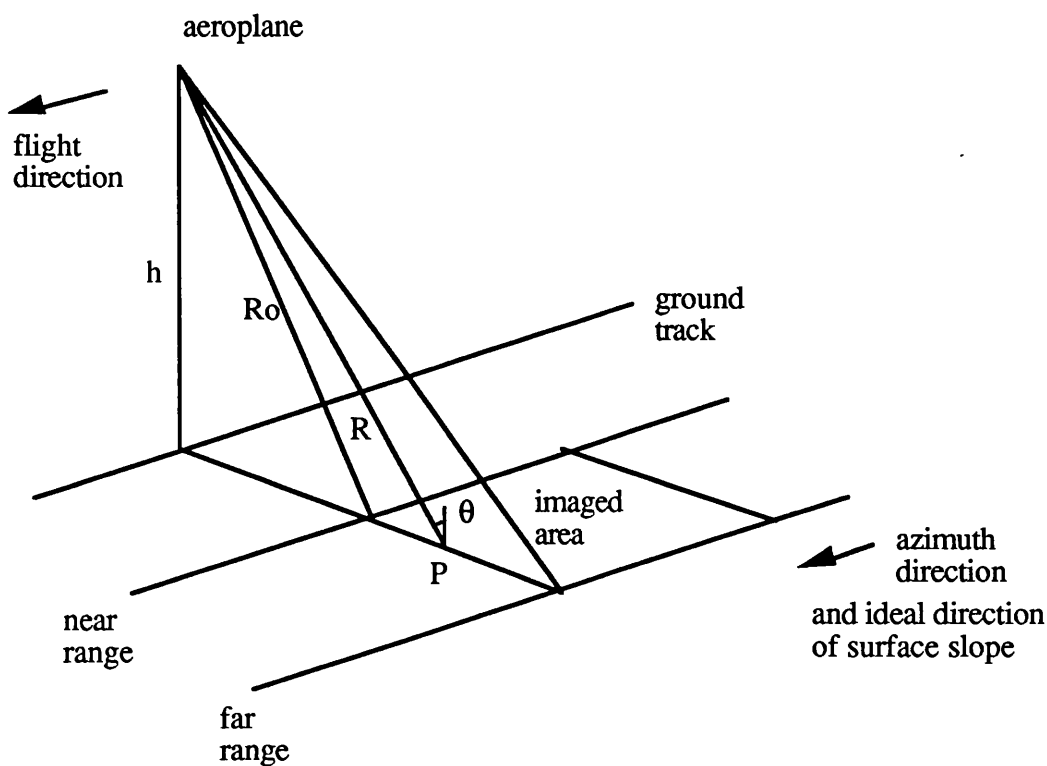
Figure 3.12: Geometry of AIRSAR system showing effect of surface slope on calculation of local incidence angle, where Ro = slant range to near edge of image, R = slant range to imaged point P, θ = incidence angle at point P and h = altitude.

page 124

Note that for the AIRSAR system, flying up or down the ice sheet in the direction of the main surface slope would keep the local incidence angle constant as the direction of the wave incident on the surface from the imaging radar (viewing to one side of the plane) is perpendicular to, and therefore unaffected by, the surface slope. Details of the AIRSAR flight direction and surface slope values for the images of each zone of the ice sheet are discussed in chapter 5.

The passive data as measured by the SSM/I are average values, taken over a large area (~25*25km^2), and processed into the gridded data. The relative direction of the flight direction and that of the surface slope should be considered.

For the work undertaken in this thesis, the mean daily brightness temperature for each area is considered. This mean signal is taken from the average value of the 6 daily passes of the satellite, 3 day and 3 night (3 ascending and 3 descending passes). The effect of the surface slope is reduced by considering the mean value of these different passes. The local incidence angle for the ascending passes due to the surface slope is different to that of the descending passes, and the effect of the surface slope is masked by taking the average daily value of the data.

If data from a single pass are used, then, when using the inversion technique, the surface slope of the ice sheet should be taken into account. The change in surface slope is greatest for the ablation zone (8°), resulting in a potential change in local incidence angle of ±8°. For the SSM/I system the local incidence angle may change from 53.2^o by ±8° , giving a range of possible local incidence angles from 45.2^o to 61.2^o. If the local incidence angle is known, then the theoretical polarization ratio for a range of dielectrics may be computed for this specific value of incidence angle and the dielectric constant of the imaged surface may be inferred from the measured polarization ratio data. The % wetness content can then be calculated without introducing any additional errors from the surface slope.

If data of the surface slope are not available, the error in predicting the dielectric value of the surface will result in errors in the calculation of the % wetness content. The theoretical polarization ratio for the two extreme values of local incidence angles (45.2^o and 61.2^o), for the complete range of dielectrics Er = 1 to 3, and Er = 2 to 80 is computed (Appendix A1.5). The error in predicting the dielectric constant of the imaged surface using the measured polarization ratio due to a possible change in surface slope may then be estimated for each data point as required. Any errors in predicting the dielectric value will affect the calculation of the water content of the imaged surface. The error in predicting

the water content may then be determined for each calculation as necessary.

Using information of the value and direction of the surface slope from the slopes database derived from altimeter data to determine the local incidence angle, and then computing the theoretical polarization ratio for the amended incidence angle avoids these errors for the inversion technique. This combines data from active radar and the passive system to produce information on % wetness content of a particular area of the ice sheet.

4 Measurements, campaigns and data analysis -

Active polarimetric microwave radar data from the three frequency NASA/JPL AIRSAR system and satellite data from the passive microwave DMSP SSM/I are analysed for the four zones of the ice sheet. A map showing the positions of the four sites of interest in the dry zone, percolation, and soaked and ablation zones is given in chapter 1 (figure 1.10) with details of the coordinates of the various test-sites (table 1.3). K.Jezek's field party undertook simultaneous measurements at the test-site in the percolation zone (Crawford point) providing surface observations. These concurrent airborne, spaceborne and surface measurements are analysed to investigate the radar response of the ice sheet.

4.1 Greenland AIRSAR campaign, June 1991.

The NASA DC-8 aircraft with the JPL AIRSAR system flew over the Greenland ice sheet on June 10, 1991, taking images at each of the test-site areas in the four zones.
The DC-8 aeroplane travelled up the ice sheet on a flight path originating from Southwestern Greenland to the test-site at Crawford point, then continued on to the "Swiss camp" in the ablation zone (the test-site occupied by the Swiss Technological Institute (ETH) field party) then flew back over the Crawford point test-site in an Easterly direction before continuing up to the GISP2 test-site in the dry zone (U.S.National Science Foundation Deep Drilling Project).

4.1.1 Field campaign.

Prior to the AIRSAR overflight K.Jezek's field party deployed a series of corner reflectors at the test-site in the percolation zone (Crawford point). These are used for calibration and location purposes. The six corner reflectors are positioned approximately 1km apart along a 5km line, subsequently located to within 50m using handheld GPS units, and levelled using conventional surveying techniques (K.Jezek, 1992).

The field party undertook snow characterization studies. Several snow pits were dug and the physical parameters of density, temperature, grain size and orientation, and the stratigraphy of the snow were measured. The location of the snow pits may be found using the positions of the corner reflectors (site map given in figure 4.1). The stratigraphy of the snow and the content of the snowpack are given in figure 4.2. These sample pits show a surface layer of fine grained winter snow covering a subsurface layer of depth hoar at approximately 1.4m below the surface. The surface snow has some horizontal

layering as shown in the diagrams (figure 4.2). Large ice particles were found deeper within the snowpack, above large ice bodies at depths of approximately 1.8m. The roughness of each interface was measured using a simple comb gauge. Some of the large subsurface ice bodies were found to have very rough surfaces. These subsurface ice layers are formed by the refreezing of melt water at depth within the snowpack. The snow pits show the position of the previous year's ice layer, and the beginning of the annual melt cycle is noted in the last snowpit dug at the base camp, where the melt water has percolated through the surface snow layer and frozen at a horizontal discontinuity within the snowpack.
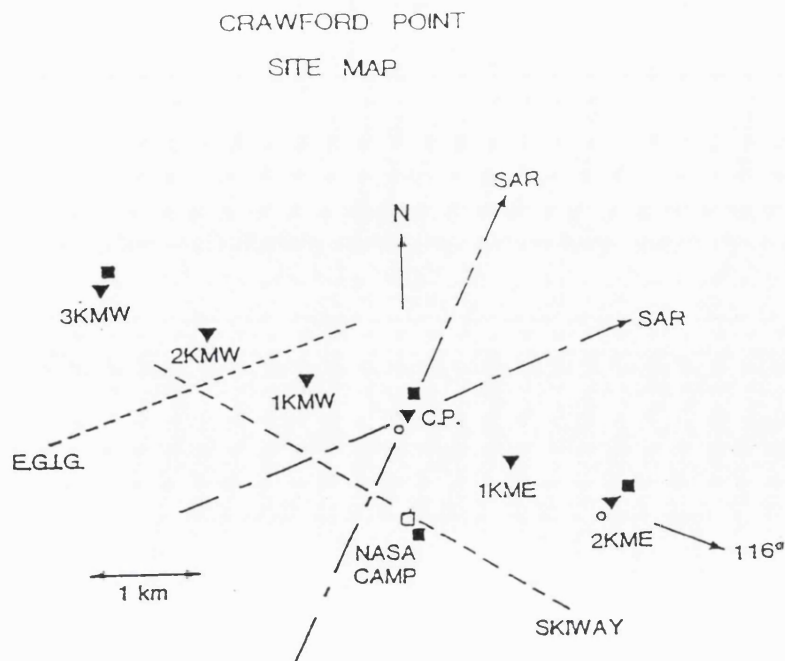
Figure 4.1: Corner reflector positions for percolation zone scene (zone 2) and direction of AIRSAR overflight (from K.Jezek, Feb.1993).
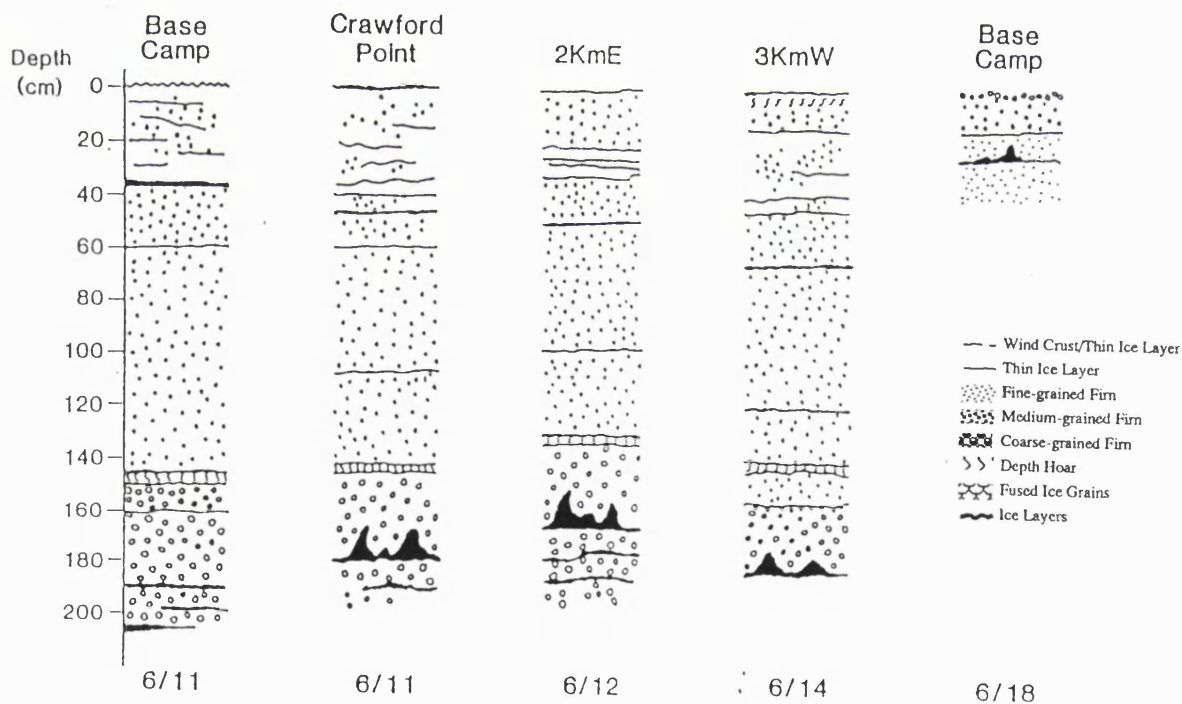
Figure 4.2: Snowpit data for percolation zone (zone 2) (from K.Jezek, Feb.1993).

4.2 Active microwave data analysis.

Data of the four different test-sites on the Greenland ice sheet as measured by the NASA/JPL active microwave AIRSAR remote sensing system are analysed. Details of this multifrequency fully polarimetric airborne imaging radar system are given previously in chapters 1 and 2.

4.2.1 Multifrequency fully polarimetric imagery.

For each location on the Greenland ice sheet full polarimetric images at the three operating frequencies: P, L and C band are available. These images may be displayed as total power images (TP), or any polarization combination for the receive and transmit antennas can be simulated and the resulting polarimetric image is synthesized and displayed (for example: HH, VV, HV, VH, RR, LL or any other combination of polarimetric states). A review of the use of polarimetry and polarimetric theory may be found in chapters 1 and 2.

The polarimetric AIRSAR image data are displayed using the NASA/JPL MacMultiview and MacSigma0_11 software (Norikane, 1990, 1992).

The total power images for P, L and C bands for all four zones, and the P band images for the linear polarizations VV and HH for each location are given in chapter 5.

These images are checked by eye to detect any unusual features: For example; the different frequency images (P, L and C band) of the same area may show different features, and so may the polarimetric images for each scene.

4.2.2 Radar response from measured data.

4.2.2.1 Numerical data.

The numerical data of the Greenland images are analysed using MacMultiview and MacSigma0_11 software.

The MacMultiview program allows the 3D polarimetric response of a particular area of any displayed image to be determined and the response of the sampled area is plotted. The 3D response curves show the normalized co and cross polar power return as a function of the ellipticity and orientation of the incident wave (figure 2.4).

The MacSigma0_11 program allows a statistical analysis of the data. Values of TP, HH, HV, VV power and HHVV* phase for any sampled area of any displayed image are calculated. Details of the necessary calculations to determine these values from the Stokes matrices of the measured data sets are given by Norikane (1990, 1992).

4.2.2.2 Power values.

The return power for each image is determined using MacSigma0_11. This program is used to calculate the power values for line averages at the near and far edge of the image and for intermediate positions to determine the variation of the return power with the incidence angle for each scene.

The difference in the return power for each image, for the three frequencies and the various polarization states, is analysed for each zone of the ice sheet.

The noise floor of the AIRSAR system is ~-40dB. Low power data can produce a misleading shape of polarimetric response as the output response is plotted on a normalized scale. A small change in power for low power signals then causes a relatively large change in the shape of the response. In order to approach this problem of accurate representation of the measured data a minimum of 15dB difference signal:noise is required to ensure the signal strength, and a significant sample size is required. The accuracy of the results is proportional to $1/\sqrt{n}$ from Noise theory, where n is the number of data takes, or number of individual elements in a sample. Taking a line average sample of data helps to overcome this problem for uniform, high power images.

The data sets analysed in this work are as supplied by JPL using the standard calibration for the campaign. Additional calibration work using data from the corner reflector array has not been included in this thesis as the results and data are not available. These data would, however, be useful for determining any polarization imbalance and for calculating the absolute value of return power.

The approach to the analysis work in this thesis involves considering the power ratio for the two linear polarization signals, and therefore tends to remove the need to know the absolute power level. The consideration of the relative power level between scenes measured on the same day gives the relative difference in the return power for the different zones of the ice sheet.

The polarimetric nature of the return signal from each of the four zones is investigated. The measured polarization response is given as a normalized signal for each plot so the difference in the polarimetric content of each of the return signals for each zone may each be determined independent of the absolute power value.

4.2.2.3 Polarization response 3D plots.

The type of scattering behaviour of the different zones of the ice sheet is investigated using the 3D polarimetric response plots for each image. The information contained within these polarimetric response plots gives details of the dominant scattering mechanism (Freeman and Durden, 1992) as discussed in chapter 2. The physical mechanism for these types of scattering behaviour is shown in figure 2.5(i) and the typical polarimetric response plots (co and cross polar power) for direct scattering, double bounce and diffuse/ volume scattering are given in figure 2.5(ii).

The polarization response for each zone of the ice sheet is investigated and the variation of the measured polarization response with incidence angle, and with frequency is analysed for each scene. The measured polarization response is compared with theoretical values to explain the variation of the shape of the response with the change in the incidence angle of the radar.

4.2.2.4 Theoretical classification method.

The theoretical classification method using the polarimetric content of the return signal as described in chapter 3 (section 3.3) is applied to the measured data of the C233-1 AIRSAR image over the ablation zone. This image was measured by the active polarimetric airborne imaging radar system during a previous campaign further down the Greenland ice sheet (August 1989). A copy of the total power image is given in chapter 5. This image shows distinct light and dark regions, with the dark regions indicating the position of melt pools on the surface of the ice sheet, and is therefore used in the application of the classification method. The classification method is used to distinguish the different dielectric material of the ice sheet as imaged by the radar.

4.2.2.5 Position of subsurface ice layer.

The measured polarimetric P band AIRSAR data of the percolation zone is analysed and compared with the theoretical signal to infer the depth of a subsurface ice layer using the

method described in chapter 3 (section 3.3.4.3). The position of the subsurface layer predicted by the theoretical analysis of the measured polarimetric signal is compared with the actual values of the snowpack layers at the test site as measured by K.Jezek's field party (figure 4.2).

A line average of data from the measured image is taken from the line corresponding to that containing the 6th corner reflector marked 2KmE in the site map (figure 4.1) which contains the position of the snow pit marked 2KmE (figure 4.2). Information on the actual position along the line of the image of the snow pit as dug by the field party is not available, so the line average (of the same incidence angle) is used. The measured values of HH and VV polarization return power and VV-HH phase of the return polarimetric signal are used to give the measured data point on the power ratio vs. phase difference plot in chapter 5 (figure 5.11). This measured data point is then compared with the theoretical values for the simulated system of snow and ice layers to predict the depth of the surface layer of firn and hence the position of the subsurface ice layer. This is then compared with the measured snowpit data.

The standard deviation of the measured data point is calculated from the relative standard deviation of the data as given by the NASA/JPL MacSigma0_11 software (Norikane, 1992). The relative standard deviation is a term used by JPL and equation 4.1 below shows the relationship with the more usual value of standard deviation.

4.2.2.6 Statistical analysis.

The relative standard deviation, $\sigma_{relative}$, is given by equation 4.1, where σ is the standard deviation and m is the mean value (fractional value, not dBs).

$$\sigma_{relative} = \left(\frac{m + \sigma}{m}\right)$$

Equation 4.1: Standard deviation relationship (Norikane, JPL, 1992).

Error bars are plotted on the figures to show the 68.3% confidence interval (±1 standard deviation). Further work on the statistical analysis of the measured data is given with the results in chapter 5 and in Appendix A1.6.

4.3 Passive microwave data analysis.

Data from the passive microwave SSM/I satellite remote sensing system of the four different zones of the ice sheet are analysed. Details of the DMSP SSM/I system are given previously (chapters 1 and 2).

4.3.1 Brightness temperatures.

The mean daily vertical and horizontal polarization brightness temperatures (K) for each of the four zones are analysed using both the 19 and 37 GHz signals. A complete year of data (April 1990 - March 1991) is plotted to show the temporal change, and the data for the same time as the AIRSAR overflight are also analysed (June 1991). The data are shown as moving averages (taking a simple average for every 7 days) with the unaltered data for each day also plotted on each plot. This assists with the comparison of the annual cycle for each zone of the ice sheet.

4.3.2 Polarization ratio of the emitted signal and determination of snow moisture content.

The standard polarization ratio $(T_{Bv} - T_{Bh}) / (T_{Bv} + T_{Bh})$ and the simple ratio T_{Bv} / T_{Bh} are investigated. The measured values are compared with the theoretical computed values for the incidence angle 53.2 degrees (as for the SSM/I instrument) and the dielectric constant of the imaged area is inferred as described in chapter 3 (section 3.4). This value of dielectric constant is then used to calculate the wetness content of the snow. The mixing formula of Mätzler (1987) is used to calculate the mean % wetness by volume of the snow.

4.3.3 Melt season.

The change in the passive emitted signal during the spring - summer melt season (April - June 1991) is investigated using data from all four of the different zones of the ice sheet. The difference in the return signal due to the two frequencies is plotted for the complete year of data (March 1990 - April 1991) for the two linear polarizations $(19\text{-}37)T_{Bh}$ and $(19\text{-}37)T_{Bv}$. Data from the four different areas of the ice sheet are investigated. This frequency difference signal during the spring - summer seasons is analysed in detail to show the change in the emitted signal during melt.

5 Results -

5.1 Results from active microwave data.

5.1.1 Total power images.

Copies of the total power AIRSAR images for each of the scenes measured over the Greenland ice sheet in June 1991, and for each frequency for each scene in order P, L, C band, are given in figure 5.1 i-xii.

Figure 5.1 i) - iii): P, L, C band images (i7, i8, i9) of the dry zone (zone 1)

        iv) - vi): P, L, C band images (i10, i11, i12) of the percolation zone (zone 2)

        vi) - ix): P, L, C band images (i1, i2, i3) of the soaked/ablation zone (zone 3)

        x) - xii): P, L, C band images (i13, i14, i15) of the ablation zone (zone 4).

The colour images have the ROGIBIV colour scale, where red denotes high return power and violet low return power, with bright white for saturation.

The orientation and location of the images is given by considering the heading of the DC8 plane, the flight line details and target coordinates. The heading changes for the different AIRSAR images (refer to chapter 1, figure 1.10, for the approximate location of the AIRSAR images on the Greenland ice sheet and the flight line direction). The direction of the aeroplane travel is from right to left across the top of the AIRSAR image, and the image is measured by antennas on the left-hand-side of the aeroplane.

The P band, HH polarization AIRSAR images for:

 i) percolation zone (zone 2),

ii) soaked/ ablation zone (zone 3), and

iii) ablation zone (zone 4),

showing the approximate orientation of features, and estimated direction and inclination of downwards slope, are given in figure 5.2. The image of the dry zone (zone 1) is not included here as it is featureless.

Figure 5.1 i): Total power P band AIRSAR image (i7) of the dry zone of the Greenland ice sheet, measured 10 June 1991.

Figure 5.1 ii): Total power L band AIRSAR image (i8) of the dry zone of the Greenland ice sheet, measured 10 June 1991.

Figure 5.1 iii): Total power C band AIRSAR image (i9) of the dry zone of the Greenland ice sheet, measured 10 June 1991.
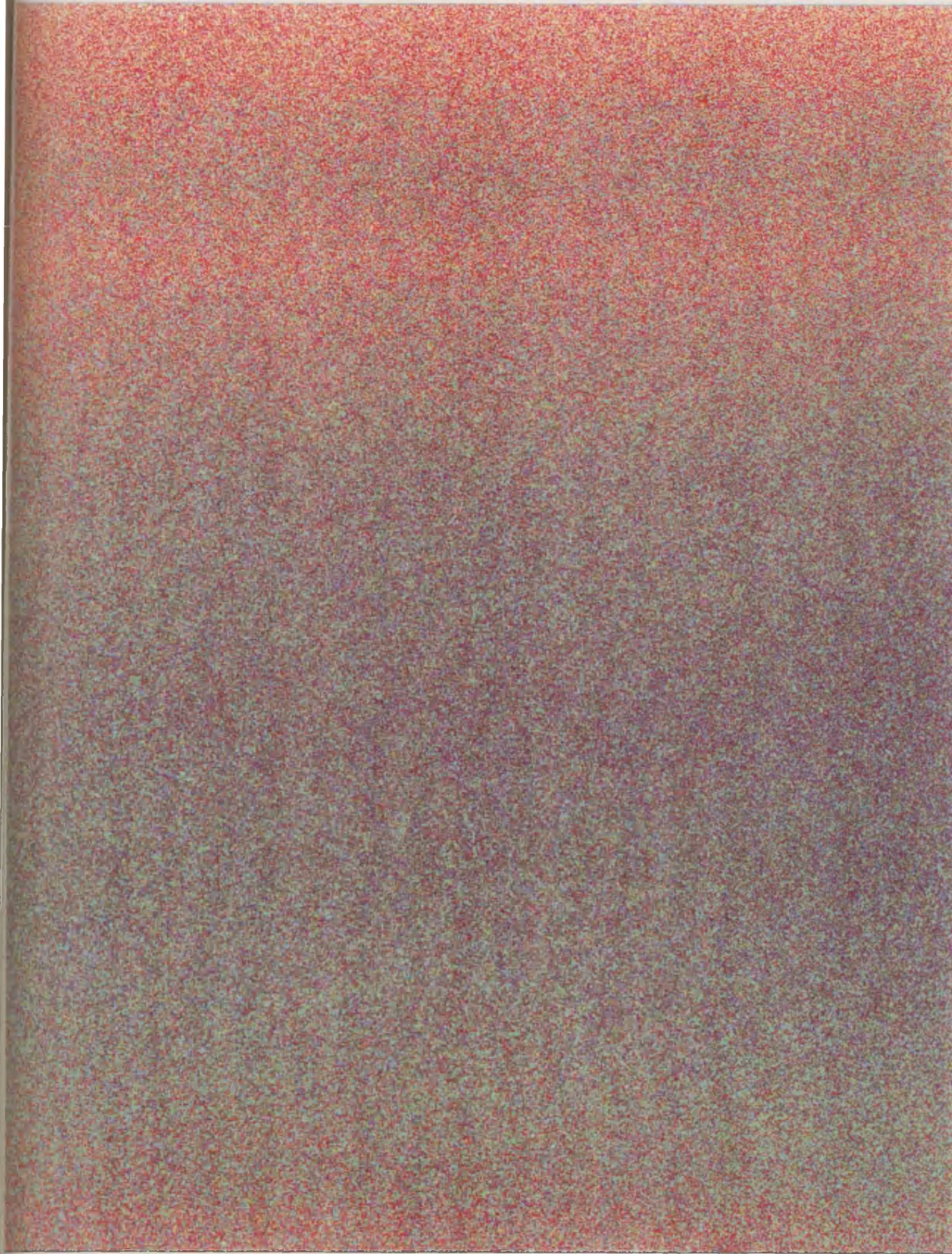
Figure 5.1 iv): Total power P band AIRSAR image (i10) of the percolation zone of the Greenland ice sheet, measured 10 June 1991.
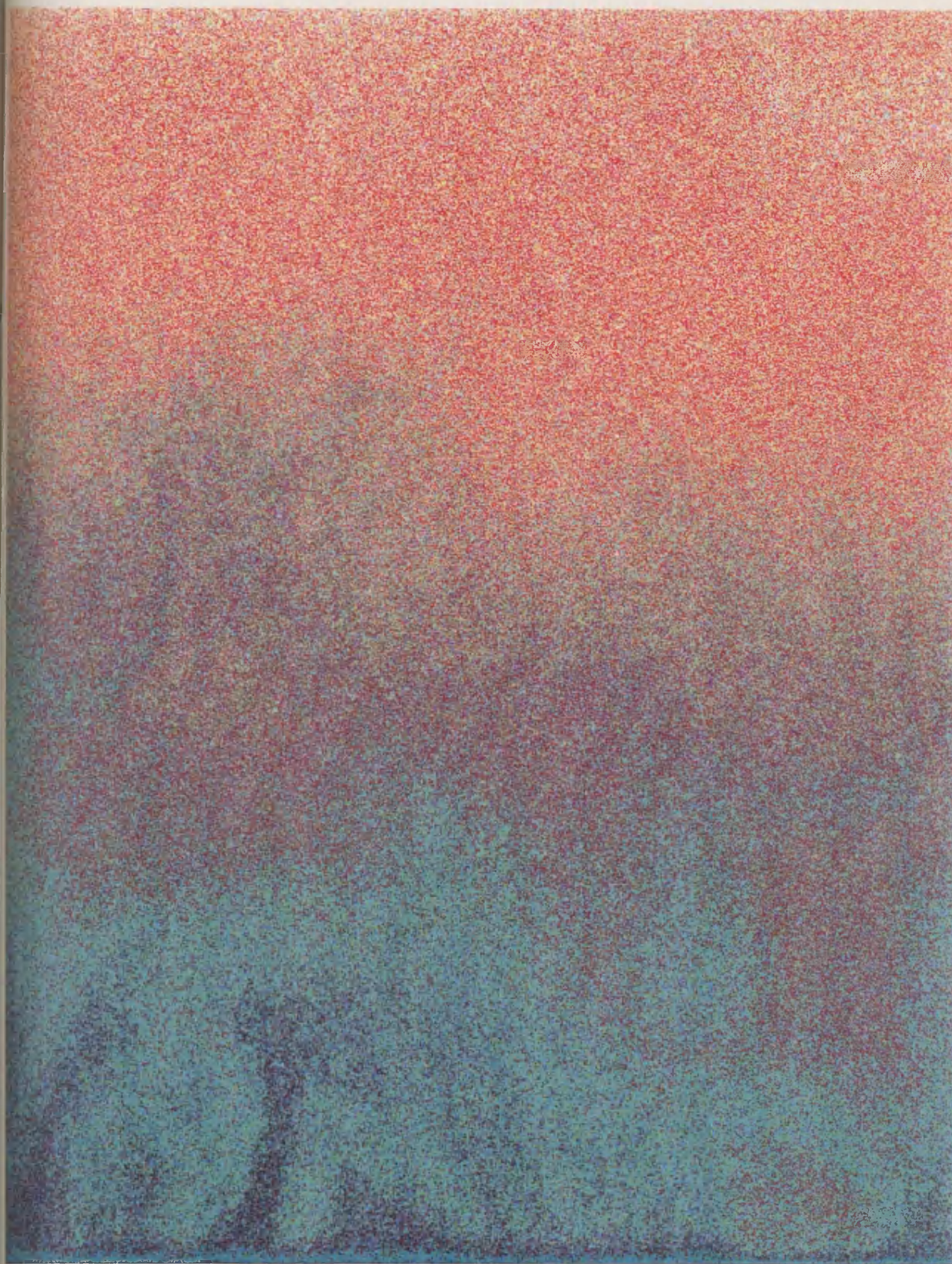
Figure 5.1 v): Total power L band AIRSAR image (i11) of the percolation zone of the Greenland ice sheet, measured 10 June 1991.

Figure 5.1 vi): Total power C band AIRSAR image (i12) of the percolation zone of the Greenland ice sheet, measured 10 June 1991.
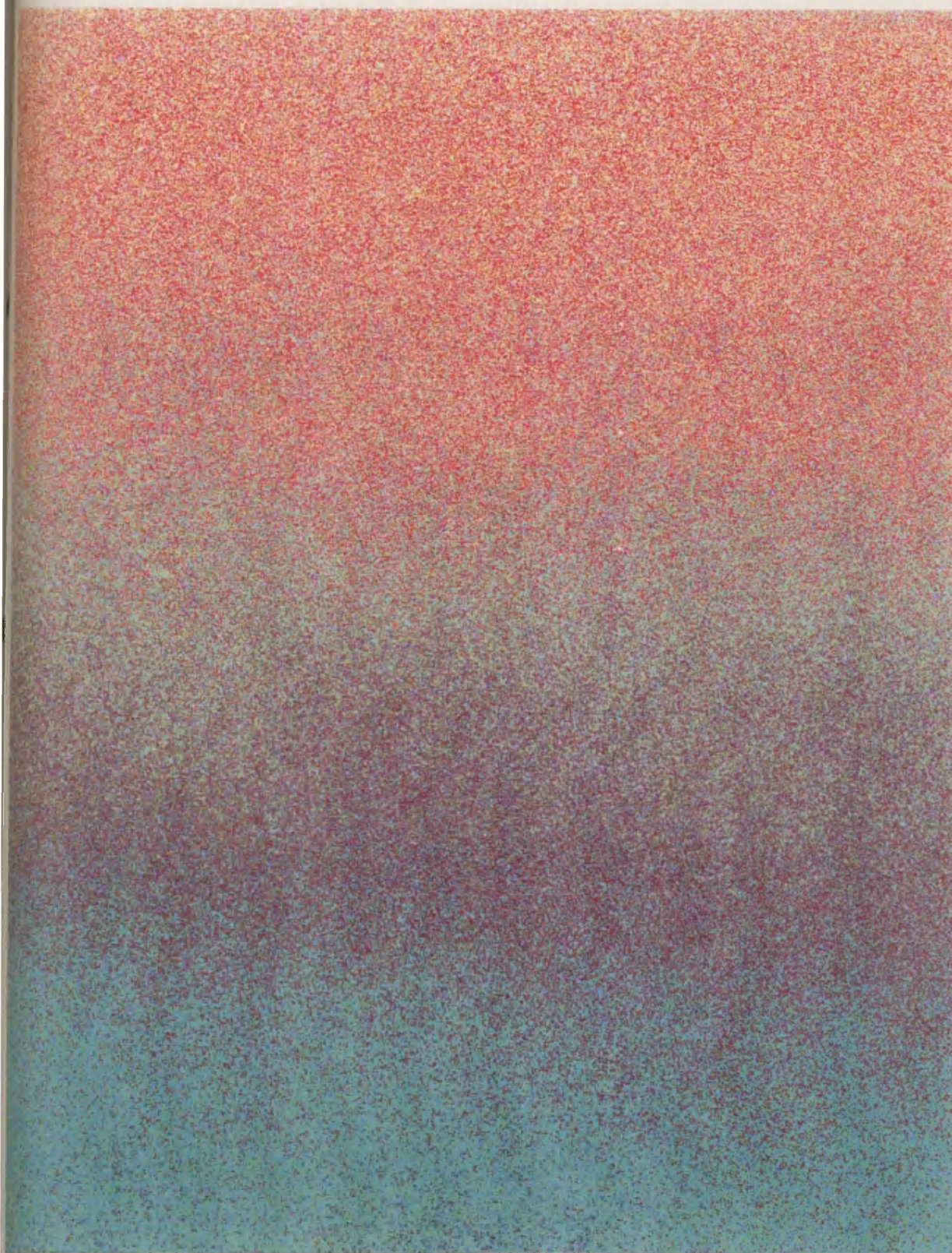
Figure 5.1 vii): Total power P band AIRSAR image (i1) of the soaked/ablation zone of the Greenland ice sheet, measured 10 June 1991.

Figure 5.1 viii): Total power L band AIRSAR image (i2) of the soaked/ablation zone of the Greenland ice sheet, measured 10 June 1991.
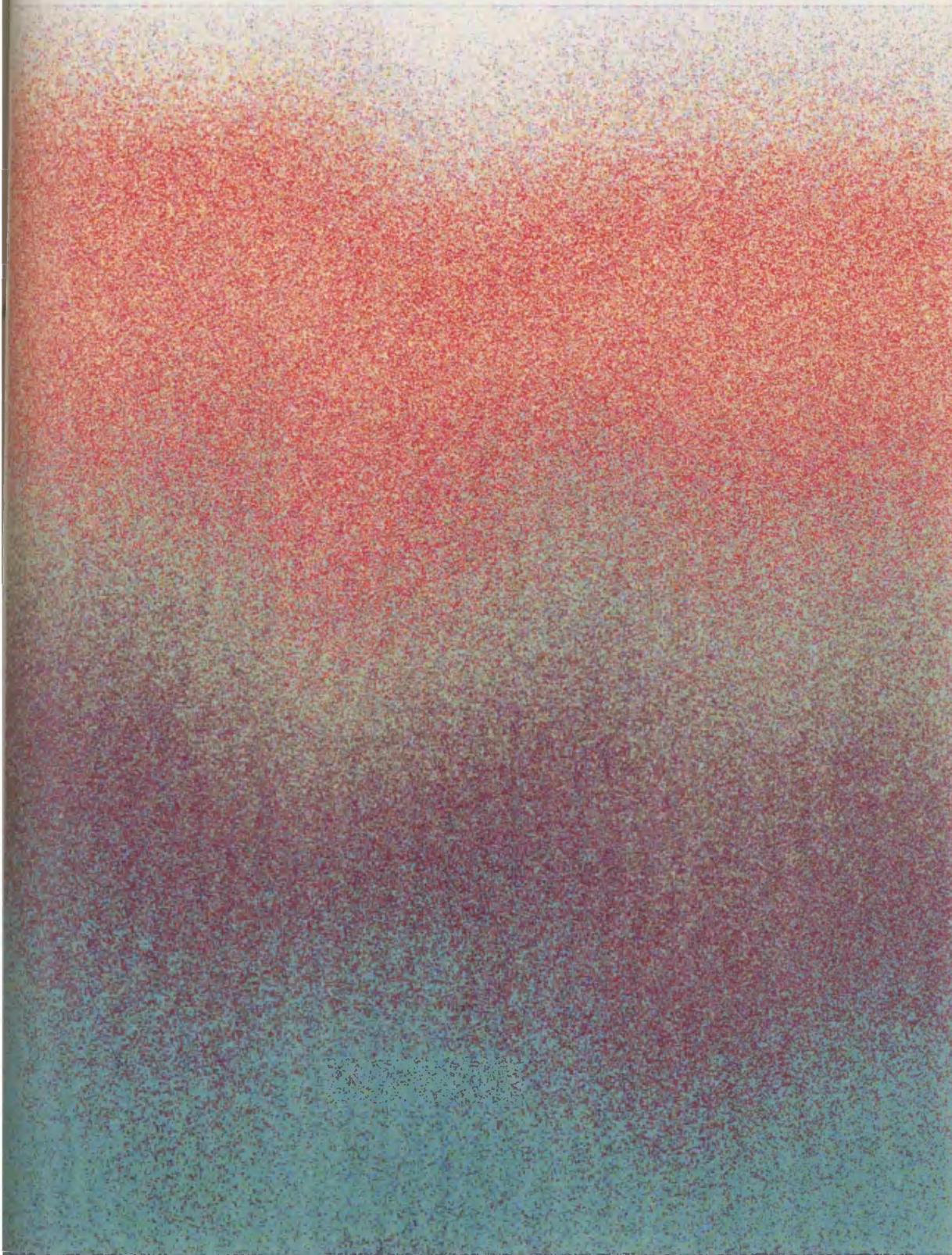
Figure 5.1 ix): Total power C band AIRSAR image (i3) of the soaked/ablation zone of the Greenland ice sheet, measured 10 June 1991.

Figure 5.1 x): Total power P band AIRSAR image (i13) of the ablation zone of the Greenland ice sheet, measured 10 June 1991.

Figure 5.1 xi): Total power L band AIRSAR image (i14) of the ablation zone of the Greenland ice sheet, measured 10 June 1991.

Figure 5.1 xii): Total power C band AIRSAR image (i15) of the ablation zone of the Greenland ice sheet, measured 10 June 1991.

The images of the **dry** region of the ice sheet (zone 1) are taken at the GISP2 test-site. The P, L, and C band images of this area (i7, i8, i9 as given in figure 5.1 i) - iii)) are all uniform images, showing a decrease in intensity of the return radar signal on descent of the image as the incidence angle is increased. The scattering characteristics of dry snow with respect to frequency and change in incidence angle are investigated from the numerical data of these images. This area is reasonably flat (surface slope < 0.1 degrees) with no apparent discontinuities.

The second area considered is in the **percolation zone** of the ice sheet (zone 2). This scene is of the Crawford Point test site and shows the corner reflectors as deployed by K.Jezek's field party. The corner reflectors are positioned at intervals approximately a kilometre apart down the images, and show up as bright points on the total power images due to the high return of these antennas.

All the three frequency images (i10, i11, i12 for P, L, C band respectively) show a decrease in the return power for the imaged area as the incidence angle is increased. The P band image (i10) shows some interesting features which are not visible on either the L (i11) or C band (i12) images. The frequency dependence of these features suggest that the discontinuity causing the change in return power is a subsurface effect. The P band radar penetrates further than either the L band, or C band radar, and will therefore be more sensitive to subsurface discontinuities. It is suggested that the dark patches of the P band image may indicate the presence of smooth subsurface higher dielectric ice (or increase in water content) as this would cause specular reflection of the incident radar away from the receive direction, causing a decrease in the return power measured.

Smooth subsurface ice layers are produced in the percolation zone by the localized collection of melt water, which refreezes at depth within the snowpack. The location of these discontinuities may be indicative of the bedrock topography as the collection of melt water occurs in the depressions of the ice sheet which are generally related to the bedrock topography.

Multitemporal radar imagery might possibly be used to show the rate and direction of flow of the ice sheet by measuring the position and location of these features over a series of time. The motion of a particular dark area, if measured from season to season, could be used to indicate the flow of the ice sheet and permit the estimation of the ice velocity.

The flight line direction for this image is 24.4 degrees (from North). The dark circular

areas in the middle of the image seem to be aligned in an approximate N/S direction (~174 degrees), and those at the far edge of the image lie in an approximate NE direction (~40 degrees) as shown in figure 5.2 i). Information on the surface topography from radar altimeter data (J. Morley, personal communication) indicates that the surface slope in this area is ~ 0.36 degrees, with the downslope direction being 16.5 degrees (from North) or ~NNE. This information is obtained from the ERS-1 radar altimeter FD data, with resolution $25*25km^2$.

The two series of dark circular areas noted in the AIRSAR image do not seem to lie in a direction related to that of the estimated slope from the altimeter data. The local direction of the slope of this fairly flat area as covered by the AIRSAR image may, however, differ from the mean slope as estimated by the radar altimeter data.

The third scene is of the **soaked/ablation** zone (zone 3). The AIRSAR image of this area is fairly uniform and the image gets increasingly darker (lower return power) on descending the image from the near to far edges. This is due to the decrease in value of total power returned as the incidence angle increases. The P band image (i1) shows some interesting features which increase in clarity towards the far edge of the image. These dark patches are not visible on the L band image (i2), or on the C band image (i3). The frequency dependence of measuring these features again suggests that a subsurface discontinuity causes this effect. The dark areas may indicate the possible location of subsurface ice streams and the shape of the dark patches seen on the P band image may indicate the flow of the ice sheet.

The heading for the soaked/ablation (i1) image is 68.1 degrees (i.e. plane travelling in ~NE direction). The dark central line of this image is orientated in an approximate SE direction (~160 degrees) and the dark areas at the far edge of the image are orientated in an approximate NE direction (~30 degrees) as shown in figure 5.2 ii). The surface slope is estimated to be 0.68 degrees, and the direction of this slope, -51.1 degrees, ~NW (from radar altimeter data). The dark areas at the far edge of the AIRSAR image therefore appear to lie in a direction approximately perpendicular to that of the estimated slope.

The fourth area measured by the AIRSAR is of the **ablation** zone (zone 4), at a site occupied by the Swiss Camp. The three frequency images P, L and C band (i13, i14, i15) show some interesting features. The features are most detailed on the P band image, and similar features are shown in the L band image, but not as clearly. The C band image just shows the location of the central linear feature. The circular bright areas of the P and L band images are thought to be subsurface discontinuities, strongly reflecting towards

the receive antenna. These are barely visible with the C band radar. The flight heading of this scene is 159.1 degrees so the central feature is orientated in an approximate NE direction (~45 degrees) as shown in figure 5.2 iii). The surface slope of this ablation area is estimated to be 6.47 degrees, with downwards direction 49 degrees, ~NE. The magnitude of the estimated slope here is rather greater than the slope of the other areas further up the ice sheet. The central linear feature of the AIRSAR image of this area is orientated in approximately the same direction as the estimated downwards slope.

The location and direction of the features of these images are discussed further in chapter 6, with reference to the typical snowpack characteristics of the different zones of the ice sheet.

Figure 5.2 i) percolation zone

N

direction of features

40°

6° N

N

16.5°
downslope direction

value 0.36°

r edge

N

24.4°

aeroplane direction

near edge
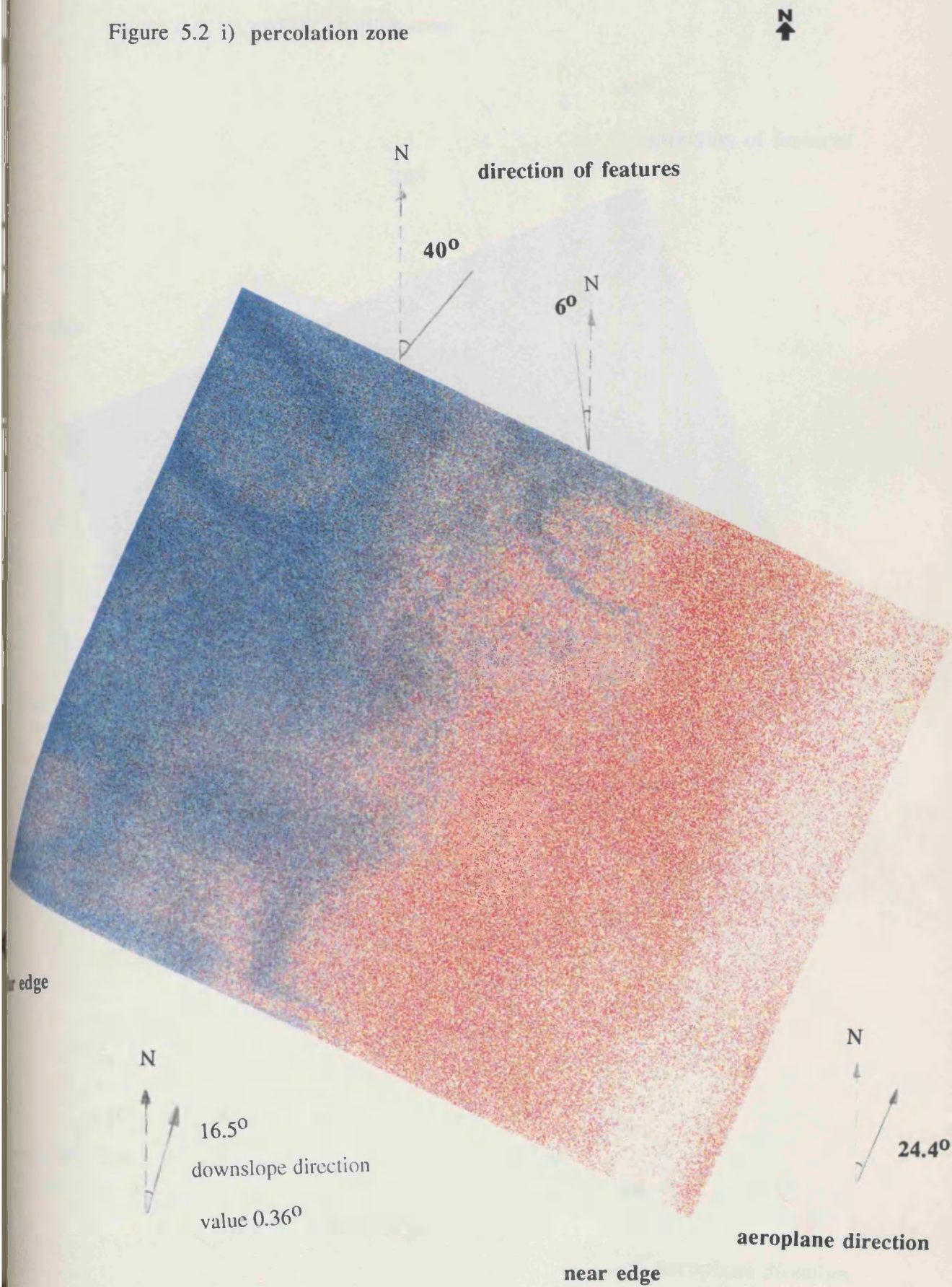
Figure 5.2 ii) soaked/ ablation zone

far edge

N

20°

N

N
30°

direction of features

-51.1°

N

nslope direction

ue 0.68°

near edge

N

68.1°

aeroplane direction

page 152
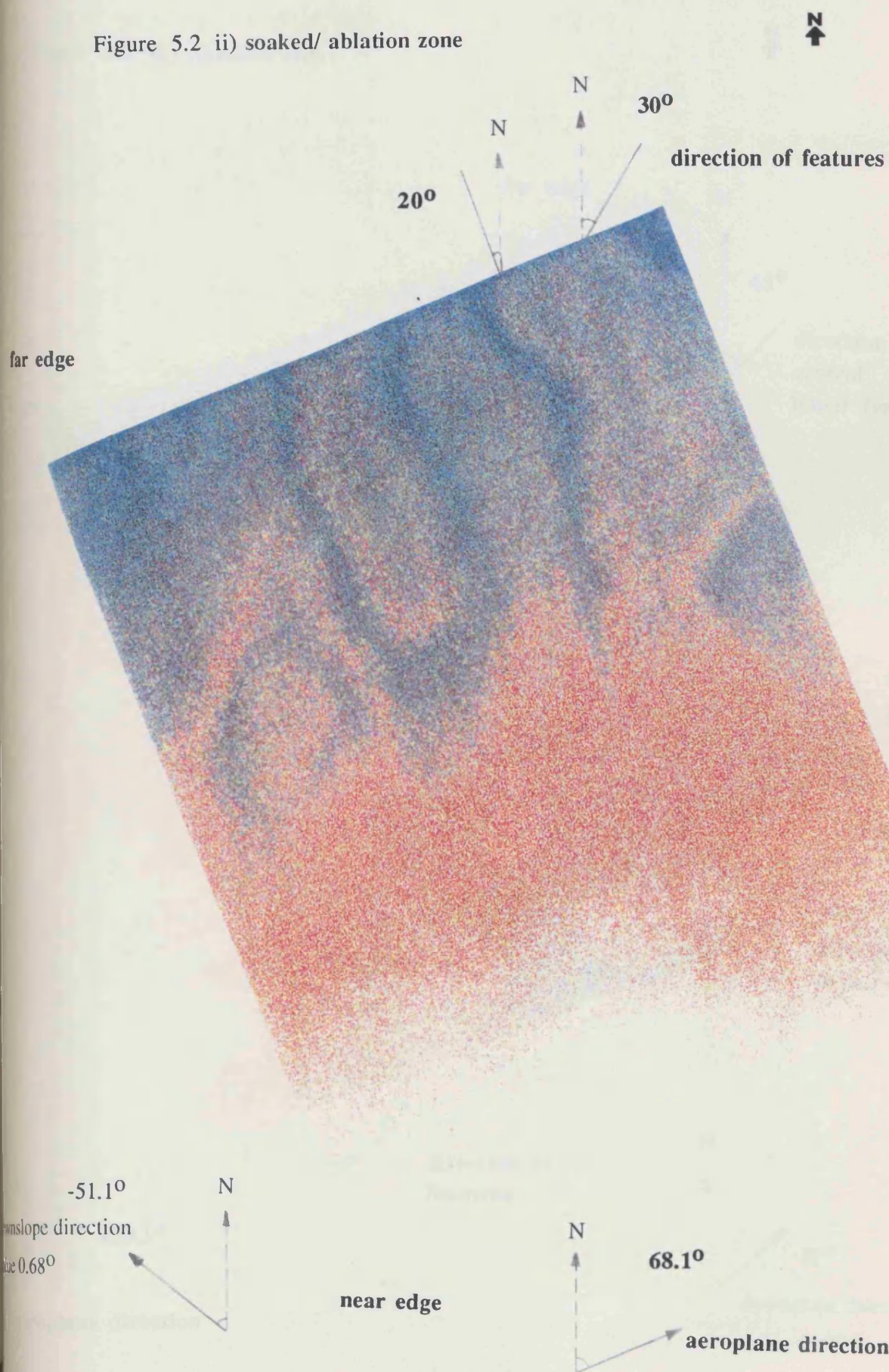
Figure 5.2 iii) ablation zone
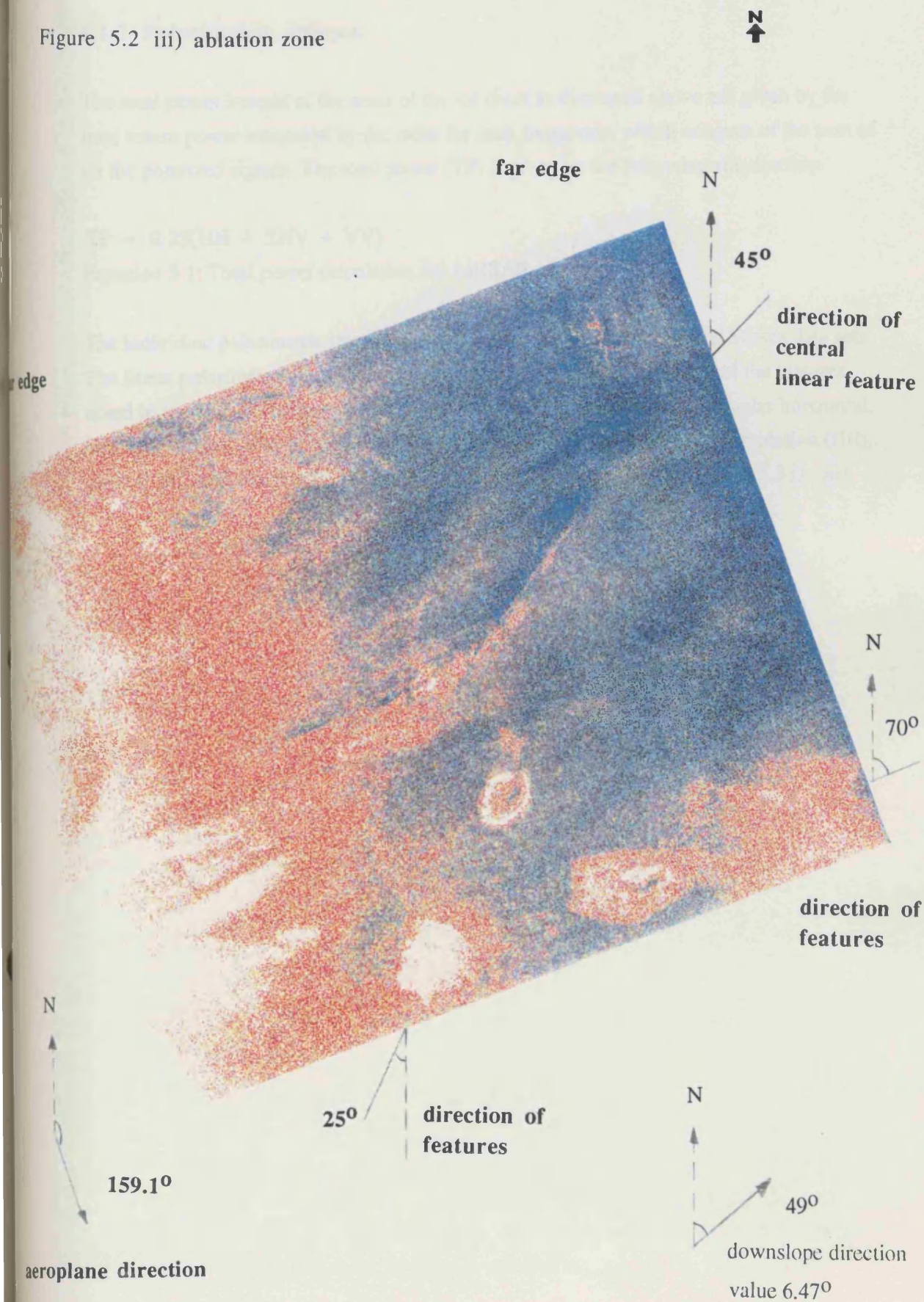
5.1.2 Polarimetric images.

The total power images of the areas of the ice sheet as discussed above are given by the total return power measured by the radar for each frequency, which consists of the sum of all the polarized signals. The total power (TP) is given by the following relationship:

$$TP = 0.25(HH + 2HV + VV)$$

Equation 5.1: Total power calculation for AIRSAR images.

The individual polarimetric images may be calculated from the measured Stokes data sets. The linear polarimetric images for each scene are displayed to see if any of the features noted in the total power images are polarization dependent. The linear co polar horizontal, HH, and vertical, VV, polarization images for the P band images of the percolation (i10), soaked (i1), and ablation (i13) scenes (zones 2, 3 and 4) are given in figure 5.3 i) - iii).

i10 P band, percolation zone, HH polarization

i10 P band, percolation zone, VV polarization
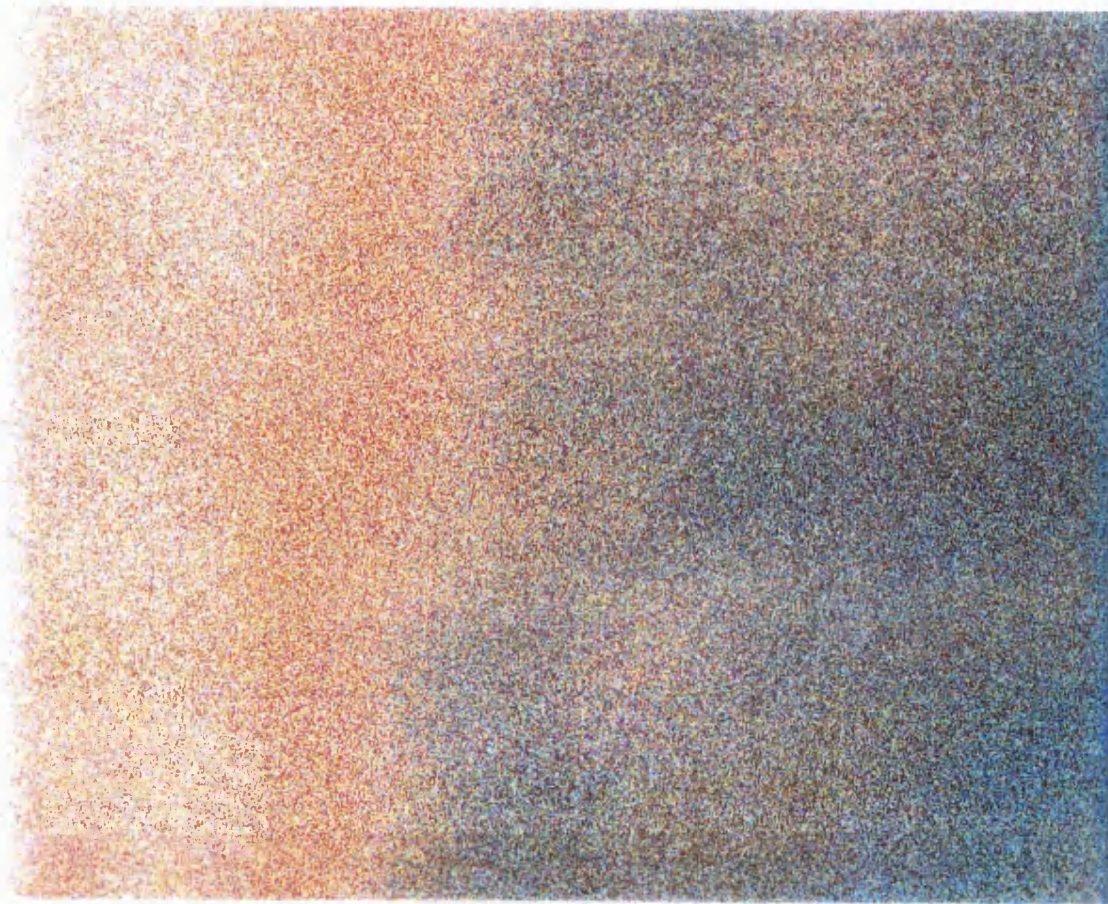
Figure 5.3 i): Linear co polar horizontal, HH, and vertical, VV, polarization images for the P band image (i10) of the percolation scene (zone 2).

il P band, soaked / ablation zone, HH polarization
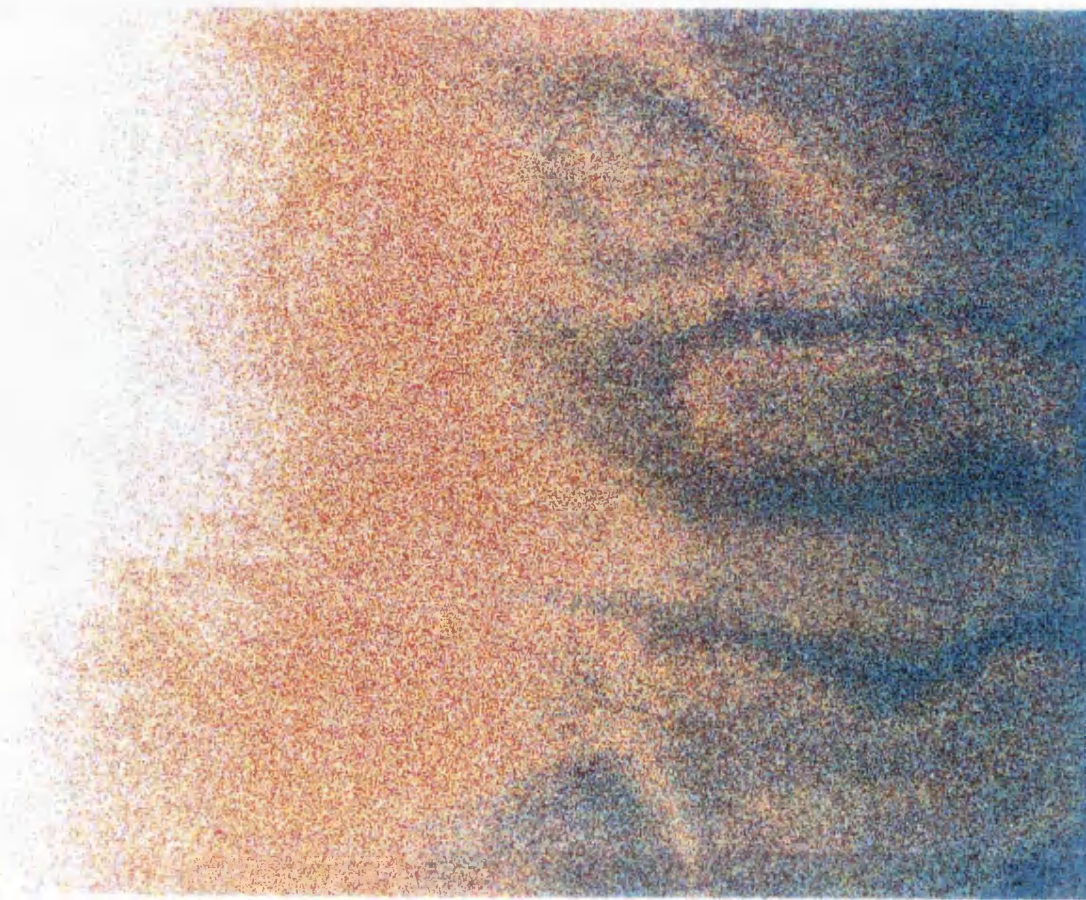
il P band, soaked / ablation zone, VV polarization
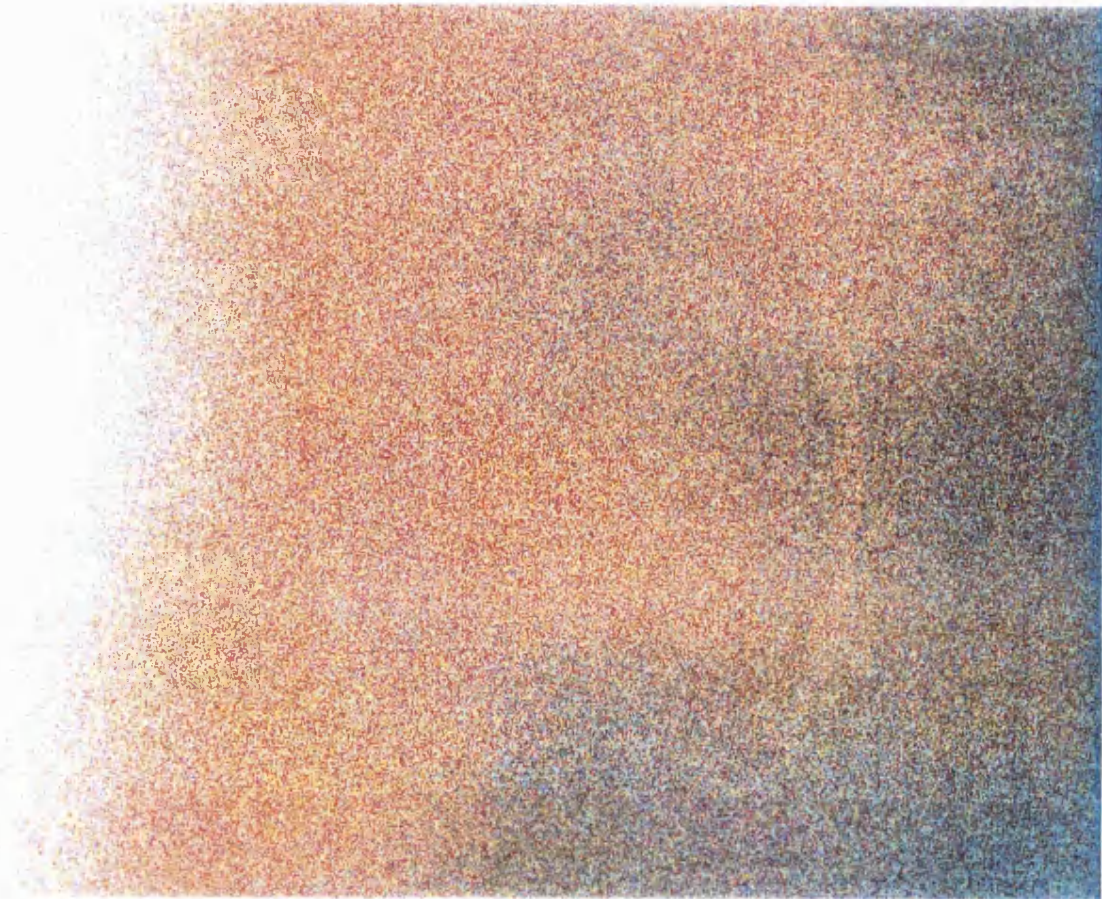
Figure 5.3 ii): Linear co polar horizontal, HH, and vertical, VV, polarization images for the P band image (il) of the soaked/ablation scene (zone 3).

i13 P band, ablation zone, HH polarization
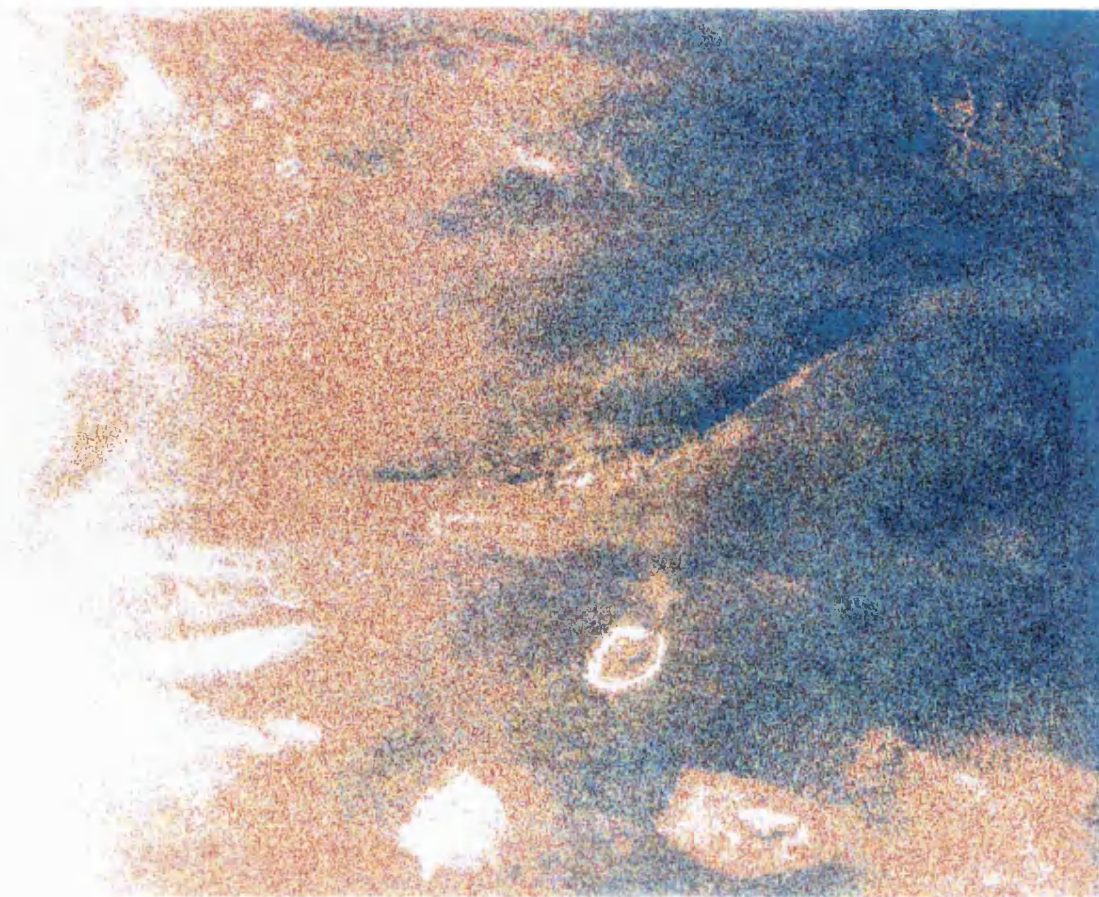
i13 P band, ablation zone, VV polarization
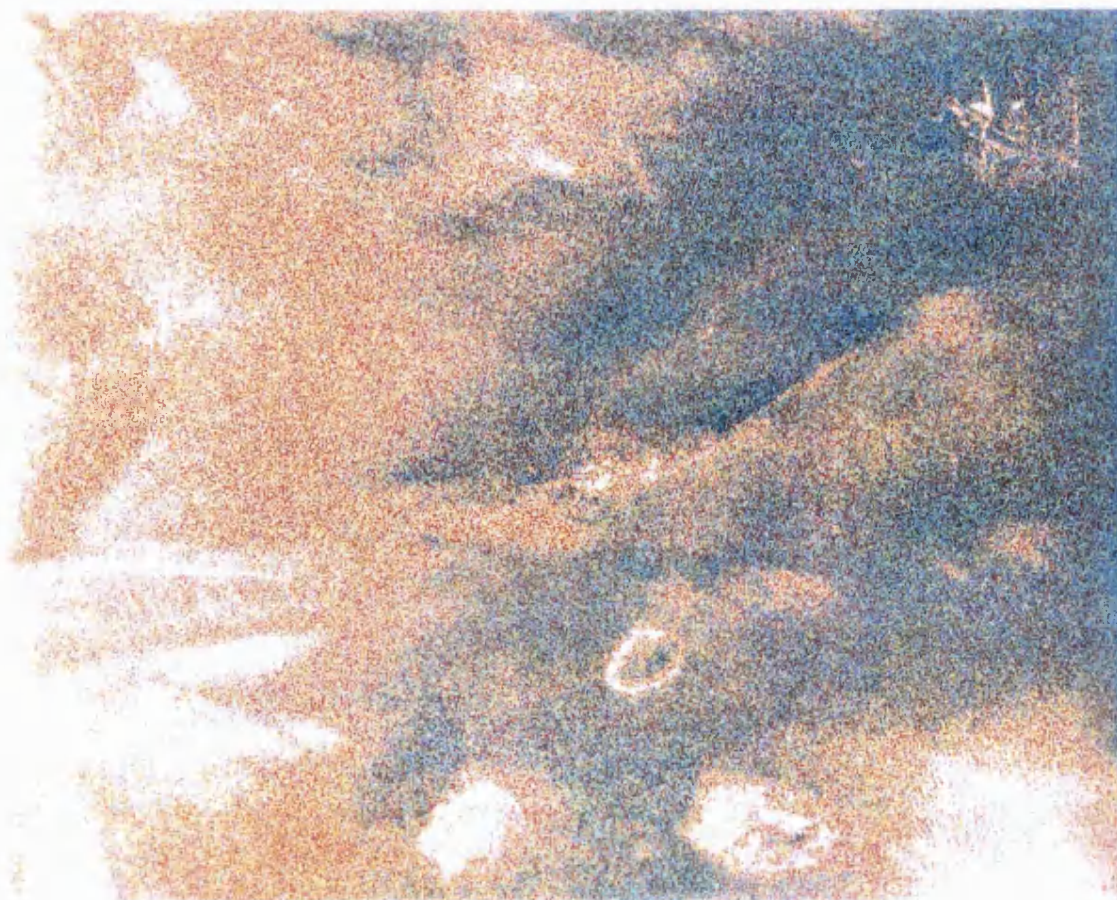
Figure 5.3 iii): Linear co polar horizontal, HH, and vertical, VV, polarization images for the P band image (i13) of the ablation scene (zone 4).

page 157

The features noted in the percolation (i10) and soaked (i1) P band images (zones 2 and 3) are found to be present in the HH images of these areas and not for the VV image. The polarization dependence of these features may be related to the orientation of the discontinuity and that of the direction of the E vector of the incident radar wave. The features are apparent for horizontal polarization and not for vertical polarization which suggests that the discontinuities are orientated horizontally. These discontinuities would then resonate with the incident radar wave causing a change in the level of return power. The presence of subsurface ice lenses orientated horizontally, and of a size comparable to the incident radar wavelength (~750mm for P band) would act as strong scatterers for HH polarization at this frequency.

The features noted in the ablation zone image (i13, i14, i15) (zone 4) are present to some extent (decreasing clarity with increasing frequency) for all three frequencies. The polarimetric images for the P band image (i13) are investigated to check for any polarization dependence of the features. The features noted in this ablation scene are present for both HH and VV polarization (and for HV) showing that there is no apparent polarization dependence for the features of this scene.

5.1.3 Total power values for different zones.

The total power returned for each of the scenes depends on the type of scattering that occurs from the ice sheet and is dependent on the zone that is measured. The return power is also dependent on the frequency of the incident radar signal and the incidence angle. The multifrequency AIRSAR data sets over the different zones of the ice sheet show the change of return power with frequency for the different zones and the effect of the incidence angle on the return power is also noted as each AIRSAR scene covers a range of incidence angles from ~20 to ~60 degrees.

The measured return power (VV polarization only) for the AIRSAR images over the different zones of the Greenland ice sheet is shown in figure 5.4. The line average value of the return power for C, L, P band radar taken at the near edge (200 lines in) of the AIRSAR images (and so at approximately the same incidence angle) is plotted. High return power is measured over the percolation region (zone 2) and the soaked/ablation zone (zone 3) for all three frequencies. The dry zone (zone 1) and the ablation zone (zone 4) scene give a much lower return power.

The return power for each scene is dependent on the frequency of the radar. Generally,

the higher the frequency, the greater the return power. There is more power returned for C band, than for L, or P band signals for all the scenes. The only anomaly to this general frequency dependence of return power is for the L band ablation region image (i14) which for some reason appears brighter at the near edge than for either the P (i13) or C (i15) band images.

The return power of the radar signal also depends on the incidence angle of the radar. The return power tends to decrease as the incidence angle increases (where the value of incidence angle is measured away from normal, i.e. nadir = 0 degrees). This dependence of return power on the value of the incidence angle is seen in most of the AIRSAR images as the images tend to become darker on descent of each image (over an incidence range of ~20 to 60 degrees). The values of the measured return power for the percolation zone scene with change in incidence angle (or y position of line average value) is plotted in figure 5.5.

Measured VV return power, near edge of image, ice sheet zones 1 - 4.
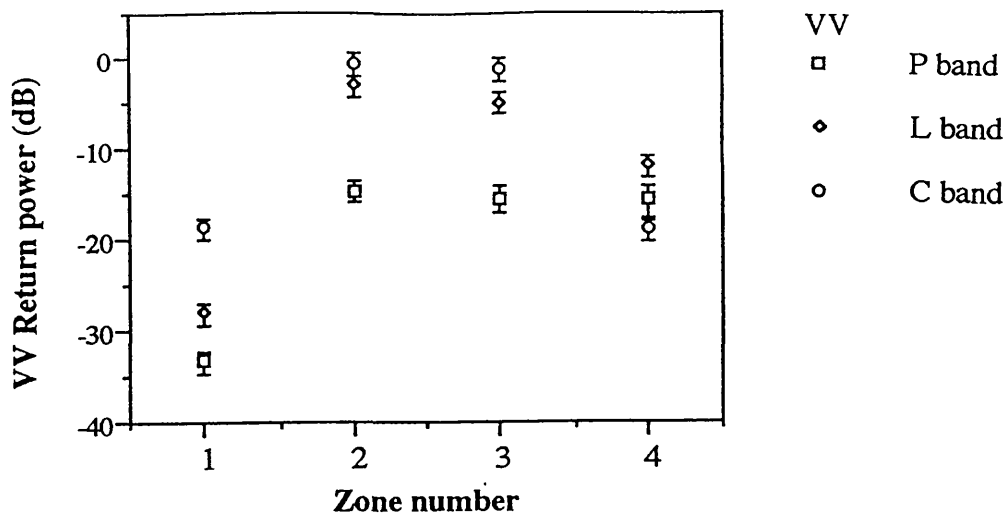
Figure 5.4: Measured AIRSAR return power (VV polarization) for P, L, C band radar for near edge of image (~same incidence angle) for the different zones of the Greenland ice sheet.

zone 1 : dry   zone 2 : percolation   zone 3 : soaked/ablation
zone 4 : ablation

Measured return power for the percolation zone.
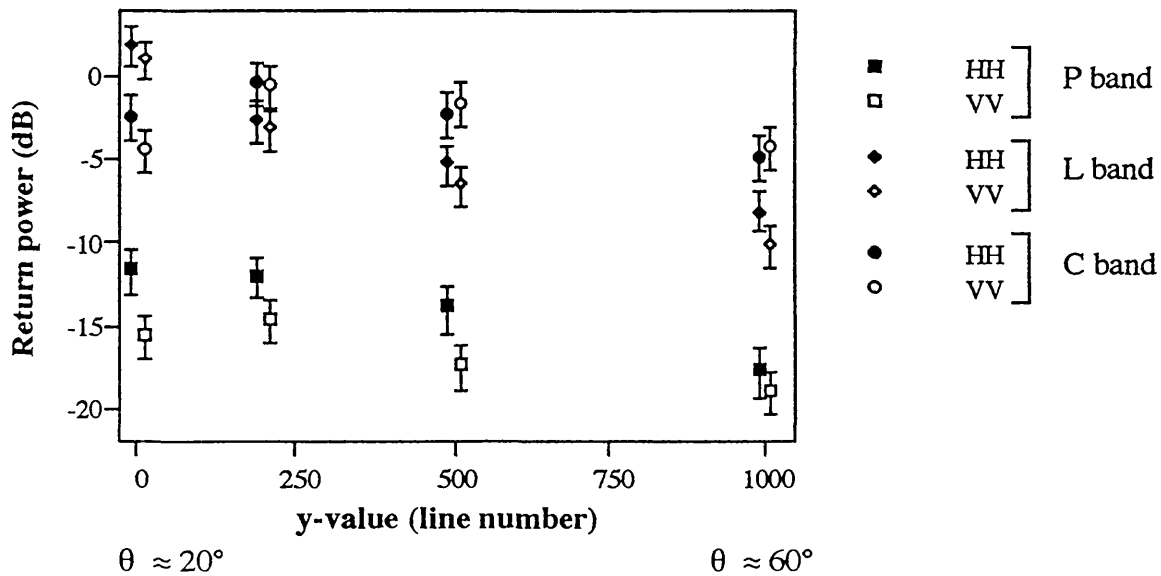
Figure 5.5: Measured AIRSAR return power (VV, HH polarizations) for P (i10), L (i11), C (i12) band radar with change in incidence angle over percolation zone of Greenland ice sheet (~20 to ~60 degrees).

page 160

5.1.4 Correlation with ERS-1 SAR data.

The values of the power returned for the AIRSAR measurements (C band, VV polarization) over particular zones of the ice sheet may be correlated with that measured by the ERS-1 SAR, thus combining airborne and spaceborne radar measurements over the same area. The satellite SAR data is measured for an incidence angle of 23 degrees, for C band and VV polarization only.

A printout of the ERS-1 SAR images and location over the Greenland ice sheet, with a plot of the mean backscatter for ERS-1 track 186-1 (March 3 1992) (as calculated using the formulae given by Laur, 1992) is given in figures 5.6, 5.7 and 5.8 (data supplied by K.Jezek, Byrd Polar Research Lab. Ohio).

The ERS-1 track covers all zones of the ice sheet as it tracks diagonally over an entire section of the Greenland ice sheet in an approximate NE direction. The highest radar return signal (the brightest area of the image) is over the percolation zone corresponding to the area of strongest backscatter. The value of the return signal then falls by approximately -20dB on entering the dry zone of the ice sheet, and this value then increases for some (at present) unknown reason on continuing to even higher latitudes. This may be due to the local topography of the surface or, more likely, to be due to the increasing presence of ice causing a stronger return.

The values of the return power (VV polarization, C band) for the AIRSAR data over the percolation (i12) and dry zones (i9) (taken for line averages, at a position within 2km of the near edge of image) are ~= 0dB for the percolation zone and ~= -18dB for the dry zone showing a drop of ~ -18dB which correlates well with the measured ERS-1 values. The above measured AIRSAR data values of return power are the approximate values for a line average of each image taken within 2km of the near edge of each image. The incidence angle is not exactly the same for each image so direct comparison of the results for different zones is not possible, and also the different localized features in the sample lines for each image lead to specific results for these images. The AIRSAR data from these line averages may therefore not be directly compatible with the larger sample areas from ERS-1 imagery, but can be used to give an approximate correlation. The date of acquisition of the AIRSAR data does not correspond with that of the satellite data so direct comparison of the actual values of return power measured by the two systems is not possible, but the relative difference in the return power for the different zones may be compared.
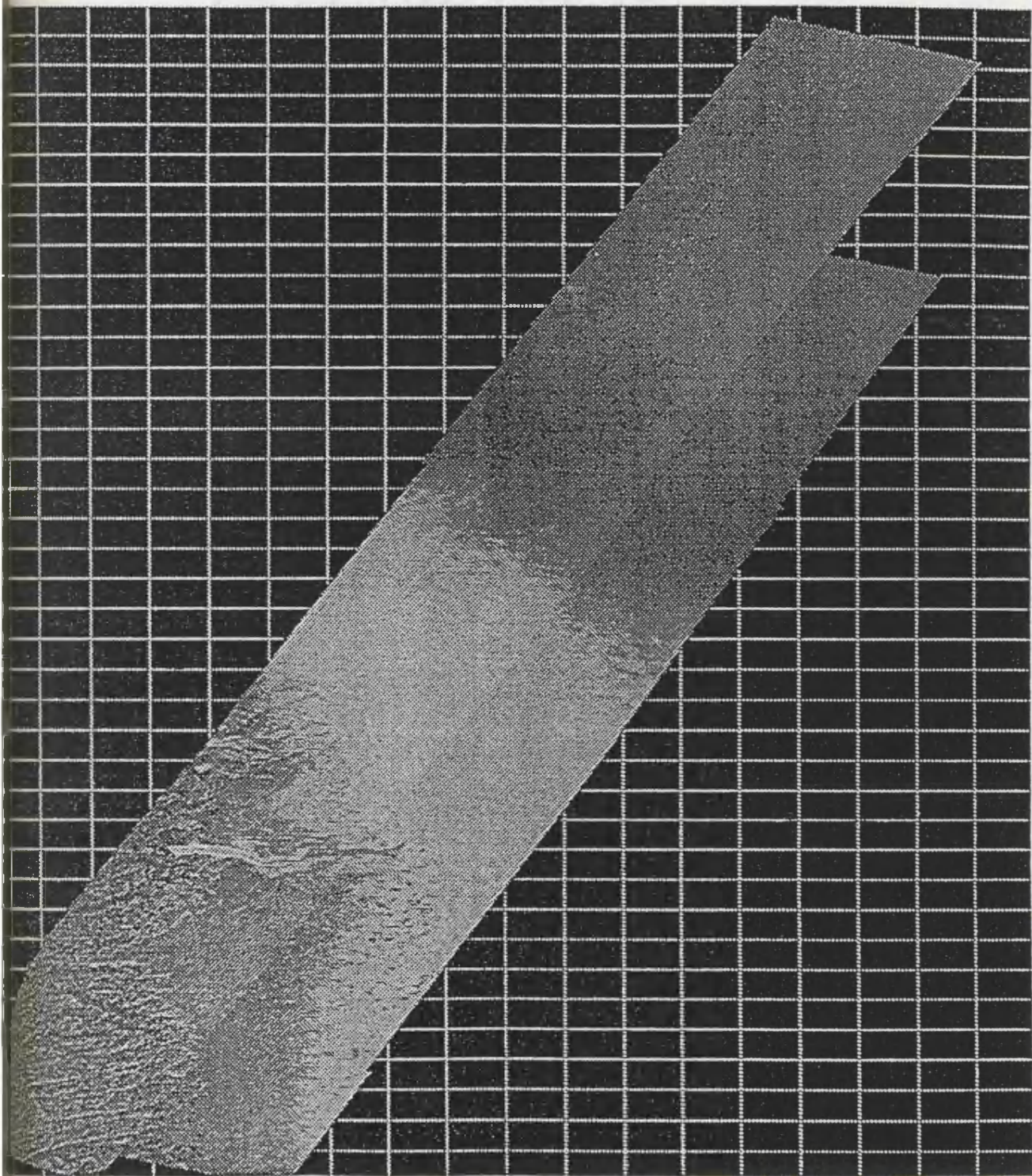
Figure 5.6: Mosaic of ERS-1 SAR images over Greenland ice sheet (~NE direction), tracks measured March 3, 1992 (186-1) and October 2, 1991 (location given by figure 5.7).
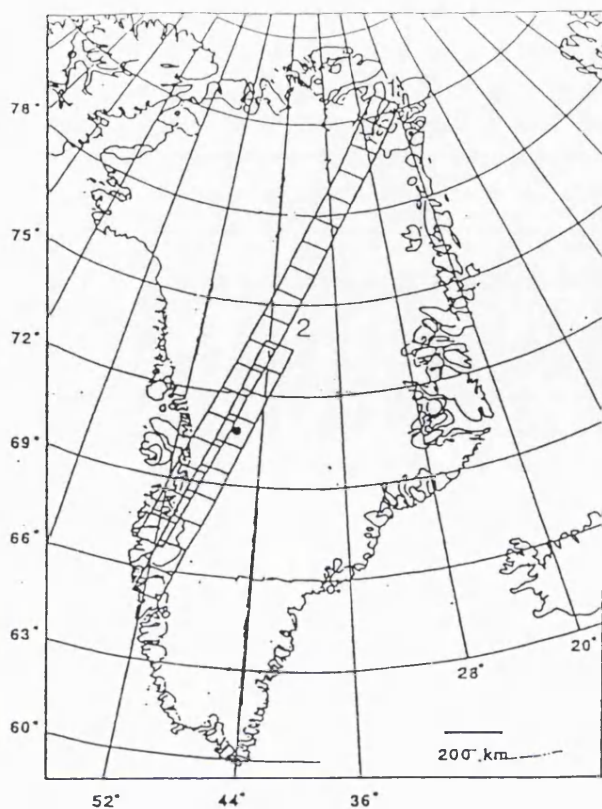
Figure 5.7: Location of ERS-1 SAR images over Greenland ice sheet (~NE direction), tracks measured March 3, 1992 (186-1) and October 2, 1991.
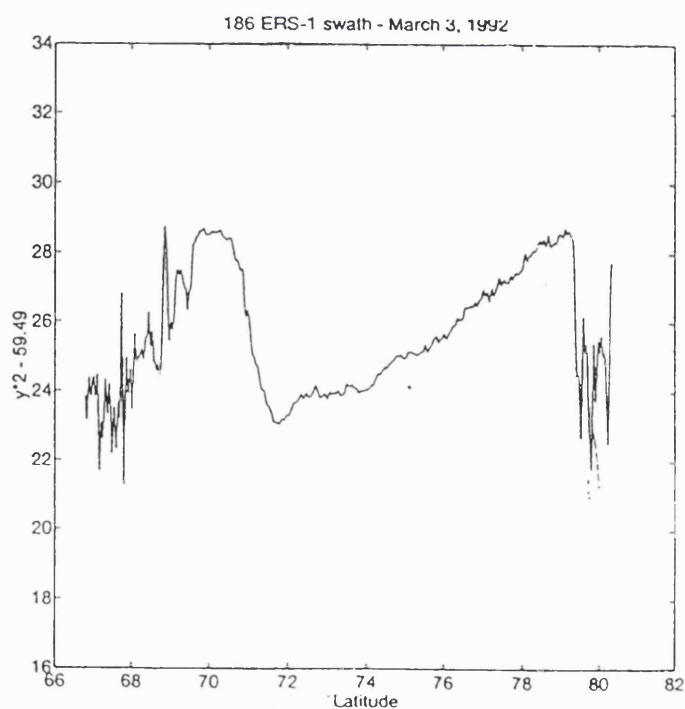
Figure 5.8: Mean backscatter values for ERS-1 track 186-1, March 3, 1992 (as calculated using the formulae given by Laur, 1992).

page 163

5.1.5 Polarization response for different zones.

The polarimetric response for each of the images is described below (table 5.1 and figure 5.9). The variation of the shape of the response with frequency, and also with the incidence angle for each scene is noted. The shape of the response indicates the dominant type of scattering which occurs for each zone of the ice sheet.

Shape of measured 3D polarimetric response for each zone.

zone 1: dry zone

i7 P reflector like for the near edge, with single dip. The height of the centre of the plot increases after line $y = 100$, giving ~single hump shape at the far edge of the image.

i8 L unsymmetrical response for the near edge, reflector like, then double dip shape appears and pedestal height increases as the image is descended.

i9 C double dip, pedestal high. Centre increases and pedestal height increases as the image is descended.

zone 2: percolation zone

i10 P direct scattering throughout image? reflector like with single dip, remaining with same shape as the image is descended, with pedestal height increasing.

i11 L slight single dip, with a higher pedestal than for P band. Height of pedestal increases as the image is descended.

i12 C much higher pedestal which increases slightly as the image is descended. Very flat response, single dip then ~double dip as the image is descended.

zone 3: soaked/ablation zone

i1 P direct scattering. Reflector like plots with single dip, pedestal height increases from near to far edge of image.

i2 L slight dip, pedestal height greater than for P band, increasing slightly as the image is descended.

i3 C slight dip then centre hump appears, pedestal height large and increases as the image is descended.

zone 4: ablation zone
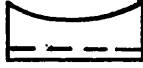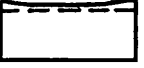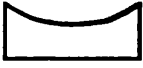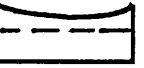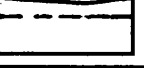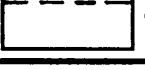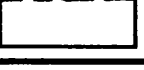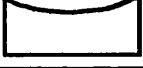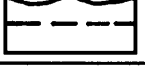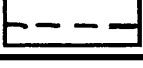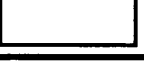
i13 P reflector like single dip for near edge. Pedestal height increases as the image is descended and centre hump increases.

i14 L flatter response, higher pedestal, single dip then double dip as the image is descended (only slight dips noted).

i15 C reflector like for near edge of image, centre hump increases as the image is descended, pedestal height also increases.

Table 5.1: Polarization response for ice sheet data, AIRSAR images, zones 1 to 4.

co polar response summary

zone no / freq.	near	mid	far region of image
1 i7 P	centre increases after y=100	centre increasing	single hump VV>HH
i8 L	unsymmetrical	double dip	high pedestal
i9 C			higher pedestal
2 i10 P	single dip reflector-like response	pedestal increasing	flatter response
i11 L	pedestal increasing		
i12 C	very flat response	higher pedestal	flat response almost double dip
3 i1 P	single dip		pedestal increasing
i2 L		higher pedestal	
i3 C	very flat response	centre hump	centre hump VV>HH
4 i13 P	single dip	pedestal increasing	
i14 L			slight dips
i15 C			higher pedestal

Greenland AIRSAR images, measured 10 June 1991.

Figure 5.9: Summary of the change of the measured co polar response with incidence angle and frequency for the different zones of the ice sheet. The normalized return power for the linear polarization states are shown, corresponding to the centre line (ellipticity = 0) of the 3D polarimetric response as measured by the AIRSAR system. The pedestal height, shown as a dotted line, tends to increase with frequency and incidence angle for each scene. Comments on the general shape of the response are also included.
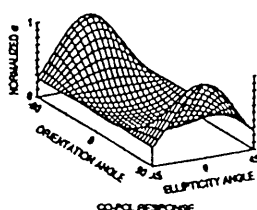
Linear polarization states taken from centre line of 3D polarimetric response.

page 165

5.1.5.1 Direct scattering in near region of images.

A trihedral reflector like response is noted for a distinct region at the near edge of the image for all the scenes and for all frequencies. This type of response, measured over a range of incidence angles adjoining the near edge of the image (up to ~200 lines in) indicates that direct scattering occurs. It is not thought to be just an edge effect (from poor calibration of instrument) as it occurs over a sizeable part of each image (equivalent to an area ~2km wide on the ground). This reflector like response at the near edge of the majority of the images suggests that direct scattering is the dominant mechanism for most of the images for a region at the near edge of the image. This occurs for images of the dry zone, the percolation zone and the soaked and ablation zones of the Greenland ice sheet, for all frequencies. The only exception to this is the C band, dry zone (i9) image, which shows a double dip probably due to low return power in this case (the measured value is -22 dB total power at the near edge of i9).

A reflector like response is noted throughout the i10,11,12 (P, L, C) images of the percolation zone indicating that direct scattering is the main scattering mechanism, independent of the incident angle. Direct scattering tends to be more noticeable for lower frequencies, and for a distinct region at the near edge of the images for all the other scenes.

The single dip shape of the co polar 3D response plot for direct scattering may be explained by considering the power ratio (VV/HH) on reflection from smooth dielectric surfaces. This is less than unity for near normal incidence when specular direct scattering occurs. The centre position of the normalized return power plot (corresponding to VV polarization; orientation 90, ellipticity 0) is lower than the central part of the near and far edges (HH polarization; orientation 0 (or 180), ellipticity 0) and hence the single dip shape occurs.

The change in the shape of the 3D polarimetric response for direct scattering when the incidence angle is increased is illustrated by the measured and theoretical data for dry snow at 20, 40 and 60 degrees incidence, corresponding to the range measured by the NASA/JPL AIRSAR (figure 5.10).

The line averages from the measured P band AIRSAR image, taken at the near, mid and far edges of the image (at positions down the image approximately corresponding to the above values of incidence angles) are shown in figure 5.10 i). These measured values of

the polarimetric response of the ice sheet are of the backscattered signal from the imaged terrain.

The theoretical response is shown in figure 5.10 ii). This is computed for a uniform deep homogeneous layer of dry snow (0% snow, percentage water content by volume) for P band radar, for forward scatter at the above values of incidence angles.

The theoretical and measured values show good comparison particularly for 20 degree incidence. The theoretical and measured response show similar changes in the shape of the 3D polarimetric return signal as the incidence angle increases. The shape of the co polar power plots show an increase in the central dip as the incidence angle increases. These plots, however, show the normalized power, and the decrease in return power with increase in incidence angle means that a small change in return power at high incidence angles results in a comparatively larger change in the general shape of the normalized response.

i) measured backscattered polarimetric response from AIRSAR data:

20⁰

40⁰
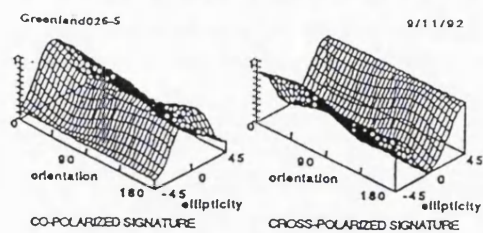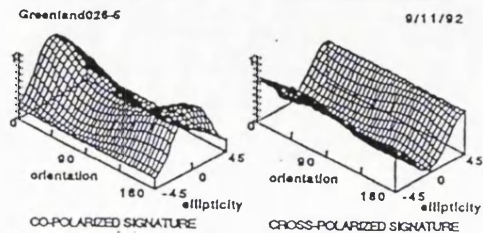
60⁰
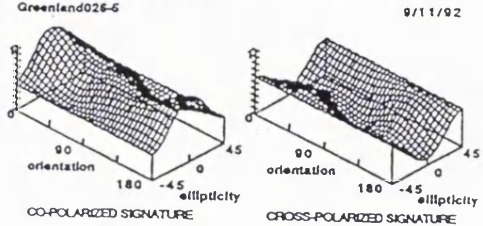
ii) computed forward scattered polarimetric response:

20⁰

40⁰
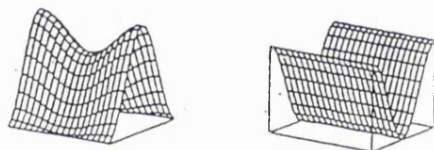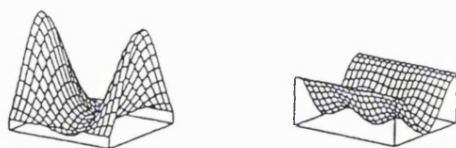
60⁰
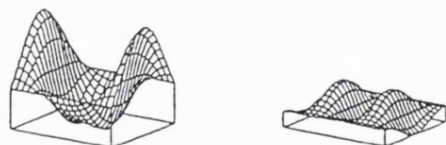
Figure 5.10 i) and ii): 3D polarimetric response for i) measured P3206 (i10) AIRSAR image PERCOLATION ZONE (for line averages at ~20, 40, 60 degree incidence) and ii) theoretical values for dry snow at P band at these incidence angles.

5.1.5.2 Diffuse, double bounce and rough surface scattering.

The measured polarimetric response of each of the AIRSAR images show that, in general, the pedestal height of the response increases with frequency, and with incidence angle (i.e. as the image is descended). This indicates that the diffuse scattering component of the return signal becomes more dominant for higher frequencies, and for larger incidence angles for all the scenes.

A double dip response is sometimes noted to occur for high frequencies and for large incidence angles. This is probably due to the low return power for these occasions. The measured polarization response is plotted on a normalized scale and small changes in the return signal power can result in large changes in the shape of the response for low power signals as explained in chapter 2.

If a strong return signal is of this form then the dominant scattering mechanism is termed "double bounce", commonly found in the double reflection from a dihedral corner reflector. This effect is usually found on reflection from buildings in urban areas, or from the trunk: ground interaction in forested areas. For the ice sheet areas a dielectric discontinuity in the vertical direction together with another dielectric discontinuity in the horizontal direction (simulating a dihedral corner reflector) would cause a double bounce effect. This is possible in areas where there are distinct layers with vertical discontinuities, for example horizontal ice layers and vertical ice walls in the percolation zone. It could also occur for sudden changes in topography, for example at the ice wall at the edge of the ice sheets, or for crevassed areas where the separation of the return signal is greater than the wavelength of the operating radar (figure 2.5, chapter 2).

This effect is not found, however, for the strong return signal of the measured AIRSAR data over the percolation zone (June 1991), although horizontal ice layers and vertical ice pipes were found at the test-site there by the field party (K.Jezek, personal communication). The data for this scene are analysed further in sections 5.1.7 and 5.1.8.

A centre hump response is noted for the co polar response for some of the scenes, with the height of the central hump (i.e. VV polarization) increasing with increasing incidence angle, and for higher frequencies. For rough surfaces the power ratio (VV/HH) becomes greater than unity, showing that rough surface scattering appears to be more dominant when the incidence angle is greater, at the far edge of the images. The value of incidence angle, θ, is measured away from the normal, so a large incidence angle means a shallow

approach to the ground and normal incidence is given by $\theta = 0$. The same surface also appears to be rougher for higher frequencies. This is due to the height of surface irregularities being greater relative to the incident wavelength for the higher frequencies.

5.1.6 Application of theoretical classification method to measured AIRSAR data.

The data of the C band 233-1 AIRSAR image of the ablation zone further down the ice sheet measured on a previous campaign (August 1989) are used in the application of the theoretical classification method as described in chapter 3 (section 3.3.2). This image shows distinct areas of different intensity. Figure 5.11 shows the total power AIRSAR image, with the ROGIBIV colour table as before (refer to figures 5.1 and 5.2; red areas represent high return power, violet for low return power, with bright white for saturation). The particular line of data used for the analysis is also shown.
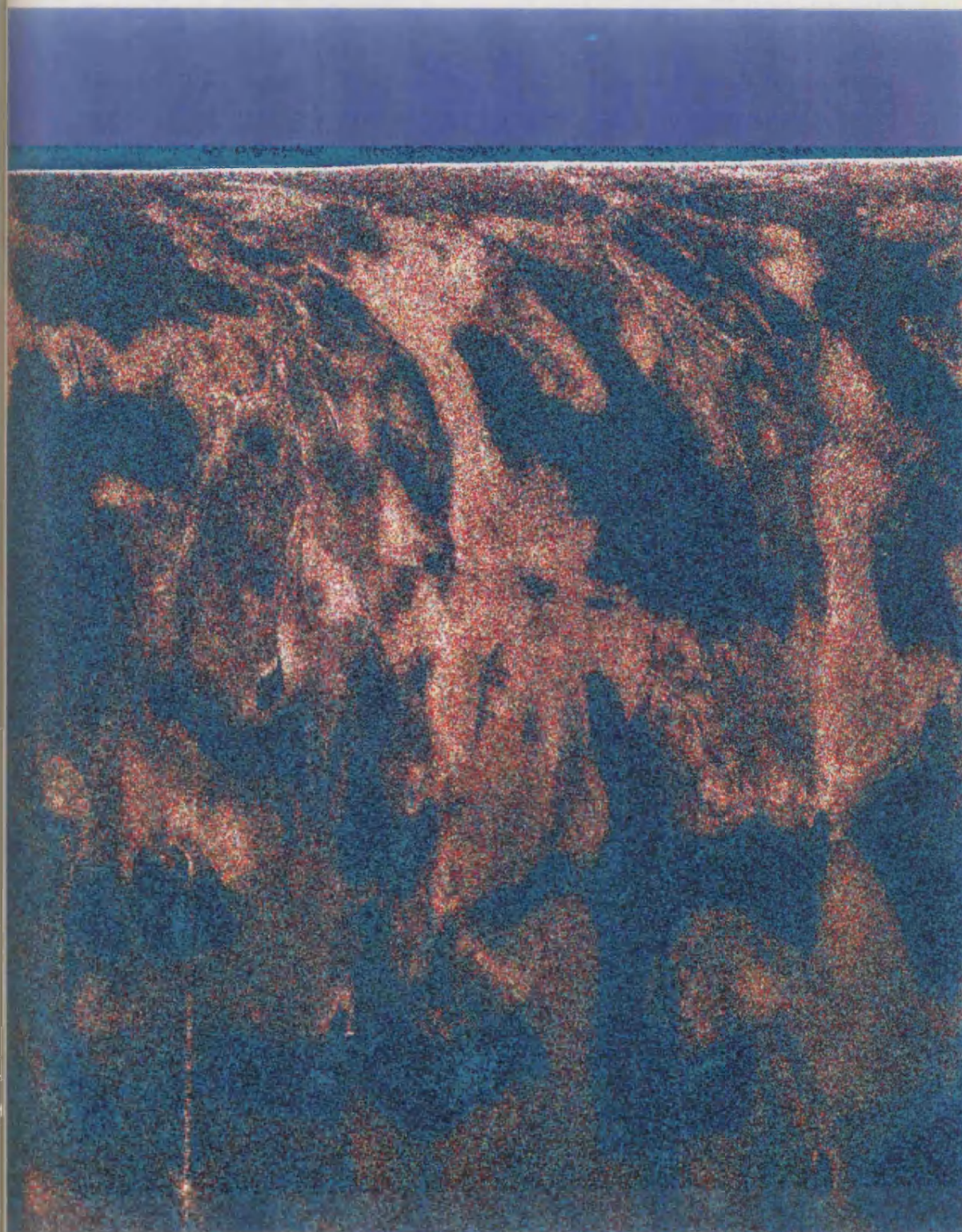
Figure 5.11: Total power AIRSAR C band 233-1 image over the ablation zone in South Western Greenland, coordinates 64° 30.7' N, 48° 48.7' W, flight direction 229.1 degrees, date August 31, 1989.   Position of dataline shown.

The measured data points corresponding to dark and light areas of this image, for 20° incidence angle, are given in figures 5.12 (i) and (ii). This data line is marked on the image (figure 5.11). The complete line of data is divided into 25 pixel samples, and these samples are further grouped into adjacent dark and light areas, with equal weighting for each data point. Figure 5.12 (i) gives the power ratio plot (VV/HH power) and figure 5.12 (ii) gives the total power plot (shown as relative power for each sample). The absolute power for this data set is not available and so no statistical analysis is undertaken. The measured data is of very low power (van Zyl, personal communication). The total power returned should be ~ -17 dB for snow at 20° incidence, for C band radar (table 2.6).

The measured data points shown in figure 5.12 i) are compared with the theoretical power ratio values given in chapter 3 (figure 3.8).

i)

C 233-1 power ratio (VV/HH), 25 pixel samples from 12 areas (~20deg.)
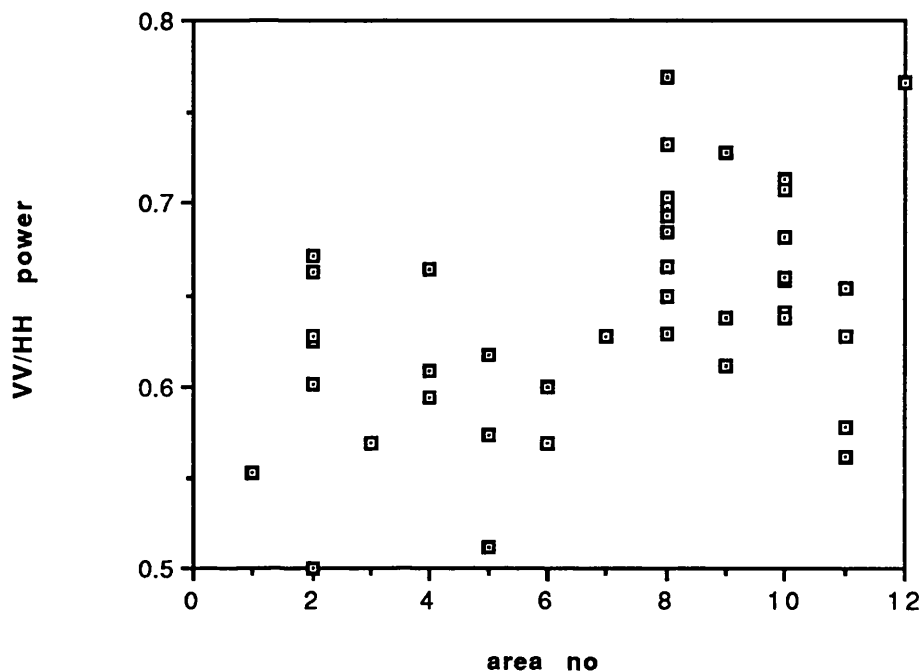
ii)

C 233-1 total power, 25 pixel samples from 12 areas (~20deg.)
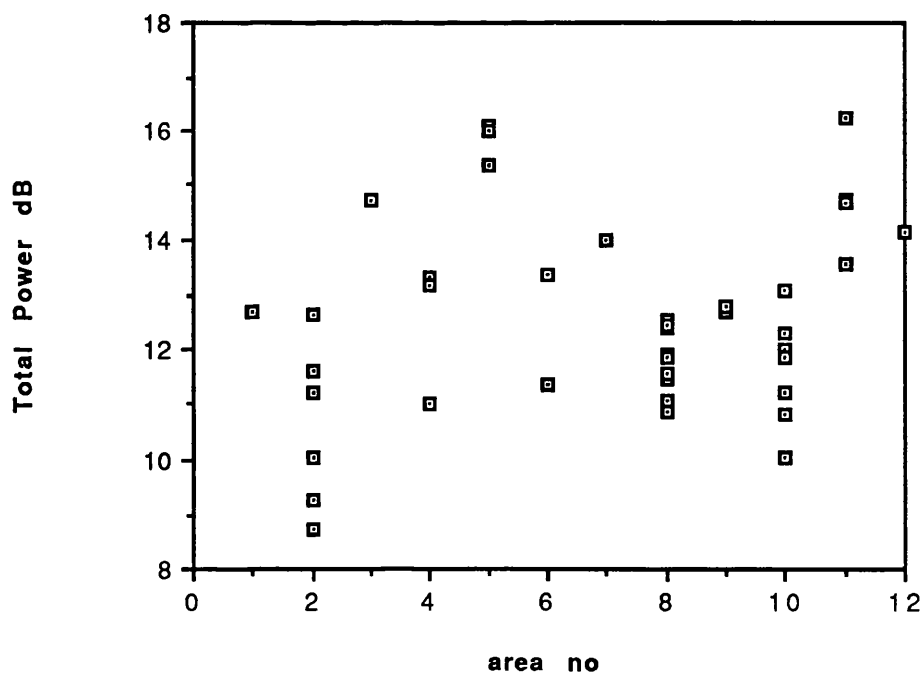
Figure 5.12: i) and ii); fractional power (VV/HH) ratio plot (i) and total power (TP) plot (ii) for measured data from C band 233-1 AIRSAR image over the ablation zone.

The points correspond to 25 pixel samples taken from 20° incidence angle line divided into 12 bright and dark areas.

Areas 3, 5 and 11 are the brightest areas with the highest values of return power. Areas 1 and 12 could give misleading data as they include the first and last 25 pixels of the line, taken from the edge of the image.

The points corresponding to the dark areas (low return power) occupy the highest regions of the power ratio plot, and those of the brighter areas (higher return power) tend to be positioned lower on the power ratio plot. The dark areas are therefore of a higher dielectric constant than the bright areas, as a high dielectric constant has a higher polarization ratio (VV/HH power) than a lower dielectric constant. The relative positions occupied by the measured data on the power ratio plot therefore indicate that the light areas are of drier snow (of low dielectric constant and low moisture content) than the dark areas (of greater dielectric constant and higher moisture content). This result is consistent with Jezek *et al.* (1993) who describe the dark areas of the image as seasonal melt pools and the surrounding brighter areas as drier snow, as discussed earlier in chapter 1 (section 1.3.1.2).

It should be noted that, for the 233-1 image, the backscattered signal is of very low power and hence a misleading shape of the polarimetric response may be measured due to the weak return signal. This may explain why the values of VV/HH power also seem to be rather low compared with the theoretical data. The light and dark areas of the image do, however, show a relatively low and high VV/HH power ratio, indicating low and higher values of dielectric constant respectively.

These results indicate that the VV/HH ratio from measured polarimetric data may therefore be used (as in this classification method) to indicate the different types of surface cover of the imaged area, and hence classify the imaged terrain.

Further analysis of the measured polarization response of the 233-1 image is given in Appendix A1.7, which also details the format of the polarimetric data. The apparent scattering mechanism is determined from the polarimetric response and found to be of double bounce form throughout the image. The possible causes of this form of scattering from the ice sheet is discussed with reference to the physical characteristics of the soaked/ablation zone.

5.1.7 Subsurface ice lenses.

The measured 3D polarimetric response may be used to detect unusual shaped objects, for example, the presence of cylindrical ice lenses within the percolation region of the ice sheet. The theoretical polarimetric radar response of cylindrical objects is given by Ulaby and Elachi (1990) as discussed previously in chapter 2 (section 2.2.2.3). The form of the 3D polarimetric response for cylindrical objects is plotted, and the change in the response due to the relative orientation of the cylindrical object to the E vector of the radar is shown (figure 2.12, i ii and iii).

The dark areas of the (i10) percolation zone image are thought to be caused by subsurface discontinuities (as discussed earlier in section 5.1) and may possibly indicate the presence of subsurface ice lenses. The measured AIRSAR 3D polarimetric response for these particular areas tend to be of the first form (3D plot of co polar response shows HH>VV), which may indicate the location and horizontal orientation of the buried cylindrical ice lenses. Some of the measured response plots from this image seem to show slight asymmetry, which may be indicative of vertical discontinuities, such as the cylindrical vertical ice pipes found in this percolation region.
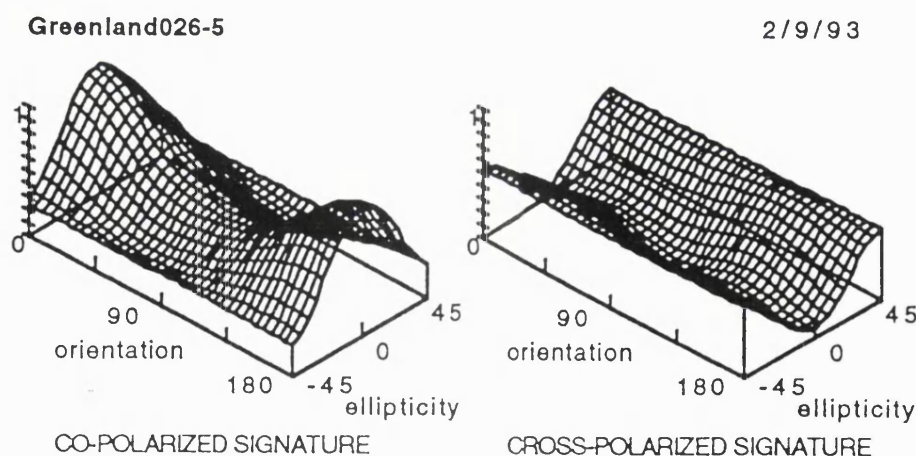
Figure 5.13: Measured 3D polarimetric response for percolation zone P band image (zone 2).

5.1.8 Subsurface position of ice layer.

The position of a subsurface ice layer beneath a surface layer of firn is found to affect the polarization response as discussed in chapter 3 (section 3.3.4.3). A system of snow and ice layers is simulated and the polarimetric content of the computed return signal is shown on a power ratio vs. phase difference plot. The theoretical analysis suggests that the position of an ice layer within the snowpack may be inferred from measured polarimetric signals, by comparing the measured polarimetric signal with the theoretical data. The polarimetric content of the measured backscattered signal is compared with that of the theoretical computed values for forward scattered signals from a simulated system of snow and subsurface ice layers, where the depth of the surface firn layer is increased. The measured data from the P band AIRSAR image of the percolation zone are used in this analysis as ice layers were found in this region by the field party (Jezek, 1992). Details of this field campaign are given in chapter 4.

Actual values for the different components of the measured return signal are given in table 5.2 below. These values are for the line average of data of the same incidence angle of the P band AIRSAR image.

Measured AIRSAR data of the percolation zone:

		measured value	relative standard deviation
	TP	-15.39 dB	1.276
	HH	-11.44 dB	1.299
	HV	-28.50 dB	1.339
	VV	-13.88 dB	1.292
phase	**HHVV***	-17.51 degrees	8.30 degrees (standard deviation)

Table 5.2: Measured values of line average data (y = 33) for AIRSAR P3206 image, using MacSigma0-11 software (Norikane, JPL, 1992). Note HHVV* phase is equivalent to (HH-VV) phase difference(mod.90) from Stokes matrix (from MacSigma0-11 document, Norikane, 1992).

The relative standard deviation, $\sigma_{relative}$, is given by equation 4.1, chapter 4, and used to calculate the standard deviation (σ) using the mean value (m). The measured fractional values and the standard deviation of the HH and VV return power are calculated and given in table 5.3 below. The fractional value is obtained by converting from power in dBs to volts^2, using volts^2 = -10 $\log_{10}$ dBs.

Measured AIRSAR data of the percolation zone:

	measured fractional value	standard deviation
HH	0.0718	0.02146
VV	0.0409	0.01195

Table 5.3: Measured fractional values and standard deviation of line average data (y=33) for AIRSAR P3206 image.

This gives the value of the measured linear polarization ratio VV/HH as 0.57, by dividing the mean fractional line average VV value by the corresponding HH value.

The standard deviation of the ratio VV/HH for the line average value is not calculated using the JPL software statistics package. This standard deviation may be calculated by considering the values of VV/HH for each of the pixels in turn and determining each individual deviation for each value of VV/HH for each pixel from the mean value of VV/HH for the line average. The standard deviation for the ratio VV/HH is not equal to the standard deviation of the VV values divided by that for the HH values, but these figures are given in table 5.3 for comparison. Further work on the statistics of the measured data is given in Appendix A1.6.

Figure 5.14 shows the theoretical power ratio vs. phase difference plot for P band radar at 20° incidence for a change in position of ice layer from 50 to 800mm depth, in 50mm steps, together with the measured data point from the P3206 AIRSAR image over the percolation zone (symbol X). The measured data point, X, represents a line average of data, at the same incidence angle. This line average of data is taken from the line corresponding to that containing the 6th corner reflector (marked 2KmE in the site map, figure 4.1) which is almost hidden in the bright return signal at the top of the AIRSAR image. The snow pit data as measured by the field party (K.Jezek *et al.*) are given in figure 4.2.
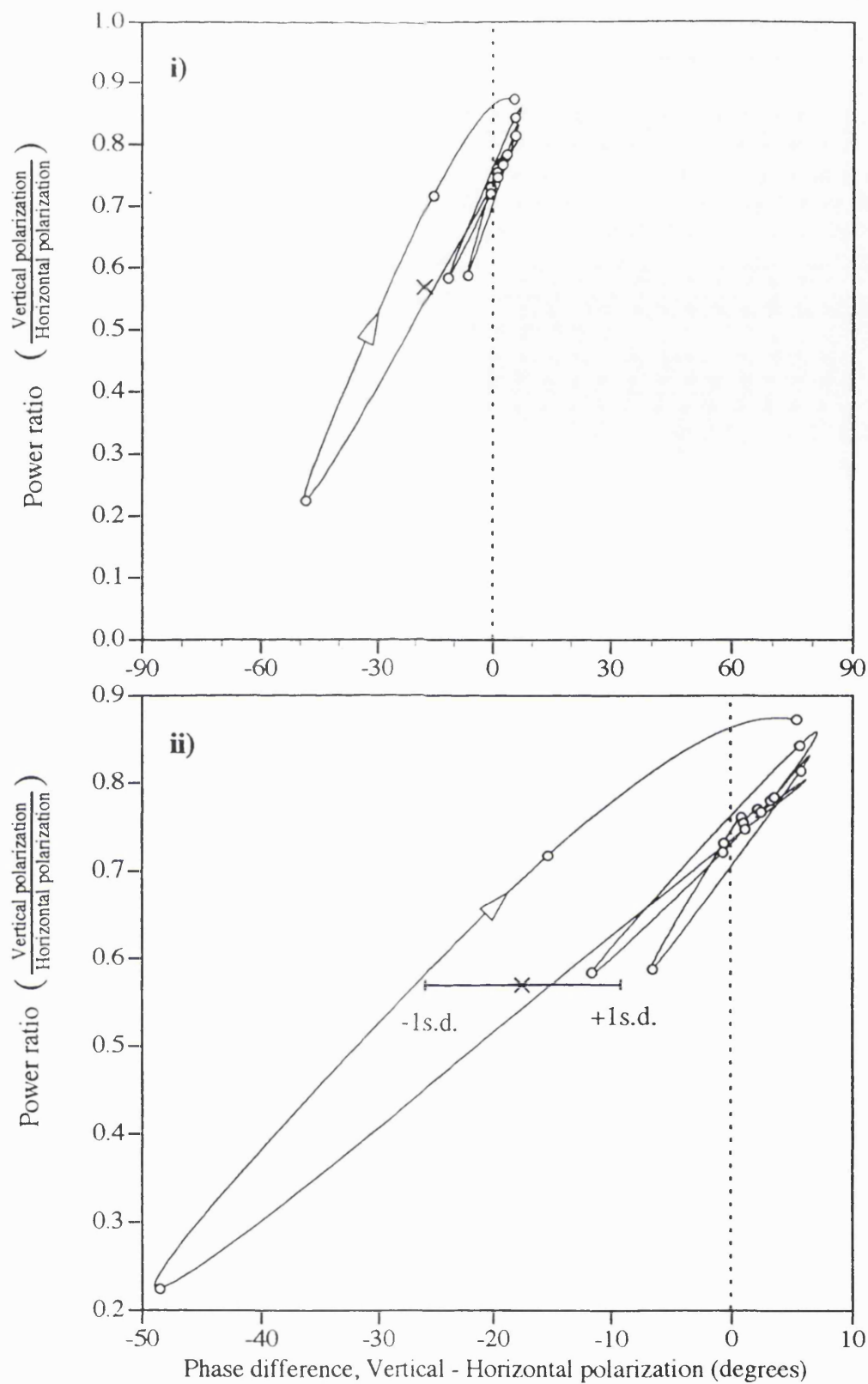
Figure 5.14 i) and, expanded scale ii): Theoretical power ratio versus phase difference plot for VV and HH polarization (P band, 20 degree incidence angle, forward scatter) for change in position of ice layer (depth of firn) to 800mm (50mm steps), and position of measured data point from AIRSAR P3206 image given by X (backscattered data).

The measured point (VV/HH power 0.57, VV-HH phase -17 degrees) may correspond to an ice layer at depth 450mm. This is a possibility as ice layers were discovered by the field party in this region and the measured data from the snow pit (labelled 2KmE) show a distinct layer at approximately this depth (figure 4.2).

5.2 Results from passive microwave data.

5.2.1 Measured brightness temperature.

Plots of the measured brightness temperatures for the four zones of the Greenland ice sheet, for a complete year (April 1990 - March 1991), are shown below in figure 5.15. The mean daily values of the passive signal for the 19Ghz and 37GHz data are plotted for both vertical and horizontal polarization.
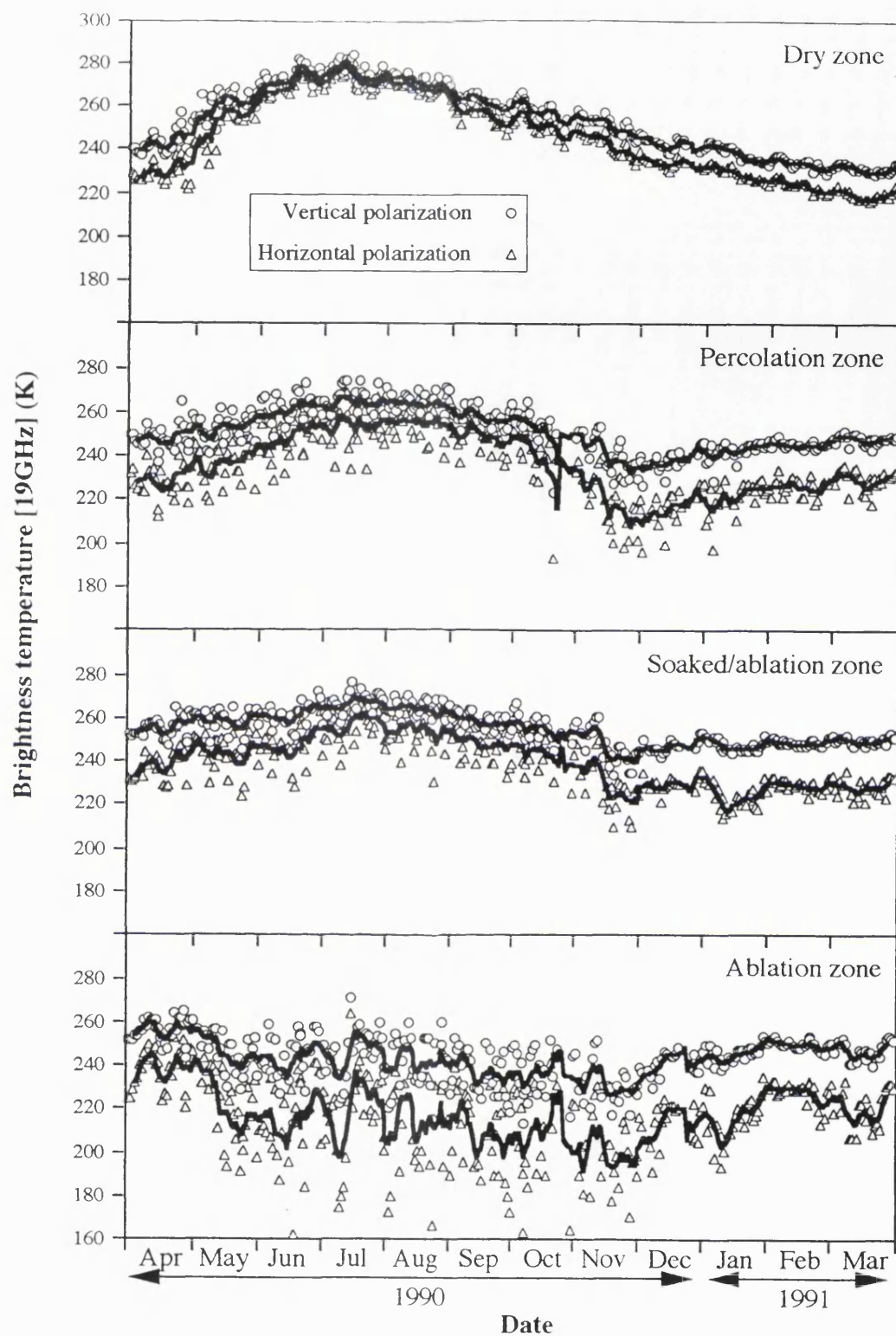
Figure 5.15 i): Annual change in measured brightness temperature T_B for the four different zones of the Greenland ice sheet using 19GHz SSM/I data for both vertical and horizontal polarization signals, April 1990 - March 1991, for the test areas of the dry zone, percolation zone, soaked/ablation zone and the ablation zone respectively. The points are daily averages and the lines are 7-day running means.
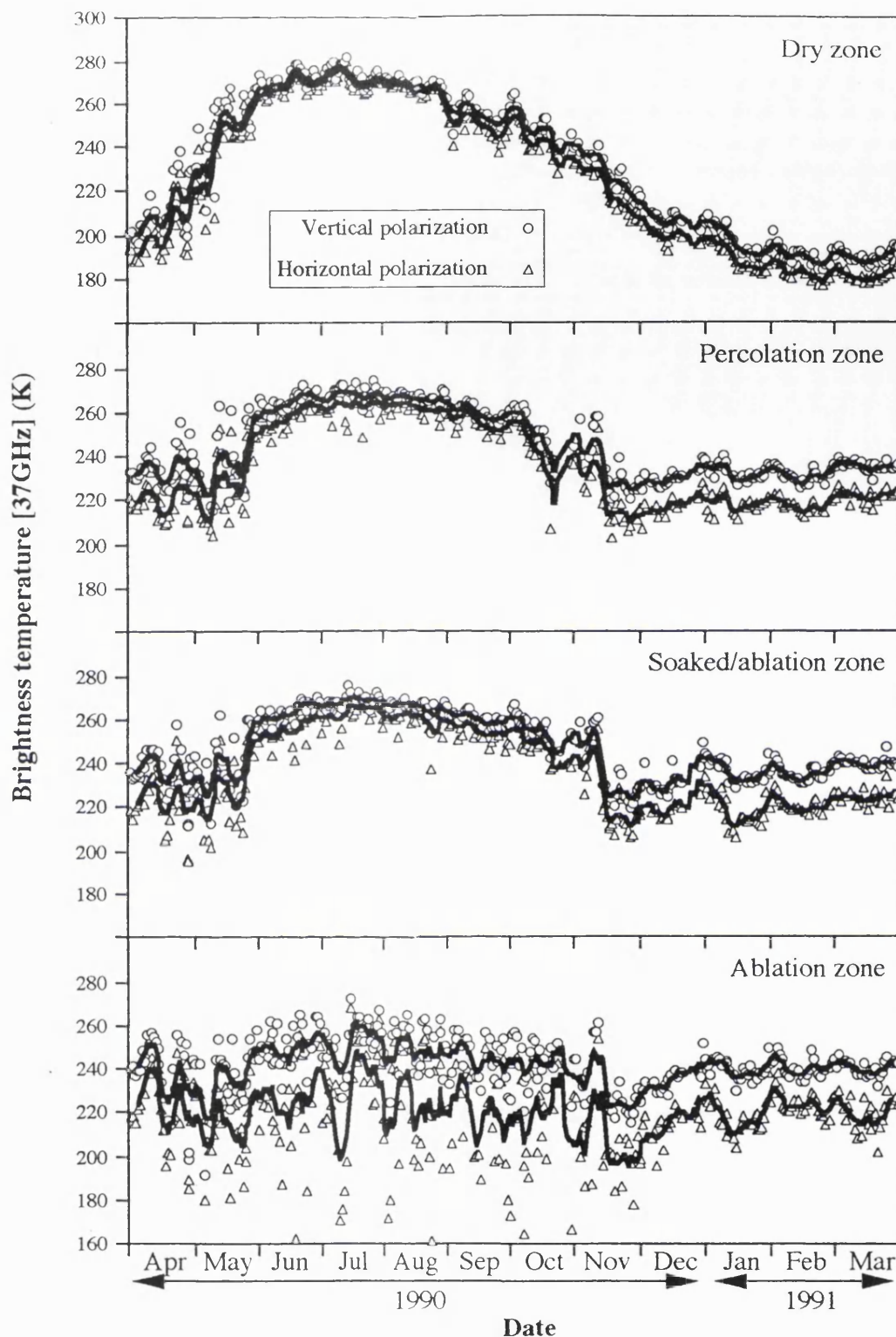
Figure 5.15 ii): Annual change in measured brightness temperature T_B for the four different zones of the Greenland ice sheet using 37GHz SSM/I data for both vertical and horizontal polarization signals, April 1990 - March 1991, for the test areas of the dry zone, percolation zone, soaked/ablation zone and the ablation zone respectively. The points are daily averages and the lines are 7-day running means.

The annual cycle of the measured brightness temperatures is noted for each of the four zones of the Greenland ice sheet. The brightness temperatures for horizontal polarization tend to be less than that for vertical polarization as predicted in section 3.4.1.

The measured values of brightness temperatures are seasonal and depend on the surface temperature changes. The values of the brightness temperatures are highest in summer when the surface temperatures are highest, and decrease during winter on an annual cycle.

The data for the dry zone show the greatest annual change in brightness temperature, with the highest values of brightness temperature (T_B ~= 280K) during the summer for both vertical (V) and horizontal (H) polarization, at both 19 and 37 GHz, then decreasing in winter to ~220K and ~180K for the 19 and 37GHz data respectively.

The brightness temperature values decrease for the different zones of the ice sheet, with the highest values for the dry zone, then decrease on descent of the ice sheet, through the percolation zone to the soaked and ablation zones at the edge of the ice sheet. This reduction in the measured brightness temperature values across the zones of the ice sheet is due to the change in emissivity of the different zones. The emissivity of wet snow (of high dielectric constant) is less than that for drier snow (and hence lower dielectric constant), so the measured brightness temperatures are lower for wetter areas.

The data for the dry snow region are compact and show a smooth annual change, whereas the data for the wetter areas show more day to day variation. The measured brightness temperature for the dry region follows the smooth cyclical pattern due to the annual temperature change over the uniform area. The data for the wetter regions are more diffusely scattered due to the partial melting and refreezing of a portion of the imaged area. This results in variable emissivity of the wetter areas as recorded by the changes in the measured brightness temperatures.

For the dry zone the lowest values recorded by the 19 and 37GHz channels are ~220K and ~180K respectively, during the winter. This is due to the physical temperatures being very low in this region, the cold, dry interior of the ice sheet. The difference in the values for the two frequencies is due to the increased penetration of the 19GHz signal. In winter the dry cold snow is of very low reflectivity (of low dielectric constant) and hence greater penetration occurs. The 19GHz data originate from subsurface layers of the snowpack which are warmer than the surface during winter due to the thermal capacitative effect of the snowpack. The 37GHz data are from the colder surface material. The 19GHz

brightness temperature is therefore greater than that for the 37GHz signal for this same area at the same time. A diagram showing the penetration of the 19GHz signal into the snowpack, and the typical temperature change of the snowpack with depth is given in figure 5.16 below.
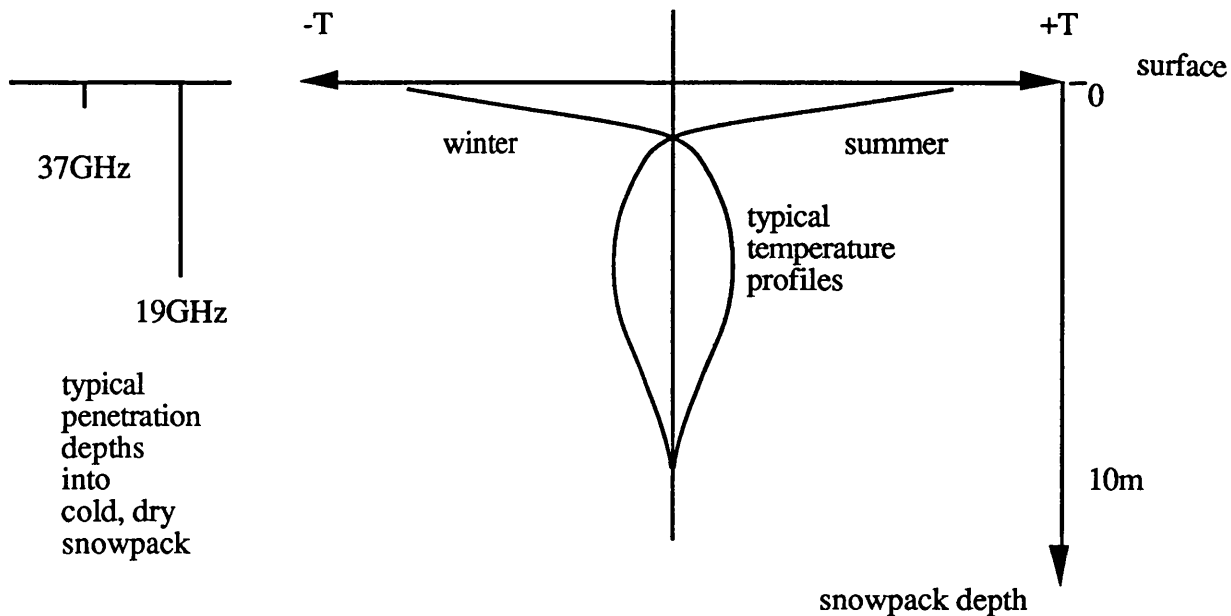
Figure 5.16: Typical thermal gradient of snowpack with depth, in winter and summer, together with typical penetration depths of 19 and 37GHz signals into cold, dry snowpack.

The temperature profile of the snowpack oscillates from season to season as the surface air temperatures cause the surface snow temperature to change. This change in surface temperature is transmitted into the subsurface snowpack layers causing a temperature gradient within the snow layers. The resulting heat flux with depth lags behind the changing surface temperatures due to the capacitative effect of the snow. The heat transfer within the snow layers causes the profile to change from season to season as shown above in figure 5.16 (K.Jezek, personal communication).

5.2.2 Measured Polarization ratio, and inversion to give dielectric values (wetness content of snow).

The annual change in the measured polarization ratio, T_{Bh}/T_{Bv}, for 19GHz and 37GHz data for each of the four zones is given in figure 5.17. Individual plots of the measured polarization ratio for each of the four zones of the ice sheet, for both 19 and 37Ghz data, for the full year April 1990 - March 1991, are given. The values are taken from SSM/I

data using the measured mean daily brightness temperature values T_B for each of the four locations on the ice sheet. The simple polarization ratio is highest for zone 1 (dry snow) and decreases on descent of the ice sheet (with increasing water content of the snow). The value of the polarization ratio is higher for 37GHz than for 19GHz data.

The difference between the emitted radiation for the two polarizations (Δpol.= T_{Bv} - T_{Bh}) is most noticeable for the soaked and ablation zones (zones 3 and 4, the wet areas) for 19GHz data (refer to figure 5.15 i)). There is only a slight difference in the values of Δpol. for the two frequencies 19 and 37 GHz. The values of Δpol. for 19GHz tend to be slightly greater than that for the corresponding 37GHz data. This difference in values for the two polarizations Δpol. is most noticeable for the time of year January -March, (winter - spring).

The values of (Δpol.) for the dry zone are greatest during winter. This is due to the increased depth of penetration of the 19GHz signal into the cold dry snowpack of low dielectric material and interaction with subsurface discontinuities.
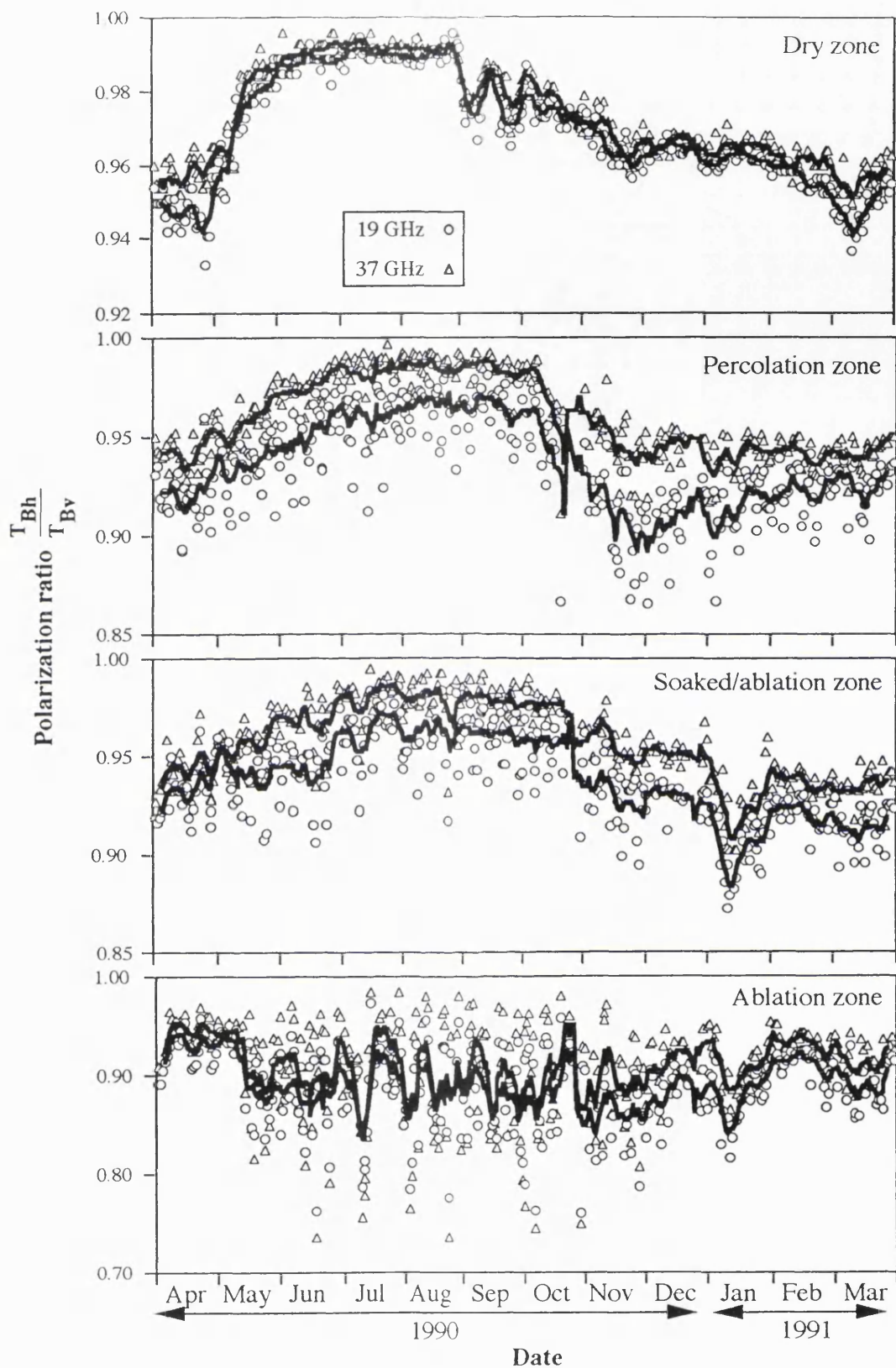
Figure 5.17: Measured polarization ratio T_{Bh} / T_{Bv} (SSM/I data, for 19GHz and 37GHz) for zones 1 to 4 of the Greenland ice sheet for the period April 1990 - March 1991. The points are daily averages and the lines are 7-day running means.

5.2.2.1 Measured Polarization ratio from SSM/I data.

The approximate range of the simple polarization ratio, T_{Bh}/T_{Bv}, for 19GHz data for each of the four zones of the ice sheet is:

(1) dry zone, highest T_B ratio ~0.94 - ~0.99

(2), (3) percolation zone, soaked/ablation zone, T_B ratio ~0.9 - ~0.95

(4) ablation zone, lowest T_B ratio ~0.8 - ~0.9

The lowest values of the brightness temperatures T_B (H and V) are found in winter, and the highest values of T_B occur in summer due to the quasi-sinusoidal annual temperature cycle (figure 5.15). Taking the ratio of the brightness temperatures for the two polarizations tends to reduce the dependence on the surface temperature.

The values of the polarization ratio T_{Bh}/T_{Bv} for 19 GHz for all the zones are also found to show this sinusoidal annual effect, with the lowest ratio in winter and the highest in summer. It is most noticeable for the dry zone (figure 5.17).

A low ratio E_h / E_v (= T_{Bh}/T_{Bv}) indicates a higher value of dielectric constant, indicating greater moisture content. The highest ratio appears for the dry zone at the beginning of the summer, and then decreases as summer progresses with the minimum value in mid winter. The ratio then increases again during spring indicating drier snow (less moisture content and hence lower dielectric constant, resulting in a higher polarization ratio (E_h / E_v)). The ratio for the other zones also follows this trend, with the numerical value of the ratio decreasing with the location of the zone down the ice sheet, due to the higher moisture content of the snow in the percolation, soaked and ablation zones.

A similar trend is found for the 37GHz data, except that the data for zones (2) and (3) are more compactly distributed, and the data for zone (4) are possibly slightly more dispersed than for the 19GHz data set.

The polarization ratio is generally higher for 37GHz than for 19GHz. There are two factors which may explain this: the difference in penetration for these signals of different frequencies, and the difference in the apparent value of the dielectric constant for the two frequencies.

The 19GHz signal has a greater penetration depth than the higher frequency (37GHz). The greater penetration depth causes greater difference between the polarizations for

19GHz, and a lower polarization ratio. Also, scattering within the snowpack caused by the physical size of the ice particles becomes more important for higher frequency emission data, and becomes the dominant form of emission (rather than from the absorption/ emission properties of the bulk of the material) for 37GHz data. The scattering coefficient is independent of the polarization for spherical ice particles (equal for parallel and perpendicular polarization states). There is therefore less difference between the two polarizations for 37GHz resulting in a higher polarization ratio than for the 19GHz data.

The value of the dielectric constant for snow of the same moisture content is smaller for higher frequencies due to the frequency dependence of the dielectric constant of water. This results in a higher polarization ratio (E_h /E_v) for the higher frequency data of the same area.

5.2.2.2 Inversion of passive microwave (SSM/I) data using theoretical polarization ratio.

The theoretical reflection coefficient for different dielectrics is used to compute the theoretical polarization ratio for the emitted radiation at 19.2GHz, 53.2 degrees incidence corresponding to that of the SSM/I instrument (refer to chapter 3, section 3.4.1). The variation of the theoretical polarization ratio of the emitted radiation with increasing dielectric constant is given in figure 3.11. The polarization ratio is found to decrease steadily from: i) ~1.0 to ~0.8 and ii) ~0.9 to ~0.45 on increasing the value of the dielectric constant (Er) of the imaged area from: i) 1 - 3.15 and ii) 2 - 80.

The theoretical computed reflection coefficient data gives the value of the emitted polarization ratio Eh/Ev as 0.930 for Er = 1.7, 0.954 for Er = 1.5, 0.966 for Er = 1.4 and 0.978 for Er = 1.3 using the relationship $\dfrac{E_h}{E_v} = \dfrac{(1-R_h)}{(1-R_v)}$.

Changing the value of tanδ, the loss tangent, does not change the power of the reflection coefficient (just the value of the reflected phase) for a uniform deep homogeneous layer of snow (Appendix A1.3.4).

The value of the dielectric constant may be determined from the polarization ratio of the measured passive SSM/I data. The polarization ratio of the measured emitted radiation for the dry zone (SSM/I data, point 1) gives a mean value of Eh / Ev = ~0.97. Using this value of the measured passive polarization ratio to determine the dielectric constant gives

Er ~= 1.4 for the dry snow area. This equates well with field measurements of the dielectric constant of snow at a test site in Antarctica @13.8GHz as measured in early 1992. The values of dielectric constant are ~1.4 for dry snow, rising to ~1.6 with ice crust, due to the higher density causing the higher value of dielectric constant (J. Ridley, personal communication).

The measured polarization ratio data for the dry zone show that the polarization ratio is highest in spring, decreases during the summer and is the lowest in autumn, before increasing again during the winter and spring (figure 5.17). A high polarization ratio indicates a low dielectric constant, and the lower polarization ratio indicates a higher dielectric constant. The high values of dielectric constant may be caused by increasing wetness content of the snow, or by the formation of ice. The low polarization ratio measured for the dry zone in winter is thought to be caused by the formation of a wind crust of ice on the surface. The dielectric constant of the ice is higher than that of snow, and hence the measured polarization ratio is lower. The higher polarization ratio noted during spring indicates a lower dielectric constant which represents the cold dry snow at the surface.

Thin layers of ice indicating surface crust formed by localized wind events are found in the snowpits at the GISP2 test-site in the dry zone (K.Jezek, personal communication). The presence of these thin layers of ice on the surface and also within the snowpack will reduce the level of the emitted signal. Formation of ice at the surface would tend to have the greatest effect on the received signal, although subsurface layers will also affect the signal. Ice has a higher dielectric constant than snow, a higher reflectivity and hence a lower emissivity, which therefore causes a reduction in the power of the measured passive microwave signal, and a decrease in the polarization ratio of this signal.

5.2.2.3 Inversion of passive microwave data (SSM/I) for Greenland ice sheet zones 1 - 4 for complete year.

The polarization ratio of the measured mean daily brightness temperature data from SSM/I (for the period April 1990 to March 1991; 19GHz data) is used to determine the change in dielectric constant (Er), and hence to infer the variation of the water content of the imaged zones over the year. The calculated values of dielectric constant are for a uniform deep layer of this material (using Fresnel reflectivity values at 53.2° corresponding to the incidence angle of the SSM/I).

The results are summarized in table 5.4 below:

Greenland ice sheet data:

zone	pol.ratio $19T_{Bh}/T_{Bv}$ (measured sequence)	Er (calculated values)	% wetness (inferred values)
1 Dry	~ 0.94 - 0.99 - 0.94	~ 1.6 - 1.2 - 1.6	~8 - 0 - 8
2 Percolation	~ 0.92 - 0.95 - 0.9	~ 1.8 - 1.5 - 2	~12 - 6 - 12
3 Soaked/ablation	~0.92- 0.96- 0.9	~ 1.8 - 1.45 - 2	~12 - 5 - 16
4 Ablation	~ 0.9 - 0.8 - 0.9 (diffuse)	~ 2 - 3 - 2	~16 - 36 - 16

Table 5.4: Measured annual sequence of polarization ratios for zones 1-4 of the Greenland ice sheet; calculated values of dielectric constant and inferred mean % wetness content.

The mean % wetness for each of the zones increases during the summer months (from June onwards). The predicted values of the dielectric constant are inversely related to the polarization ratio of the measured brightness temperatures (T_{Bh}/T_{Bv}), and the emissivity ratio for the two polarizations (Epara./Eperp.) from the relationship given in equation 3.15. This shows that with decreasing measured polarization ratio, the mean dielectric constant of the imaged snow surface increases. The mean dielectric constant of this imaged area increases with the % wetness content of the snow (as given by equation 3.17). The % wetness content of the snow of each of the zones is shown to increase during the summer months (from June onwards) and decreases during winter and the spring months. A summary plot showing the yearly change in % wetness of the snow for each zone is given in figure 5.18 below.

The % wetness content is calculated from the value of the dielectric constant retrieved from the measured passive microwave data. The presence of ice would increase the predicted value of the dielectric constant and may account for the high values of wetness content in the dry zone.
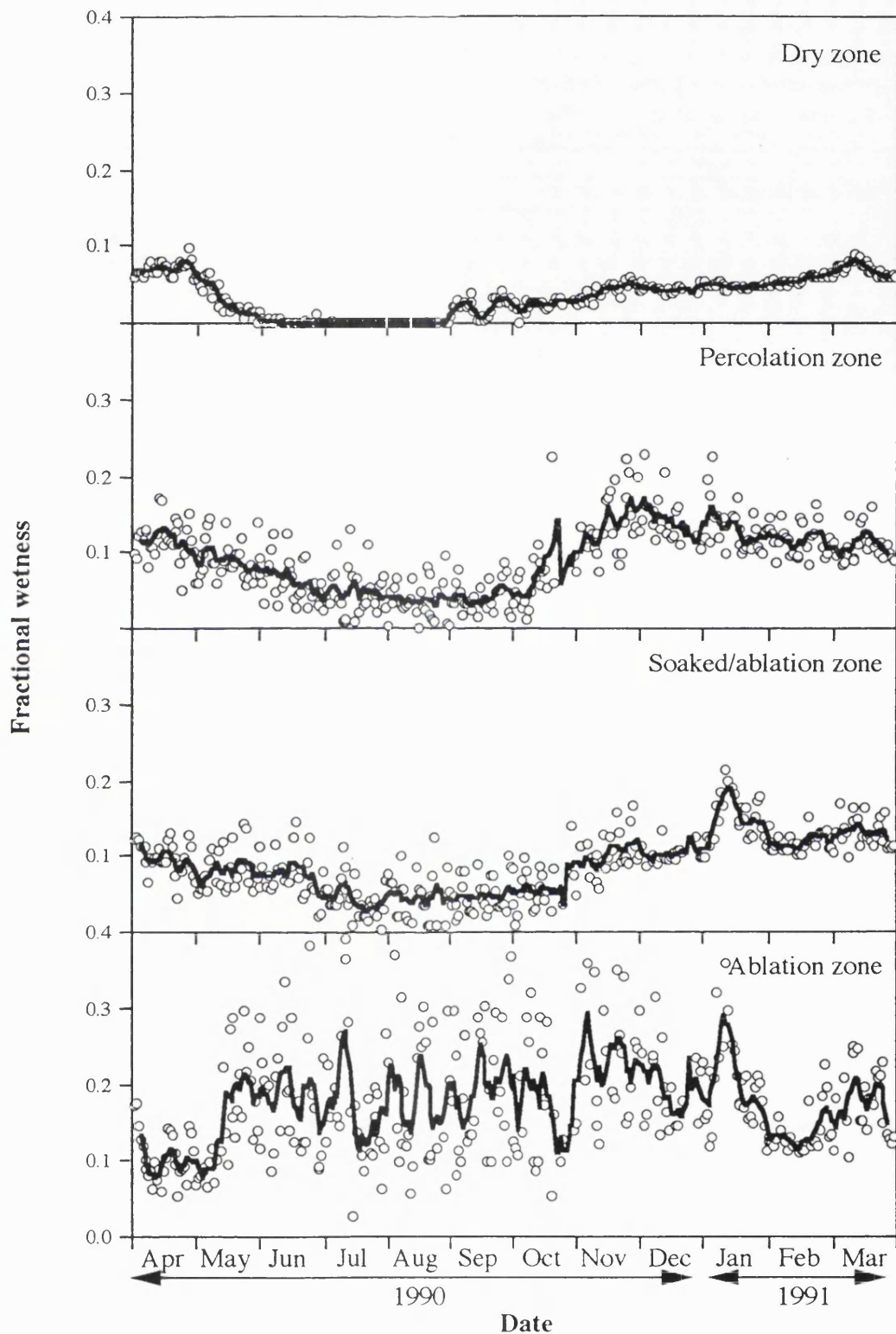
Figure 5.18: Annual variation of fractional wetness content of the snow for each zone, using 19GHz SSM/I data for the full year (April 1990 - March 1991). The points are daily averages and the lines are 7-day running means.

Wetness is a parameter derived from the calculated dielectric constant.

page 191

On increasing the water content of snow, the water first coats the surface of the ice particles within the snow, then occupies the air spaces between these particles. The mean % wetness content of snow may increase up to ~50% volume. During this time the physical nature of the snow becomes increasingly wetter and is seen to turn to slush.

The data for the ablation zone show a rapidly varying mean dielectric constant (and hence mean water content of the imaged snow) indicating that this area is undergoing several freeze/thaw cycles during this time. The data may be analysed further to determine the extent of surface water in the form of melt pools that would give similar emissivity values for the two polarizations as measured. The imaged area may be considered to consist of a mixture of both water covered surfaces of the melt pools and that of the surrounding wet snow. If the extent of the imaged area covered by surface water is represented by the fraction x, and the remaining area (1 - x) is considered to be of snow of water content 16% (typical value for ablation zone, Jezek *et al.*, 1993), then the measured brightness temperatures (and emissivity) of the imaged area may be represented by the following relationships:

for horizontal polarization:

$$x \, T_{Bh \, water} + (1 - x) \, T_{Bh \, snow} = T_{Bh \, mix}$$

similarly for vertical polarization:

$$x \, T_{Bv \, water} + (1 - x) \, T_{Bv \, snow} = T_{Bv \, mix}$$

giving:

$$\frac{T_{Bh \, mix}}{T_{Bv \, mix}} = \frac{x \, T_{Bh \, water} + (1 - x) \, T_{Bh \, snow}}{x \, T_{Bv \, water} + (1 - x) \, T_{Bv \, snow}}$$

If the surface temperature of the melting snow is considered to be the same as that of the surface water of the melt pools, the expression may be written in terms of emissivities E, rather than the brightness temperatures T_B, for each polarization
(h = parallel, v= perpendicular polarization):

$$\frac{E_{h \, mix}}{E_{v \, mix}} = \frac{x \, E_{h \, w} + (1 - x) \, E_{h \, s}}{x \, E_{v \, w} + (1 - x) \, E_{v \, s}}$$

where w = water, s = snow.

This expression may be re-written to give x as subject:

$$x = \cfrac{1}{\left\{ \left[\cfrac{\left(E_{vw}E_{h\,mix} - E_{v\,mix}E_{hw}\right)}{\left(E_{h\,s}E_{v\,mix} - E_{v\,s}E_{h\,mix}\right)} \right] + 1 \right\}}$$

or in terms of polarization ratios:

$$x = \cfrac{1}{\left\{ \left[\cfrac{E_{vw}\left(\cfrac{E_{h\,mix}}{E_{v\,mix}} - \cfrac{E_{hw}}{E_{vw}}\right)}{E_{vs}\left(\cfrac{E_{hs}}{E_{vs}} - \cfrac{E_{h\,mix}}{E_{v\,mix}}\right)} \right] + 1 \right\}}$$

The relative dielectric constant (Er_s) of snow of 16% wetness content at 19.2GHz is (using Mätzler mixing formula, equation 3.17):

$$Er_s = \frac{0.16}{0.2036} + 1.2 = 1.986$$

The effective dielectric constant (at 53.2° to correspond to SSM/I incidence angle) is:

$$Er_{effective\ snow\ \|} = 1 - \frac{(Er_{snow} - 1)}{\cos^2 \theta_0} = 3.7474$$

$$Er_{effective\ snow\ \perp} = \frac{Er_{snow}^{\ 2}}{Er_{effective\ snow\ \|}} = 1.0524$$

(using equation 3.4)

The Fresnel reflectivity at incidence angle 53.2° for snow of 16% wetness content is:

0.1016 for parallel polarization, and

0.000163 for perpendicular polarization,

giving an emissivity (E) of 0.8984 and 0.9998 for parallel and perpendicular polarization respectively.

The polarization ratio for the snow emissivities is given by:

$$\frac{E_{snow\ \|}}{E_{snow\ \perp}} = \frac{0.8984}{0.9998} = 0.8985$$

Similarly for water (w), dielectric constant Er~20 (at 19.2GHz):

The effective dielectric constant (at 53.2° to correspond to SSM/I incidence angle) is:

$$Er_{effective\ water\ \|} = 1 + \frac{(Er_{water} - 1)}{\cos^2 \theta_0} = 53.95$$

$$\text{Er}_{\text{effective water } \perp} = \frac{\text{Er}_{\text{water}}^{2}}{\text{Er}_{\text{effective water } \parallel}} = 7.414$$

The Fresnel reflectivity at incidence angle 53.2° for water is:

0.5781 for parallel polarization, and

0.2142 for perpendicular polarization,

giving an emissivity (E) of 0.4219 and 0.7858 for parallel and perpendicular polarization respectively.

The polarization ratio for the water emissivities is given by:

$$\frac{E_{\text{water } \parallel}}{E_{\text{water } \perp}} = \frac{0.4219}{0.7858} = 0.5369$$

The fraction x (area covered by water) may now be calculated from:

$$x = \frac{1}{\left\{ \left[\frac{E_{vw}\left(\frac{E_{h\,mix}}{E_{v\,mix}} - \frac{E_{hw}}{E_{vw}}\right)}{E_{vs}\left(\frac{E_{hs}}{E_{vs}} - \frac{E_{h\,mix}}{E_{v\,mix}}\right)} \right] + 1 \right\}}$$

using the measured value of Eh./Ev.mix of ~0.8 from the SSM/I data for zone 4 during melt, which gives:

$$x = \frac{1}{\left\{ \frac{[0.7858(0.8 - 0.5369)]}{[0.9998(0.8985 - 0.8)]} + 1 \right\}} = 0.3226$$

These calculations show that area covered by water is approximately 32% for this point in the ablation zone (using single pixel of SSM/I passive microwave data). The mean daily average value for the measured data is used in the above analysis.

The extent of water is calculated to be ~32% of the surface of the imaged area and that of the surrounding snow (taken to be of 16% wetness) is the remaining 68% of the area for the day when the polarization ration is 0.8. The mean value of polarization ratio over the year is 0.88 giving a mean wetness content of ~6%.

The formation of ice during the freeze/thaw routine would be an intermediate stage. The dielectric constant (Er) of ice is less than that for water, but greater than that for snow:

$$\text{Er}_{\text{snow}} < \text{Er}_{\text{ice}} < \text{Er}_{\text{water}}$$

and therefore the emissivity (E) of ice is between that of water and snow also:

$$E_{\text{snow}} > E_{\text{ice}} > E_{\text{water}}$$

The measured brightness temperatures (and emissivity values) for the intermediate ice stage lie between the minimum values of emissivity (corresponding to maximum melt) and the maximum values (driest snow). The measured brightness temperature fluctuates rapidly during the freeze/thaw cycles in the ablation zone during summer as the emissivity of water is greatly different to that of snow. These diffusely scattered points for the measured brightness temperature data of the ablation zone are shown above in figure 5.17.

5.2.3 Correlation with AIRSAR overflight.

10th June 1991 is the date of the AIRSAR flight. The mean daily brightness temperatures for the four different areas as measured by the SSM/I instrument for this particular day are given in table 5.5 below and used for the comparison work with the active AIRSAR data.

Polarization ratio for Greenland ice sheet zones:

zone:	(1)	(2)	(3)	(4)
T_{Bh}/T_{Bv}:	0.989	0.950	0.953	0.881
Er:	1.20	1.53	1.51	2.16
W:	0%	6.7%	6.3%	19.6%
C band Er:	1.66	2.86	2.79	5.17
P band Er:	1.66	3.20	3.11	6.16

Table 5.5: Measured mean daily polarization ratio (19 T_{Bh}/T_{Bv}) for points 1-4 on 10.6.91; with the calculated mean values of dielectric constant (Er) and the corresponding % wetness content (W).

Values of the real part of the dielectric constant for snow of 6% wetness (by volume) given by Rott et al. (1992) and Jezek et al. (1993) are given in table 5.6:

Dielectric constant of snow:

	C band	P band
Jezek (6%)	2.08	2.26
Rott (6%)	2.95	3.25
calc.value (for 6.3%)	2.79	3.11

Table 5.6: Values of the real part of the dielectric constant for snow of 6% wetness (by volume) given by Rott *et al.* (1992) and Jezek *et al.* (1993) and calculated values from table 5.5.

These values of calculated dielectric constant Er (at C and P band) lie between the values given by Rott *et al.* (1992) and Jezek *et al.* (1993) for approximately the same water content (6%) and are therefore assumed to give a typical representation of the electrical properties of the snow.

5.2.4 Signal during Spring - Summer seasons.

The passive microwave mean daily brightness temperature data for the period April - June 1991 for the four zones are plotted in figure 5.19, giving the change of the mean daily brightness temperatures for the four different zones of the ice sheet with the progression from spring into summer at the start of the melt season (for both horizontal and vertical polarization, 19 and 37GHz SSM/I data).
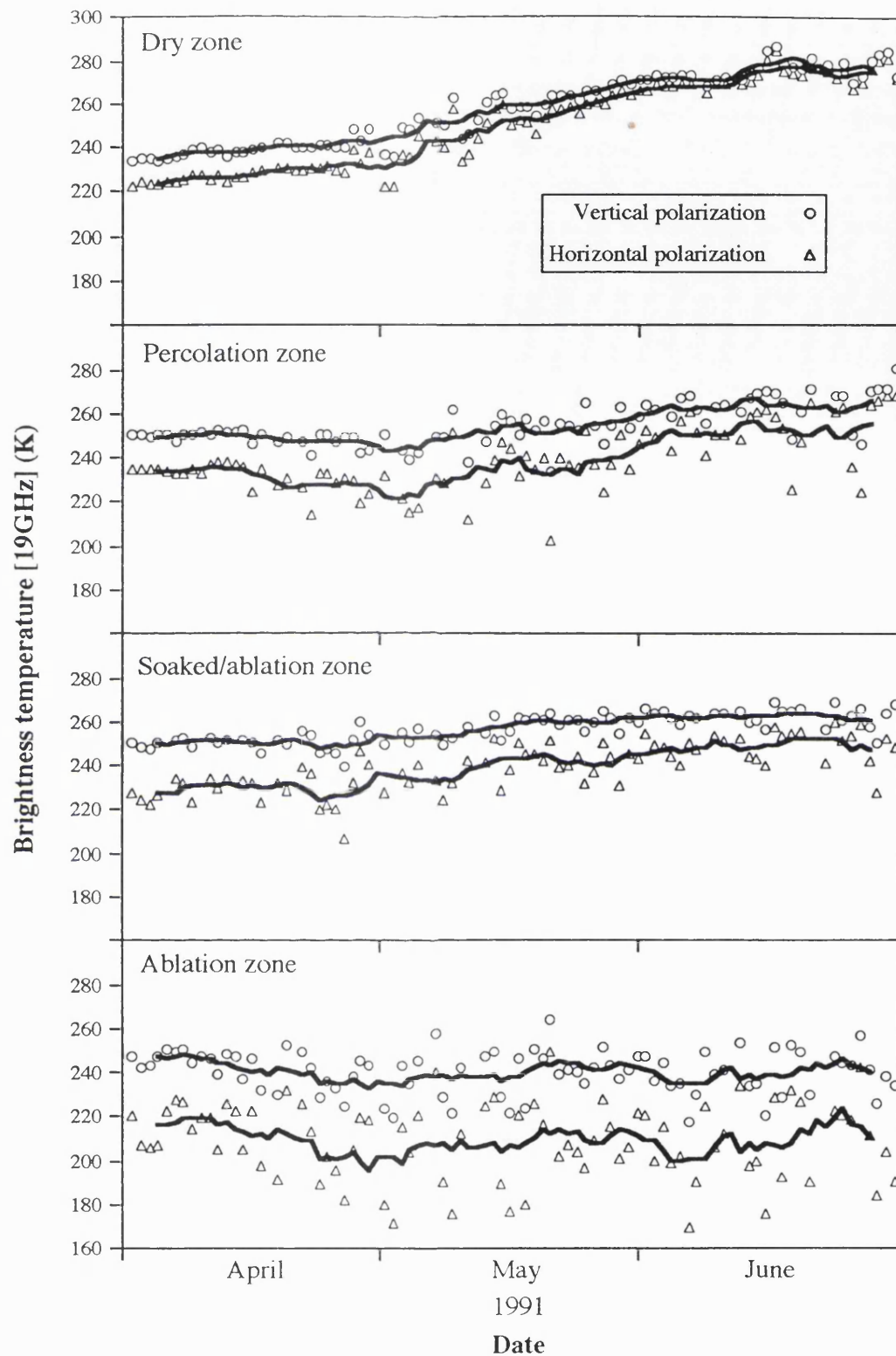
Figure 5.19 i): Mean daily brightness temperature (T_{Bv}, T_{Bh}, 19GHz SSM/I data) for the four zones of the Greenland ice sheet (April - June 1991). The points are daily averages and the lines are 7-day running means.
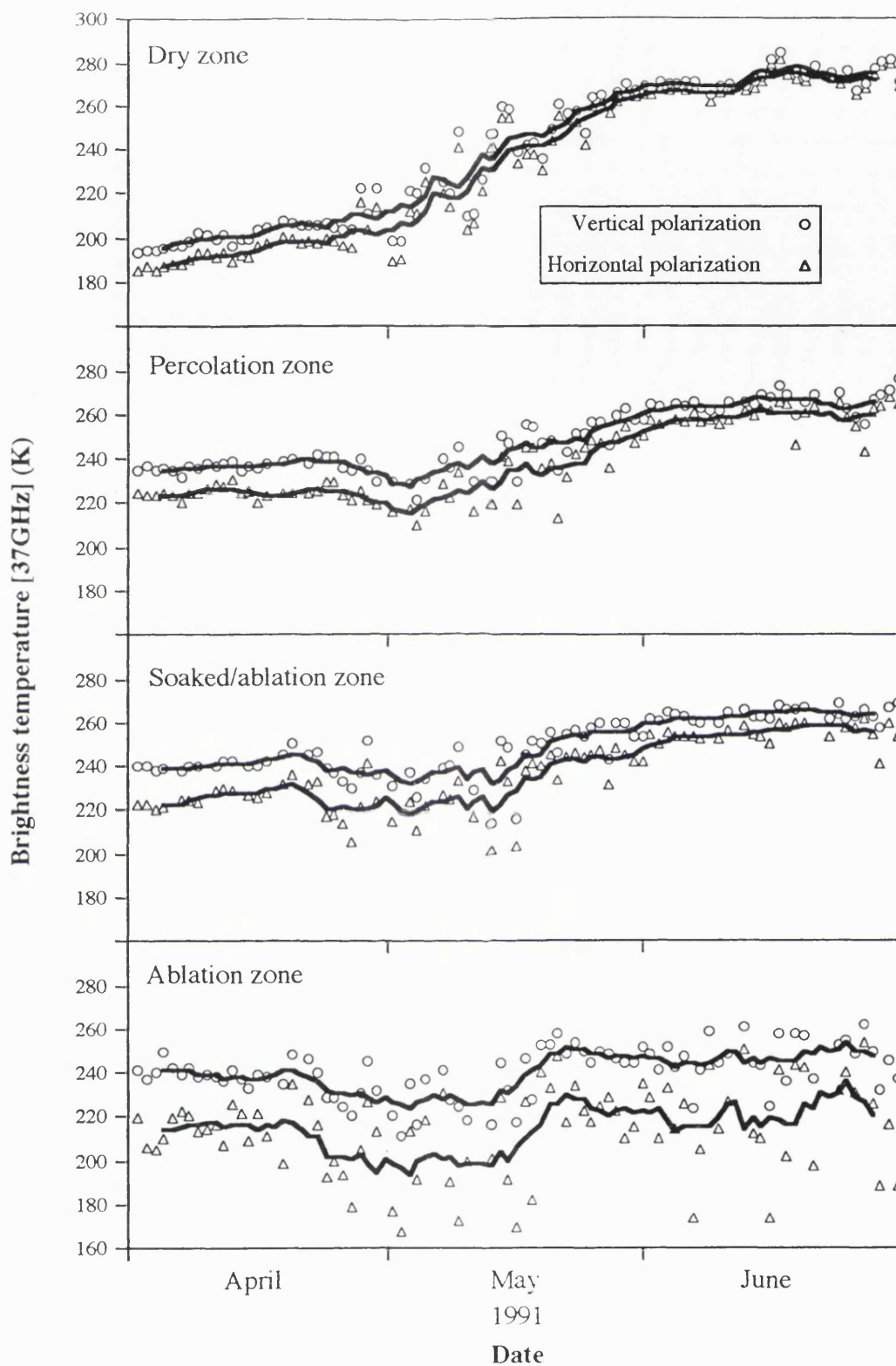
Figure 5.19 ii): Mean daily brightness temperature (T_{Bv}, T_{Bh}, 37GHz SSM/I data) for the four zones of the Greenland ice sheet (April - June 1991). The points are daily averages and the lines are 7-day running means.

In general the values of the mean daily brightness temperatures for horizontal polarization are less than that for vertical polarization; and those for 19GHz data are greater than for 37GHz. For both the 19GHz and 37GHz data, the values increase with the progression of date into summer (during the period April to June 1991) corresponding to the increase in temperature during this time.

The above plot (19GHz data, figure 5.19 i)) shows that the dry zone shows the greatest change of values (~linear rise). The data for the percolation and soaked/ablation zones show similar values, but are more scattered than those for the dry zone and also show less change with date. The data for the ablation zone have the lowest and most scattered values of brightness temperatures. A similar pattern is found for the 37GHz data, but with the values less for 37GHz than for 19GHz data.

There is more variation (spread of data) in the measured brightness temperature values with the increase in % wetness of the snow (corresponding to the position down the ice sheet). The wetter areas also show a more gradual change with date.

The data for the previous year (April - June 1990) are also analysed and found to be similar to the 1991 data.

5.2.5 SSM/I data, difference with frequency, (19-37)T_{Bh} and (19-37)T_{Bv}.

The differences in the mean daily brightness temperatures for the SSM/I data at the two frequencies 19 and 37 GHz, for both horizontal and vertical polarization, are plotted as (19-37)T_{Bh} and (19-37)T_{Bv} in figure 5.20 below. Data for the four zones of the Greenland ice sheet are given for the complete year covering the period April 1990 - March 1991.

The full year data set shows that the difference with frequency decreases for the wetter regions of the ice sheet, and also shows a drop in the level during summer. This is due to the 19 and 37 Ghz channels recording similar values of brightness temperatures for the wetter areas as the penetration is minimal if free water is present. Both the 19 and 37GHz signals then record the similar surface values.

The data for the dry zone also shows a vast drop in level (19-37)T_{Bv}, T_{Bh} during summer. This seems to suggest that the dry zone experiences some change of state also.
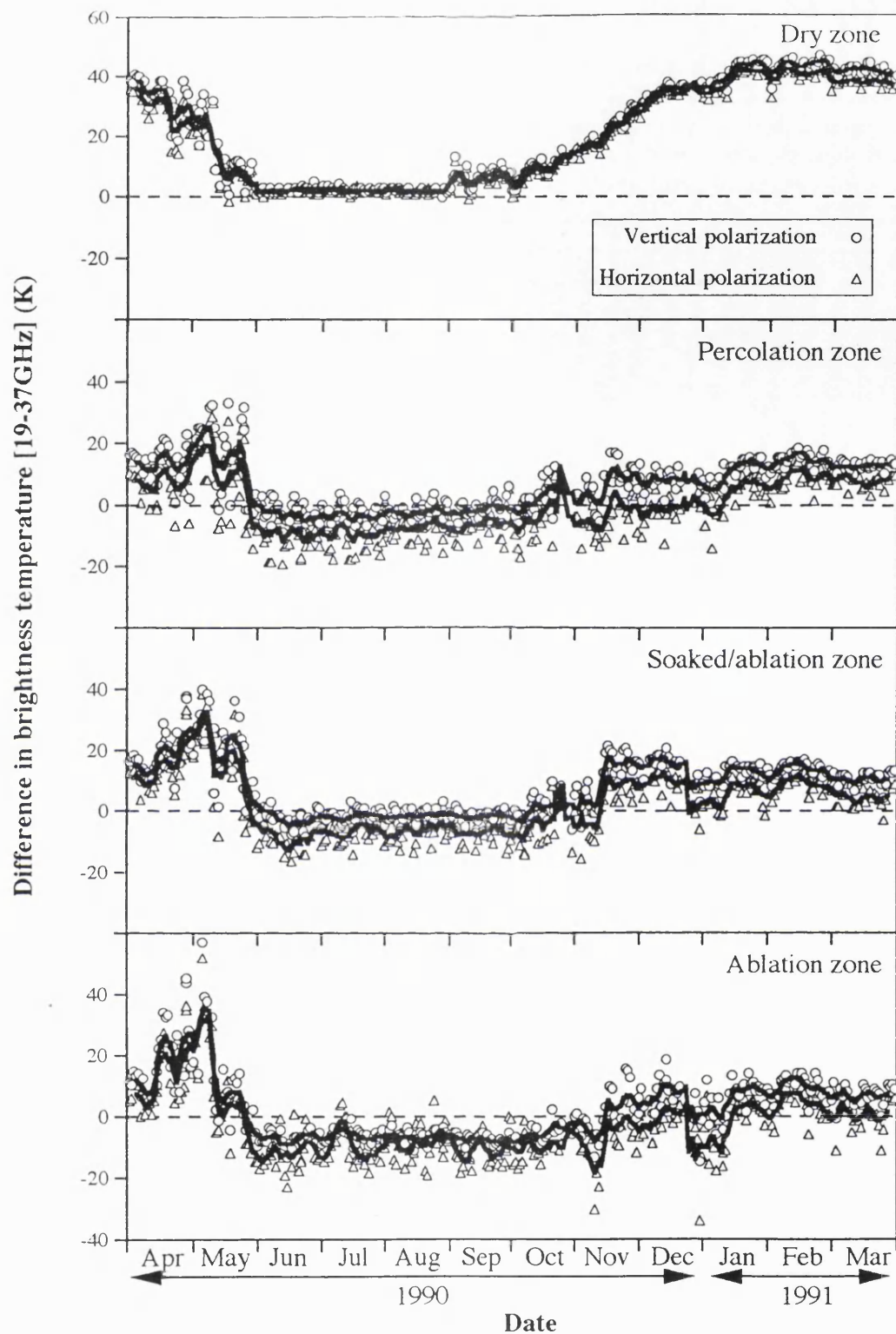
Figure 5.20: Brightness temperature differences with frequency for both horizontal and vertical polarization, (19-37)T_{Bv} and (19-37)T_{Bh}, for the four zones of the ice sheet for the full year (April 1990 - March 1991). The points are daily averages and the lines are 7-day running means.

5.2.5.1 Signal at start of melt season (April - June 1991 data).

The measured brightness temperature data for the four zones of the Greenland ice sheet are also investigated in detail for the period April - June 1991. The difference in the mean daily brightness temperatures for the SSM/I data at the two frequencies for both horizontal and vertical polarizations for this period is plotted in figure 5.21 below.

The value of the difference in the brightness temperatures at these two frequencies is greatest for the dry zone and decreases for the other zones with increasing snow wetness content (and with the position down the ice sheet). The start of the melt season appears as a sudden change in level for the dry zone (sudden decrease), and is noted by peaks and gradual fall in the frequency difference data for the other three zones, both for vertical and horizontal polarization.
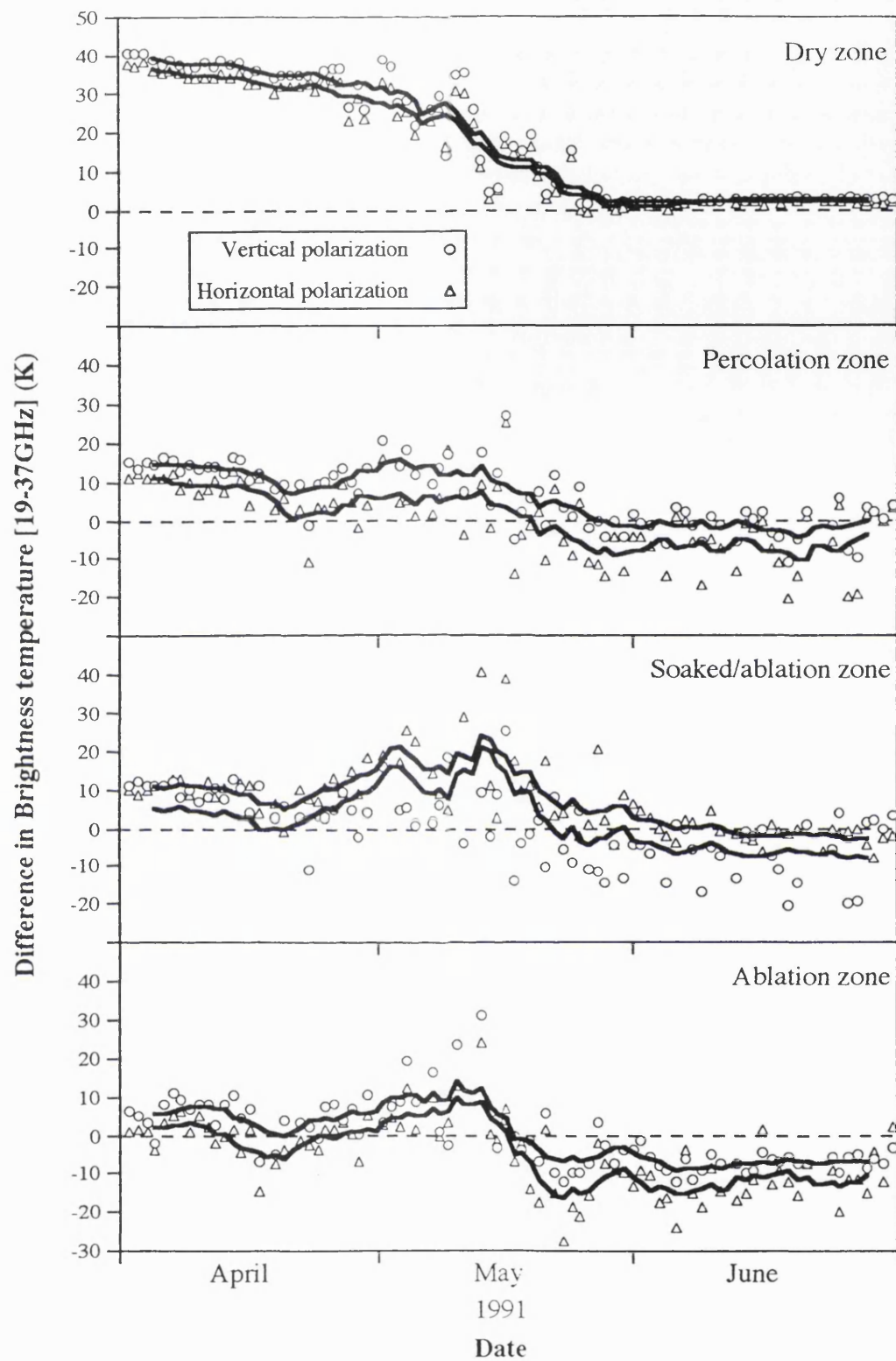
Figure 5.21: Mean daily brightness temperature (T_{Bv}, T_{Bh} , SSM/I data, 19GHz, 37GHz) for the four zones of the Greenland ice sheet (April - June 1991) plotted to show the difference with frequency. The points are daily averages and the lines are 7-day running means.

Plots of the individual brightness temperatures for vertical and horizontal polarizations at 19 and 37 GHz for this period for each of the zones are given previously in figure 5.19.

The dry zone clearly shows the difference in the brightness temperatures for the two frequencies during April (19GHz data from warmer subsurface snow, 37GHz data from colder surface material) and then shows the change in levels as the snow becomes warmer during May, and the two frequencies record similar values by June.

The data for the percolation, soaked and ablation zones respectively show peaks in the difference with frequency during this period.

The individual brightness temperatures for the two frequencies show a steady increase in values for 19GHz data due to the increase in physical temperature, and the 37GHz data show a brief fall in values, therefore producing the peaks in the T_B(19-37) data.
A decrease in the 37GHz T_B data may be due to the top surface snow beginning to melt (emissivity decreases with increase in moisture content) in part of the imaged area. The 37GHz radar is more susceptible to changes in the surface dielectric than the 19GHz radar (due to the difference in penetration depth) and so the 37GHz data shows a more marked change than the 19GHz data. As the days proceed the areal extent of this partial localized increase in moisture content due to surface melting from changes in the daily physical temperatures at the surface varies (from the freeze/thaw cycle due to local temperature changes) until the physical temperature increases sufficiently to cause a uniform surface moisture content. At this point the data for the two frequencies becomes more similar and the value of T_B(19-37) decreases.

Similar results are found for the data for the previous year (April - June 1990), except that the data for the dry zone shows larger peaks than for the 1991 data.

The results indicate that probably this effect happens every year, during spring, at the onset of melt and it occurs for both polarizations. The dry zone shows a greater drop in T_B(19-37) data than for the other zones, and the wetter regions show large peaks in the data which are most noticeable for zone 3 (soaked/ablation zone).

5.2.6 Effect of ice layers on passive signal.

The effect of ice layers on the passive response from the imaged surface would be to reduce the received power of the emitted signal. Ice is of a higher dielectric constant than snow and so the reflectivity of ice is greater than that of snow, and hence the emissivity of ice is less than that of snow.

This effect is noted for the passive microwave SSM/I data of the dry zone during the winter season as discussed in section 5.2.2.2. The seasonal formation of a surface crust of ice due to localized wind conditions causes the emission from this zone to decrease.

The measured brightness temperatures for the percolation zone are less than that for the dry zone throughout the year (figure 5.15, section 5.2.1), and the measured polarization ratio for the percolation zone is also less than that for the dry zone. This data indicates higher dielectric material in the percolation zone than in the dry zone. This higher value of dielectric is caused by the % wetness content of the snow being greater in the percolation zone than in the dry zone, and also may indicate the presence of higher dielectric ice. The presence of subsurface ice layers in the percolation zone - caused by the melting of snow and subsequent percolation of this melt water through the snowpack then refreezing at depth, or alternatively from the production of large ice crystals at depth in the formation of depth hoar -will act to decrease the emissivity of the snowpack of the percolation zone and therefore decrease the value of the measured passive signal. The formation of the subsurface ice layers occurs during late summer/ autumn when the summer melt water refreezes at depth. This corresponds to a decrease in the measured polarization ratio for the percolation zone during this season.

The radiometric data as measured by Swift *et al.* (1985) as discussed in chapter 1, section 1.3.2.2, using an airborne system flying across Southern Greenland (Oct.1979), show that the measured passive signal is less over the percolation zone than over the dry zone due to the presence of ice in the percolation zone. This is consistent with the effect noted using the SSM/I data set as discussed above (section 5.2.1).

It is important to note that the effect of the presence of ice layers acts to increase the level of the backscattered signal for active microwave radar. This is the opposite effect to that shown by data from the passive systems, where the presence of ice acts to decrease the measured signal. This may be explained by considering the increase in dielectric constant due to the presence of ice; the increase in reflectivity and the corresponding decrease in

emissivity of the snowpack, resulting in an increase in the level of the backscattered active radar signal and a decrease in the measured passive emitted microwave signal. Volume scattering within the snowpack also increases with the presence of the ice layers which further acts to increase the active signal and reduce the emitted signal from the snowpack.

6 Discussion and Conclusions -

6.1 Active microwave data results.

6.1.1 Polarimetric imagery.

It is well known that multifrequency radar imagery exhibits return power dependence on the operating frequency of the radar. The total power images of the ice sheet as measured by the multifrequency AIRSAR instrument show that the return power from each zone is dependent on the operating frequency. In general, it is found that the higher the frequency, the greater the return signal for all the imaged areas of the ice sheet (return power for C band > L band > P band). The value of the return power for each image is also found to vary with the incidence angle. The return power tends to decrease as the incidence angle increases from nadir. These results are consistent with published data on the return signal from snow by Ulaby and Dobson (1989).

Some of the highest measured values of return signal are found to occur for the percolation zone and the lowest for the dry zone of the ice sheet. The AIRSAR values show ~-18dB difference between the measured (VV polarization) return signal (C band) at ~20 degree incidence for these two zones. The values of the return power measured by the AIRSAR instrument are found to compare well with that of the ERS-1 SAR over the same area, showing the correlation between airborne and satellite data over the ice sheet. These results are noted by Jezek (1992).

Investigation of the use of polarimetry shows that some features of the ice sheet are apparent only for a particular combination of incident and receive polarization states. The polarimetric images as measured by the multifrequency AIRSAR show that the dry zone images are fairly uniform and featureless for all three frequencies. The images of the percolation and the soaked/ablation zones, however, show features which are both frequency and polarization dependent (apparent for HH polarization and P band radar only). The images of the ablation zone show features which appear to be mainly independent of polarization, but decrease in clarity with increase in the operating frequency of the imaging radar.

The features of the multifrequency radar images are thought to indicate the presence of subsurface ice layers in the percolation zone, and ice streams in the soaked and ablation zones. The low frequency (P band) radar identifies these subsurface discontinuities more

clearly due to the greater penetration depth at this frequency (compared with L and C band).

The polarization dependence of the subsurface discontinuities of the P band percolation and soaked/ablation zone AIRSAR images may be related to the orientation of the scatterers. Horizontal ice lenses could cause the measured change in the return radar signal. Alternatively, as the value of the transmitted signal into the snowpack is greater for vertical than horizontal polarization (for active signals) the value of the transmitted horizontally polarized signal will decrease more rapidly than the vertically polarized signal. However, displaying the polarimetric images with the same scale factor still does not show the features for VV polarization although they remain apparent for HH polarization.

The presence of the discontinuities may be related to the bedrock topography as melt is likely to occur in localized depressions of the ice sheet which can correspond to undulations in the bedrock. Similarly, surface and subsurface ice streams will form in depressions of the ice sheet and at localized discontinuities within the snowpack. The direction of flow of these streams as they travel through the low density ice and wet snow may possibly be related to the surface slope of the ice sheet. An estimation of the ice velocity and flow rate of the ice sheet could be made by considering the movement of the discontinuities within an imaged area over a period of time using multitemporal data of the same area.

The orientation of the AIRSAR images and the location of the various features within the HH polarization P band images are given in chapter 5 (figure 5.2). The surface slope is estimated using the slopes database from ERS-1 radar altimeter data with a resolution of $25*25km^2$ (J. Morley, personal communication). It should be noted that this is the mean value for a larger area than that covered by the airborne SAR images ($12*8km^2$), and so the local value of the slope and the downslope direction of the area covered by the AIRSAR images may be rather different to the estimated value using the radar altimeter data. The value of the estimated slope at the position of the images for each zone increases on descent of the ice sheet, from the dry central zone ($< 0.1^o$ slope) to the ablation zone (6.47^o slope) at the edge of the ice sheet.

The estimated slope of the percolation zone image is small (0.36^o) and the imaged features (two series of dark circular patches) are orientated in the direction 40° and -6° from North. The orientation of these features - thought to be subsurface effects, possibly smooth subsurface ice layers from the localized collection of melt water - does not seem to

be related to that of the surface slope (direction 16.5° from North). The direction and value of the local surface slope for the high resolution AIRSAR imaged area, however, may be different to the mean value given by the lower resolution radar altimeter data.

The features of the soaked/ablation zone image are thought to indicate the position of subsurface ice streams. The dark patches may indicate the presence of smooth subsurface ice of higher dielectric constant (or increase in water content of the snow) which causes specular reflection away from the receive direction, causing a decrease in the measured return power. The dark central line lies in a direction approximately parallel to that of the mean surface slope (value 0.68°, in direction -51.1° from North), whereas the dark areas at the far edge of the image seem to lie in a direction approximately perpendicular to that of the estimated slope. This dark central line appears to be an icestream following the local gradient of the ice sheet. The other dark areas may indicate the location of the subsurface collection of melt water.

The features of the ablation zone image include the bright circular areas (visible for P and L band, but not for C band) and the central linear feature (apparent for all frequencies). The circular bright areas may indicate subsurface discontinuities, strongly reflecting towards the receive antenna. The central linear feature is visible for all three frequencies (increasingly apparent using lower frequencies) showing the presence of a near surface discontinuity, possibly a melt stream. The orientation of this central linear feature is in approximately the same direction (45°) as the estimated surface slope (value 6.47°, direction 49°). The flow of the stream is therefore seen to be in the same direction as the surface slope.

An estimation of the ice velocity and flow rate of the ice sheet may be made by considering the movement of the discontinuities within an imaged area over a period of time using multitemporal data of the same area when available. This information of the surface state of the ice sheet in the different zones, and the ice velocities, is important in studies of the temporal changes of the ice sheet which may be found to indicate climate change. Knowledge of the surface velocities of the ice sheet is important for calculating the dynamics of the ice sheet, and for determining the ablation rate which is useful for mass balance studies.

6.1.2 Polarization response and scattering mechanism.

The basic shape of the 3D polarimetric radar response gives information on the dominant scattering mechanism. For each of the snow surfaces studied over the Greenland ice sheet the dominant scattering mechanism as measured by the AIRSAR instrument is found to be direct scattering for the near regions of the images. Much of the incident wave penetrates the snowpack and is attenuated within the layers and scattered further at boundaries and by discontinuities.

The shape of the measured 3D polarimetric response for the AIRSAR images of the different zones of the ice sheet are found to vary with the incidence angle and with the operating frequency of the radar. A summary of the different 3D polarimetric plots for the measured AIRSAR data for the different zones of the ice sheet is given in figure 5.9.

For a distinct region at the near edge of the majority of the images, direct scattering is the main mechanism. Direct scattering is also found to be the dominant form of the radar response for the percolation zone, for all the different frequency images of the region, independent of the incidence angle. The polarimetric response for the far edge of some of the images for the other zones show the return to be of the form associated with that from a rough surface. This tends to occur only for higher frequencies and for high incidence angles, and are for low power signals. The level of the pedestal (amount of diffuse scattering) is found to increase with frequency and with the value of incidence angle. The diagram given in figure 2.5 shows the typical scattering mechanisms for glaciated surfaces. The types of scattering mechanisms as illustrated in this figure may be referred to the different zones of the ice sheet as previously described in section 2.1.3.

For the dry snow of zone 1 diffuse volume scattering from within the low permittivity snow is the expected scattering mechanism. This is apparent in the measured data as the pedestal height (which indicates diffuse scattering) of the polarimetric response increases for the higher frequency data and for high values of incidence angle (at the far edge of the image). The double-dip response noted for the dry zone (for C band and high incidence angles) is thought to be caused by the low power of the return signal for this zone.

For the percolation zone, the presence of ice lenses causes a high power return signal. The form of the measured polarimetric response for all frequencies and all incidence angles is that of a single dip which indicates direct scattering. The presence of cylindrical ice lenses within the snowpack can also cause this shape of polarimetric response (see figure 2.12 for the theoretical response for cylindrical objects and figure 5.13 for

measured data from P band image of percolation zone).

The wet snow of the soaked/ablation zone is of higher reflectivity than the dry snow of zone 1, so surface scattering becomes more dominant and the received power of the return signal is greater than that for the dry zone as shown in figure 5.4. The value of the return power is greater for the wetter snow (of zone 3) than for the dry snow (of zone 1) and the shape of the response is generally that of a single dip, showing that the main scattering mechanism is direct scattering. The normalized plots of the polarimetric response show that the height of the pedestal increases with frequency and with incidence angle indicating the increase in the diffuse scattering component with increasing frequency and incidence angle. A slight hump is noted for the 3D plot for C band at the far edge of the image. This indicates that the relatively low power return signal for the C band radar at this higher incidence angle is jointly from rough surface scattering and the high pedestal indicates the contribution from volume scattering within the snowpack.

The data for the ablation zone image show that the polarimetric response indicates direct scattering for the near edge of the image, then rough surface scattering as the incidence angle is increased. The pedestal height (diffuse scattering component) increases with frequency and incidence angle.

The polarimetric response for the 233-1 image in the ablation zone is of the same form as that for double bounce scattering. The shape of the response is probably due to the low return power of the signal. However, a distinct surface layer with vertical discontinuities could cause this effect. This may be caused by a thin layer of saturated snow above the ice, a thin layer of ice over the melt pools or on the snow surface, or a distinct surface frost layer. The seasonal melt pools give surface water which causes direct scattering of the incident wave in the specular forward direction away from the receive direction of the radar, and therefore a low power return signal is received. As this shape of response is noted for very low power signals (using theoretical computed values), care must be taken to determine the correct scattering mechanism.

The polarimetric response for the dry zone for high incidence angles shows rough surface scattering for P band and double bounce for both L and C band for data at the far edge of the image. This effect could be caused by the presence of a wind roughened surface. The local wind conditions cause ridges (sastrugi) to form on the snow surface and these are of increasing amplitude and smaller distance apart with increasing wind speeds. Typical sizes of the height and distance apart of these ridges are 200mm, 1m for strong wind and 50mm, 10m for less wind. For C, L and P band radar the operating wavelengths are

56mm, 250mm and 750mm respectively. For the surface to appear rough the Rayleigh criterion (equation 2.12) requires the mean surface heights of the surface to be greater than 7.52, 33.24, 99.76mm for C, L and P band respectively for 20° incidence (i.e. at the near edge of the image) and 14.16, 62.52, 187.52mm for the far edge of the image. Sastrugi with amplitudes of 200mm (strong wind) would appear rough for P band, and may be rough enough to cause double bounce scattering for both L and C band. The distance between the ridges (~1m for strong winds) is also great enough (>λ radar) for a coherent signal to be retained for L and C band radar. The P band polarimetric response then shows the single "hump" for rough scattering and the L and C band response would show the double dip form, indicating double bounce scattering. This is found for the data at the far edge of the dry zone image. However the same effect should also be found at the near region of the image which is not the case for this data set. It is thought that the shape of the double dip measured co polar response for the dry zone is simply due to the low power of the received signal as discussed above.

The potential of using the multifrequency polarimetric data to indicate the presence of sastrugi on the surface of the ice sheet is, however, illustrated by this analysis.

The polarimetric data of the different zones of the ice sheet as measured by the AIRSAR enable the different scattering mechanisms to be determined for the various types of snow and ice surface encountered in the different zones of the ice sheet. The variation in the scattering mechanisms for the different zones with both frequency and incidence angle is investigated. This knowledge of the type of scattering and the relative importance of each mechanism increases the understanding of the radar response of the polar surfaces.

6.1.3 Polarimetric response and snowpack characteristics, including subsurface ice layers.

The theoretical 3D polarimetric response plots show that the shape of the polarimetric response depends on the dielectric constant of the surface and subsurface material and that they change with the value of incidence angle and operating frequency of the radar. The response is dependent on the depths of the various surface and subsurface layers, so the position of, for example, a subsurface ice layer beneath a surface layer of dry snow is found to affect the response. The theoretical response for snow surfaces is found to correlate well with measured data of the percolation zone (figure 5.14).

A possible new method of determining the dielectric constant and potentially the depth of

layers from the polarimetric signal is investigated. This polarimetry work involves comparing the power ratio and phase difference of the HH and VV components of the measured return signal. The theoretical polarimetric response of different dielectric materials to represent the various types of polar terrain (for example: water, pure ice and snow of different wetness content) is analysed and the results indicate that the polarimetric content of the coherent part of the received signal may be used to indicate the dielectric constant and hence type of surface of the imaged terrain. High dielectrics have a high polarization ratio, VV/HH (for active radar signals), and low dielectrics have a lower polarization ratio.

This classification method is applied to the measured AIRSAR polarimetric data over the ablation zone (233-1 image). This image shows distinct dark regions which are thought to indicate the location of melt pools on the surface of the ice sheet. Smooth water specularly reflects the incident radar away from the receive direction and so low power is returned, causing a dark area on the image which represents the location of the melt pools. The surrounding snow scatters the incident wave and the return signal is therefore greater than that for the melt pools, and so the snow surface shows as brighter areas on the AIRSAR image. The high dielectric constant of the water causes a high polarization ratio for the active signal, and the lower dielectric constant of the snow gives a lower polarization ratio. By comparing the measured polarization ratio for the different areas of the image with the theoretical values for different dielectrics for the particular incidence and operating frequency, the dielectric constant of the imaged terrain may be inferred from the measured polarimetric signal. The imaged area may then be classified into the typical type of terrain. This classification method successfully distinguishes between the different areas of the 233-1 ablation zone image, indicating the high dielectric melt pool areas and the lower dielectric saturated snow areas. This method of classification requires no initial knowledge of the type of terrain.

In this way the surface state of the ice sheet may be determined; for example, the presence of melt pools and the extent of snow covered areas may be measured over the ice sheet, giving information on the ablation rate. It may also be possible to infer the depth of the surface layer and the position of subsurface discontinuities; for example, the position of a subsurface ice layer beneath the surface layer of firn (dry snow) in the percolation zone of the ice sheet may be measured as discussed below. This method may be useful in monitoring the accumulation rate of the ice sheet by indicating the different layers in the snowpack corresponding to the variation in snowfall and different localized conditions.

The radar signal from the different zones depends on the state of the snowpack within the

imaged region. In the cold, dry zone the snow is of low dielectric constant and therefore much of the incident radar signal is transmitted into the snowpack where diffuse volume scattering occurs. In the percolation zone the radar signal penetrates through the surface layer of firn (snow of a low dielectric constant) and a strong reflected signal is recorded from the snow to ice discontinuity at the most recent subsurface ice layer (of higher dielectric constant). For both the soaked and ablation zones the wetter snow is of higher dielectric constant and the radar signal is strongly attenuated.

The strong reflected signal from the subsurface ice layer in the percolation zone may be explained by the coherent backscatter effect (Hapke, 1990; Hapke and Blewett, 1991). Coherent backscattering can produce a strong radar signal when the scattering inhomogenieties are of a size comparable to (or larger than) the operating wavelength of the radar (Peters, 1992), and the refractive index of the scatterers is less than 1.6 (or the dielectric constant Er < 2.56) (Mishchenko, 1992). Rignot *et al.* (1993) suggest that this coherent backscatter effect may explain the strong radar signal recorded by the AIRSAR over the percolation zone of the Greenland ice sheet for a range of incidence angles up to 40°.

The effect of a strong subsurface scatterer on the return radar signal may dominate the radar response. Ground radar measurements at the test-site in the percolation zone by Jezek and Gogineni (1992) show that subsurface ice layers are the major source of the reflected radar signal, for both C and Ku band.

The position of a subsurface layer within the snowpack is found to affect the polarimetric signal received. The theoretical variation of the polarimetric signal is computed by modelling the effect of changing the position of a subsurface ice layer within snowpack. The results from the comparison of measured AIRSAR data with the theoretical signals show that it may be possible to determine the position of ice layers within snowpack from the polarimetric content of the measured return signal. As an example, the measured AIRSAR data of the percolation zone for a line average of data (@~20° incidence angle) are used to compare with the theoretical computed response. The VV/HH power ratio and VV-HH phase values of the measured data are found to correspond to a subsurface layer of ice at a depth of 450mm within the snowpack by comparison with the theoretical data (figure 5.14). The snowpit data from the test-site show that there is a distinct ice layer at this depth (figure 4.2). The theoretical computed signal for a subsurface ice layer is seen to correlate with the measured AIRSAR data and also agrees with the ground truth information as measured by the field party at the test-site. The potential of using the polarimetric data as measured by the AIRSAR to indicate the existence and position of ice

layers within the snowpack is therefore shown. This correlation of the remotely sensed airborne data with the theoretical computer model and ground truth information of the surface and subsurface snowpack material show that the polarimetric AIRSAR data may be used to indicate the dielectric constant of the imaged terrain and also, potentially, the position and content of subsurface layers.

This use of the AIRSAR system can assist with terrain classification and mapping purposes. This information gained from the various zones of the ice sheet, particularly from temporal studies over the ice sheet to show changes in the seasonal extent of each zone, and any changes from year to year, is important for climate related studies.

6.2 Passive microwave data results.

6.2.1 Brightness temperatures.

The passive emitted radiation from each of the four zones of the ice sheet is determined for a complete year of data, showing the effect of seasonal changes on the passive microwave response for each location. The measured values of brightness temperatures depend on the emissivity and the temperature of the snowpack and follow the quasi-sinusoidal annual cycle of the surface temperature changes, with the highest values of brightness temperature being recorded in the summer, and the lowest in the colder winter months (section 5.2.1).

The brightness temperature values decrease for the different zones of the ice sheet, with the highest values for the dry zone and the lowest values for the wetter zones on descending the ice sheet. This decrease in the measured brightness temperature with descending location on the ice sheet is due to the emissivity changes with increasing moisture content of the snow. The dielectric constant for wet snow is higher than that for dry snow, and hence wet snow has a lower emissivity, and therefore a lower brightness temperature.

The measured brightness temperature data for the dry zone are more compact and show a smooth annual change, whereas that for the wetter areas of the ablation zone are more diffusely distributed. This is due to the lower emissivity of the wetter areas and the partial melting and refreezing of the imaged area causing a variation in the measured brightness temperatures for the wetter areas.

The difference in the measured brightness temperatures for 19 and 37GHz for the dry zone are greatest in winter, when $T_{B19} > T_{B37}$ due to the thermal capacitive effect of the snowpack. This difference in the values for the two frequencies is due to the increased penetration of the 19GHz signal into the deeper warmer snowpack layers during the winter months as the dry snow is of low dielectric constant. The 37GHz data simultaneously records the colder surface values (section 5.2.1).

6.2.2 Passive polarimetric signals, dielectric constant and wetness content of snow.

The difference in the measured data for the two polarizations is greatest for the wetter areas (zones 3 and 4, the soaked and ablation zones) as the mean dielectric constant to represent the wetter snow of these areas is greater than that for drier snow. The measured polarization ratio from the brightness temperature data for the two linear polarizations (T_{Bh}/T_{Bv}) may be used to predict the mean dielectric constant of the imaged surface. An inversion technique is developed to infer the mean % wetness content of the snow (W) directly from the polarization ratio (T_{Bh} / T_{Bv}) of the measured passive microwave signals (section 3.4).

The highest values of polarization ratio are noted for the dry zone during spring. This indicates the very low dielectric constant of the cold dry snow imaged over this area during these months. The lowest values of polarization ratio are noted for the wetter areas during the summer months due to the increasing water content causing the dielectric constant to increase and the measured polarization ratio of the passive signals to decrease. The annual change in polarization ratio and the mean % wetness content of the snow is analysed for each of the zones of the ice sheet using a complete year of data (figures 5.17 polarization ratio, and 5.18 mean % wetness content).

For each of the zones the mean % wetness increases during the summer months due to an increase in the dielectric constant of the snow. It then decreases during the winter and spring months. The data for the ablation zone show a rapidly varying mean dielectric constant (and hence mean % water content) of the snow, indicating that it is experiencing melt conditions (rapid freezing and thawing of the surface). The data are analysed further to calculate the extent of the surface water in the form of melt pools by considering the measured SSM/I data of emissivity for the two polarizations. The area covered by surface water for this data set is calculated to be ~32%, and the remaining area (~68%), snow of 16% wetness content (section 5.2.2.3).

The SSM/I passive microwave data for the date of the AIRSAR overflight (10th June 1991) are used to predict the mean dielectric constant and % wetness content of the snow of the imaged surface for each of the zones. The polarization ratio from the passive data (@19GHz) gives the mean value of dielectric constant as 1.2, 1.53, 1.51 and 2.16 for zones 1 to 4 respectively, which indicates a mean % water content of 0%, 6.7%, 6.3% and 19.6% for each of the zones in turn. The dielectric constant of the imaged surface and the water content of the snow surface increases on descending the ice sheet.The high dielectric constant of the percolation zone is thought to be due to the presence of ice in this region (of a higher dielectric constant than snow). The dielectric constant at C and P band for snow of 6.3% water content (corresponding to that of the ablation zone as imaged) is calculated to be 2.79 and 3.11 respectively. These values lie between the values given by Rott *et al.* (1992) and Jezek *et al.*(1993) for snow of approximately the same water content (6%) and are therefore considered to be a typical representation of the electrical properties of the snow. The dielectric constant of the snow at the AIRSAR frequencies may therefore be determined from the polarimetric passive data from SSM/I (19GHz) of the same surface. This correlation work, using data from both the active and passive systems assists with the understanding of the response of the imaged snow surfaces of each of the zones of the ice sheet.

6.2.3 Emitted signals during melt season.

The passive signal for the spring-summer season (April-June 1991) is analysed in detail for each of the four zones. The mean daily brightness temperatures are found to rise gradually during this time indicating the increase in surface temperatures (figure 5.19). The data for the dry zone shows the greatest rise (approximately linear) and the data for the other zones show a less steep rise and have increasingly scattered values due to the increasing wetness content of the snow in these zones. The vastly scattered values of data for the ablation zone indicate the partial melting and refreezing of the surface during this time, as discussed above. The emissivity of water is less than that of snow and hence the brightness temperature values are lower for the ablation zone data.

The 37GHz data show similar patterns, but with lower values. This is due to the dielectric constant of water being less at 37GHz than for 19GHz. The emissivity of wet snow is therefore lower at 37GHz than for 19GHz, which is shown by the lower values of the measured brightness temperatures for 37GHz compared with the 19GHz data. The greatest change in the data for the two frequencies is noted for zone 1 (dry zone) in April 1991. The data for the previous year (April-June 1990) are also analysed and are found to show the same effects.

The effect of the two frequencies is analysed by considering the variation of the measured brightness temperature values $(19\text{-}37)T_{Bh}$ and $(19\text{-}37)T_{Bv}$ for each of the zones for the complete year of data, and also particularly during the spring-summer seasons (figures 5.20, 5.21). The full year data set shows that the difference with frequency decreases for the wetter zones of the ice sheet and shows a drop in the level during the summer months. This is due to the 19 and 37GHz signals recording similar values of brightness temperatures for the wetter areas as penetration is minimal if free water is present. Both frequencies then record the similar surface values. The frequency difference data for the dry zone show a simple drop in level during spring-summer.

The signal at the start of the melt season is considered in detail. It is found that the frequency difference data show that the difference in the brightness temperature values for the two frequencies is greatest for the dry zone and decreases for the other zones with the position down the ice sheet. This is due to the difference in penetration depth of the signals. For low dielectric (dry snow) the penetration of 19GHz signal is greater than that of the 37GHz signal and hence the two frequency signals record different temperatures. For wetter areas the difference in penetration of the two frequency signals is not so large and the values recorded are more similar.

At the start of the melt season the frequency difference data for the dry zone shows a large decrease in values, whereas that for the other three zones show peaks and a more gradual fall in values. The fall in the values for the dry zone is due to the 19GHz data measuring the warmer subsurface snow in April with the 37GHz signal from the colder surface material. As the snow then becomes warmer during May the difference between the brightness temperatures measured by the two frequencies decreases and the two frequencies record similar values by June.

The peaks recorded in the frequency difference data for the wetter regions arise from the difference in the individual brightness temperatures for the two frequencies. The data for 19GHz show a simple rise in values during this time (recording the physical temperature rise of the snow) whereas the 37GHz data show a brief fall. This causes the peaks in the frequency difference data. This is due to the top snow surface beginning to melt, causing a reduction in emissivity. The 37GHz data is more susceptible to changes at the surface (due to the difference in penetration depth) and therefore shows a more marked change than the 19GHz data. The extent of this localized increase in surface moisture content from surface melting varies (due to thawing/refreezing caused by changes in the physical

temperature) until the physical temperature increases sufficiently to cause a uniform surface moisture content. At this stage the data for the two frequencies become more similar. This effect is also noted for data for the previous year (1990). These results indicate that this effect probably happens every year at the beginning of melt; it occurs for both polarizations, and is shown by a drop in the frequency difference data for the dry zone, and by peaks and a more gradual decrease in values for the wetter zones.

6.2.4 Effect of ice layers.

The effect of ice layers on the passive signal is also investigated. The presence of ice tends to reduce the passive emitted signal as the emissivity of ice is less than that for snow. This effect is noted for the passive microwave SSM/I data for the dry zone during winter as a surface wind crust ice layer forms, decreasing the emission from the surface (section 5.2.2.2).

The annual brightness temperature data for the percolation zone are less than those for the dry zone throughout the year due to the presence of subsurface ice layers. These ice layers - caused either by the refreezing of melt water at depth, or alternatively by production of large ice crystals in the formation of depth hoar - act to decrease the emissivity of the snowpack of the percolation zone and decrease the value of the measured brightness temperature data. These ice layers form during late summer/autumn, and a corresponding decrease in the measured brightness temperatures and polarization ratio of the passive emitted signals is noted during this season.

The effect of the ice layers is to decrease the measured brightness temperatures for passive systems, whereas the presence of ice tends to increase the level of the backscattered signal for active radar systems. This may be explained by considering the increase in dielectric constant due to the presence of ice within the snow and the resulting increase in reflectivity and corresponding decrease in emissivity. This results in an increase in the level of the active signal and a decrease in the measured passive emitted microwave signal. Volume scattering within the snowpack also increases with the presence of the ice layers which further acts to increase the level of the active signal and reduce the passive emitted signal from the snowpack.

6.3 Future work, synergistic applications and future directions in polarimetric remote sensing.

6.3.1 Future work.

6.3.1.1 Continuation of work using data over the Greenland ice sheet.

The Greenland ice sheet should be monitored over a series of time to map the different zones and to note the seasonal changes and the duration and extent of the melt season. This information on the surface state of the ice sheet is important for mass balance work and for detecting climate change. It is suggested that future work could include the use of both active and passive microwave data to map the different zones of the ice sheet, and the seasonal changes within the zones. The response from particular areas representing the different zones of the ice sheet is discussed in this thesis (chapter 5).

The seasonal differences of the ice sheet may be monitored by the change in the return signal due to, for example, the variation in depth of surface firn, the presence of ice layers, the moisture content of the snow, and the occurrence of melt pools as investigated in chapters 3 and 5. Multitemporal data may be used to indicate the surface state of the ice sheet, the duration of the melt season and the extent of the ablation area.

High resolution active microwave images for the same region over a series of time may be used to track the movement of discontinuities and irregularities of the ice sheet as indicated in chapter 5. This information may be used to infer ice velocities and the flow of the ice sheet, thus indicating the ablation rate. It may be possible to correlate the location of the discontinuities with the underlying bedrock topography.

This work over the Greenland ice sheet adds to studies of mass balance and surface state which are particularly important for the detection of climate change.

6.3.1.2 Continuation of theoretical work.

The understanding of the response from the different zones of the ice sheet is of particular interest, including the effect of the polarization of the return signals, and the effect of the surface and subsurface content of the imaged area (for example, the effect of ice layers in the percolation zone of the Greenland ice sheet). To further the understanding of the measured signals from the imaged areas and to increase the information obtained on the

behaviour of the ice sheet, it is necessary to continue the theoretical work on the active/passive balance of radar signals, including the effect of rough surfaces and inhomogenieties, thus leading to the overall total energy balance.

The radar response for typical areas of the ice sheet are discussed in chapter 5. The scattering mechanism is determined and the change with incidence angle is investigated. To increase the understanding of the response further, the relative importance of the surface scatter and volume scatter components must be determined, with reference to the scattering mechanisms for the different zones of the ice sheet.

The origin of the coherent and diffuse scattering components is not a simple problem and needs further investigation. A usual assumption is that the surface scatter is coherent and the volume scatter is diffuse, and the coherent and diffuse components of the return signal are used to indicate the relative importance of the surface and volume scatter. The surface scatter is mainly coherent for smooth surfaces, but may also have a diffuse component. In particular, the scattering from rough surfaces will show some depolarization. The scattering that occurs within the volume of the snowpack material also has both a coherent and a diffuse component. The coherent part is due to the distinct layering of the material and the diffuse part originates from the scattering between the individual snow and ice particles within the snowpack.

The polarimetric AIRSAR data may be used for this investigation. The height of the pedestal is commonly used to indicate the diffuse component. This is, however, due to the diffuse scattering components from both the surface and volume of the imaged material. However, the pedestal height is not necessarily due to just diffuse scattering. An apparent pedestal appears for the coherent signal as the incidence angle is increased away from nadir. The change in the apparent pedestal height as a result of changing the incidence angle for the coherent component (from the theoretical response) has been studied in this thesis (chapters 3 and 5). The measured data over the percolation zone show a similar response, and indicate the importance of determining the source of this effect.

The investigation of the active and passive balance should be continued. Changing particular parameters (for example, the snow moisture content, or the presence of a subsurface ice layer) has a resulting effect on both the active and passive microwave signals, including the polarimetric content of the return signal. A greater understanding of the relationship between the active and passive response leads to a more complete understanding of the return signals and the measured behaviour of the imaged area.

The effect of the position of ice layers on the received signal should be investigated further, using both theoretical calculations and actual measurements. The variation of the theoretical (coherent) return signal from a snow surface with a subsurface ice layer at different depths is investigated in chapters 3 and 5. The results indicate that the complex coherent return signal may be used to infer the position of the ice layer within the snowpack. The resulting effect on the measured passive and active microwave signals should be determined.

6.3.1.3 Continuation of correlation work.

An increased understanding of the response from the imaged surfaces may be made by correlation work. The measurements made by active radar from airborne systems (as studied here) correlate with that from satellite systems, which enable greater coverage, both in extent and time.

Data from active airborne radar systems (e.g. AIRSAR) and satellite systems (e.g. ERS-1 SAR), and from passive systems (e.g. SSM/I), together with ground radar measurements and field measurements (e.g. snow density and depths of layers), may be linked with theoretical models to provide a greater understanding of the response from the ice sheet. It is suggested that the ERS-1 SAR radar backscatter measurements (VV) should be used to map the different zones for the entire ice sheet, and to show any changes in the extent of each zone with time. The passive microwave data from SSM/I imagery over the Greenland ice sheet may also be used to correlate with active measurements.

6.3.1.4 Coincident polarimetric and interferometric data (topography).

Interferometric data are used for topographic mapping. The NASA/JPL TOPSAR instrument (Airborne interferometer) is described by Zebker and Goldstein (1986) and Zebker et al.(1992), with a brief description in chapter 1. Future work may include coincident polarimetric and interferometric data sets (JPL are constructing a new processor for coincident polarimetric and interferometric data sets).

It is necessary to have both polarimetric and interferometric data over the same area as the multifrequency polarimetric data give information on the method and type of scattering, allowing the dielectric constant of the surface (and subsurface) material to be inferred. These characteristics are necessary to be known for the particular area to ensure that the interferometric information gives an accurate topographic map of the area.

It has been shown that the C band TOPSAR interferometer records the height of the tops of trees in a forested area, and that of the forest floor in clearings (Zebker *et al.*, 1992). The multifrequency polarimetric data would show the type of scattering that occurs for the different frequencies (lower frequencies (P band) would penetrate the canopy and show diffuse scattering, high frequencies (C band) would show direct scattering off the top of the canopy). The transition from the wooded area to the clearing may be shown in the polarimetric data by double bounce scattering occurring off the tree trucks and ground surface.

For polar surfaces the amount of penetration of the radar signal at different frequencies should be considered when interferometric data sets are used to produce topographic maps of the area. The lower frequency radar will penetrate the low dielectric snow to quite some distance (typical skin depth of firn is 6176m @Pband, 2058m @Lband and 233m @Cband; and for pure ice is 370m @Pband, 136m @Lband and 3m @Cband).
The position at which the main return signal is coming from within the snow and ice is important. A subsurface ice layer may reflect more energy than the initial surface air:snow interface. This effect is measured by Jezek and Gogineni (1992) during their field campaign on the Greenland ice sheet. Ground radar measurements at the test-site in the percolation zone show that the major source of the radar return is from a subsurface ice layer for both C and Ku band (SAR and altimeter frequencies).

The topographic information derived from the interferometric data over polar surfaces should take this penetration factor into account. This is a major factor to be considered for mass balance and volume change work over ice sheets (section 1.3.1.2).

6.3.2 Synergistic Applications.

6.3.2.1 Multifrequency polarimetric SAR studies of different areas (e.g. deserts, sea ice).

The understanding of polarimetric data is useful for studies over many different surfaces. The general understanding of the polarimetric signals over the Greenland ice sheet as investigated here may be applied to studies of other relatively smooth surfaces, for example; desert areas such as the Simpson desert in central Australia.

Polarimetric data from desert areas may be analysed to determine the moisture content.

The radar response from the desert surface will depend on the dielectric mismatch at the air to sand interface, and also on the subsurface values of dielectric constant. The value of the dielectric constant depends mainly on the water content of the sand, which may therefore be determined from the return radar signal. The moisture content of desert areas and the extent of desertification are important factors in studies of hydrology for climate research. Variation in the desert surface and subsurface layers and changes in the extent of the desert are indicative of climate change. Understanding the radar response from our desert surfaces may also assist with understanding the radar response of other planetary surfaces.

Sea ice may also be measured with SAR. The extent of sea ice and the ice type and movement may be monitored. The dielectric constant, and hence the salinity and age/type of the sea ice may be determined from the return radar signal. The high contrast in the dielectric constant of sea ice and that of open water allows the coverage of sea ice to be tracked. It may also be possible to determine the thickness of sea ice layers using multifrequency SAR. Changes in the dielectric constant causes radar reflections and details of the component reflections and the depth at which they occur may be extracted from the total received signal. The classification and monitoring of sea ice is important due to the effect of sea ice in the heat exchange between the atmosphere and the ocean, and the role this plays in regional and global climate.

6.3.2.2 Use of energy balance model for active:passive correlation.

The theoretical work described here is based on conservation of energy and uses a matrix model of polarimetric scattering from a system of layered material to calculate the reflected, transmitted and absorbed energies. The amplitude and phase components are considered so that phase coherency is maintained. The imaged surface is represented by the complex dielectric constant of natural materials (which, for the snow surfaces considered in this thesis, is dependent largely on the water content).

This theoretical work is relevant for both active and passive microwave radar as used in this thesis, and also may be used for radiometry (e.g. using ATSR - Along Track Scanning Radiometer; this instrument is described by Ulaby *et al.*, 1986). The theoretical analysis work is applicable for various remote sensing instruments, at all frequencies, and any combination of incidence angles, polarizations; for both active and passive systems.

6.3.3 Future directions in polarimetric remote sensing and applications for other instruments and systems.

Future advances include the operation of new satellite and spaceborne systems which will offer additional coverage of the ice sheet.

The airborne, multifrequency, fully polarimetric, AIRSAR system was built to precede the SIR-C/X-SAR system (Shuttle imaging radar). The AIRSAR system was used as a flying test bed for the shuttle system allowing initial investigations of the various applications to be undertaken, providing the opportunity to determine the required modes of operation for the different studies. SIR-C is the first spaceborne radar system with a multifrequency fully polarimetric SAR (launched April 1994). SIR-C collects multipolarization data at C and L band, and single polarization (VV) data at X band (~10GHz) (Curlander and McDonough, 1991). The latitude, coverage and time of flight are, however, limited.

Present satellite data from the ERS-1 SAR is of single frequency and one polarization only (C band, VV polarization). ENVISAT is the proposed European satellite system due for launch at the end of the decade, presently planned to have dual polarized antennas to provide linear polarization images (HH and VV). RADARSAT is a Canadian Earth Observation satellite due for launch in 1995 and is of single frequency and polarization only (C band, HH polarization) (Langham, 1993).

Future passive remote sensing systems include the multichannel radiometer planned for the polar platform (Pampaloni, 1989). This system is designed to have greatly improved spatial resolution.

The future satellite radar and space systems will offer a multi-temporal, uniform and reliable source of data. This is an increasingly important method of data collection over remote regions such as the Greenland ice sheet.

A general understanding of the polarimetric radar response is useful for future planetary studies. The polarimetric model may be applied to future planetary data. The current Magellan space probe using a SAR antenna to collect data of Venus is of single polarization only and operates at S band, 2.4GHz (Saunders *et al.,* 1992).

Studies of the radar response from the percolation zone of the Greenland ice sheet may

assist with the understanding of the response from the icy surfaces of other planets. Rignot *et al.* (1993) report similarities in the radar response of the percolation zone with that from Jupiter's icy Galilean satellites (Europa, Ganymede and Callisto). Strong radar return signals and high polarization ratios are measured from both the icy planetary surfaces and from the percolation zone of the Greenland ice sheet. The strong radar return signal of the percolation zone of the Greenland ice sheet is due to the increased signal from the subsurface ice lenses which form during seasonal melting and refreezing. The subsurface heterogeneities from meteoroid bombardment of the Galilean satellites are, however, not likely to resemble the subsurface discontinuities of the Greenland percolation zone, but the analysis of the source and cause of the radar return from the percolation zone of the Greenland ice sheet is used to assist with the understanding of the response from the icy satellites. High radar reflectivity is also noted for other planetary surfaces: The South polar ice cap of Mars, parts of Titan, and from the ice in craters at the poles of Mercury (Muhleman *et al.*, 1990, 1991; Slade *et al.*, 1992; Harmon and Slade, 1992, 1994).

Understanding the climate system of other planets, particularly near neighbours (Mars and Venus), may assist with the understanding of the Earth's climatic system. Taylor (1994) reviews the current knowledge of the atmospheres of these planets, and states that the overall problem is to understand the origin and evolution of the planets, and their atmospheric stability and surface environment or climate, to assist with predictions for the future evolvement. Studies of the volcanic surface of Venus are underway with the Magellan orbiter, and research of the atmosphere of Mars is continuing with future Mars missions.

Studies of the polarimetric response from geophysical surfaces have many different possible uses in future climate related research. The theoretical computer model may be used for this future research and applied to the data from the systems described above. Analysis of the measured data and future theoretical investigations of the response from different terrains will enable a greater understanding of remotely sensed data and the implications of the results of climate studies.

6.4 Conclusions.

The aim of the thesis is to investigate the active and passive polarimetric microwave response of the four different zones of the Greenland ice sheet. This is achieved by the above analysis of the multifrequency polarimetric microwave data of the Greenland ice sheet, giving a greater understanding of both the active and the passive response of the different zones as summarized below.

The use of the multifrequency polarimetric radar for detecting features and changes in the different zones of the ice sheet is discussed in the thesis. Details of ice sheet dynamics may be made by measuring the rate and direction of ice flow by temporal studies of the movement of the imaged discontinuities within the ice sheet. The location and extent of melt areas may also be determined. The ability to map the different zones of the ice sheet and potentially to indicate the location of surface and subsurface discontinuities such as sastrugi, ice layers from refrozen melt water and depth hoar is investigated. This information may then be used in studies of the ablation and accumulation rate and the overall mass balance of the ice sheet.

The active multifrequency polarimetric AIRSAR system gives high resolution imagery and the data for sample areas of the ice sheet are analysed to determine the active polarimetric radar response at P, L and C band for the different snow conditions of each zone. The passive SSM/I data covering a larger area at each of the sample points are analysed to correlate with the active data and also to show the annual change in the emitted radiation from each of the four zones of the ice sheet. The active and passive response of each zone is investigated and this information may be used in future studies of the ice sheet.

The multifrequency fully polarimetric imagery from the AIRSAR system show that P band and HH polarization are the optimum operating frequency and polarization state of the active radar for detecting the features shown in the percolation and soaked/ablation zones of the ice sheet. These features - thought to indicate the presence of subsurface ice streams - are apparent only for this particular combination of polarization and frequency.

The polarimetric response of this multifrequency data set is analysed to show the dominant scattering mechanism for each of the four zones of the ice sheet. The theoretical and measured polarimetric response is found to be dependent on the operating frequency and incidence angle of the radar, and the dielectric constant of the imaged terrain (the

surface and subsurface content).

A theoretical computer model is developed and used to provide a classification method of the imaged terrain. This model is applied to the 233-1 AIRSAR image of the ablation zone and successfully distinguishes between the melt pools and the surrounding snow areas. This classification method does not require any prior knowledge of the surface.
The potential of using the polarimetric data as measured by the AIRSAR to indicate the existence and position of ice layers within the snowpack is demonstrated. The measured AIRSAR data for the percolation zone image are correlated with theoretical data to infer the depth of a subsurface ice layer. The results are found to correlate with the snowpit measurements as made by the field party at the test-site.

The passive microwave SSM/I data for each of the four zones of the ice sheet are analysed to show the seasonal change in the measured emitted radiation. The data show the quasi-sinusoidal annual temperature cycle and the decrease in emissivity for the wetter areas on descent of the ice sheet. An inversion technique to calculate the mean % wetness content of the snow directly from the measured polarimetric passive microwave data is demonstrated. The measured polarization ratio is inverted to indicate the dielectric constant of the imaged terrain and the mean % wetness content of the snow is inferred. The annual change in moisture content of each of the four zones is determined and the mean areal extent of water covered surface (in the form of melt pools) for the summer ablation zone data is calculated. The ability of using the SSM/I data to map the different zones of the complete ice sheet and to determine the mean % wetness of the snow and the approximate area of melt pools is illustrated.

The passive SSM/I data for the date of the active microwave AIRSAR overflight are used to predict the mean dielectric constant and % wetness content of the imaged surface for each of the zones. The dielectric constant of the mean surface of the snow at the AIRSAR frequencies is successfully derived from the measured passive microwave data.

The change of the measured passive microwave signal during the spring-summer melt season is investigated in detail for each zone of the ice sheet. The measured brightness temperatures for the dry zone show an approximately linear rise, whereas the data for the wetter areas have a less steep rise and have more scattered values due to the increased moisture content of the snow. The data for the ablation zone show the most scattered values indicating the changing emissivity from the partial thawing and refreezing of the melt areas.

The difference in the measured brightness temperature values for the two frequencies (19 and 37GHz) are analysed and effect of the difference in penetration depths for the two frequencies and the thermal capacitive effect of the snowpack is noted. The full year data set shows that the difference with frequency decreases for the wetter areas of the ice sheet and shows that the level decreases during summer, due to the two frequency channels recording similar surface data due to the presence of free water.

The frequency difference data for each of the zones are analysed in detail for the beginning of the melt season and show distinct effects - a greater drop for the dry zone data and peaks and fall for the wetter areas. This effect is noted at the beginning of the melt season for the previous year of data also, and is found to occur for both polarizations.

The effect of ice layers on the passive response is to lower the measured brightness temperatures. This is due to the decrease in emissivity of the ice compared with snow. It is important to note that the passive signal is reduced by the presence of ice, whereas the active signal is increased.

Remote sensing techniques are becoming an increasingly important method in data collection over the polar regions. The multifrequency polarimetric data of the Greenland ice sheet as analysed above may be used to determine the surface state of the ice sheet. Temporal studies of the extent of the different zones are necessary to determine the dynamics of the ice sheet. Any changes in the accumulation and ablation affect the overall mass balance of the ice sheet and may be linked to climate change.

References

Barrick, D.E. and Peake, W.H. (1968) A review of scattering from surfaces with different roughness scales. *Radio Science, 3*. 865-868.

Beckmann, P. and Spizzichino, A. (1963) *The scattering of electromagnetic waves from rough surfaces*. Pergamon Press, Oxford.

Benson, C. (1962) *Stratigraphic studies in the snow and firn of the Greenland ice sheet*. CRREL res. Rep. 70, CRREL, Hanover, NH.

Benson, C. (1971) *Stratigraphic studies in the snow at Byrd station, Antarctica, compared with similar studies in Greenland*. (Antarctic research series, Volume 16, Antarctic snow and ice studies 2). American Geophysical Union, Washington, DC.

Bindschadler, R., Jezek, K. and Crawford, J. (1987) Glaciological investigations using the synthetic aperture radar imaging system. *Annals of Glaciology, 9*. 11-19.

Born, M. and Wolf, E. (1980) *Principles of optics: 6th Edition*. Pergamon Press, New York.

Cady, W.M., Karelitz, M.B. and Turner, L.A. (1948) *Radar scanners and radomes*. McGraw-Hill, New York.

Chen, M.F. and Fung, A.K. (1988) A numerical study of the regions of validity of the Kirchoff and small-perturbation rough surface scattering models. *Radio Science, 23*. 163-170.

CIRES (1992) *DMSP SSM/I brightness temperature grids for the polar region on CD-ROM*. National snow and ice data center, Cooperative Institute for Research in Environmental Sciences, University of Colorado, Boulder, Colorado.

Colbeck, S.C. (1991) The layered character of snow covers. *Reviews of Geophysics, 29*. 81-96.

Curlander, J.C. and McDonough, R.N. (1991) *Synthetic aperture radar: Systems and*

signal processing. Wiley, New York.

Durden, S.L. (1986) *Microwave surface scattering from the ocean surface*. PhD thesis, Stanford University (scientific report No. D901-1986-1 June 1986).

Feynman, R.P., Leighton, R.B., and Sands, M. (1963) *The Feynman lectures on Physics: Volume 1*. Addison-Wesley, Reading, Mass.

Foster, J.L., Hall, D.K., Chang, A.T.C. and Rango, A. (1984) An overview of passive microwave snow research and results. *Reviews of Geophysics, 22*. 195-208.

Freeman, A. and Durden, S.L. (1992) *Fitting a three-component scattering model to polarimetric SAR data*. Third annual JPL airborne geoscience workshop, NASA/JPL, Pasadena, California, USA. June 1992.

Fung, A.K. (1982) A review of volume scatter theories for modeling applications. *Radio Science, 17*. 1007-1017.

Giuli, D. (1986) Polarization diversity in radars. *Proceedings of the IEEE, 74*. 245-269.

Glen, J.W. and Paren, J.G. (1975) The electrical properties of snow and ice. *Journal of Glaciology, 15*. 15-38.

Goldstein, R.M. and Zebker, H.A. (1987) Interferometric radar measurement of ocean surface currents. *Nature, 328*. 707-709.

Guzkowska, M.A.J., Rapley, C.G., Ridley, J.K., Cudlip, W., Birkett, C.M. and Scott, R.F. (1990) *Developments in inland water and land altimetry*. ESA CR-7839/88/F/FL.

Hall, D.K. and Martinec, J. (1985) *Remote sensing of ice and snow*. Chapman and Hall, London.

Hapke, B. (1990) Coherent backscatter and the radar characteristics of outer planet satellites. *Icarus, 88*, 2, 407-417.

Hapke, B. and Blewett, D. (1991) Coherent backscatter model for the unusual radar reflectivity of icy satellites. *Nature, 352*, 6330, 46-47.

Harmon, J.K. and Slade, M.A. (1994) How ice survives on fiery Mercury, *New Scientist*, p.16, 28.5.94.

Harmon, J.K. and Slade, M.A. (1992) Radar mapping of Mercury: Full disc images and polar anomalies. *Science, 258*, 640-643.

Hecht, E. and Zajac, A. (1974) *Optics*. Addison-Wesley, Reading, Mass.

Houghton, J.T. and Morel, P. (1984) The world climate research programme, in Houghton, ed., *The global climate*, Cambridge University Press, pp1-11.

Houghton, J.T., Jenkins, G.J. and Ephraums, J.J. (1990) *Climate change: the IPCC scientific assessment*. Cambridge University Press, Cambridge.

Jezek, K. and Gogineni, S. (1992) Microwave remote sensing of the Greenland icesheet. *IEEE Geoscience and Remote Sensing Society Newsletter*, December 1992. 6-10.

Jezek, K.C. (1992) Spatial patterns in backscatter strength across the Greenland ice sheet. pp269-272 in *Proceedings First ERS-1 Symposium - Space at the Service of our Environment*, Cannes, France, 4-6 November 1992, ESA SP-359 (March 1993).

Jezek, K.C., Drinkwater, M.R., Crawford, J.P., Bindschadler, R. and Kwok, R. (1993) Analysis of synthetic aperture radar data collected over the Southwestern Greenland ice-sheet. *Journal of Glaciology, 39*. 119-132.

Jezek, K.C., Gogineni, P., and Shanableh, M. (1994) Radar measurements of Melt Zones on the Greenland Ice Sheet *Geophysical Research Letters,* vol.21, no.1, 33-36, January 1, 1994

Kong, J.A. (1990) *Progress in electromagnetics research; Volume 3: Polarimetric remote sensing*. Elsevier, New York.

Kuhn, M.H. (1989) The role of land ice and snow in climate. pp. 17-28, *in* Berger, A., Dickinson, R.E. and Kidson, J.W. (eds)*Understanding climate change*. (Geophysical monograph 52, IUGG Volume 7). American Geophysical Union,

Washington, DC.

Langham, E.J. (1993) RADARSAT: A new source of data for resource management. pp. 113-117, *in:* Winkler, P. (ed) *Remote sensing for monitoring the changing environment*. Balkema, Rotterdam.

Laur, H. (1992) ERS-1 SAR calibration: Derivation of backscattering coefficients in ERS1.SAR.PRI. *ESA, ESRIN, 1*.Rev.0. 17th October 1992.

Massom, R. (1991) *Satellite remote sensing of polar regions: Applications, limitations and data availability*. Belhaven press, London.

Matzler, C. (1987) Applications of the interaction of microwaves with the natural snow cover. *Remote Sensing Reviews, 2*. 259-387.

Mishchenko, M.I. (1992) Polarization characteristics of the coherent backscatter opposition effect. *Earth, moon and planets, 58*, 2, 127-144.

Mott, H. (1986) *Polarization in antennas and radar*. Wiley, New York.

Muhleman, D.O., Grossman, A.W., Butler, B.J. and Slade, M.A. (1990) Radar reflectivity of Titan. *Science, 248*, 975-980.

Muhleman, D.O., Butler, B.J., Grossman, A.W. and Slade, M.A. (1991) Radar images of Mars. *Science, 253*, 1508-1513.

Noll, J. and Borgeaud, M. (1992) Selection of theoretical surface scattering models from the properties of polarimetric radar data. *URSI*, 2C-1-4, IEEE.

Norikane, L. (1991) *User's guide to MacMultiview 5.0*. California Institute of Technology, JPL, Pasadena, California.

Norikane, L. (1992) *User's guide to MacSigmaO 3.1*. California Institute of Technology, JPL, Pasadena, California.

Oerlemans, J, and van der Veen, C.J. (1984) *Ice sheets and climate* D.Reidel Publishing Company, Dortrecht/Boston/Lancaster

Paren, J.G. and Glen, J.W. (1978) Electrical behaviour of finely divided ice. *Journal of Glaciology, 21.* 173-191.

Paterson, W.S.B. (1981) *The Physics of Glaciers* Pergamon Press, Oxford.

Peters, K.J. (1992) Coherent - backscatter effect -a vector formulation accounting for polarization and absorption effects and small or large scatterers. *Physical Review B - Condensed matter, 46,* 2, 801-812.

Rignot, E.J., Ostro, S.J., van Zyl, J.J. and Jezek, K.C. (1993) Unusual radar echoes from the Greenland ice sheet. *Science, 26,* 1710-1713.

Rott, H. (1989) Multispectral microwave signatures of the Antarctic ice sheet. pp. 89-101, *in:* Pampaloni, P. (ed) *Microwave radiometry and remote sensing applications* (proceedings of the specialist meeting held in Florence, Italy, 9-11 March 1988). VSP, Utrecht, NL.

Rott, H., Davis, R. and Dozier, J. (1992) Polarimetric and multifrequency SAR signatures of wet snow. *IGARSS '92*, IEEE, p.1658-1660.

Saunders, R., Spear, A., Allin, P., Austin, R., Berman, A., Chandlee, R., Clark, J., Decharon, A., Dejong, E., Griffith, D., Gunn, J., Hensley, S., Johnson, W., Kirby, C., Leung, K., Lyons, D., Michaels, G., Miller, J., Morris, R., Morrison, A., Piereson, R., Scott, J., Shaffer, S., Slonski, J., Stofan, E., Thompson, T. and Wall, S. (1992) Magellan Mission Summary. *Journal Of Geophysical Research-Planets 97* , 13067-13090.

Seligman, G.A. (1980) *Snow structures and ski fields: Being an account of snow and ice forms met with in nature and a study of avalanches and snowcraft.* International Glaciological Society, Cambridge.

Shi, J. and Dozier, J. (1992a) *Snow wetness retrieval algorithm for SAR.* Third annual JPL airborne geoscience workshop, NASA/JPL, Pasadena, California, USA. June 1992.

Shi, J. and Dozier, J. (1992b) Radar backscattering response to wet snow. *IGARSS'92*, IEEE, p.927-929.

Shi, J., Dozier, J. and Rott, H. (1992) Capability of mapping snow-covered area using SAR.*URSI*, PP-28-31, IEEE.

Shi, J., Soares, J., Hess, L., Engman, E. and van Zyl, J. (1991) Soil moisture measurements from airborne SAR. pp. 68-77, *in:* van Zyl J.J. (ed) *Proceedings of the third airborne synthetic aperture radar (AIRSAR) workshop, May 23 and 24 1991*. NASA/JPL, Pasadena, California.

Skolnik, M.I. (1990) *Radar Handbook*. McGraw-Hill, New York.

Slade, M.A., Butler, B.J. and Muhleman, D.O. (1992) Mercury radar imaging: Evidence for polar ice. *Science, 258*, 635-640

Sturm, K. and Rott, H. (1992) C and X band signatures of snow. *URSI*, 2D-27-30, IEEE.

Stutzman, W.L. (1993) *Polarization in electromagnetic systems*. Artech House, Boston.

Swift, C.T., Hayes, P.S., Herd, J.S., Jones, W.L. and Delnore, V.E. (1985) Airborne microwave measurements of the Southern Greenland ice sheet. *Journal of Geophysical Research - Solid Earth and Planets, 90*. 1983-1994.

Taylor, F.W. (1994) The atmospheres of the inner planets. *Current Science, 66*, 7-8, 512-524.

Tsang, L. and Kong, J. (1980) Thermal microwave emission from a three layer random medium with three-dimensional variations. *IEEE Transactions of Geoscience and Remote Sensing, 18*. 212-216.

Tyler, G., Simpson, R., Maurer, M. and Holmann, E. (1992) Scattering Properties Of The Venusian Surface - Preliminary-Results From Magellan. *Journal Of Geophysical Research-Planets 97* , 13115-13139.

Ulaby, F.T. and Elachi, C. (1990) *Radar polarimetry for geoscience applications*. Artech House, Norwood, Mass.

Ulaby, F.T. and Dobson, M.C. (1989) *Handbook of radar scattering statistics for*

terrain. Artech House, Norwood, Mass.

Ulaby, F.T., Moore, R.K. and Fung, A.K. (1986) *Microwave remote sensing: Active and passive. Volume 3: From theory to applications*. Artech House, Boston.

Van der Veen, C.J. and Jezek, K.C. (1993) Seasonal variations in brightness temperature for central Antarctica. *Annals of Glaciology, 17*. 300-306.

van Zyl, J.J., (1992), ed., Third annual JPL airborne geoscience workshop, NASA/JPL, Pasadena, California, USA. June 1992.

van Zyl, J.J., Carande, R., Lou, Y., Miller, T. and Wheeler, K. (1992) *The NASA/JPL three frequency polarimetric AIRSAR system*. Third annual JPL airborne geoscience workshop, NASA/JPL, Pasadena, California, USA. June 1992.

van Zyl, J.J., Zebker, H.A., and Elachi, C. (1987) Imaging radar polarization signatures: Theory and observation. *Radio Science, 22*. 529-543.

Vornberger, P.L. and Bindschadler, R.A. (1992) Multi-spectral analysis of ice sheets using co-registered SAR and TM imagery. *International Journal of Remote Sensing, 13*. 637-645.

Wen, B.H., Tsang, L.U., Winebrenner, D.P. and Ishimaru, A. (1990) Dense medium radiative transfer theory: Comparison with experiment and application to microwave remote sensing and polarimetry. *IEEE Transactions of Geoscience and Remote Sensing, 28*, 1, 46-59.

Zebker, H.A. and Goldstein, R.M. (1986) Topographical mapping from interferometric synthetic aperture radar observations. *Journal of Geophysical Research - Solid Earth and Planets 91*. 4993-4999.

Zebker, H.A., Madsen, S., Martin., J., Alberti, G., Vetrella, S. and Cucci, A. (1992) *The TOPSAR interferometric radar topographic mapping instrument*. Third annual JPL airborne geoscience workshop, NASA/JPL, Pasadena, California, USA. June 1992.

Zebker, H.A., van Zyl., J.J., and Held, D.N. (1987) Imaging radar polarimetry from wave synthesis. *Journal of Geophysical Research - Solid Earth and Planets, 92*.

683-701.

Appendix 1 Theory -

A1.1 Definition of parallel and perpendicular polarization as used for all the work in this thesis.

The sign convention and definition of parallel and perpendicular polarization are as shown in figure A1.1.

The parallel component is that part of the incident E field which lies parallel to the surface, and the perpendicular component is the part of the incident E field which is normal to the parallel component, and also to the direction of propagation of the wave as shown above. Any incident E field may be described by these two mutually perpendicular complex components, E parallel and E perpendicular, both normal to the direction of propagation of the electromagnetic wave.

For the case of normal incidence, E parallel = E perpendicular, and there is therefore no difference between horizontal and vertical polarization. For oblique incidence the definition of parallel and perpendicular polarization must be strictly followed.

The definition of polarization is dependent on the orientation of the surface. For the horizontal ground surface as seen by radar remote sensing systems, vertical polarization is perpendicular to the surface and horizontal polarization is parallel to the surface. If the surface is orientated vertically, then vertical polarization becomes parallel polarization and horizontal becomes perpendicular polarization. It is therefore important to consider the orientation of the surface and the components of the incident E field parallel and perpendicular to the surface when determining the polarization of the signal.
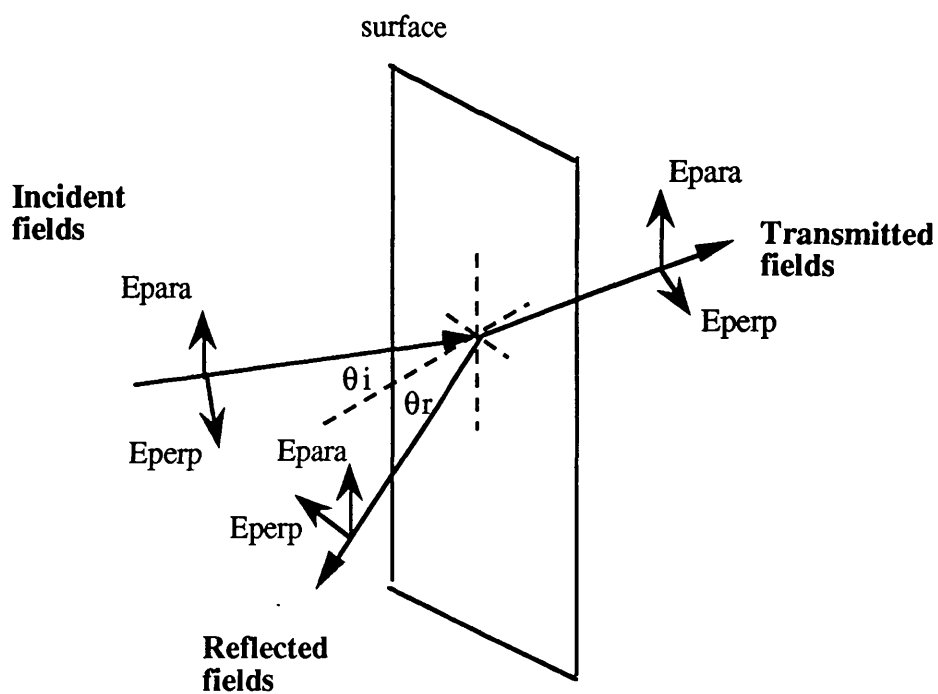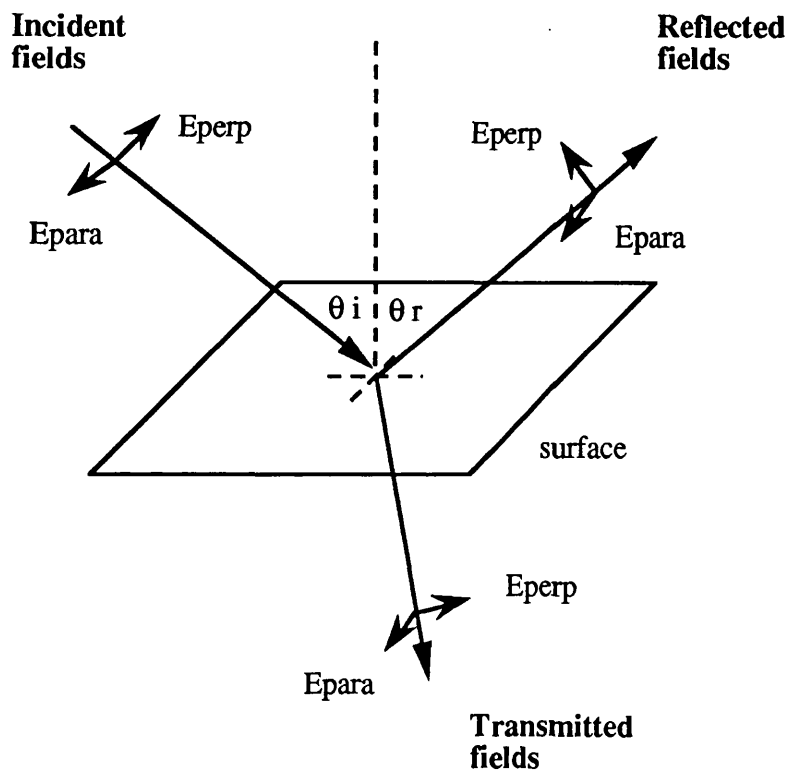
Figure A1.1: Polarization convention for horizontal and vertical surfaces.

A1.2 Validation and correlation of model.

Confidence in the computer model is gained by correlating the computed values of output power and phase with theoretical design curves, published theoretical values, and published measured results over geophysical surfaces.

A1.2.1 Theoretical design curves.

The output power and phase from single and multiple layered complex dielectric material, for both parallel and perpendicular polarization, at normal and oblique incidence is computed. These computed results compare well with theoretical design curves as given by Skolnik (1990).

A1.2.2 Theoretical data.

The reflected signal from various terrestrial surfaces is computed and the theoretical results are compared with published values.

The plot giving the variation of the theoretical calculated emissivity of an ice layer with changing depth is given in figure 3.7 in this thesis (refer to chapter 3). This correlates well with the plot given by Ulaby *et al.*, 1986, chapter 18, p.1483.

As an additional example the emissivity and brightness temperatures for: soils of different moisture content for a range of incidence angles are calculated. The computed emissivity of soil of various moisture contents is plotted below (refer to figure A1.2). This also correlates well with the calculated brightness temperature given by Ulaby *et al.*, 1986, chapter 19, p.1523.

i)

Theoretical computed emissivity of dry, moist and wet soils.
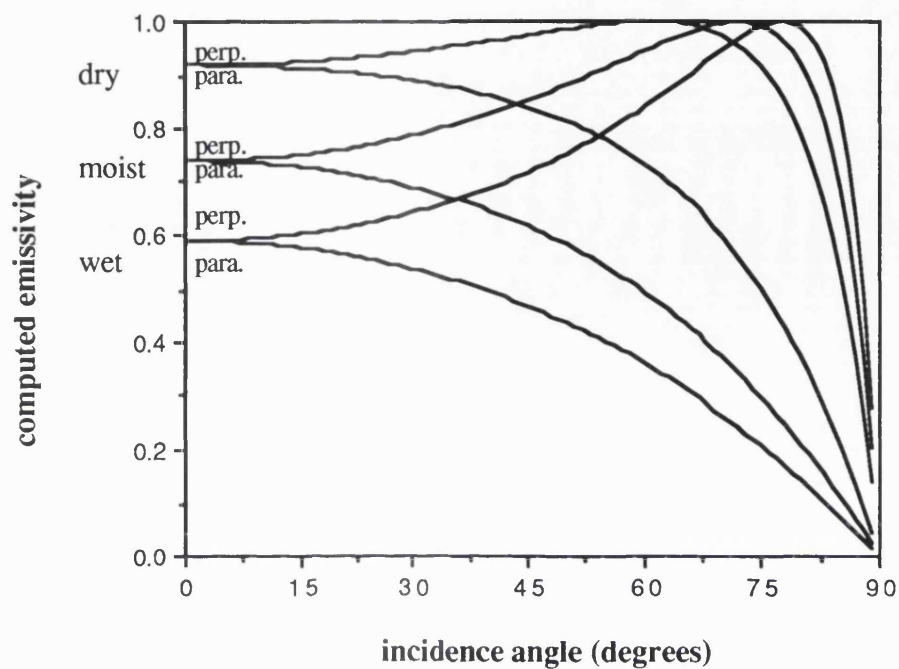
ii)
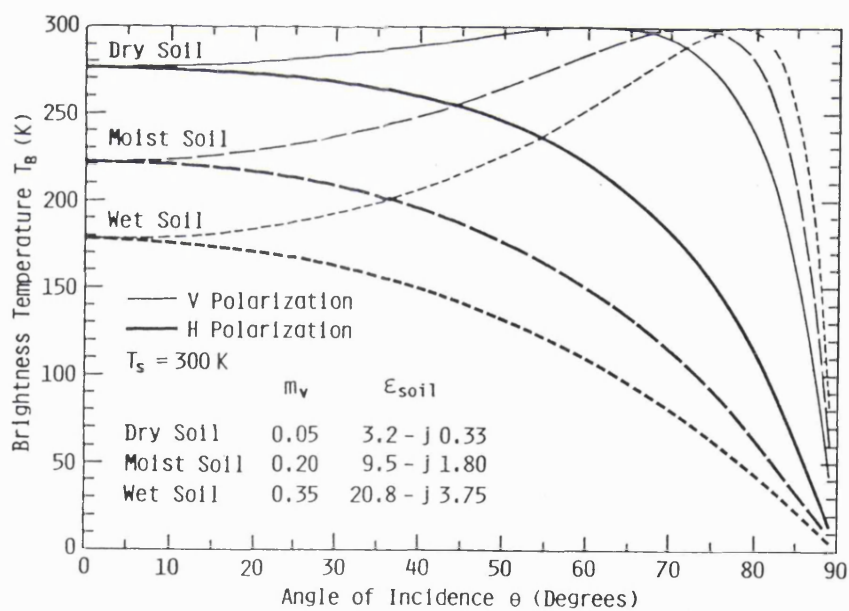
Figure A1.2: i) Theoretical computed emissivity of dry, moist and wet soils, over a range of incidence angles 0-90°:

ii) published data from Ulaby *et al.*, 1986, chapter 19, p.1523.

A1.2.3 Measured data.

Published measured results from field campaigns in Antarctica and the Alps (Sturm and Rott, 1992; Rott *et al.* 1992) are used as input data for the computer model. The theoretical computed reflected signal is compared with the field measurements of brightness temperature and polarimetric data of the test-sites as measured by the NASA/JPL DC8 AIRSAR.

A1.2.3.1 Antarctica field data.

Field measurements (Feb.1992) from the Ronne Ice Shelf, Antarctica are used as inputs to the model (Sturm and Rott, 1992). A 5m deep snow pit is sampled and measurements of snow density and temperature are made for the snow layers at 50mm intervals. The presence of an ice layer is also noted (layer 39). The measured data are given in figure A1.3 below.

Snow cover profile from a 5m deep pit near location D236 on Ronnne Ice Shelf, Antarctica (-77°55'22"/-55°55'19"), 9. Feb. 1992.

Abbreviations: ri - rime, dr - depth hoar, cr - crust (wind blown or clustered grains after a melt-freeze cycle), ice - horizontal icelayer.
Grain size estimated individually. Hardness classified by "Hand test". Very soft - R1, Very hard - R5, Ice - R6, respectively.
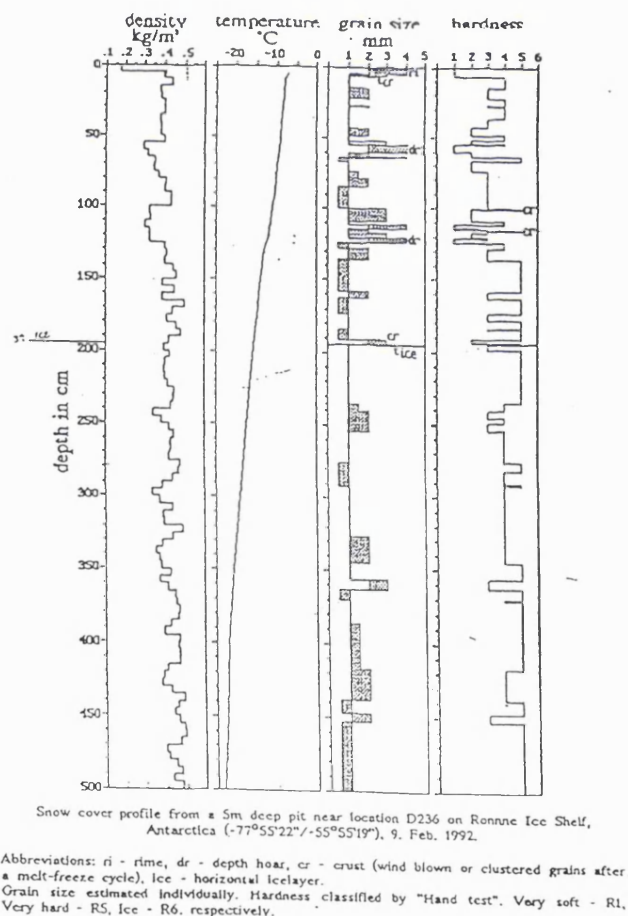
Figure A1.3: Antarctic snow layers data.

The values of snow density and temperature are used to infer the dielectric constant of each of the snow layers.

The real part of the dielectric constant, Er, is calculated from the snow density using the relationship:

$$Er = (1 + 0.51\rho_s)^3$$

from Glen and Paren, 1975; Ulaby *et al.*, 1986, Appendix E, p.2061, 2080.

The imaginary part of the dielectric constant is dependent on the temperature (and density, and frequency), Ulaby *et al.*, 1986, Appendix E, p.2066.

The values of Er, $\tan\delta$ for the 100 layers of snow as measured are used as input for the program. The theoretical emissivity (α(1-reflected power)) for a range of incidence angles is computed and plotted for both C and X band data sets. The average values of emissivity for each set of data is also computed and plotted.
The computed theoretical emissivity is found to correlate well with the field measurements of brightness temperature.

Figure A1.4 gives i) the computed emissivity of Antarctic snow layers, average value, C band data and ii) the measured brightness temperature.

i)

Theoretical computed C band emissivity for Antarctic snow layers.
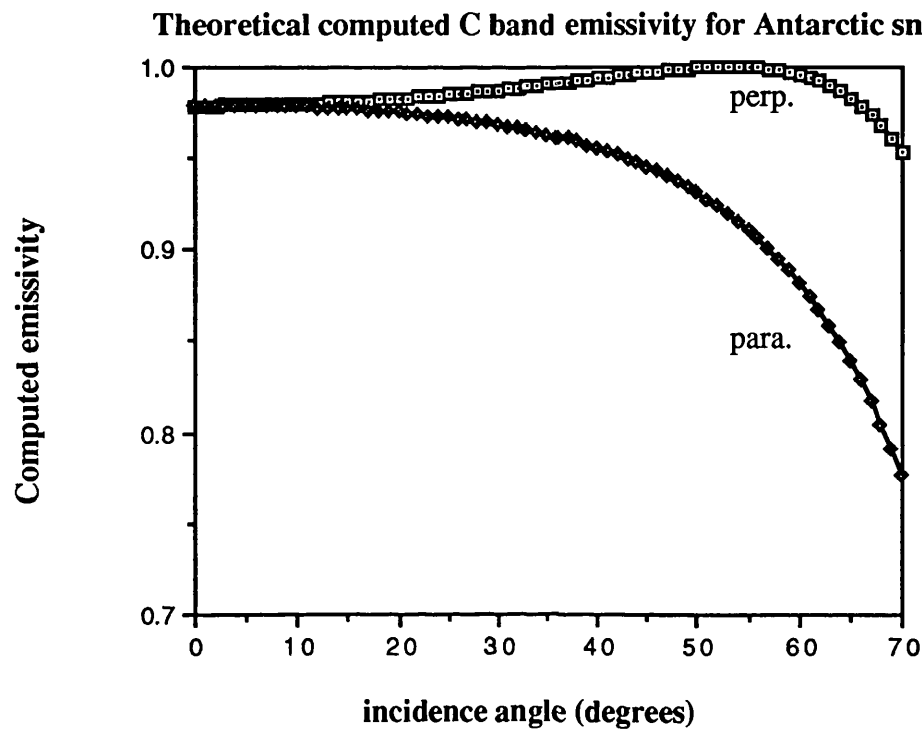
ii)
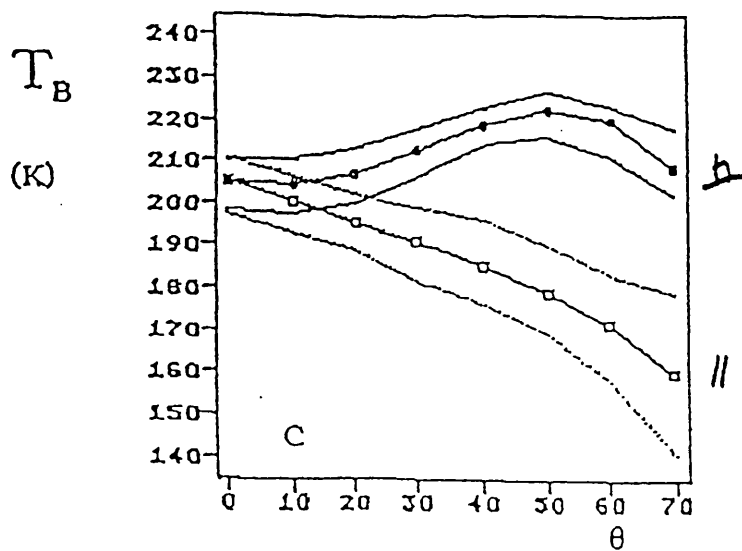
Figure A1.4: i) Computed emissivity of Antarctic snow layers, average value, C band data, and ii) the mean measured brightness temperature for perpendicular and parallel polarizations, dark and light data points (dotted lines indicating the range of measured values).

A1.2.3.2 Alps field data.

The dielectric content of a wet snow covered test-site in the Alps is determined by field measurements (Summer 1991) prior to an overflight by the NASA/JPL AIRSAR (Rott *et al.*, 1992). This information about the snow cover is used as data input for the computer model. The top layer of the snow cover is wet snow (6% water content) and extends to a depth of 1.5m. The underlying layer of drier snow (2% wetness) extends a further depth of 0.5m, and a lossy layer to simulate the ice is added below (of depth equal to the skin depth of ice at the operating frequency). The values of dielectric constant to describe these layers (from Rott *et al.*, 1992) are given in table A1.1 with a diagram showing the modelled snow and ice layers (figure A1.5).

The theoretical polarization response for 45 degrees incidence angle is computed. The co and cross polar C band response is given in figure A1.6, together with the C band AIRSAR polarimetric response for this test-site.

The C band response as measured by the AIRSAR over an artificially rough surface is also given.

Using the Barrick (1968) formula for rough surfaces, the co polar response HH, VV values are calculated.

Dielectric values and skin depths (m)

material	C band		
	Er	tanδ	skin depth (m)
6% snow	2.95	0.1936	0.054
2% snow	2.32	0.0819	0.144
pure ice	3.15	0.0032	3.172
	L band		
6% snow	3.23	0.05263	0.841
2% snow	2.41	0.02365	2.167
pure ice	2.95	0.00034	137
	P band		
6% snow	3.25	0.01877	7.055
2% snow	2.42	0.00826	18.579
pure ice	2.90	0.00038	370

Table A1.1: Dielectric values for 6%, 2% snow and pure ice (from Rott *et al.*, 1992).
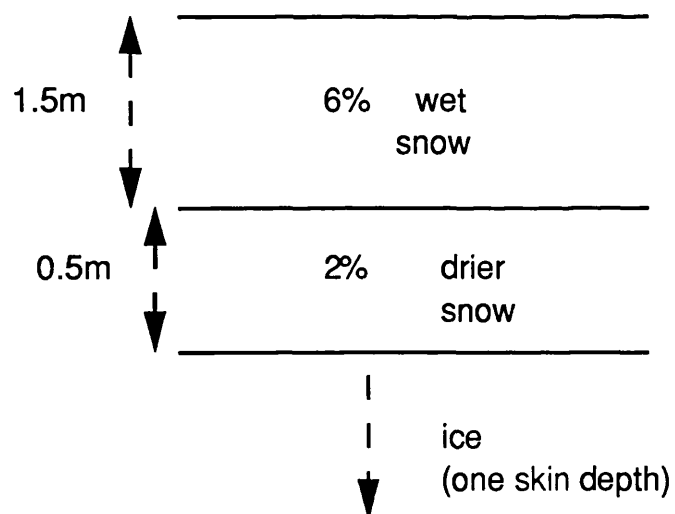
Figure A1.5: Diagram of snow/ice layers for Alpine test-site.

i)

ii)

iii)

iv)

C-band

v)

vi)
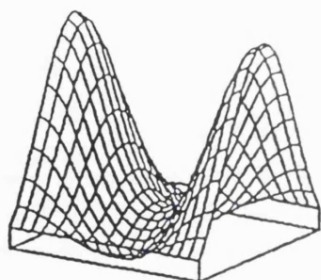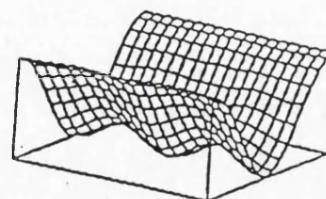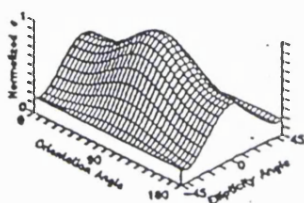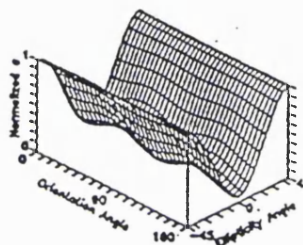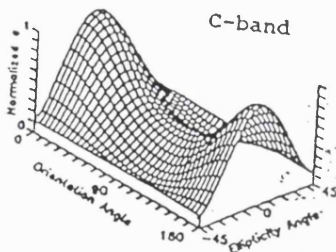
C-band

HH 0.4326

VV 1.0

HV 0.6584

Figure A1.6: i + ii) computed co and cross polar response for C band data,
iii + iv) AIRSAR co and cross polar response for test-site, also
v) measured co polar response for roughened test-site, and
vi) computed co polar response (linear polarizations HH, HV, VV values only) for rough
surface.

The figures A1.6 i) to vi) given above show that the basic shape of the computed C band response for cross polar (ii) is comparable to that of the measured AIRSAR data (iv), but the co polar response as computed (i) is more similar to the measured response from the roughened test-site (v) than that of (iii).

Note that the measured P band polarimetric response from previous campaigns over the same region (1989) shows much higher HH value than VV, but this is not seen in the 1991 results.

The rough response (vi) as computed is similar to the measured co polar response (iii) for the test-site. The normalized fractional values HH, VV and the pedestal height of the computed and measured data are given in table A1.2 below.

normalized fractional (co polar) return power

data	HH	VV	pedestal height
computed i)	1.0	0	0.0982 (apparent)
measured iii)	~0.6	1.0	~0.2
measured v)	1.0	~0.3	~0.1
computed vi)	0.4326	1.0	0

Table A1.2: Measured and computed co polar return power.

Note that the apparent pedestal height (= 0.0982) of the co polar response as calculated (i) for the smooth surface is of the same fractional value (~0.1) as the pedestal height of the measured response for the rough surface at the test-site (v).

The relative HH and VV values of the measured co polar response for the test-site surface (iii) gives HH/VV ~=0.5 if the pedestal height is ignored. The HH/VV ratio as calculated for the rough response is 0.4326 using the Barrick equations.

A1.3 Theoretical investigations.

A1.3.1 Theory of Brewster work.

The Brewster angle is given by $\theta_B = \tan^{-1}(\sqrt{Er})$. At this incidence angle the reflected signal for perpendicular polarization is of zero power and undergoes a rapid phase change of 180°.

For an example dielectric (Er = 4.2) the reflected signal from both a loss-less ($\tan\delta = 0$) and lossy ($\tan\delta = 0.014$) material is considered. The discontinuity at the Brewster angle (= 63.99°) is found to give a sudden discontinuous phase change of 180° for the loss-less material, and undergoes a sudden, but continuous, phase change of 180° for the lossy material. This behaviour of the reflected signal is as according to theory given by Hecht and Zajac (1974).

Figure A1.7 gives the sudden continuous 180° phase change of the computed reflected signal (perpendicular polarization) at the Brewster angle for the lossy dielectric material (Er = 4.2, $\tan\delta = 0.014$).

Phase change at Brewster angle (perpendicular polarization).
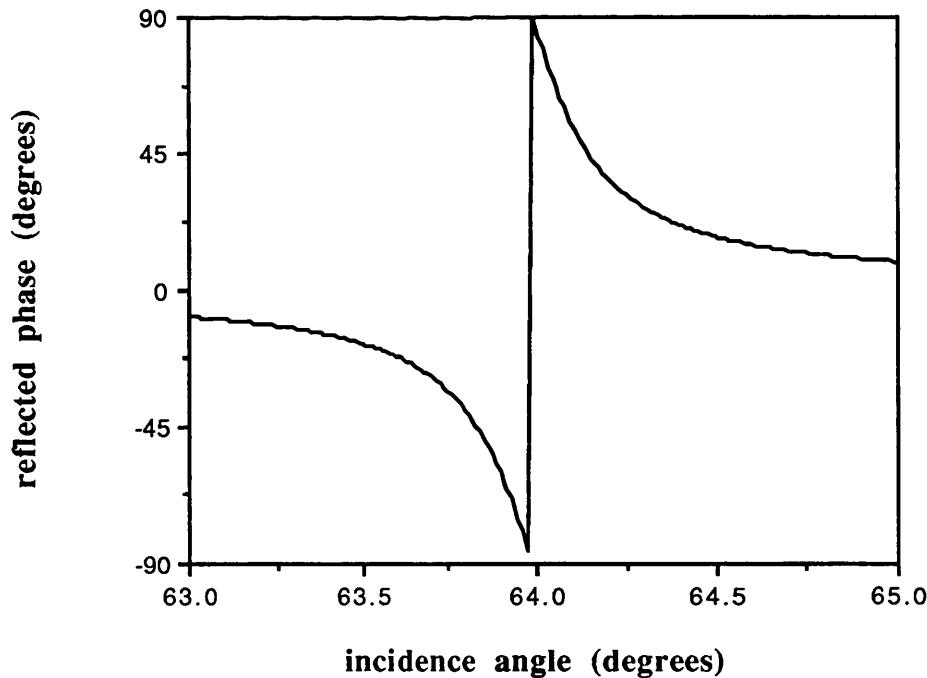
Figure A1.7: Continuous reflected phase change of 180° at Brewster angle for lossy dielectric (Er = 4.2, $\tan\delta = 0.014$), perpendicular polarization.

A1.3.2 Depth work.

The penetration depth of radar signals is given by the value of skin depth (refer to chapter 2, section 2.1.4.1.2).

The change in the reflected signal (amplitude and phase data) is investigated for normal incidence on a layer of variable depth. Increasing the depth of the single layer of complex dielectric material and considering the reflected power and phase shows that the reflected power and phase tends to converge to a constant value. The oscillatory nature of the return signal before this depth is reached is due to multiple reflections taking place within the layer. Multiple reflections do not take place when the depth of the material is such that very little power reaches the bottom surface of the material and an approximately constant value for the return signal is then achieved (equal to the Fresnel value for the material at the operating frequency). The depth at which this occurs may usually be taken to be around 2.5*skin depth of the material, where the skin depth, δ_S (mm), is given by:

$$\delta_s = \frac{300}{\pi \, F \sqrt{Er} \, \tan\delta}$$

The skin depth for the material considered ($Er = 4.2$, $\tan\delta = 0.014$, at 2GHz) is 1.664m. The Fresnel value of reflectivity is 0.118 (power).

An approximately constant value of reflected power (0.118) is reached by a depth of 4m.

Variation of reflected signal with increasing depth of layer.

Figure A1.8: Variation in reflected power and phase due to increase in depth of layer for normal incidence ($Er = 4.2$, $\tan\delta = 0.014$).

This effect may be seen in the plots for terrestrial surfaces used for the validation analysis work. Refer to figure 3.7, chapter 3, in this thesis for depth change plots of an ice layer over sea water.

A1.3.3 Time work (transients).

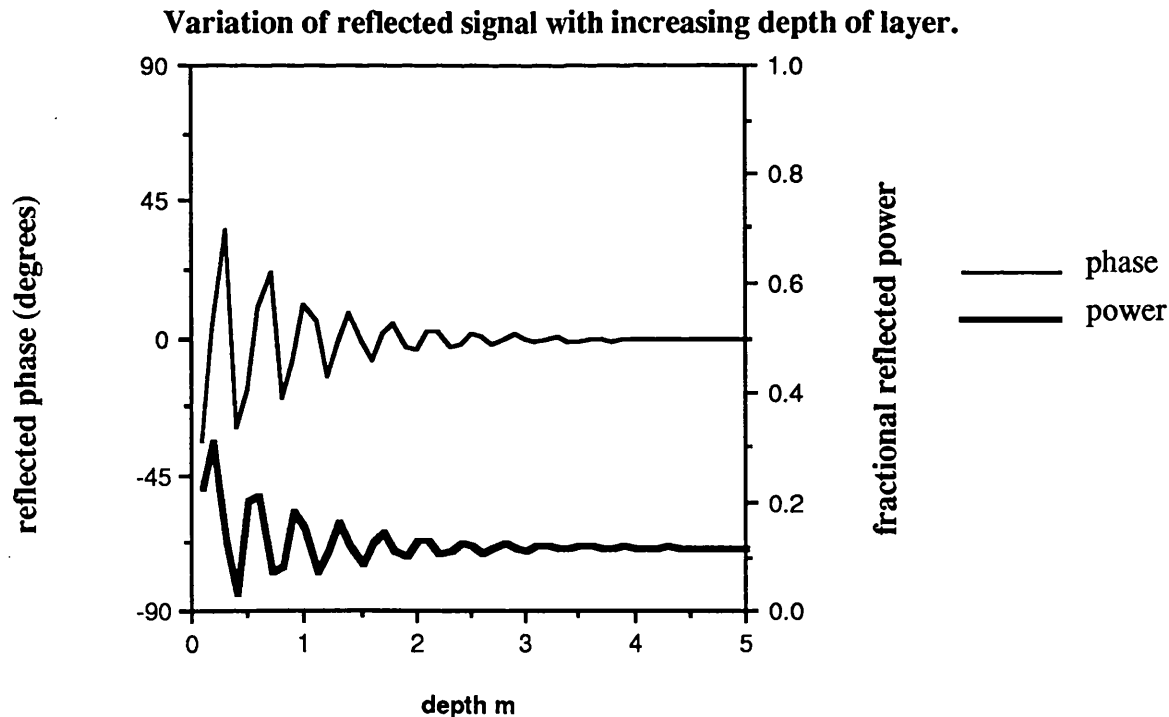The variation of the reflected signal with time is calculated as multiple reflections take place within a layer of finite thickness. For this theoretical work a layer of lossy dielectric (Er = 4.2, tanδ = 0.014) of thickness 15mm, operating frequency 2GHz, 0 degrees incidence is used. The variation of the output signal with time is investigated. The initial response is given by the Fresnel reflectivity of the surface, then a transient signal is obtained before the steady-state signal is reached.

This effect may be noted for natural surfaces where a distinct surface layer occurs, for example, as discussed in chapter 2 and above, for a layer of sea ice over sea water, or a layer of ice over a lake.

For the polar surfaces a distinct surface layer may also occur where a distinct saturated snow layer occurs over the surface of a glacier, or where a thin layer of surface water exists. The presence of a surface crust (from an icy frost layer for example) could also produce a distinct surface layer causing this effect.

A subsurface discontinuity could also produce a distinct layer, for example the ice layers produced at depth due to the compaction of snow and depth hoar formation and unique frost or wind events.

The signal received by remote sensing instruments is time dependent. The actual received signal (power and phase information) depends on how the instrument measures the data, and how this data is processed.

The Fresnel value (initial signal) is usually used in interpreting the data, but this may not be accurate enough as the steady state response may be rather different as shown in figure A1.10 below.
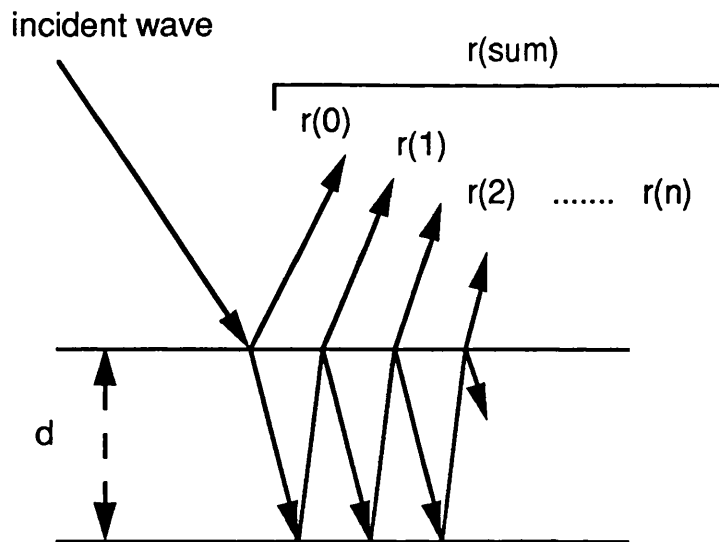
Figure A1.9: Transient signal from single layer due to multiple reflections.
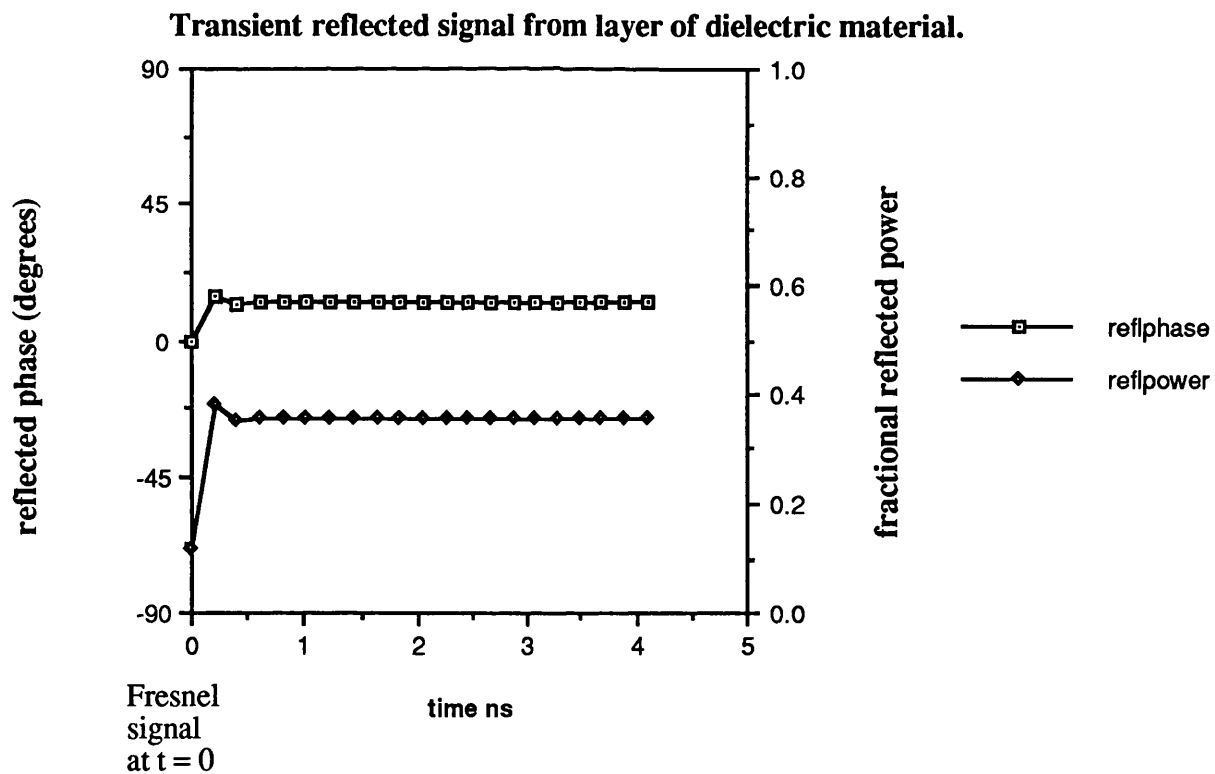
Figure A1.10: Plot of the transient signal attained from a single layer of dielectric material (Er = 4.2, tanδ = 0.014).

The transient signal (r(t)) may be greatly different to the initial Fresnel value (r(0)) , and may differ from the steady-state signal (r(sum)).

In the above example the reflected power and phase varies as shown in figure A1.10 with the values tabulated below (table A1.3):

signal	time(ns)	reflected phase(deg.)	reflected power(fractional)
r(0)	0	-0.5	0.1184
Fresnel			
r(0)+r(1)	0.204	14.57	0.3800
Transient, sum to t = 1			
r(sum)	~4	12.40	0.3539
Steady-state			

Table A1.3: Components of reflected signal.

The relative values of output power are given by:

$$10\log_{10}\left[\frac{(r(0)+r(1))}{r(sum)}\right] = +0.3dB$$

$$10\log_{10}\left[\frac{r(sum)}{r(0)}\right] = +4.75dB$$

$$10\log_{10}\left[\frac{(r(0)+r(1))}{r(0)}\right] = +5.06dB$$

The power received is therefore dependent on the part of the reflected signal received. The actual values depend on the surface variables.

The value of the Fresnel reflection coefficient is compared with the multiple reflected signal (steady state value). For the above case there is ~5dB difference. This is equivalent to ~3 times the received power.

A1.3.4 Reflected signal variation with dielectric constant, and angle of incidence.

A theoretical investigation of the variation of the reflected signal (amplitude and phase) with change in dielectric constant (Er, tanδ) and incidence angle is undertaken.

The reflection coefficient r_{ab} (at boundary between materials a:b) may be written as :

$$r_{ab} = M1\,e^{-jM2}$$

where amplitude, $M1 = \dfrac{\left(\sqrt{Er} - 1\right)}{\left(\sqrt{Er} + 1\right)}$

and phase, $M2 = \tan^{-1}\left(\dfrac{\sqrt{Er}\,\tan\delta}{Er - 1}\right)$

The reflected power is independent of $\tan\delta$, but dependent on Er. An increase in the real part of the dielectric constant, Er, causes more reflected power (due to the greater discontinuity).

The reflected phase is dependent on both Er and $\tan\delta$. Increasing $\tan\delta$ increases the phase change of the reflected signal. Increasing Er is seen to decrease the phase change for the same $\tan\delta$.

A1.4 Method of classification of imaged terrain - the effect of frequency, dielectric constant, incidence angle and depths of layers.

The polarimetric content of the return signal varies with the operating frequency of the radar, the complex dielectric constant of the imaged terrain, the angle of incidence of the radar and the position and depths of layers. The change in the position of the theoretical polarimetric signal on the power ratio vs. phase difference plots for each of these variables is investigated below.

A1.4.1 Theoretical power ratio versus phase difference plots for polar surfaces.

The theoretical power ratio versus phase difference plots for various types of polar surfaces are plotted for C, L, and P band, for a range of incidence angles. The polarimetric reflected signal for snow of different moisture content (0, 6, 15% water content by volume) and for pure ice and free water is analysed to produce the power ratio vs. phase difference plots for these surfaces.
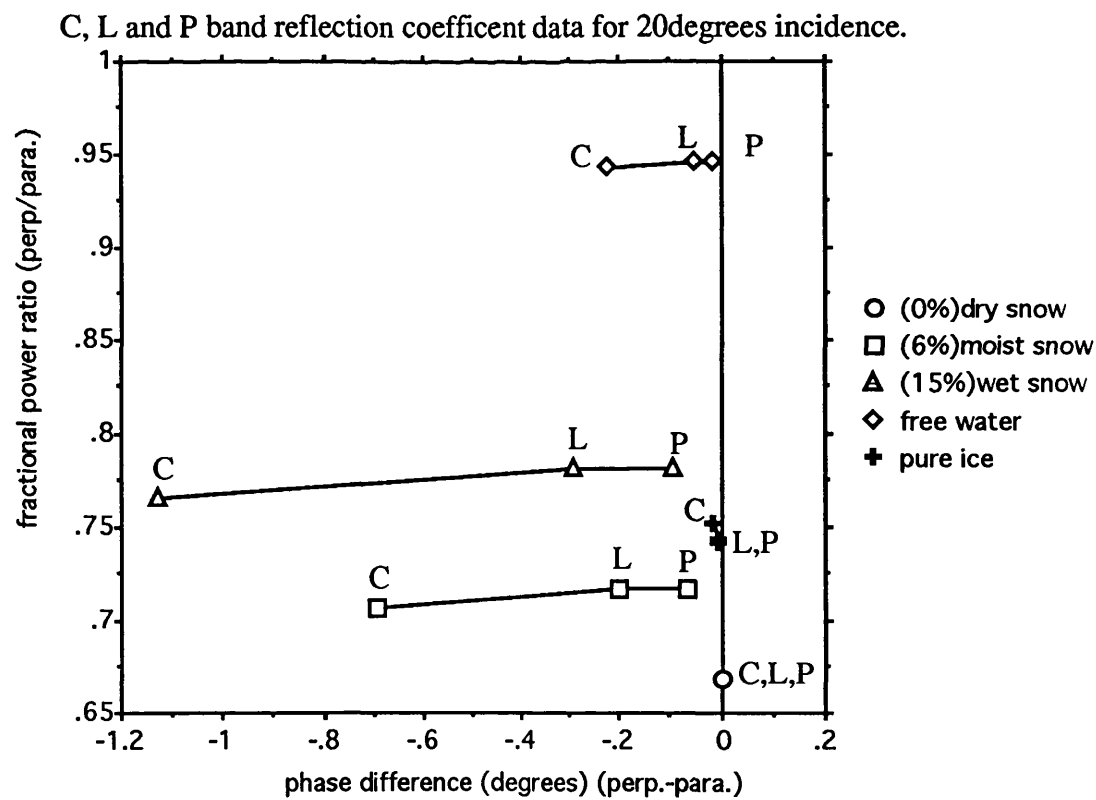
Figure A1.11: Theoretical power ratio vs. phase difference plot for various polar surfaces for C, L and P band, reflection coefficient for 20 degree incidence angle.

Theoretical C band data is found to give more distinct classification for the types of polar surfaces considered. L and P band give less distinct areas for the different surfaces on the power ratio versus phase difference plots, but the multifrequency data may be used to confirm the prediction gained from C band data.

As an example the theoretical C band power ratio versus phase difference plot for dry snow and free water is given in figure A1.12. The values for 20 to 60° incidence angle are given to correlate with the typical range of incidence angles covered by the NASA/JPL AIRSAR.

Using these plots the content of the surface material may be inferred from the polarimetric reflected signals and the terrain may be classified. The power ratio versus phase difference method of analyzing the polarimetric reflected signal gives a method of classification of polar terrain without any prior knowledge of the surface or ground data. This method is applied to airborne SAR measurements of the Greenland ice sheet in chapter 5, section 5.1.6.

Theoretical Cband plot for free water and dry snow surface 20 - 60 degrees incidence.

free water
θ increasing

dry snow
θ increasing

□ dry snow
♦ free water

fractional power ratio (perp./para.)

phase difference (degrees) (perp.-para.)
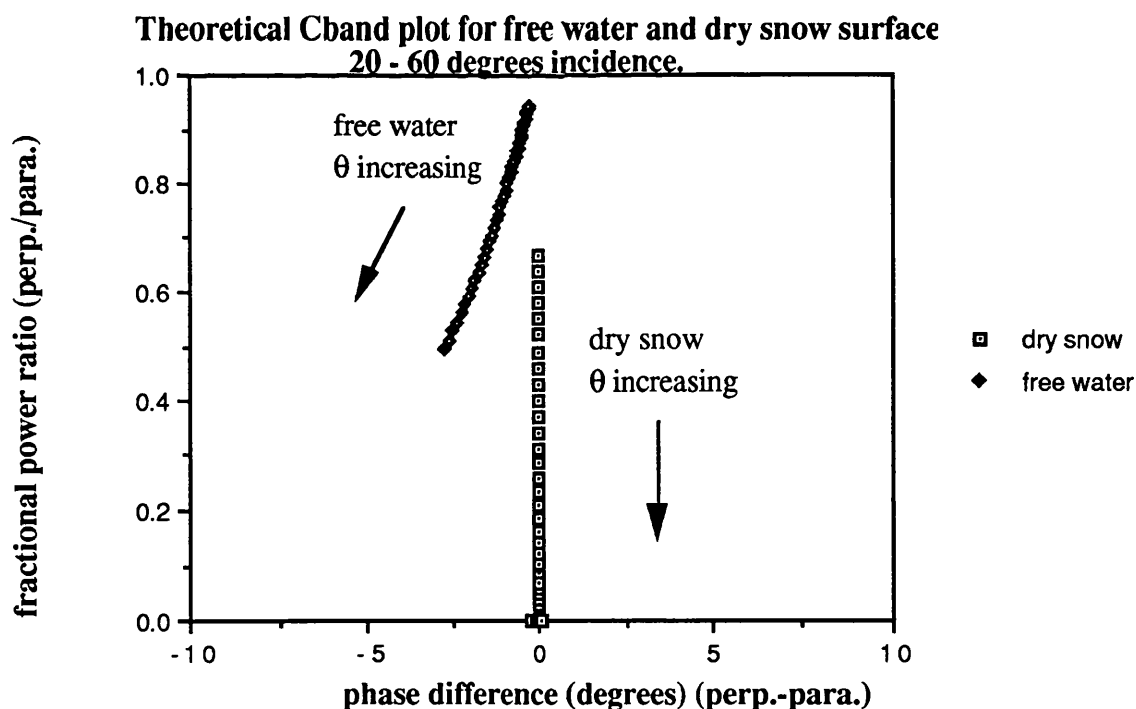
Figure A1.12: Theoretical C band power ratio versus phase difference plot for reflection coefficients of free water and dry snow surfaces for 20 - 60° incidence angles.

A1.4.2 Theoretical analysis of the variation in position of points on the power ratio versus phase difference plots.

In order to investigate the sensitivity of the position of points on the power ratio versus phase difference plots, the dependence on the dielectric constant is studied. Both the real and imaginary parts of the dielectric constant are changed and the resulting change in position of the point on the power ratio versus phase difference plot is noted. Figure A1.13 shows the change in position on the plot due to the change in the real and imaginary components of the complex dielectric constant.

Theoretical plot for dielectric change at 20 degree incidence.
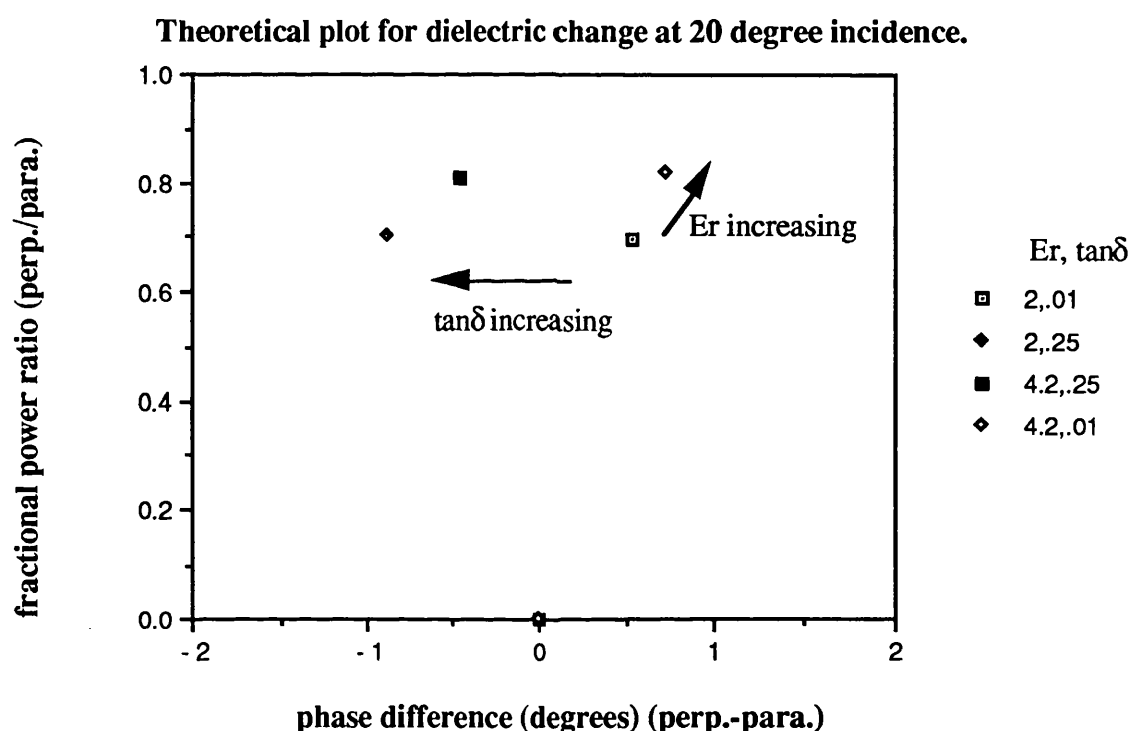
Figure A1.13: Movement of point position on theoretical power ratio versus phase difference plot due to change in values of the complex dielectric constant; Er (2 to 4.2) and tanδ (0.01 to 0.25), reflection coefficient for 20° incidence angle.

A1.4.3 Theoretical change with layer depth and incidence angles for polar surfaces.

The theoretical C band power ratio vs. phase difference plot for a layer of dry snow of changing depth (to 3*skin depth) is given for a range of incidence angles (figure A1.14). The values of the depth change of the layer of dry snow are from 25 to 700m, in 25m increments (skin depth of dry snow is 233m at C band).

The response for 20 to 60° incidence angles is given to correlate with typical NASA/JPL AIRSAR values.

Similar plots from measured data over polar surfaces may be compared with these theoretical plots to infer the likely content. If the incidence angle is known, the position of the measured data point on the power ratio vs. phase difference plot for co polar signals will indicate the likely surface material.
Information from multifrequency data sets may be used to confirm the prediction from C band data.

The terrain may therefore be classified into dielectric content, and hence the material type (e.g. dry snow, free water, pure ice for the polar surfaces) and the measured data may also possibly be used to infer the depth of layers of material. This method of terrain classification does not require any prior knowledge of the surface.
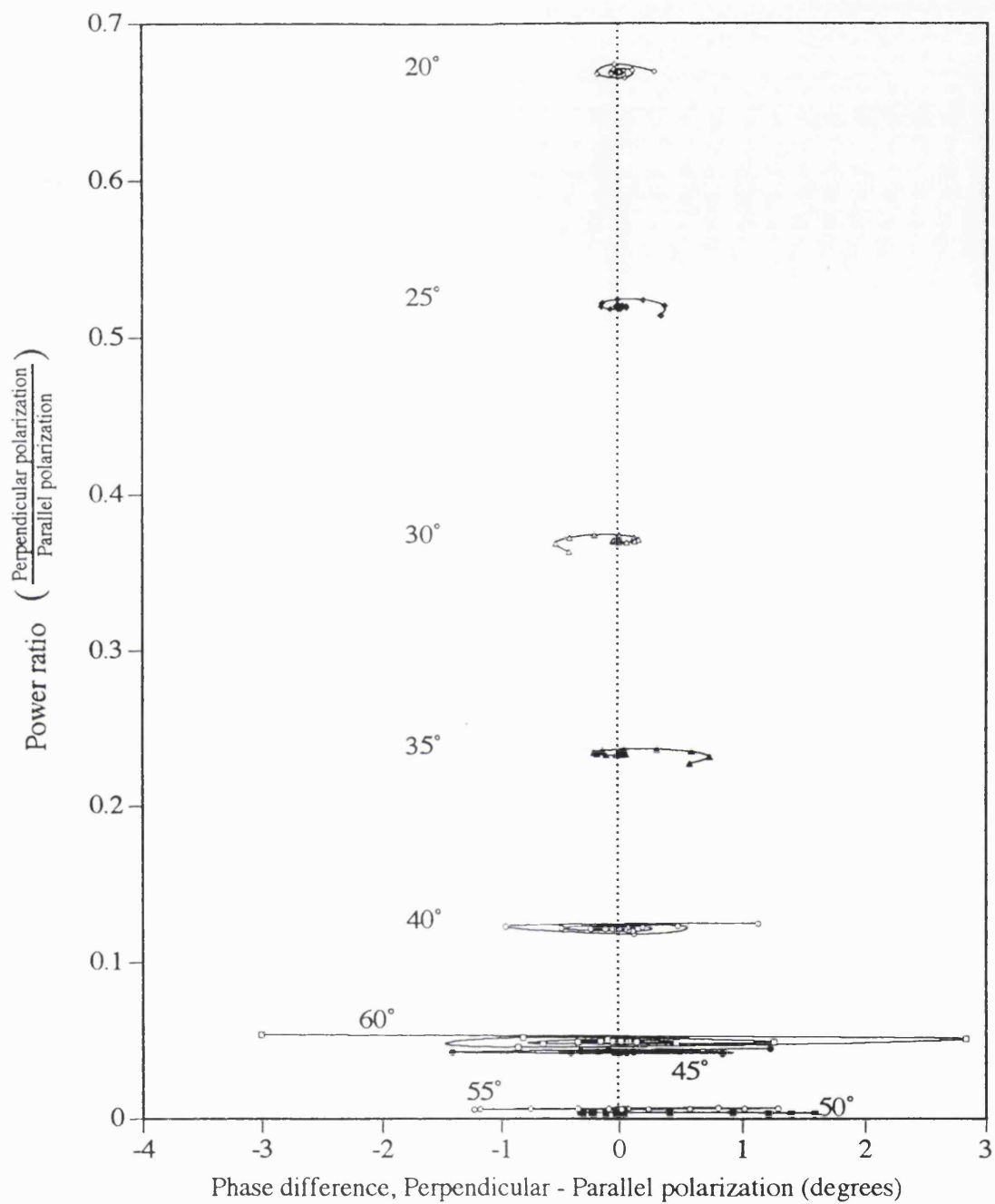
Figure A1.14: Theoretical C band power ratio vs. phase difference plot for a layer of 0% snow of changing depth to ~3*skin depth (from 25 to 700m, in 25m steps) for a range of incidence angles (20 to 60°).

A1.5 Theoretical polarization ratio.

The theoretical polarization ratio of emitted radiation (Epara/Eperp) is plotted for a range of dielectrics i) Er = 1 - 3, and ii) Er = 2 - 80, for values of local incidence angle 45.2^{o}, 53.2^{o} and 61.2^{o} (figure A1.15).

These theoretical values may be used in the inversion technique (section 3.4.3) to give the dielectric and % wetness of the surface from measured passive microwave data.

i) Er = 1 - 3

Theoretical polarization ratio, Er = 1 - 3, incidence angle 45.2, 53.2, 61.2 degrees.

ii) Er = 2 - 80

Theoretical polarization ratio, Er = 2 - 80, incidence angle 45.2, 53.2, 61.2 degrees.
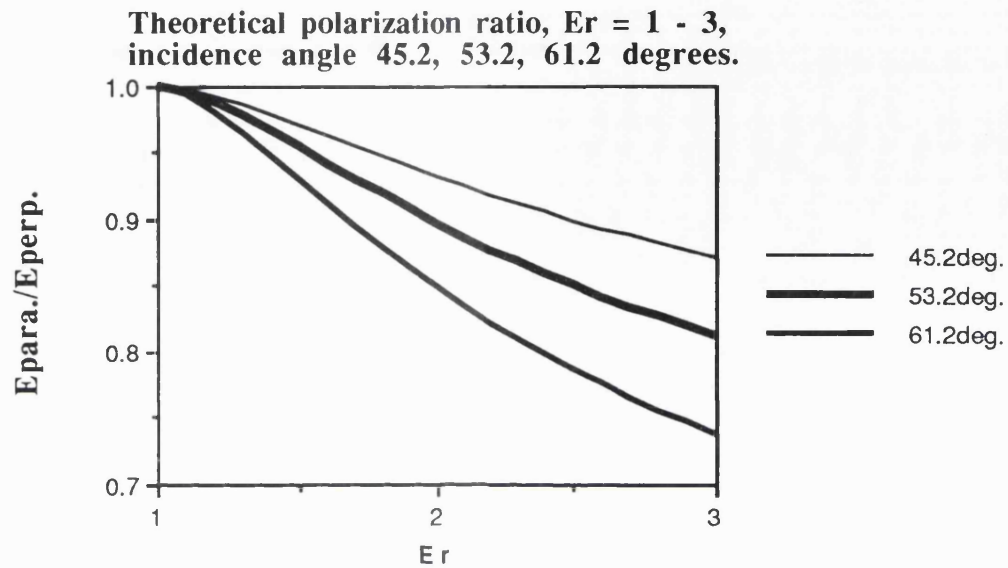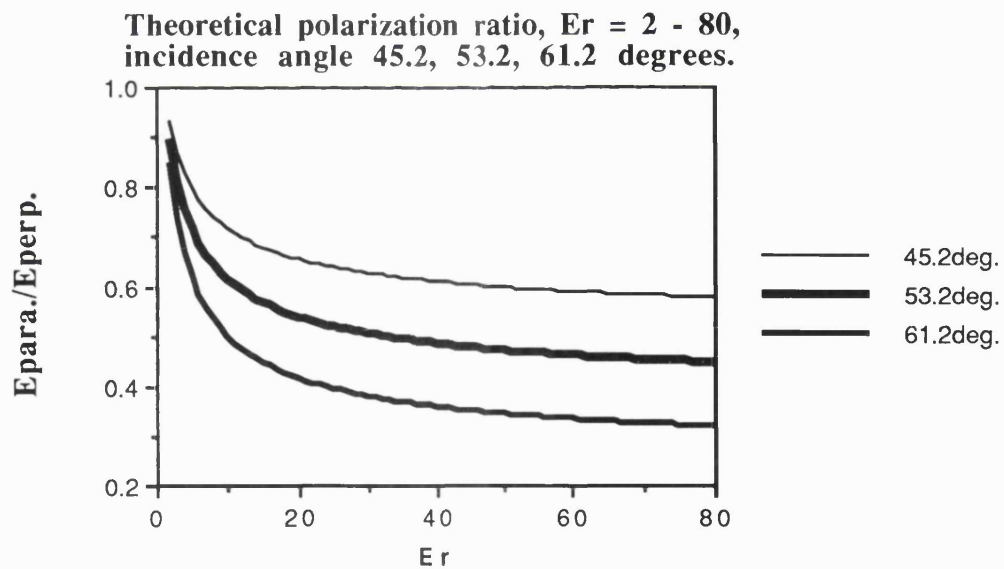
Figure A1.15 i and ii): Theoretical polarization ratios Epara/Eperp for range of dielectrics i) Er = 1 - 3 and ii) 2 - 80 for incidence angles 45.2º, 53.2º and 61.2º.

A1.6 Statistical analysis.

A1.6.1 Mean power ratios and phase differences for the two polarizations.

A line average of data is used in the analysis of the P3206 image (i10). The average value of the complete line of data is taken to maximize the sample size at the particular incidence angle. The complete line of data consists of 1023 pixels.

The standard software package (MacSigma0-II) as supplied by JPL (Norikane, 1992) calculates the mean value of the co polar return power for each of the two polarizations HH and VV. These values are then used to calculate the "mean" value of the return power ratio VV/HH for the line. This value is, however, not equal to the mean of the sum of the individual ratios VV/HH calculated for each pixel of the sample.

i.e.

$$\frac{\frac{1}{n}\sum_{i=1}^{n} VV_i}{\frac{1}{n}\sum_{i=1}^{n} HH_i} \neq \frac{1}{n}\sum_{i=1}^{n} \frac{VV_i}{HH_i}$$

where HH_i and VV_i are the return power values for horizontal and vertical polarization respectively for each pixel, and n = 1023, the number of individual pixels in the line, for a line average.

The individual power ratios for each of the pixels could be determined by further analysis of the image, but this would need changes to the JPL software.

However the mean phase difference between the two polarizations (VV-HH) for the complete line of data as calculated by the standard software is equal to that of the average for each of the pixels.

i.e. average phase difference is given by:

$$\frac{1}{n}\sum_{i=1}^{n}\left(\phi VV_i - \phi HH_i\right)$$

where the values of the return phase for the two polarizations are given here by ϕVV and ϕHH.

The precise location of the snowpits are not given [(i, j) coordinates within the image].

The line of the image containing each snowpit is determined from the site map given in figure 4.1, chapter 4. The "j" value of the position of the snowpit is determined by correlating to the j value of the location of the relevant corner reflector which is identified by the very bright (high power) return in the Total Power image. The snowpit of interest for the ice layer work in chapter 5 is positioned in line number 33 from the top of the image. The average of this line of data is therefore used for the analysis work.
This assumes that the physical properties of the imaged terrain are similar across the image, which is not necessarily true. For more accurate results the precise location of the snowpit is needed.

A1.6.2 Standard deviation.

The relative standard deviation ($\sigma_{relative}$) of the mean values (m) of the return signals for the two polarizations are given by the standard software. For the line average of data the relative standard deviation of the mean HH and VV return power, and the standard deviation of the mean (VV-HH) phase are given in table 5.2, chapter 5. The standard deviation (σ) of the mean HH and VV return power are calculated and given in table 5.3, chapter 5, where:

$$\sigma_{relative} = \left(\frac{m + \sigma}{m} \right)$$

The standard deviation of the phase signal is 8.31 degrees, and this value is used to give the error bars ($\pm$ 1s.d) for the measured data point on the x axis of the power ratio vs. phase difference plot (figure 5.14, chapter 5). This range gives the 68.3% confidence interval, assuming the data are of a Gaussian (normal) distribution.

The relative standard deviation for the mean power ratio VV/HH cannot be determined from the relative standard deviations of the mean VV and HH values. To determine the standard deviation of the mean VV/HH for the data, the individual values of the VV/HH ratio must be calculated for each pixel, and the mean (m) determined. The standard deviation (σ) may then be calculated by the difference of each VV/HH value (x_i) from the mean (m) as follows:

$$m = \frac{1}{n} \sum_{i=1}^{n} \frac{VV_i}{HH_i}$$

$$x_i = \frac{VV_i}{HH_i}$$

$$\sigma^2 = \frac{1}{n} \sum_{i=1}^{n} (x_i - m)^2$$

or

$$\sigma^2 = \frac{1}{n} \sum_{i=1}^{n} x_i^2 - m^2$$

The standard deviation of the mean power ratio for the image cannot be determined with the present version of the JPL software. There are therefore no error bars plotted for the measured data point on the vertical (y) axis of the power ratio vs. phase difference plot (figure 5.14, chapter 5).

A1.7 NASA/JPL AIRSAR measured polarization response (233-1 image).

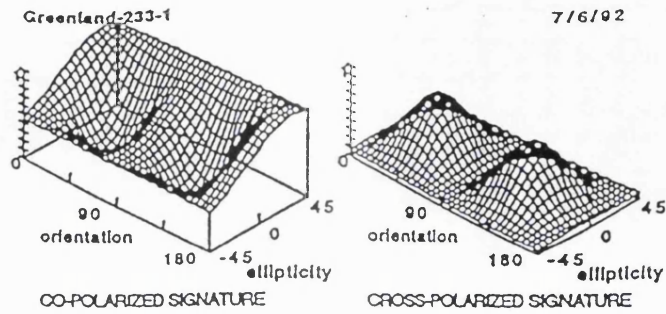### A1.7.1 Variation of polarization response with incidence angle.

The polarization response plots for line averages of the C band 233-1 image at 20°, 40°, and 60° incidence angles shown in figure A1.16 are all of double bounce form, which indicates that this is the dominant scattering mechanism. The pedestal height of the plots increases on increasing the incidence angle from 20 to 40°, and then remains at a constant level (~0.8 of normalized plot) for further increases in incidence angle up to ~60°. This shows that the contribution from diffuse scattering increases with incidence angle up to 40° incidence and then remains at a constant value for further increases in incidence angle. The polarization responses for single pixels taken from positions down the centre line of the image are of the same form as the mean value for the corresponding line average. The co polar response for 20° incidence shows a tilt (LHS < RHS) but the cross polar response has a small even pedestal. On increasing the incidence angle (above 30°) the pedestal for co polar plots becomes level.

The basic shape (double bounce) of the polarization response does not change throughout the image. This is rather unexpected as the incidence angle varies from 20° to 60° down the image, and these results would suggest that the scattering mechanism is independent of incidence angle. Alternatively, if the signal to noise ratio is small for the C band measurements (as suggested by van Zyl, personal communication, June 1992) the results from detailed analysis of the signal may be misleading. The actual return power for this data set is low and the absolute power value is not given. The relative difference in the power values for each polarization and for each area of different intensity is therefore studied.

A1.7.2 Variation of polarization response with intensity.

The data for each line is divided into adjacent 25 pixel samples to utilize all the information for a particular incidence angle, enabling the line to be divided up into light and dark areas with equal weighting for each point. The 25 pixel samples are grouped into bright and dark areas for this line of data. The 25 pixel samples are investigated to see if there is any difference in the shape of the polarization plots for areas of different intensity. The results for 60° incidence show that the response for areas of different intensity are slightly different (figure A1.17). The response for the 3rd sample (denoting area 2 (light)) is of slightly different form to the first two samples (denoting area 1 (dark)), and also different to the 4th and 5th samples (denoting area 3 (dark)).

i)

Greenland-233-1   7/6/92

orientation   90   orientation   90
                    180   -45   180   -45
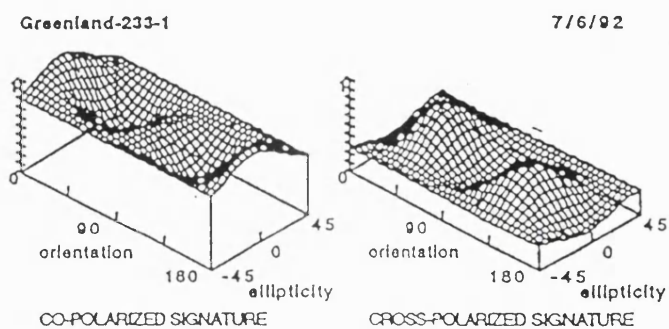   ellipticity   ellipticity
        CO-POLARIZED SIGNATURE   CROSS-POLARIZED SIGNATURE

ii)

Greenland-233-1   7/6/92

orientation   90   orientation   90
                    180   -45   180   -45
                              ellipticity   ellipticity
        CO-POLARIZED SIGNATURE   CROSS-POLARIZED SIGNATURE

iii)

Greenland-233-1   7/6/92

orientation   90   orientation   90
                    180   -45   180   -45
                              ellipticity   ellipticity
        CO-POLARIZED SIGNATURE   CROSS-POLARIZED SIGNATURE

Figure A1.16: Co and cross polar response for line averages of AIRSAR C band 233-1 image i) 20° , ii) 40° , iii) 60° incidence angle.
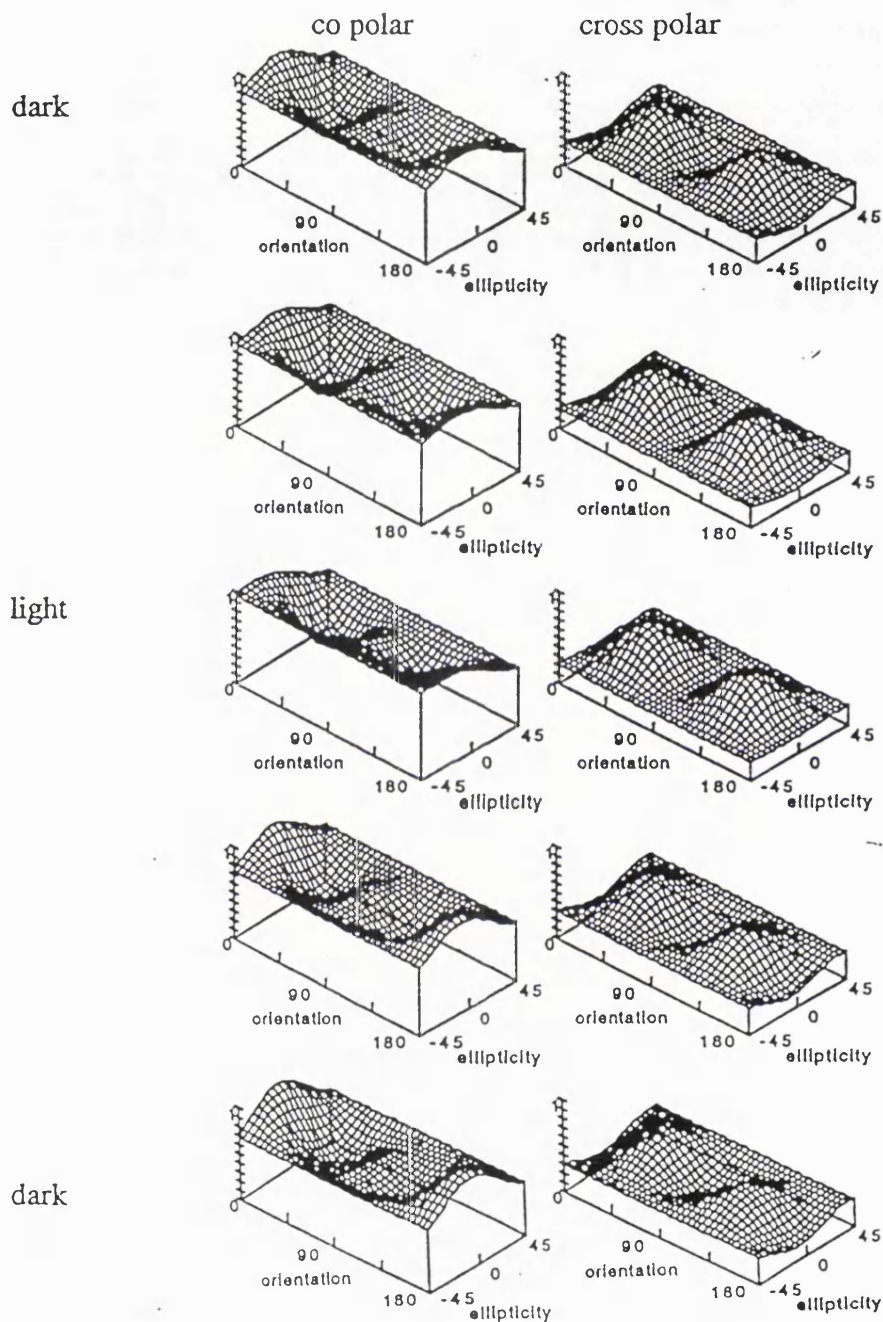
page 265

Figure A1.17: Polarimetric response for areas of different intensity C233-1 AIRSAR image, 60° incidence angle, first five samples (of 25 pixels).

A1.7.3 Physical explanation of polarimetric response.

The double bounce effect may be found in SAR images over glaciers where a distinct surface layer exists causing the reflected signal to undergo two sudden reflections as shown in figure A1.18. This could occur where an ice layer exists over a lake or where a distinct saturated snow layer occurs over the surface of the glacier, if there are discontinuities within the surface material to produce the return signal. The presence of a surface crust (from an icy frost layer for example) could also produce a distinct surface layer causing this effect. For the 233-1 image a distinct layer of saturated snow over the surface could cause the double bounce effect noted in the measured polarization response plots.
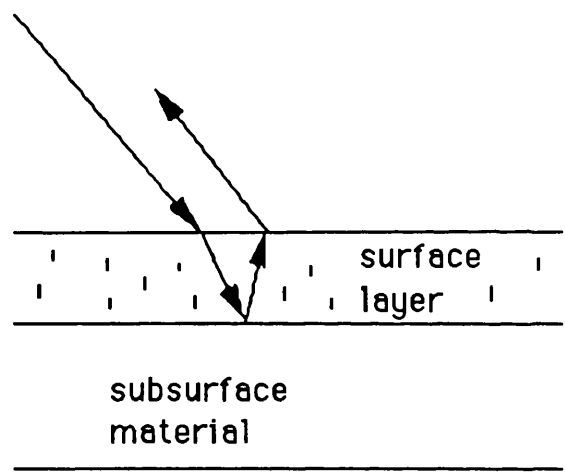

Figure A1.18: Distinct surface layer causing double bounce effect.

The thickness of the surface layer would need to be less than the skin depth for the material at the operating frequency for this effect to occur. Table A1.4 gives the values of the skin depths of typical polar materials at P, L, and C band, relating to AIRSAR frequencies.

| material | skin depths (m) for | | |
	P	L	C band
6% snow	11.9036	1.292	0.0893
pure ice	368.917	136.27	3.172

Table A1.4: Skin depths (m) of typical polar surfaces at P, L, C band.

The typical scattering mechanisms for glaciated regions is discussed in chapter 2 of this thesis (section 2.1.3). A diagram showing the main scattering sources for the ablation and wet snow region of the glacier corresponding to the area covered by the AIRSAR image 233-1 is given in figure 2.6.

The measured AIRSAR data (233-1) show that the level of the diffuse scattering component (indicated by the pedestal height of the 3D plot) increases with increasing incidence angle showing that the contribution from volume scattering increases with incidence angle. This is because the specular component from surface scattering is directed further away from the receive antenna on increasing the incidence angle and the received signal is then therefore mainly composed of the volume scattering component from diffuse scattering within the ice medium.

The tilt of the pedestal noticed for 20° incidence shows that there is a greater response for one sense of circular polarization than the other. The theoretical response for a helix gives a tilt in the co polar response but it is uncertain how this would relate to a natural surface. There may be some specific detail of the topography or content of the surface which may cause this difference in the response for the two different senses of polarization.

The slight change in form of the polarization response for areas of different intensity noted for 60° incidence indicates some change in the contribution from different scattering processes. The lighter area gives a flatter pedestal for co and cross polar response compared with the pedestal for the response of neighbouring darker areas (at the same incidence angle). The diffuse scattering component of the light area is uniform (more independent of polarization) than that for the dark areas. The light areas denote snow covered surfaces which gives a constant value of volume scattering given by the flatter response. The response from the darker areas of the seasonal melt pools are possibly slightly more polarization dependent.

"Rumpantur libros nec corda cestra rumpitur"

"Ride, ride and hurry across the sand !
The sun is sinking behind Eagle Peak
Many unclean spirits are on the move
Now that shadows start falling on the glacier.
God guide my horse !
The last stage of the journey will be hard"

- Icelandic poem